AWARD NUMBER: W81XWH-19-1-0046

TITLE: A Targeted Alpha Particle Radiopharmaceutical for Bone Metastatic Breast Cancer

PRINCIPAL INVESTIGATOR: Thaddeus Wadas, Ph.D.

CONTRACTING ORGANIZATIONS: Wake Forest University Health Sciences
University of Iowa

REPORT DATE: May 2020

TYPE OF REPORT: Annual report

PREPARED FOR: U.S. Army Medical Research and Materiel Command
Fort Detrick, Maryland 21702-5012

DISTRIBUTION STATEMENT: Approved for Public Release;
Distribution Unlimited

REPORT DOCUMENTATION PAGE

Form Approved
OMB No. 0704-0188

1. REPORT DATE	2. REPORT TYPE	3. DATES COVERED
May 2020	Annual	04/01/2019 – 03/31/2020

4. TITLE AND SUBTITLE

A Targeted Alpha Particle Radiopharmaceutical for Bone Metastatic Breast

Cancer

5a. CONTRACT NUMBER

5b. GRANT NUMBER
W81XWH-19-1-0046

5c. PROGRAM ELEMENT NUMBER

6. AUTHOR(S)

Yusuke Shiozawa, MD, PhD; Thaddeus Wadas, PhD

E-Mail: yshiozaw@wakehealth.edu, thaddeus-wadas@uiowa.edu

5d. PROJECT NUMBER

5e. TASK NUMBER

5f. WORK UNIT NUMBER

7. PERFORMING ORGANIZATION NAME(S) AND ADDRESS(ES)

Wake Forest University Health Sciences   University of Iowa
Medical Center Blvd.,   Iowa City, IA 52242
Winston-Salem NC 27157

8. PERFORMING ORGANIZATION REPORT NUMBER

9. SPONSORING / MONITORING AGENCY NAME(S) AND ADDRESS(ES)

U.S. Army Medical Research and Materiel Command
Fort Detrick, Maryland 21702-5012

10. SPONSOR/MONITOR'S ACRONYM(S)

11. SPONSOR/MONITOR'S REPORT NUMBER(S)

12. DISTRIBUTION / AVAILABILITY STATEMENT

Approved for Public Release; Distribution Unlimited

13. SUPPLEMENTARY NOTES

14. ABSTRACT

The proposed studies will develop and evaluate a new therapeutic strategy for treating breast cancer bone metastasis by disrupting the interactions between breast cancer cells and sensory neurons within bone using alpha particle-emitting radiopharmaceuticals that target the CGRP-CRLR axis. The successful completion of this project will establish a new therapeutic target for cancer-induced bone pain and bone metastatic breast cancer; while providing the foundation required to develop new therapies that will decrease suffering and improve survival of breast cancer patients with bone metastases.

During this period, Dr. Wadas accepted a new position at the University of Iowa as an Associate Professor of Radiology, the Director of the Small Animal Imaging Center and the Managing Director of the clinical Theranostics Center. This cGMP laboratory employs a production team of five radio-and analytical chemists and produces radiotherapies for clinical use. He has successfully completed the transfer of his partnering award (BC180720P1) to the University of Iowa. Before Dr. Wadas' move, the research team found that ^{225}Ac-PTCA-CGRP$_{27-37}$ was stable in human serum. The team also developed CRLC-down-regulated BCa cells which will be used to test in vitro biding affinity of ^{225}Ac-PTCA-CGRP$_{27-37}$ to CRLR in the next year.

15. SUBJECT TERMS
Breast Cancer; Bone metastasis; Cancer-induced bone pain; Radiopharmaceuticals; Calcitonin receptor-like receptor; Actinium-225

16. SECURITY CLASSIFICATION OF:			17. LIMITATION OF ABSTRACT	18. NUMBER OF PAGES	19a. NAME OF RESPONSIBLE PERSON USAMRMC
a. REPORT	**b. ABSTRACT**	**c. THIS PAGE**	Unclassified	124	**19b. TELEPHONE NUMBER** *(include area code)*
Unclassified	Unclassified	Unclassified			

Standard Form 298 (Rev. 8-98)
Prescribed by ANSI Std. Z39.18

Table of Contents

1. INTRODUCTION:

When breast cancer (BCa) patients develop bone metastases, their 5-year survival rate declines by more than 70%. External beam radiation is used primarily for palliative treatment for patients with bone metastases. Bisphosphonate and anti-receptor activator of nuclear factor κB ligand (RANKL) antibody to decrease bone resorption can reduce the onset of pain, but they ultimately fail to improve overall survival. Radium-223 (^{223}RaCl$_2$) can extend overall survival of prostate cancer patients with bone metastases, but only to a limited extent. Since these treatments mainly target bone remodeling, **new approaches that target factors other than bone remodeling are needed.**

Cancer-induced bone pain is the most common and intractable symptom of bone metastases, and it substantially impairs quality of life. Eighty percent of patients with bone metastasis have cancer-induced bone pain, and its management is a tremendous challenge for patients and caregivers. It has also been suggested that cancer-induced bone pain <u>may be a negative indicator of survival</u>. The ALSYMPCA trial, which investigated the role of ^{223}RaCl$_2$ in prostate cancer patients with bone metastases, revealed that decreased pain levels corelated with increased overall survival. Thus, treating bone metastases by targeting pain signals are a promising approach to improve mortality.

Calcitonin gene-related peptide (CGRP), a 37-amino acid neuropeptide widely distributed in the peripheral and central nervous systems, is closely associated with pain behavior. Sensory nerves that express CGRP were enriched in the periosteum and bone marrow of a murine model of BCa bone metastasis. Patients with bone metastatic prostate cancer have elevated serum levels of CGRP. Sensory nerve-derived CGRP stimulated lung cancer growth. <u>We have also found that</u>: (i) bone metastatic prostate cancer directly affects sensory nerves to induce bone pain; (ii) sensory nerves that express CGRP are enriched in the marrow of those with bone metastatic prostate cancer; (iii) prostate cancer patients with bone metastatic disease have elevated serum levels of CGRP; (iv) samples from patients with bone metastatic BCa expressed higher levels of a CGRP receptor, calcitonin receptor-like receptor (CRLR); and (v) CGRP induces proliferation of BCa cells through CRLR. These data suggest that the CGRP/CRLR axis influences bone metastatic progression and could be a valuable therapeutic target.

The recent therapeutic efficacy of alpha particle ^{223}RaCl$_2$ ($t_{1/2}$ = 11.4 d; $E\alpha_{max}$ = 6-7 MeV) for treatment of prostate cancer patients with bone metastases has renewed interest in the development of alpha particle-based therapies. The effectiveness of ^{223}RaCl$_2$ results from its ability to form complexes with hydroxylapatite in remodeling bone. ^{223}RaCl$_2$ emits alpha particles and deposits substantial ionizing energy via high linear energy transfer (LET) over < 100 μm within bone tissue. When DNA is exposed to high LET, irreparable double-stranded breaks occur, resulting in cell death. ^{223}RaCl$_2$ is more potent than low LET β-emitting bone-seeking agents, and its cytotoxicity is not affected by hypoxia or mechanisms of radio- or chemoresistance. However, its chemical properties make it difficult to conjugate to molecular delivery systems, such as antibodies that target solid tumors.

There is growing consensus that actinium-225 (^{225}Ac) ($t_{1/2}$ = 10 d; $E\alpha_{max}$ = 6-8 MeV) could be a superior alternative for targeted alpha particle therapy of bone metastases. Unlike other alpha particles, ^{225}Ac of high specific activity and radionuclide purity is available. It has a long half-life, which synergizes well with the biological half-life of a circulating antibody. At the target site, it releases a large amount of kinetic energy per nuclear decay, making it highly cytotoxic when properly targeted. **Unlike ^{223}RaCl$_2$, ^{225}Ac's chemistry is amenable to chelation and conjugation to targeting molecules such as antibodies and peptides**. Recent *in vivo* preclinical evaluation of ^{225}Ac radiotherapeutics demonstrates that ^{225}Ac may provide new strategies for targeted alpha particle therapy development. Although the recent clinical success of ^{225}Ac radiotherapeutics that target prostate-specific membrane antigen (PSMA) demonstrate that targeted alpha particle therapy approaches

could have a significant and positive impact on the management of prostate cancer, targeting PSMA is not applicable for other cancer types including breast cancer.

Hypothesis:

The delivery of alpha particle radiation to bone metastatic foci using CRLR-targeting ligands will reduce BCa tumor burden and cancer-induced bone pain.

Specific Aims:

Aim 1: Determine the best alpha particle radiopharmaceuticals targeted to the CRLR.

We will develop CRLR-targeted peptide ($CGRP_{27-37}$) conjugated with actinium-225 (^{225}Ac, ^{225}Ac-$CGRP_{27-37}$). Then, the binding affinity of ^{225}Ac-$CGRP_{27-37}$ to CRLR will be determined *in vitro*. The biodistribution of ^{225}Ac-$CGRP_{27-37}$ and organ dosimetry will be determined *in vivo*.

Aim 2: Determine the impact of CRLR-targeted alpha particle therapy on BCa bone metastases and cancer-induced bone pain.

Using an *in vivo* bone metastatic model that allows us to measure tumor growth, bone remodeling, skeletal innervation, and pain behaviors within each mouse, we will determine the safety and efficacy of ^{225}Ac-$CGRP_{27-37}$ in the treatment of bone metastatic progression and its resultant pain.

Our proposal would be the first to rigorously investigate the use of ^{225}Ac-based targeted alpha particle therapy to target the CRLR, a receptor for the pain-related neuropeptide CGRP, in breast cancer bone metastases. If successful, the proposed studies will yield a paradigm-shifting treatment strategy for BCa patients with bone metastases.

The **immediate benefits** of this research will provide essential preliminary data for the design of subsequent clinical translational studies. Our results could be quickly translated into novel treatment strategies to reduce breast cancer-associated morbidity and mortality.

The potential for **long-term and positive impact** of our work is substantial. This work will inform new treatment strategies to address both bone metastatic progression and cancer-induced bone pain of BCa.

2. KEYWORDS:

Breast Cancer; Bone metastasis; Cancer-induced bone pain; Radiopharmaceuticals; Calcitonin receptor-like receptor; Actinium-225

3. ACCOMPLISHMENTS:

What were the major goals and objectives of the project?

This application will test a new and innovative approach for ^{225}Ac-based targeted alpha particle therapy of breast cancer bone metastases by exploiting CRLR as a potential therapeutic target for breast cancer bone metastases, with the goal of improving both patients' quality of life and overall survival.

Task 1: *In vitro* selection of CRLR-targeted alpha particle radiopharmaceuticals.

Months 1-12.

- Synthesize the CGRP$_{27-37}$ (**Months 1-2; Dr. Shiozawa**).

- Conjugate CGRP$_{27-37}$ to ^{225}Ac-PCTA (**Months 3-5; Dr. Wadas**).

- Test the serum stability of ^{225}Ac-CGRP$_{27-37}$ (**Months 6-8; Dr. Wadas**).

- Establish CRLR-down-regulated, CRLR-overexpressed breast cancer cells (**Months 6-8; Dr. Shiozawa**).

- Perform receptor binding assays and internalization assays (**Months 9-12; Dr. Wadas**).

Task 2: *In vivo* selection of CRLR-targeted alpha particle radiopharmaceuticals.

Months 1-18.

- Submit documents for local IACUC review. (**Months 1-2; Dr. Shiozawa**).

- Submit IACUC approval and necessary documents for review by the Animal Care and Use Review Office (ACURO). (**Months 3-4; Dr. Shiozawa**).

- Perform biodistribution and dosimetry assays (**Months 13-18; Drs. Shiozawa and Wadas**).

Task 3: Determine the maximum tolerated dose of CRLR-based targeted alpha particle therapy.

Months 18-24.

- Perform maximum tolerated dose studies (**Months 18-24; Drs. Shiozawa and Wadas**).

- Co-author comprehensive review of radiopharmaceutical treatment and bone metastasis. (**Months 20-14; Drs. Shiozawa and Wadas**).

Task 4: Determine treatment efficacy of CRLR-based targeted alpha particle therapy.

Months 25-34.

- Test the effects of ^{225}Ac-CGRP$_{27-37}$ on tumor growth in the marrow, bone remodeling, and pain-related behavior within the same animal (**Months 25-34; Drs. Shiozawa and Wadas**).

- Co-authored manuscript summarizing all the results. (**Months 33-36; Drs. Shiozawa and Wadas**).

What was accomplished under these goals?

(2019-2020)

The Award Transfer (Drs. Wadas and Shiozawa).

As of 12/01/19, the Partnering PI, Dr. Wadas accepted a position as an Associate Professor at the University of Iowa. Upon his arrival at the University of Iowa, Dr. Wadas has been working on obtaining the necessary institutional approvals (Institutional animal care and use committee, Institutional biosafety committee, etc) to submit the grant transfer request to the Department of Defense from the Wake Forest University Health Sciences (WFUHS) to the University of Iowa. Currently, the award has been transferred and all necessary institutional approvals have been obtained for studies to commence at the University of Iowa.

Additionally, to accomplish the remaining goals of the award at Wake Forest, Dr. Shiozawa was required to obtain approval for his own radioactive materials protocol. Currently, he has received the necessary didactic training provided by WFUHS Radiation Safety Committee. However, before his protocol is approved, the WFUHS Radiation Safety Committee has required him to gain "hands-on" training at the University of Iowa from Dr. Wadas, who is an internationally recognized expert in the safe use of alpha-particle-emitting radionuclides. Unfortunately, The University of Iowa shut-down and non-essential air travel restrictions put in place due to the COVID-19 outbreak have delayed this training.

^{225}Ac-PCTA-CGRP$_{27-37}$ was stable in human serum (Dr. Wadas).

To assess the stability of ^{225}Ac-PCTA-CGRP$_{27-37}$, we first synthesized the CGRP$_{27-37}$ by conjugating with a PCTA chelator (**Fig. 1A**) and radiolabeling it with ^{225}Ac using standard protocols (Tafreshi NK et al., J. Nucl. Med. 2019; 60:1124-33) (**Fig. 1B**). Formation of ^{225}Ac-PCTA-CGRP$_{27-37}$ was verified by Radio-TLC (**Fig. 2**) as well as Radio-HPLC (**Fig. 3**). Then, *in vitro* stability of ^{225}Ac-PCTA-CGRP$_{27-37}$ was determined by incubating with 500 µL of human serum at 37ºC. The radiopharmaceutical was stable after 10 days in human serum at 37ºC (**Fig. 4**).
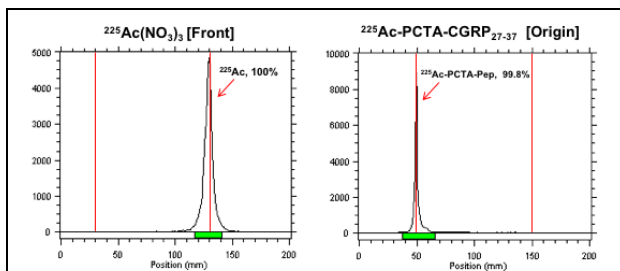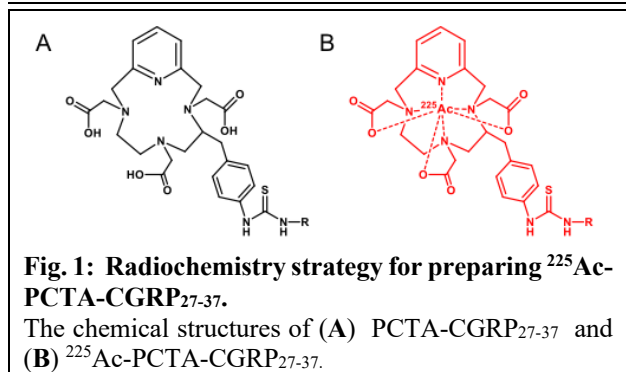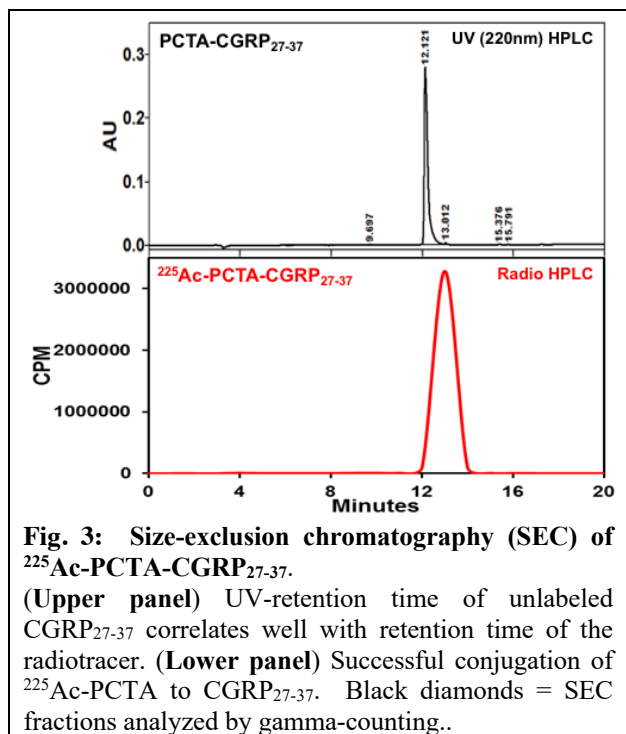
Fig. 1: Radiochemistry strategy for preparing ^{225}Ac-PCTA-CGRP$_{27-37}$.
The chemical structures of (**A**) PCTA-CGRP$_{27-37}$ and (**B**) ^{225}Ac-PCTA-CGRP$_{27-37}$.

Fig. 2: Radiochemical purity of ^{225}Ac-PCTA-CGRP$_{27-37}$ by Radio-TLC.
The reaction efficiency and purity of the ^{225}Ac-PCTA-CGRP$_{27-37}$ were determined with ITLC-SA as the stationary phase and 50 mM DTPA, pH 7 as the mobile phase. ITLC-SA was analyzed by TLC scanner and quantified by gamma-counter.

Fig. 3: Size-exclusion chromatography (SEC) of ^{225}Ac-PCTA-CGRP$_{27-37}$.
(**Upper panel**) UV-retention time of unlabeled CGRP$_{27-37}$ correlates well with retention time of the radiotracer. (**Lower panel**) Successful conjugation of ^{225}Ac-PCTA to CGRP$_{27-37}$. Black diamonds = SEC fractions analyzed by gamma-counting..

Day	% Intact	
	TLC scanner	Gamma-counter
0	100	100
1	98.5 ± 0.5	98.1 ± 0.4
3	96.6 ± 0.7	96.1 ± 0.8
5	93.9 ± 0.4	93.2 ± 1.1
7	92.4 ± 0.8	91.7 ± 0.9
10	90.1 ± 0.6	89.8 ± 0.5

Fig. 4: *In vitro* serum stability of ^{225}Ac-PCTA-CGRP$_{27-37}$.
In vitro serum stability was carried out by adding 50 µL of ^{225}Ac-PCTA-CGRP$_{27-37}$ (45 µCi) to 1 mL of human serum. The solutions were incubated at 37°C for 10 days and were analysed at suitable time points by TLC scanner and quantified by gamma-counter.
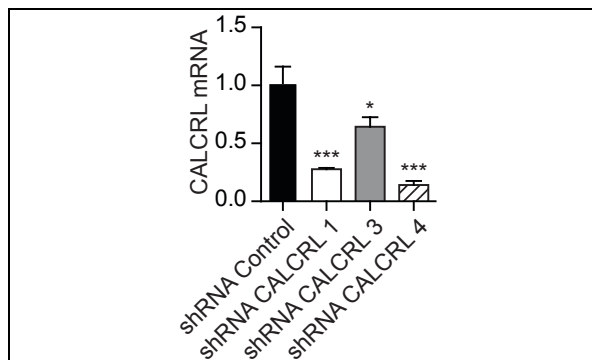
The CALCRL in breast cancer cells were down-regulated using shRNA (Dr. Shiozawa).

Fig. 5: The down-regulation of CALCRL in breast cancer cells .
CALCRL knockdown in MDA-MB-231 cells. $^*p \leq 0.05$, $^{***}p \leq 0.001$ vs. shRNA control (One-way ANOVA, Dunnett's multiple comparisons). Presented as mean fold change ± SEM.

To test the binding affinity of ^{225}Ac-PCTA-CGRP$_{27-37}$ to CRLR on breast cancer cells, we first needed to manipulate the levels of CRLR in breast cancer cells. To do so, we tested 4 different shRNAs targeting CALCRL (gene name of CRLR). Three out of four shRNAs successfully down-regulated CALCRL in MDA-MB-231 cells (**Fig. 5**), while one of them (shRNA CALCRL 2) killed cells (data not shown). Based on the knock-down efficiency, we chose CALCRL-down-regulated MDA-MB-231 cells by shRNA CALCRL 1 and 4 to be used in future binding affinity analyses.

What opportunities for training and professional development did the project provide?

(2019-2020)
Dr. Shiozawa was invited to give a talk at The U.S. Bone and Joint Initiative (USBJI) and Bone and Joint Canada (BJC) Young Investigator Initiative Workshop Spring 2019 (Rosemont, IL) on April 27, 2019.

Dr. Shiozawa was invited to give a seminar at University of North Carolina at Chapel hill, Adams School of Dentistry (Chapel hill, NC) on December 03, 2019.

Dr. Wadas gave a lecture at the University of Iowa's Free Radical and Radiation Biology Program. This lecture dealt with the use of alpha particle therapy in cancer care. University of Iowa, Iowa City, IA (February 25, 2020).

Dr. Wadas accepted the role as Guest Editor of a Special Issue of *Molecules* that focuses on the use of radiotherapy of disease. The Issue description and call for papers can be found at https://www.mdpi.com/journal/molecules/special_issues/radiopharmaceutical_chemistry_radiotherapy.

How were the results disseminated to communities of interest?

There is nothing to report currently.

AWARD: BC180720, BC180720P1
TITLE: A targeted alpha particle radiopharmaceutical for bone metastatic breast cancer
PI: Yusuke Shiozawa, M.D., Ph.D., Partnering PI: Thaddeus Wadas, Ph.D.

What do you plan to do during the next reporting period to accomplish the goals and objectives?

Currently, research at both institutions has ceased due to the COVID-19 pandemic. Once normal research operations resume the following tasks will be initiated. These include:
1) Determine the binding affinity of radiopharmaceuticals to breast cancer cells *in vitro* (Aim 1).
2) Determine the biodistribution and dosimetry of radiopharmaceuticals *in vivo* (Aim 1).
3) Dr. Shiozawa will complete his radioactive material handling training with Dr. Wadas.
4) Drs. Shiozawa and Wadas will write together a review manuscript relevant to this study.

4. IMPACT:

What was the impact on the development of the principal discipline(s) of the project?

(2019-2020)

1. We found that ^{225}Ac-PTCA-CGRP$_{27-37}$ were stable in human serum.
2. We were able to down-regulate CRLC expression levels in BCa using shRNA.

What was the impact on other disciplines?

We were able to develop new methods of radiopharmaceutical production. While specific to this project, they may have broad applicability to radiopharmaceutical development in general.

What was the impact on technology transfer?

There is nothing to report at this time.

What was the impact on society beyond science and technology?

There is nothing to report at this time.

5. CHANGES/PROBLEMS:

Changes in approach and reasons for change

 Nothing to report.

Actual or anticipated problems or delays and actions or plans to resolve them

 Nothing to report.

Changes that have a significant impact on expenditures

 Nothing to report.

Significant changes in use or care of human subjects, vertebrate animals, biohazards, and/or select agents

 Nothing to report.

6. PRODUCTS:

Publications, conference papers, and presentations

Journal Publications

Peer reviewed journal

(2019-2020)

1. Lycan TW, Hsu F, Ahn CS, Thomas A, Walker FO, Sangueza OP, **Shiozawa Y**, Park SH, Peters CM, Romero-Sandoval EA, Melin SA, Sorscher S, Ansley K, Lesser GJ, Cartwright MS, Strowd RE. Neuromuscular ultrasound for taxane peripheral neuropathy in breast cancer. **Muscle and Nerve**. 2020; 61(5):587-594. PMID: 32052458. PMCID: In Progress.
   Status of Publication: Published
   Acknowledgement of federal support: Yes

2. Tafreshi NK, Tichacek CJ, Pandya DN, Doligalski ML, Budzevich M, Kil H-J, Bhatt NB, Kock ND, Messina J, Ruiz EE. Delva NC, Weaver A, Gibbons WR, Boulware DC, Khushalani NL, El-Haddad G, Triozzi PL, Moros EG, McLaughlin ML, **Wadas TJ**, Morse DL. Melanocortin 1 Receptor–Targeted α-Particle Therapy for Metastatic Uveal Melanoma. **J. Nucl. Med.** 2019; 60(8): 1124-1133. PMID: 30733316. PMCID: PMC6681690.
   Status of Publication: Published
   Acknowledgement of federal support: No

3. Tichacek CJ, Budzevich MM, **Wadas TJ**, Morse DL, Moros EG. A Monte Carlo Method for Determining the Response Relationship between Two Commonly Used Detectors to Indirectly Measure Alpha Particle Radiation Activity. **Molecules.** 2019; 24(18): 3397-3402. PMID: 31546752. PMCID: PMC6767018.
   Status of Publication: Published
   Acknowledgement of federal support: No

4. Tafreshi NK, Doligalski ML, Tichacek CJ, Pandya DN, Budzevich MM, El-Haddad G, Khushalani NI, Moros EG, McLaughlin ML, **Wadas TJ**, Morse DL. Development of Targeted Alpha Particle Therapy for Solid Tumors. **Molecules.** 2019; 24(23): 4314-4362. PMID: 31779154. PMCID: PMC6930656.
   Status of Publication: Published
   Acknowledgement of federal support: No

Invited reviews

(2019-2020)

Nothing to report.

Book

(2019-2020)

1. Park SH, **Shiozawa Y**. (2019) Genomic mutation as a potential driver of the development of bone-related cancers. In Zaidi M (Ed.), *Encyclopedia of Bone Biology*. In Press. Elsevier.
Status of Publication: In Press
Acknowledgement of federal support: Yes

2. **Shiozawa Y**. (2019) The roles of bone marrow-resident cells as a microenvironment for bone metastasis. In Birbrair A (Ed.), *Tumor Microenvironments in Different Organs – Part A*. In Press. Switzerland: Springer Nature.
Status of Publication: Published
Acknowledgement of federal support: Yes

Presentation

(2019-2020)

1. Strowd RE, Lycan T, Thomas A, Hsu FC, Ahn C, Sangueza O, **Shiozawa Y**, Park SH, **Peters CM**, EA Romero-Sandoval, Melin SA, Sorscher S, Lesser GJ, Walker FO, Cartwright MS. Neuromuscular ultrasound for the non-invasive assessment of breast cancer patients with peripheral neuropathy from taxanes. The American Academy of Neurology 71st Annual Meeting, Philadelphia, PA, USA, May 4-10, 2019. Poster.

2. Tsuzuki S, Park S, Eber M, Widner B, Kamata Y, Kimura T, Bianchi-Frias D, Coleman I, Nelson P, Hsu F-C, **Peters C**, **Shiozawa Y**. A pain-related neuropeptide calcitonin gene-related peptide promotes bone metastatic progression of prostate cancer through p38. American Society for Bone and Mineral Research (ASBMR) 2019 Annual Meeting, Orland, FL, USA, September 20-23, 2019. Poster.

3. Park S, Eber M, Tsuzuki S, Cain R, Widner B, Kamata Y, Kimura T, Bianchi-Frias D, Coleman I, Nelson P, Hsu F-C, **Peters C**, **Shiozawa Y**. The role of the SCF/c-kit pathway in cancer-induced bone pain. American Society for Bone and Mineral Research (ASBMR) 2019 Annual Meeting, Orland, FL, USA, September 20-23, 2019. Poster.
   - **Selected as a Plenary Poster**

4. Cain R, Park SH, Eber M, Martin TJ, Parker R, Jimenez-Andrade JM, **Shiozawa Y**, **Peters C**. Characterization of a syngeneic mouse model of prostate cancer induced bone pain. Neuroscience 2019, Chicago, IL, USA, October 19-23, 2019. Poster.

Website(s) or other Internet site(s)

Nothing to report.

Technologies or techniques

Nothing to report.

Inventions, patent applications, and/or licenses

Nothing to report.

Other products

Nothing to report.

7. PARTICIPANTS & OTHER COLLABORATING ORGANIZATIONS

What individuals have worked on the project?

Name: Yusuke Shiozawa
Project Role: PI, W81XWH-19-1-0045
Researcher Identifier (e.g. ORCID ID): orcid.org/0000-0001-9814-9230
Nearest person month worked: 1.2
Contribution to Project: Dr. Shiozawa is an Assistant Professor in the Department of Cancer Biology. He has extensive experience in the study of prostate cancer bone metastasis, and will provide oversight of the entire program including development and implementation of all policies, procedures, and processes. In this role, Dr. Shiozawa will be responsible for the completion of the project and for ensuring that systems are in place to guarantee institutional compliance with US laws, including biosafety and animal research guidelines, data collection and analyses, and facilities. Dr. Shiozawa will supervise other personnel on the project to ensure timely and effective studies.
Funding Support: Department of Defense, National Cancer Institute, Matavivor, TEVA Pharmaceuticals

Name: Thaddeus Wadas
Project Role: Partnering PI, W81XWH-19-1-0046
Researcher Identifier (e.g. ORCID ID):
Nearest person month worked: 1.2
Contribution to Project: Dr. Wadas is an Associate Professor in the Department of Radiology at University of Iowa. Dr. Wadas will share oversight of the entire program with Dr. Shiozawa, including development and implementation of all policies, procedures, and processes. Dr. Wadas has a Ph.D. in Chemistry and has extensive experience in peptide chemistry, radiochemistry and developing *in vivo* studies in various tumor models as well as microPET imaging to evaluate radiopharmaceuticals. Dr. Wadas will assist Dr. Shiozawa's laboratory in radiochemistry, radiopharmaceutical-related *in vitro* experiments and all imaging data analysis. Dr. Wadas has access to all the resources and facilities needed to execute this research successfully, and his lab has successfully collaborated with the Dr. Shiozawa. Dr. Wadas will meet with Dr. Shiozawa remotely on a monthly basis to discuss progress on projects related to this Award.
Funding Support: Department of Defense, National Cancer Institute, Matavivor

Name: Christopher Peters
Project Role: Co-Investigator, W81XWH-19-1-0045
Researcher Identifier (e.g. ORCID ID):
Nearest person month worked: 0.6
Contribution to Project: Dr. Peters is an Assistant Professor in the Department of Anesthesiology. Dr. Peters' research interests are in central and peripheral mechanisms of pain chronicity including postsurgical, bone cancer and chemotherapy induced pain and neuropathy. Dr. Peters will be responsible for supervising and training personnel in evoked and non-evoked bone cancer pain behavioral assays. Dr. Peters will also assist with histological and immunohistochemical analysis of skeletal tissue as part of Aims 2. He has extensive experience with the behavioral analysis, immunohistochemistry, biochemical analysis and fluorescent, brightfield, and confocal microscopic imaging required for this project.
Funding Support: National Institutes of Health, Department of Defense

Name: Fang-Chi Hsu
Project Role: Co-Investigator, W81XWH-19-1-0045
Researcher Identifier (e.g. ORCID ID):
Nearest person month worked: 0.36
Contribution to Project: Dr. Hsu is a Professor in the Department of Biostatistical Sciences. She will work closely with Dr. Shiozawa and the team to analyze the results of the project.
Funding Support: National Institutes of Health, Department of Defense

Has there been a change in the other active support of the PD/PI(s) or senior/key personnel since the last reporting period?

Nothing to report.

What other organizations have been involved as partners?

Nothing to report.

8. SPECIAL REPORTING REQUIREMENTS:

QUAD CHARTS.

9. APPENDICES:

The original copies of manuscript are attached.

A targeted alpha particle radiopharmaceutical for bone metastatic breast cancer

BC180720, BC180720P1
W81XWH-19-1-0045, W81XWH-19-1-0046

PI: Yusuke Shiozawa   **Org: Wake Forest University Health Sciences**   **Award Amount:** $299,999 (Shiozawa)
Thaddeus Wadas   **University of Iowa** $299,999 (Wadas)

Study/Product Aim(s)

- **Aim 1: Determine the best alpha particle radiopharmaceuticals targeted to the CRLR.**
- **Aim 2: Determine the impact of CRLR-targeted alpha particle therapy on breast cancer bone metastases and cancer-induced bone pain.**

Approach

The proposed studies will develop a new therapeutic strategy for treating bone metastatic breast cancer using alpha-particle radiopharmaceutical. This work will lay the needed foundation to develop new therapeutic targets for both cancer-induced bone pain and bone metastatic breast cancer, to decrease suffering and improve survival of breast cancer patients with bone metastases.

Day	% Intact	
	TLC scanner	Gamma-counter
0	100	100
1	98.5 ± 0.5	98.1 ± 0.4
3	96.6 ± 0.7	96.1 ± 0.8
5	93.9 ± 0.4	93.2 ± 1.1
7	92.4 ± 0.8	91.7 ± 0.9
10	90.1 ± 0.6	89.8 ± 0.5

In vitro serum stability of ^{225}Ac-PCTA- CGRP$_{27-37}$
In vitro serum stability was carried out by adding 50 µL of ^{225}Ac-PCTA-CGRP$_{27-37}$ (45 µCi) to 1 mL of human serum. The solutions were incubated at 37°C for 10 days and were analysed at suitable time points by TLC scanner and quantified by gamma-counter.

- **We found that ^{225}Ac-PCTA-CGRP$_{27-37}$ was stable for 10 days in human serum.**

Timeline and Cost

Activities CY	19	20	21	22
Aim 1 (In vitro studies)	▇			
Aim 1 (Animal studies)		▇		
Aim 2 (Animal studies)			▇	
Estimated Budget ($K)	**$100**	**$100**	**$200**	**$200**

Updated: 03/31/2020

Goals/Milestones (Example)

CY19 Goal – Team development
✓ Set up and organize the monthly meeting
CY20 Goals – In vitro studies
❑ *In vitro* selection of ^{225}Ac-CGRP$_{27-37}$
❑ *In vivo* selection of ^{225}Ac-CGRP$_{27-37}$
CY21 Goal – Animal studies
❑ *In vivo* selection of ^{225}Ac-CGRP$_{27-37}$
❑ Determine the maximum tolerated dose of ^{225}Ac-CGRP$_{27-37}$
CY22 Goal – Animal studies
❑ Determine the maximum tolerated dose of ^{225}Ac-CGRP$_{27-37}$
❑ Determine treatment efficacy of ^{225}Ac-CGRP$_{27-37}$
Comments/Challenges/Issues/Concerns
- Nothing to report.
Budget Expenditure to Date
Projected Expenditure: $100K
Actual Expenditure: $35K (Shiozawa) + $56K (Wadas)

CLINICAL RESEARCH ARTICLE

MUSCLE&NERVE WILEY

Neuromuscular ultrasound for taxane peripheral neuropathy in breast cancer

Thomas W. Lycan DO, MHS[1] | Fang-Chi Hsu PhD[2] | Christine S. Ahn MD[3] |
Alexandra Thomas MD[1] | Francis O. Walker MD[4] | Omar P. Sangueza MD[5] |
Yusuke Shiozawa MD, PhD[6] | Sun Hee Park PhD[6] | Christopher M. Peters PhD[6] |
Edgar Alfonso Romero-Sandoval MD[7] | Susan A. Melin MD[1] | Steven Sorscher MD[1] |
Katherine Ansley MD[1] | Glenn J. Lesser MD[1] | Michael S. Cartwright MD[4] |
Roy E. Strowd MD[4]

[1]Internal Medicine: Hematology and Oncology, Wake Forest School of Medicine, North Carolina

[2]Biostatistics and Data Science, Wake Forest School of Medicine, North Carolina

[3]Dermatology, Wake Forest School of Medicine, North Carolina

[4]Neurology, Wake Forest School of Medicine, North Carolina

[5]Pathology, Wake Forest School of Medicine, North Carolina

[6]Cancer Biology, Wake Forest School of Medicine, North Carolina

[7]Anesthesiology, Wake Forest School of Medicine, North Carolina

Correspondence
Thomas Lycan, Wake Forest School of Medicine, 1st Floor Watlington Hall, 1 Medical Center Drive, Winston-Salem, NC 27157. Email: tlycan@wakehealth.edu

Abstract

Background: Our study aim was to evaluate neuromuscular ultrasound (NMUS) for the assessment of taxane chemotherapy-induced peripheral neuropathy (CIPN), the dose-limiting toxicity of this agent.

Methods: This cross-sectional study of breast cancer patients with taxane CIPN measured nerve cross-sectional area (CSA) by NMUS and compared with healthy historical controls. Correlations were determined between CSA and symptom scale, nerve conduction studies, and intraepidermal nerve fiber density (IENFD).

Results: A total of 20 participants reported moderate CIPN symptoms at a median of 3.8 months following the last taxane dose. Sural nerve CSA was 1.2 mm^2 smaller than healthy controls ($P \leq .01$). Older age and time since taxane were associated with smaller sural nerve CSA. For each 1 mm^2 decrease in sural nerve CSA, distal IENFD decreased by 2.1 nerve/mm (R^2 0.30; $P = .04$).

Conclusions: These data support a sensory predominant taxane neuropathy or neuronopathy and warrant future research on longitudinal NMUS assessment of CIPN.

KEYWORDS

breast cancer, chemotherapy, neuropathy, taxane, ultrasound

1 | INTRODUCTION

Chemotherapy-induced peripheral neuropathy (CIPN) is a common toxicity of many classes of chemotherapy, including taxanes, platinums, vinca alkaloids, and others. Taxanes, such as paclitaxel and docetaxel,

have had an increasing role in the treatment of breast cancer and are now used in the majority of patients receiving perioperative chemotherapy.[1] When chemotherapy cannot be given as intended due to dose reductions, it is associated with worse progression-free and overall survival.[2] Although spontaneous recovery is possible, in roughly half

of cases functional disability and risk of falls from CIPN persists for years.[3,4] Currently, there is no predictive method to identify patients who are at high risk for developing permanent, debilitating CIPN.

There are few clinically available point-of-care tests to objectively predict, diagnose, or monitor CIPN. Self-reported symptom scales such as the European Organization for Research and Treatment of Cancer CIPN 20 Quality of Life Questionnaire (QLQ)[5] are potentially predictive of CIPN but have inter-scale and inter-observer variability.[6,7] Quantitative sensory testing fails to predict the severity of CIPN.[8,9] Nerve conduction studies (NCSs) are insensitive to small fiber changes; typical findings include mild conduction velocity slowing at sites of entrapment or reduction of sural sensory responses.[10-12] Skin biopsy for measuring intraepidermal nerve fiber density (IENFD) is the gold standard for the diagnosis of sensory-predominant small fiber neuropathy but is not an ideal test due to its invasive nature.[3,6]

Studies have found that neuromuscular ultrasound (NMUS) can detect peripheral nerve lesions generally with enlargement of CSA in patients with demyelinating hereditary,[13,14] inflammatory,[15,16] entrapment,[17] and diabetic neuropathies[18] though reduction of CSA has also been reported (eg, amyotrophic lateral sclerosis [ALS],[19] spinocerebellar ataxia syndrome[20-23]). CSA is generally larger in demyelinating than axonal polyneuropathies[24] and more commonly reported in large fiber neuropathies, though one study of patients with small fiber neuropathies demonstrated enlargement of CSA compared with matched-healthy controls.[25]

Less is known about the usefulness of NMUS for assessing the effect of chemotherapy upon peripheral nerves. Four studies have used NMUS for the detection of CIPN among gastrointestinal cancer patients who received oxaliplatin. Compared with historical reference values, three studies found no consistent change in CSA,[24,26] although one did note an increase in peripheral nerve CSA at compression sites (median nerve at wrist, ulnar nerve at elbow).[27] The fourth study compared neurological measures before and after chemotherapy and found increased CSA of the tibial nerve and at one compression site of the fibular nerve (fibular head), but did not find changes in CSA in other nerves (sural, median, ulnar, radial).[28] Importantly, the mechanism and symptoms of neurotoxicity are markedly different between taxanes (eg, microtubular stabilization, hypoesthesia) and oxaliplatin (eg, inhibition of sodium channels; cold-induced paresthesias). Therefore, while prior studies of oxaliplatin CIPN are certainly informative, taxane-specific studies are needed to further characterize this syndrome.

In this study, our aim was to test NMUS as a noninvasive, point-of-care test to measure nerve CSA in patients with active taxane CIPN symptoms with the hypothesis that nerve CSA would be altered.

2 | METHODS

2.1 | Eligibility characteristics

Our single-arm, prospective pilot study enrolled breast cancer patients with self-reported symptomatic CIPN for comprehensive neurological assessment, including NMUS. The trial was conducted in accordance with the International Conference on Good Clinical Practice Standards and the Declaration of Helsinki. The protocol was approved by institutional review board and ethics committees of our institution and the trial was registered on ClinicalTrials.gov (NCT03139435). All patients provided informed consent. Eligible patients were ≥18-year-old women with breast cancer (any stage) and clinical symptoms of peripheral neuropathy due to either previous or current taxane exposure, as clinically attributed by the patient and their medical oncologist. We noted the presence of comorbidities (such as diabetes), which can predispose toward peripheral neuropathy with nerve enlargement.[18] We excluded patients with a self-reported or documented history of pre-existing peripheral neuropathy before initiation of the taxane. Patients were followed, either by telephone or in person, for 30 days to ensure the biopsy site healed.

2.2 | Assessments

Participants underwent a cross-sectional assessment that included focused history, neurological exam, and diagnostic testing by a neurologist at a single visit. NMUS with a GE S8 system and a routine 15-MHz linear transducer (GE Healthcare, Chicago, IL) was used to measure CSA at nerve sites as per previously described methodology and institutional practice.[29] These sites were at the posterior distal leg (sural nerve), the ankle (tibial nerve), and the forearm and distal wrist crease (DWC; median nerve). The median nerve was assessed at two places to control for enlargement that can occur just proximal to entrapment at the carpal tunnel (at the DWC) due to subclinical carpal tunnel syndrome. Reference values for NMUS were from a published historical dataset.[29] The 20-item self-reported neuropathy scale (QLQ-CIPN20) was administered as previously described with the exception of the hearing loss item; this item was excluded from data collection because taxanes are not associated with ototoxicity.[30]

NCS assessed the tibial motor nerve, median motor nerve, and the sural sensory nerve (antidromic, taken at two sites on the ankle) as per AANEM standards[31] and compared with reference values from healthy adults.[32] IENFD was measured with two skin biopsies (4–5 mm), one at the upper thigh and the second on the ipsilateral distal leg in sural nerve territory (10 cm above lateral malleolus). As previously described, biopsied tissues were cut into 50-μM sections for H&E staining and immunostaining with an antibody to protein gene product (PGP) 9.5, a neuron- and neuroendocrine cell-specific ubiquitin carboxy-terminal hydrolase expressed throughout the peripheral nervous system.[33]

Slides were processed and read by two collaborators in dermatopathology with experience in reading skin biopsy samples for IENFD. The same two dermatopathologists reviewed all cases. IENFD was measured as the linear density (per millimeter) of PGP 9.5-positive fibers that crossed the dermal–epidermal junction. Serum and additional unstained biopsy slides were stored and transferred for exploratory analyses. Although not blinded to the diagnosis of CIPN, the examiner performing NMUS did not review the patient's symptoms before performing the study and was not aware of the cumulative dose,

timing since taxane therapy, severity of clinical symptoms, or IENFD results at the time of testing. Dermatopathologists were not blinded to the patient but did not have access and were blinded to the NCS and NMUS data at the time of their analysis.

2.3 | Study endpoints

The primary outcome was tibial nerve CSA by NMUS compared with historical controls. Secondary outcomes included sural nerve CSA by NMUS and determination of whether tibial or sural nerve CSA correlated with QLQ-CIPN20, NCS, or IENFD. Exploratory outcomes included measures of median nerve CSA.

2.4 | Statistical analysis

The tibial nerve CSA, sural nerve CSA, and sural nerve amplitude were compared with historical data[29,34] from healthy patients using two-sample t-test; primary historical data were used for the analysis of CSA measures. Phase of treatment was defined as active (≤30 days since last taxane administration), recent (>30 and ≤180 days), and remote (>180 days). Comparison of CSA, QLQ scales, and IENFD measures between different phases of taxane exposure were performed using the Kruskal-Wallis tests. Spearman's rank correlation coefficients were used to study the associations between two measures (eg, distal and proximal IENFD). Linear regression models were used to examine the associations between the dependent variable (nerve CSA) and covariates of interest (NCS measures, self-reported neuropathy scale, and IENFD). Clinical factors (eg, age) that were thought to be potentially associated with nerve CSA were fitted in the model one at a time.

3 | RESULTS

Between May 4, 2017, and November 13, 2018, 25 patients were screened for eligibility; 3 did not meet inclusion criteria, and 2 declined to participate as summarized in CONSORT flow diagram (Figure 1). Recruitment was by provider referral and by paper fliers posted in both patient and provider areas of the oncology clinic. All patients completed their planned evaluation and follow-up. One patient was excluded from median nerve analysis due to symptoms and NCS findings that were diagnostic of carpal tunnel syndrome.

A total of 20 patients underwent evaluation with their baseline clinical characteristics summarized in Table 1. Average cumulative
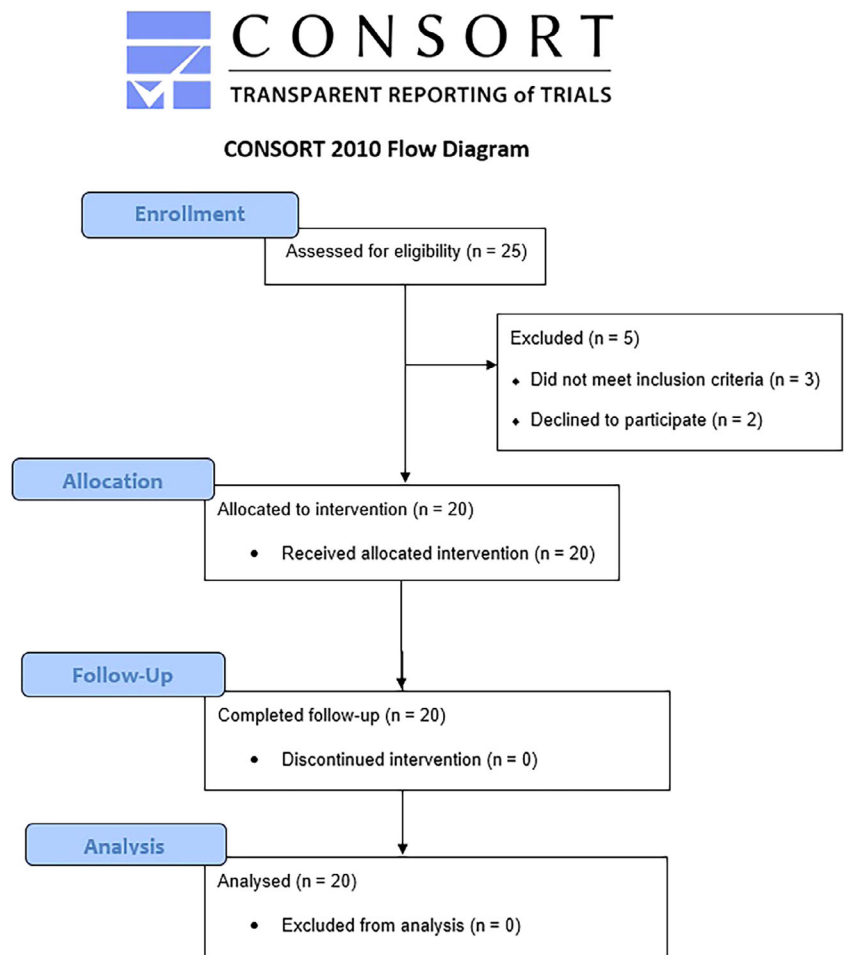

FIGURE 1 CONSORT flow diagram [Color figure can be viewed at wileyonlinelibrary.com]

taxane dose was 817 mg/m^2; for reference, the typical dosing regimen for adjuvant paclitaxel in breast cancer is 80 mg/m^2/week for 12 weeks (total cumulative dose of 960 mg/m^2). CIPN patients reported moderate-to-severe CIPN symptoms by QLQ-CIPN20, which were predominantly sensory (19.1 ± 4.9; max 32) as opposed to motor (15.6 ± 5.8; max 32) or autonomic (3.3 ± 1.6; max 8). All patients had normal strength (5/5) in foot dorsiflexion; deep tendon reflexes at the ankles were absent in 13/20 (65%), reduced in 4/20 (20%).

Sural nerve amplitude was significantly lower (mean 10.9 ± 5.8 μV) than healthy historical controls (mean 17.2 ± 10.1 μV; P < .01) with 8 patients below the normal range (<7.1 μV).[34] There were no associations between tibial nerve CSA and tibial compound muscle action potential amplitude (Spearman's r = 0.12), distal latency (−0.24), or conduction velocity (0.21). There were no associations between sural nerve CSA and sural sensory nerve action potential (SNAP) amplitude (Spearman's r = 0.20), latency (−0.26), or conduction velocity (0.27). Sural SNAP amplitude was not associated with symptom severity by QLQ-CIPN20 (Spearman rs [18] = −0.23).

Distal IENFD had mean 6.6 ± 3.8 nerves/mm (range, 2.4–15 nerves/mm) with 30% of participants below the normal range, defined as the 5th

percentile among historical healthy controls (3.8 nerves/mm). Proximal IENFD had mean 11.0 ± 6.0 nerves/mm (range, 9–24 nerves/mm) with 15% of participants below the normal range, defined as the 5th percentile among historical healthy controls (5.2 nerves/mm).[35] Distal and proximal IENFD were associated with each other (Spearman rs [19] = 0.49; P = .03). Neither distal nor proximal IENFD was associated with symptom severity by QLQ CIPN20 (Spearman rs [19] = −0.16; 0.12, respectively) or with cumulative dose (Spearman rs [20] = 0.42; 0.19, respectively). Proximal IENFD was negatively associated with tibial amplitude (Spearman r = −0.46; P = .04); otherwise, there was no association between IENFD (either proximal or distal) and any other NCS measures.

CSA was evaluated by NMUS at 74 nerve sites among the 20 patients with no repeated measurements. The average sural nerve CSA was significantly smaller than healthy historical controls (Table 2). Older age was associated with significantly smaller sural nerve CSA (Spearman rs [20] = −0.65, P ≤ .01). More days since taxane chemotherapy was also associated with smaller sural nerve CSA (rs [20] = −0.46; P = .04). Sural nerve CSA was not significantly associated with either body mass index (BMI) (Spearman rs [20] = 0.25) or cumulative taxane dose (Spearman rs [20] = 0.40); neither were the CSA of other nerves. Unadjusted sural nerve CSA did not have an association with distal IENFD, but when controlled for age and days from last taxane administration, distal IENFD reduced by 2.1 nerve/mm for each 1 mm^2 decrease in sural nerve CSA (Table 3).

Descriptive data of nerve findings by phase of treatment (active, recent, remote) are summarized in Table 4. When compared by phase of treatment and independently from each other, tibial nerve CSA (P = .44), sural nerve CSA (P = .17), proximal IENFD (P = 0.43), distal IENFD (P = .32), QLQ sensory scale (P = .46), and sural amplitude (P = .45) did not meet statistical significance by Kruskal-Wallis one-way analysis of variance.

Median nerve CSA at the compressive site (DWC) was larger than among healthy historical controls, whereas at the noncompressive site (forearm), there was no significant difference. These results were the same even when including the participant with carpal tunnel syndrome (n = 20), with median nerve CSA at the DWC larger than healthy historical controls (P = .02) and no significant difference at the

TABLE 1 Demographic and disease characteristics of the participants

Parameter		Mean (SD) or n (%)
Age, mean (SD)		55.4 (10.5)
BMI, mean (SD)		29.8 (6.9)
Stage of breast cancer, n (%)	Stage I	8 (40%)
	Stage II	5 (25%)
	Stage III	2 (10%)
	Stage IV	5 (25%)
Prior radiation therapy, n (%)		10 (50%)
Prior surgery for breast cancer, n (%)		19 (95%)
Prior hormone therapy for breast cancer, n (%)		8 (40%)
Prior lines of systemic cancer therapy, median (IQR)		1 (1–3)
Most recent taxane, n (%)	Paclitaxel	10 (50%)
	Docetaxel	8 (40%)
	Nab-paclitaxel	2 (10%)
Cumulative taxane dose, mg/m^2, mean (SD)		817.3 (414.9)
Months since last taxane dose, median (IQR)		3.8 (1.0–6.1)
Relevant comorbidities, n (%)	Diabetes, no end-organ damage	4 (20%)
	Hypothyroidism	3 (15%)
	Depression	3 (15%)
	Alcoholism	1 (5%)
	Cerebovascular disease	1 (5%)
	Vitamin B12 deficiency	1 (5%)

IQR, interquartile range; Nab, nanoparticle albumin–bound.

TABLE 2 Comparison of nerve CSA by NMUS between CIPN patients and healthy historical controls

	CIPN patients, mm^2, mean (SD)	Healthy controls, mm^2, mean (SD)	t value	P value
Tibial nerve CSA	13.0 (3.6)	14.0 (4.3)	0.94	.35
Sural nerve CSA	4.1 (1.3)	5.3 (1.8)	2.85	<.01*
Median nerve CSA (forearm)	7.3 (1.4)	7.7 (1.7)	0.89	.37
Median nerve CSA (DWC)	12.5 (3.9)	10.1 (2.7)	−2.39	.03**

*Statistically significant at α ≤ .05. Df = 138.
**Statistically significant at α ≤ .05. Satterthwaite unequal variances; Df = 16.

TABLE 3 Multiple regression analysis of factors to predict distal IENFD

Factors	Univariate		Multivariate model 1*		Multivariate model 2†	
	Beta	P value	Beta	P value	Beta	P value
Sural CSA	0.35	.13	0.99	.15	2.10	.04‡
Days since last taxane	−0.29	.21	−0.01	.25	0.19	.13
Age	−0.12	.62			−0.01	.09

*Model 1: R2 = 0.19; F(2,19) = 2.03; P = .16.
†Model 2: R2 = 0.30; F(3,19) = 2.32; P = .11.
‡Statistically significant at $\alpha \leq .05$.

TABLE 4 Comparison of findings between different phases of taxane exposure

	Active taxane, mean (SD)	Recent taxane, mean (SD)	Remote taxane, mean (SD)
No. of participants	6	9	5
Cumulative dose (taxane mg/m²)	995.8 (95.8)	713.9 (440.7)	789.0 (587.1)
Tibial nerve CSA (mm²)	14.2 (4.8)	13.2 (3.2)	11.2 (2.3)
Sural nerve CSA (mm²)	4.8 (1.6)	3.9 (0.6)	3.6 (1.5)
Forearm median nerve CSA (mm²)	7.3 (1.9)	8 (1.0)	6.2 (0.4)
DWC median nerve CSA* (mm²)	13.8 (6.5)	13.6 (3.0)	11.0 (2.4)
QLQ sensory scale	17.2 (4.3)	20.4 (5.2)	19.2 (5.4)
QLQ motor scale	12.3 (3.4)	18.6 (6.6)	14.2 (4.4)
QLQ autonomic scale	2.5 (0.5)	3.9 (1.8)	3.2 (1.6)
Proximal IENFD (nerves/mm)	13.1 (6.7)	8.9 (3.6)	12.2 (8.5)
Distal IENFD (nerves/mm)	8.9 (4.9)	5.5 (2.9)	5.9 (3.0)

*P value significant to <.05 (.0219) by Kruskal–Wallis one-way analysis of variance.
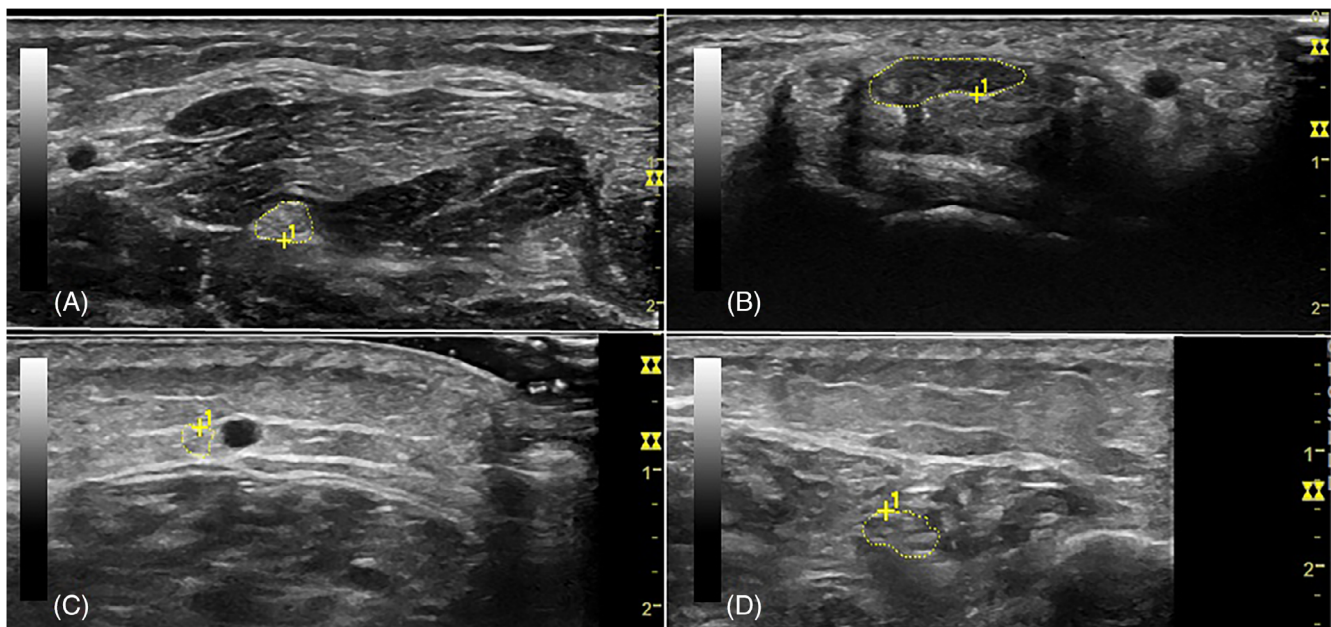
FIGURE 2 Representative imaging by NMUS. A, Median nerve at forearm in participant 3 (CSA, 9 mm²). B, Median nerve at wrist in participant 3 (CSA, 25 mm²). C, Sural nerve in participant 6 (CSA, 4 mm²). D, tibial nerve in participant 6 (CSA, 19 mm²) [Color figure can be viewed at wileyonlinelibrary.com]

forearm (P = .41). Representative NMUS imaging is shown in Figure 2. Descriptive data from all participants is shown in Supporting Information Table S1, which is available online.

The study was well-tolerated without any adverse effects and with a high uptake among participants with just 2 of 25 participants declining to complete the study protocol after registration. Skin

biopsy led to one adverse event in a patient who had redness and irritation attributed to an inflammatory local reaction and not an infection.

4 | DISCUSSION

The key findings of this study are that, compared with healthy historical controls, patients with a small fiber neuropathy caused by taxane exposure had (1) decreased sural nerve size, (2) increased median nerve size but only at a compression site, and (3) NMUS findings that correlated well with IENFD loss on skin biopsies. Reduced CSA was specific to the sural sensory nerve and was not seen in the tibial nerve. This is likely reflective of the predominantly sensory manifestation of taxane CIPN, which was confirmed in our sample using a validated symptom scale.

NMUS assessment of the median nerve at its compression site (DWC) found that CIPN patients had increased CSA compared with healthy controls. When moved proximally to assess the median nerve at a noncompressive site (forearm), there was no difference in CSA between CIPN patients and healthy controls. This discrepancy is often seen with NMUS evaluation of symptomatic carpal tunnel syndrome and other polyneuropathies.[36] These findings suggest that, at compression sites, CIPN may aggravate nerve entrapment and cause an increase in CSA of peripheral nerves. This discrepancy in the effects of CIPN between compression and noncompression anatomic sites has been described in NCS[11] and was suggested in a prior study of oxaliplatin CIPN.[27]

The finding of decreased peripheral nerve CSA is uncommon and has been reported in ALS[19] and spinocerebellar ataxia syndrome.[20-23] In vitro[37] and animal studies[38] have shown that the neurotoxicity of microtubule-targeting agents (eg, taxanes) is predominantly due damage to the dorsal root ganglion (DRG).[39,40] This leads to axonal loss in the longest sensory nerves and contributes to the clinical symptoms consistent with a ganglionopathy. In ALS, the reduction in nerve CSA is thought to reflect nerve atrophy from lower motor neuron (LMN) dropout[41] and may have utility as a marker of LMN involvement.[42] We hypothesize that the decreased CSA observed in our study may reflect the sensory ganglionopathy of taxane CIPN with sensory nerve atrophy. Because this study was limited to taxane CIPN, these results are not broadly applicable to other classes of chemotherapies whose neurotoxic mechanisms vary.

Multivariable analysis was notable for two confounding factors between CIPN and CSA, that is, age and time since taxane exposure. Age has previously been reported as having a very small negative correlation with peripheral nerve CSA.[29] The association with time is a novel finding; we hypothesize that this may be due to the gradual atrophy of damaged peripheral nerves following the initial insult. This is supported by the finding of decreased distal IENFD among patients with more time since taxane. Future studies will need to further account for these confounding factors.

There were several limitations of this pilot study, most of which were inherent to its design and small sample size. This study was designed to provide a broader evaluation of the pathophysiology of CIPN by including participants at all timepoints during and after taxane (active, recent, remote). However, this heterogeneity decreased the statistical power to detect changes in CSA, which may only occur in a time-specific manner. Because there is no intervention available for CIPN once the patient has completed taxane chemotherapy, there is little clinical utility for improved evaluation of chronic CIPN. Therefore, future studies of the clinical use of NMUS, including one that is currently enrolling patients,[43] will focus on patients with CIPN who are being considered for additional taxane chemotherapy so that dosing may be adjusted accordingly. This study was limited to female participants; reassuringly, in the prior study of healthy controls, there was no significant difference in nerve CSA by sex.[29] Prior studies[44] have reported variability among healthy controls with sural nerve CSA approximately 2–6 mm^2, our healthy control data had a mean of around 5 mm^2. Our study was not funded to support collection of another set of matched control values, which is why we used our previously published set.[29] A newer high-resolution probe could also be considered for future studies, as ultrahigh-frequency NMUS has been found to be useful for assessing changes at the fascicular level.[45]

CIPN is a common complication of breast cancer treatment with a critical need for a better diagnostic imaging modality. NMUS was found to be a rapid, noninvasive assessment of CIPN, which was well-tolerated and available at the point-of-care using a routine 15-Hz linear probe. This study's findings warrant future research on the longitudinal assessment of sural nerve CSA in CIPN.

ORCID

Thomas W. Lycan https://orcid.org/0000-0001-9475-1558

REFERENCES

1. Giordano SH, Lin YL, Kuo YF, Hortobagyi GN, Goodwin JS. Decline in the use of anthracyclines for breast cancer. *J Clin Oncol.* 2012;30(18):2232-2239.
2. Budman DR, Berry DA, Cirrincione CT, et al. Dose and dose intensity as determinants of outcome in the adjuvant treatment of breast cancer. The Cancer and Leukemia Group B. *J Natl Cancer Inst.* 1998;90(16):1205-1211.
3. Osmani K, Vignes S, Aissi M, et al. Taxane-induced peripheral neuropathy has good long-term prognosis: a 1- to 13-year evaluation. *J Neurol.* 2012;259(9):1936-1943.

4. Winters-Stone KM, Horak F, Jacobs PG, et al. Falls, Functioning, and disability among women with persistent symptoms of chemotherapy-induced peripheral neuropathy. *J Clin Oncol.* 2017;35(23):2604-2612.

5. Lavoie Smith EM, Barton DL, Qin R, Steen PD, Aaronson NK, Loprinzi CL. Assessing patient-reported peripheral neuropathy: the reliability and validity of the European Organization for Research and Treatment of Cancer QLQ-CIPN20 Questionnaire. *Qual Life Res.* 2013;22(10):2787-2799.

6. Park SB, Goldstein D, Krishnan AV, et al. Chemotherapy-induced peripheral neurotoxicity: a critical analysis. *CA Cancer J Clin.* 2013;63(6):419-437.

7. Reeves BN, Dakhil SR, Sloan JA, et al. Further data supporting that paclitaxel-associated acute pain syndrome is associated with development of peripheral neuropathy: North Central Cancer Treatment Group trial N08C1. *Cancer.* 2012;118(20):5171-5178.

8. Forsyth PA, Balmaceda C, Peterson K, Seidman AD, Brasher P, DeAngelis LM. Prospective study of paclitaxel-induced peripheral neuropathy with quantitative sensory testing. *J Neurooncol.* 1997;35(1):47-53.

9. Hershman DL, Weimer LH, Wang A, et al. Association between patient reported outcomes and quantitative sensory tests for measuring long-term neurotoxicity in breast cancer survivors treated with adjuvant paclitaxel chemotherapy. *Breast Cancer Res Treat.* 2011;125(3):767-774.

10. Chaudhry V, Rowinsky EK, Sartorius SE, Donehower RC, Cornblath DR. Peripheral neuropathy from taxol and cisplatin combination chemotherapy: clinical and electrophysiological studies. *Ann Neurol.* 1994;35(3):304-311.

11. Chen X, Stubblefield MD, Custodio CM, Hudis CA, Seidman AD, DeAngelis LM. Electrophysiological features of taxane-induced polyneuropathy in patients with breast cancer. *J Clin Neurophysiol.* 2013;30(2):199-203.

12. Kroigard T, Schroder HD, Qvortrup C, et al. Characterization and diagnostic evaluation of chronic polyneuropathies induced by oxaliplatin and docetaxel comparing skin biopsy to quantitative sensory testing and nerve conduction studies. *Eur J Neurol.* 2014;21(4):623-629.

13. Schreiber S, Oldag A, Kornblum C, et al. Sonography of the median nerve in CMT1A, CMT2A, CMTX, and HNPP. *Muscle Nerve.* 2013;47(3):385-395.

14. Cartwright MS, Brown ME, Eulitt P, Walker FO, Lawson VH, Caress JB. Diagnostic nerve ultrasound in Charcot-Marie-Tooth disease type 1B. *Muscle Nerve.* 2009;40(1):98-102.

15. Beekman R, van den Berg LH, Franssen H, Visser LH, van Asseldonk JT, Wokke JH. Ultrasonography shows extensive nerve enlargements in multifocal motor neuropathy. *Neurology.* 2005;65(2):305-307.

16. Zaidman CM, Pestronk A. Nerve size in chronic inflammatory demyelinating neuropathy varies with disease activity and therapy response over time: a retrospective ultrasound study. *Muscle Nerve.* 2014;50(5):733-738.

17. Cartwright MS, Walker FO. Neuromuscular ultrasound in common entrapment neuropathies. *Muscle Nerve.* 2013;48(5):696-704.

18. Breiner A, Qrimli M, Ebadi H, et al. Peripheral nerve high-resolution ultrasound in diabetes. *Muscle Nerve.* 2017;55(2):171-178.

19. Cartwright MS, Walker FO, Griffin LP, Caress JB. Peripheral nerve and muscle ultrasound in amyotrophic lateral sclerosis. *Muscle Nerve.* 2011;44(3):346-351.

20. Leadbetter R, Weatherall M, Pelosi L. Nerve ultrasound as a diagnostic tool for sensory neuronopathy in spinocerebellar ataxia syndrome. *Clin Neurophysiol.* 2019;130(4):568-572.

21. Pelosi L, Leadbetter R, Mulroy E, Chancellor AM, Mossman S, Roxburgh R. Peripheral nerve ultrasound in cerebellar ataxia neuropathy vestibular areflexia syndrome (CANVAS). *Muscle Nerve.* 2017;56(1):160-162.

22. Pelosi L, Mulroy E, Rodrigues MJ, Roxburgh RH. Neuronopathy and neuropathy in autosomal dominant spino-cerebellar ataxia (SCA): a preliminary peripheral nerve ultrasound study. *Clin Neurophysiol.* 2017;128(12):2436-2437.

23. Pelosi L, Mulroy E, Leadbetter R, et al. Peripheral nerves are pathologically small in cerebellar ataxia neuropathy vestibular areflexia syndrome: a controlled ultrasound study. *Eur J Neurol.* 2018;25(4):659-665.

24. Zaidman CM, Al-Lozi M, Pestronk A. Peripheral nerve size in normals and patients with polyneuropathy: an ultrasound study. *Muscle Nerve.* 2009;40(6):960-966.

25. Ebadi H, Siddiqui H, Ebadi S, Ngo M, Breiner A, Bril V. Peripheral nerve ultrasound in small fiber polyneuropathy. *Ultrasound Med Biol.* 2015;41(11):2820-2826.

26. Grimm A, Decard BF, Axer H, Fuhr P. The Ultrasound pattern sum score - UPSS. A new method to differentiate acute and subacute neuropathies using ultrasound of the peripheral nerves. *Clin Neurophysiol.* 2015;126(11):2216-2225.

27. Briani C, Campagnolo M, Lucchetta M, et al. Ultrasound assessment of oxaliplatin-induced neuropathy and correlations with neurophysiologic findings. *Eur J Neurol.* 2013;20(1):188-192.

28. Pitarokoili K, Hoffken N, Lonneker N, et al. Prospective study of the clinical, electrophysiologic, and sonographic characteristics of oxaliplatin-induced neuropathy. *J Neuroimaging.* 2019;29(1):133-139.

29. Cartwright MS, Passmore LV, Yoon JS, Brown ME, Caress JB, Walker FO. Cross-sectional area reference values for nerve ultrasonography. *Muscle Nerve.* 2008;37(5):566-571.

30. Eckhoff L, Knoop A, Jensen MB, Ewertz M. Persistence of docetaxel-induced neuropathy and impact on quality of life among breast cancer survivors. *Eur J Cancer.* 2015;51(3):292-300.

31. American Association of Neuromuscular & Electrdiagnostic Medicine (AANEM). Proper performance and interpretation of electrodiagnostic studies. [Corrected]. *Muscle Nerve.* 2015;51(3):468-471.

32. Chen S, Andary M, Buschbacher R, et al. Electrodiagnostic reference values for upper and lower limb nerve conduction studies in adult populations. *Muscle Nerve.* 2016;54(3):371-377.

33. Lauria G, Devigili G. Skin biopsy as a diagnostic tool in peripheral neuropathy. *Nat Clin Pract Neurol.* 2007;3(10):546-557.

34. Benatar M, Wuu J, Peng L. Reference data for commonly used sensory and motor nerve conduction studies. *Muscle Nerve.* 2009;40(5):772-794.

35. McArthur JC, Stocks EA, Hauer P, Cornblath DR, Griffin JW. Epidermal nerve fiber density: normative reference range and diagnostic efficiency. *Arch Neurol.* 1998;55(12):1513-1520.

36. Shen J, Cartwright MS. Neuromuscular ultrasound in the assessment of polyneuropathies and motor neuron disease. *J Clin Neurophysiol.* 2016;33(2):86-93.

37. Scuteri A, Nicolini G, Miloso M, et al. Paclitaxel toxicity in post-mitotic dorsal root ganglion (DRG) cells. *Anticancer Res.* 2006;26(2A):1065-1070.

38. Zhang H, Li Y, de Carvalho-Barbosa M, et al. Dorsal root ganglion infiltration by macrophages contributes to paclitaxel chemotherapy-induced peripheral neuropathy. *J Pain.* 2016;17(7):775-786.

39. Nicolini G, Monfrini M, Scuteri A. Axonal transport impairment in chemotherapy-induced peripheral neuropathy. *Toxics.* 2015;3(3):322-441.

40. Malacrida A, Meregalli C, Rodriguez-Menendez V, Nicolini G. Chemotherapy-induced peripheral neuropathy and changes in cytoskeleton. *Int J Mol Sci.* 2019;20(9):pii E2287.

41. Barnes SL, Simon NG. Clinical and research applications of neuromuscular ultrasound in amyotrophic lateral sclerosis. *Degener Neurol Neuromuscul Dis.* 2019;9:89-102.

42. Schreiber S, Abdulla S, Debska-Vielhaber G, et al. Peripheral nerve ultrasound in amyotrophic lateral sclerosis phenotypes. *Muscle Nerve.* 2015;51(5):669-675.

43. U.S.National Library of Medicine. Acupuncture in reducing chemotherapy-induced peripheral neuropathy in participants with stage I-III breast cancer. https://ClinicalTrials.gov/show/NCT03505671. Accessed February 17, 2020.

44. Rbia N, Nijhuis THJ, Roukema GR, Selles RW, van der Vlies CH, Hovius SER. Ultrasound assessment of the sural nerve in patients with neuropathic pain after ankle surgery. *Muscle Nerve.* 2018;57(3): 407-413.

45. Cartwright MS, Baute V, Caress JB, Walker FO. Ultrahigh-frequency ultrasound of fascicles in the median nerve at the wrist. *Muscle Nerve.* 2017;56(4):819-822.

SUPPORTING INFORMATION

Additional supporting information may be found online in the Supporting Information section at the end of this article.

How to cite this article: Lycan TW, Hsu F-C, Ahn CS, et al. Neuromuscular ultrasound for taxane peripheral neuropathy in breast cancer. *Muscle Nerve.* 2020;1–8. https://doi.org/10.1002/mus.26833

FEATURED BASIC SCIENCE ARTICLE

Melanocortin 1 Receptor–Targeted α-Particle Therapy for Metastatic Uveal Melanoma

Narges K. Tafreshi*[1], Christopher J. Tichacek*[1–3], Darpan N. Pandya*[4], Michael L. Doligalski*[1], Mikalai M. Budzevich[5], HyunJoo Kil[6], Nikunj B. Bhatt[4], Nancy D. Kock[7], Jane L. Messina[8–10], Epifanio E. Ruiz[5], Nella C. Delva[1], Adam Weaver[11], William R. Gibbons[11], David C. Boulware[12], Nikhil I. Khushalani[13], Ghassan El-Haddad[14], Pierre L. Triozzi[15], Eduardo G. Moros[1–3,10], Mark L. McLaughlin[6], Thaddeus J. Wadas[4], and David L. Morse[1,3,5,10]

[1]Department of Cancer Physiology, H. Lee Moffitt Cancer Center and Research Institute, Tampa, Florida; [2]Department of Radiation Oncology, H. Lee Moffitt Cancer Center and Research Institute, Tampa, Florida; [3]Department of Physics, University of South Florida, Tampa, Florida; [4]Department of Cancer Biology, Wake Forest University Health Sciences, Winston-Salem, North Carolina; [5]Small Animal Imaging Laboratory, H. Lee Moffitt Cancer Center and Research Institute, Tampa, Florida; [6]Department of Pharmaceutical Sciences, Health Sciences Center, West Virginia University, and Modulation Therapeutics Inc., Morgantown, West Virginia; [7]Section on Comparative Medicine, Department of Pathology, Wake Forest University Health Sciences, Winston-Salem, North Carolina; [8]Departments of Anatomic Pathology and Cutaneous Pathology, H. Lee Moffitt Cancer Center and Research Institute, Tampa, Florida; [9]Department of Dermatology, University of South Florida, Tampa, Florida; [10]Department of Oncologic Sciences, University of South Florida, Tampa, Florida; [11]Division of Research Integrity and Compliance, University of South Florida, Tampa, Florida; [12]Biostatistics Core Facility, H. Lee Moffitt Cancer Center and Research Institute, Tampa, Florida; [13]Department of Cutaneous Oncology, H. Lee Moffitt Cancer Center and Research Institute, Tampa, Florida; [14]Departments of Diagnostic Imaging and Interventional Radiology, H. Lee Moffitt Cancer Center and Research Institute, Tampa, Florida; and [15]Department of Hematology and Oncology, Wake Forest University Health Sciences, Winston-Salem, North Carolina

New effective therapies are greatly needed for metastatic uveal melanoma, which has a very poor prognosis with a median survival of less than 1 y. The melanocortin 1 receptor (MC1R) is expressed in 94% of uveal melanoma metastases, and a MC1R-specific ligand (MC1RL) with high affinity and selectivity for MC1R was previously developed. **Methods:** The ^{225}Ac-DOTA-MC1RL conjugate was synthesized in high radiochemical yield and purity and was tested in vitro for biostability and for MC1R-specific cytotoxicity in uveal melanoma cells, and the lanthanum-DOTA-MC1RL analog was tested for binding affinity. Non–tumor-bearing BALB/c mice were tested for maximum tolerated dose and biodistribution. Severe combined immunodeficient mice bearing uveal melanoma tumors or engineered MC1R-positive and -negative tumors were studied for biodistribution and efficacy. Radiation dosimetry was calculated using mouse biodistribution data and blood clearance kinetics from Sprague–Dawley rat data. **Results:** High biostability, MC1R-specific cytotoxicity, and high binding affinity were observed. Limiting toxicities were not observed at even the highest administered activities. Pharmacokinetics and biodistribution studies revealed rapid blood clearance (<15 min), renal and hepatobiliary excretion, MC1R-specific tumor uptake, and minimal retention in other normal tissues. Radiation dosimetry calculations determined pharmacokinetics parameters and absorbed α-emission dosages from ^{225}Ac and its daughters. Efficacy studies demonstrated significantly prolonged survival and decreased metastasis burden after a single administration of ^{225}Ac-DOTA-MC1RL in treated mice relative to controls. **Conclusion:** These results suggest significant potential for the clinical translation of ^{225}Ac-DOTA-MC1RL as a novel therapy for metastatic uveal melanoma.

Key Words: melanocortin 1 receptor; ^{225}Ac alpha therapy; uveal melanoma; mouse model

Uveal melanoma is the most common primary intraocular malignancy and differs from the more common cutaneous melanoma in terms of risk factors, primary treatment, anatomic spread, molecular changes, and response to systemic therapy (1,2). Patients who develop uveal melanoma metastases, primarily in the liver, have a very poor prognosis with a median survival of about 1 y. Because uveal melanomas have different characteristic mutations from cutaneous melanomas, targeted therapies that have been effective for the latter, such as BRAF, are not indicated for the former (3). Immune checkpoint inhibition therapies that are successful in cutaneous melanoma have had poor efficacy in ocular melanoma, with fewer than 10% of patients responding and with rapid recurrence (3).

The melanocortin 1 receptor (MC1R) is highly expressed in uveal melanoma metastases (4). MC1R is a member of a family of 5 G-protein–coupled melanocortin receptors, 4 of which bind melanocyte-stimulating hormone (MSH) and related ligands (MC1R, 3R, 4R, and 5R) (5). Unlike the other members of this G-protein family, MC1R is not expressed in most normal human tissues (6), lessening concern for therapy-related toxicity. Although expression is found in the brain (7) and normal melanocytes (8), this is not a major concern because conjugates can be designed to not cross
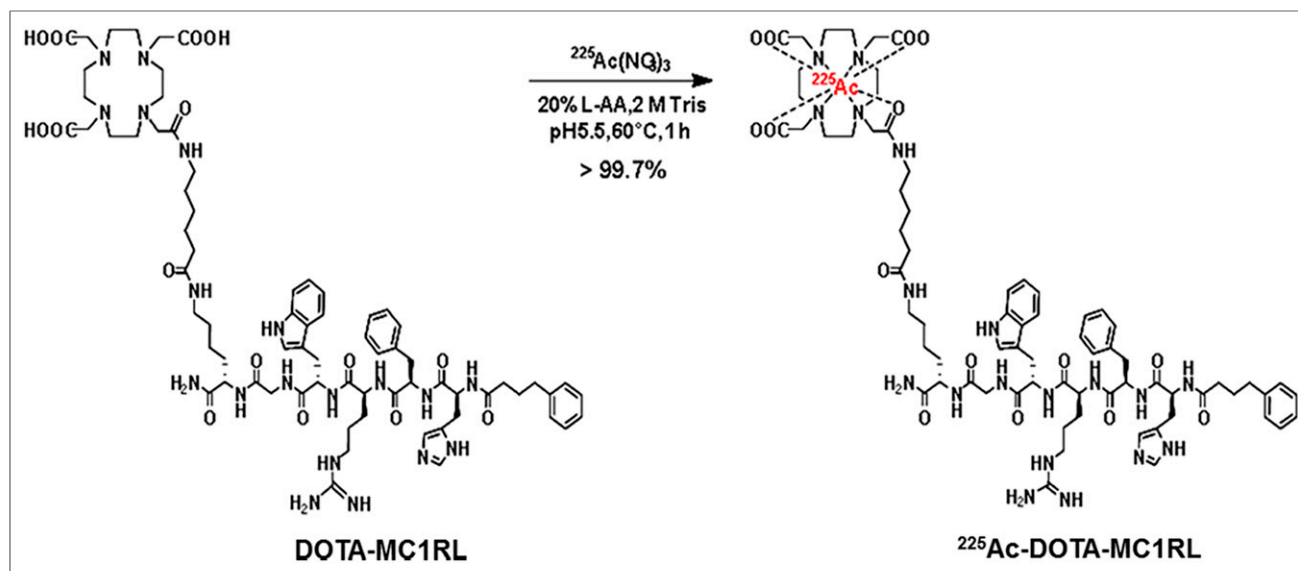
FIGURE 1. Radiochemical synthesis of ^{225}Ac-DOTA-MC1RL.

the blood–brain barrier and, in the most severe cases of melanocyte loss, the most serious symptom is vitiligo (9). MC1R expression has been reported on activated monocytes, macrophages, and dendritic cells derived from monocytes (10). This is also not a significant concern since the population of activated monocytes and macrophages can be replenished within days and lymphoid dendritic cells, which do not express MC1R, will not be depleted. MC1R is highly polymorphic (11), but the wild-type frequency is about 50% (8) and the most common mutations occur with a frequency of 21.5% in cytoplasmic domains, 19.7% in transmembrane domains, and 0% in the extracellular domain (11). Hence, most patients will have an MC1R isoform that is suitable for ligand binding. An MC1R-specific ligand (MC1RL) and conjugates were previously developed with high specificity (>200 fold) and affinity (0.2–0.4 nM inhibition constant) for MC1R (12,13). A fluorescent-dye conjugate was rapidly internalized by MC1R-expressing tumor cells, does not cross the blood–brain barrier, and is rapidly cleared from circulation (7).

Herein is reported the preclinical development and testing of a novel MC1R-targeted radiopharmaceutical, ^{225}Ac-DOTA-MC1RL, for targeted α-particle therapy (TAT) (14,15) of uveal melanoma. α-particle emissions consist of dicationic helium nuclei (He^{2+}) that have high linear-energy transfer and a short mean free path of only a few cell diameters (<100 μm) in tissue (16). ^{225}Ac is an α-particle–emitting radionuclide that has a 10-d half-life (17), 4 α-emissions in its decay chain, and high (28 MeV) total energy release (18).

MATERIALS AND METHODS

Compound Synthesis and Loading with Lanthanide

MC1RL (13) was synthesized according to a conventional N^α-fluorenylmethyloxycarbonyl (Fmoc) peptide synthesis strategy, except the Fmoc-Lys(Alloc)-OH was coupled to allow orthogonal alloc deprotection of the linker on the ε-amino group of the lysine after the linear peptide synthesis. The alloc group is removed, and Fmoc-aminohexanoic acid linker and tri-t-butyl-1,4,7,10-tetraazacyclododecane-1,4,7,10-tetraacetate (DOTA; TCI Chemicals) were coupled sequentially using O-(1H-6-chlorobenzotriazole-1-yl)-1,1,3,3-tetramethyluronium hexafluorophosphate activation. The DOTA-MC1RL peptide was cleaved

from the resin with a cocktail of trifluoroacetic acid (Chem-Impex International), water, and triisopropylsilane (Sigma-Aldrich) (95:2.5:2.5, v/v), precipitated in cold diethyl ether, pelleted/decanted, and lyophilized. The crude white powder was purified by reverse-phase high-performance liquid chromatography (Agilent) and characterized by both matrix-assisted laser desorption/ionization time-of-flight mass spectroscopy (JEOL USA Inc.) and analytic high-performance liquid chromatography. A scrambled peptide ligand (DOTA–substance P [SP]) was synthesized by changing the order of amino acids (sequence: 4-phenylbutyric acid-Trp-Gly-His-Arg-(D)-Phe-Lys(aminohexanoic acid-DOTA)-CONH$_2$). The europium–diethylenetriaminepentaacetic acid (DTPA)–MC1RL was synthesized as described before (19) except that MC1RL was used as the binding ligand (Supplemental Figs. 1A–1C; supplemental materials are available at http://jnm.snmjournals.org). Competition binding assays were performed as previously described using the europium-DTPA-NDPα-MSH ligand. The europium-DTPA-MC1RL binding affinity was determined using saturation binding assays. To determine MC1RL binding affinity for murine MC1RL, saturation binding assays were performed using the europium-DTPA-MC1RL and B16-F10 murine melanoma cells with high expression of murine MC1R (12).

Cell Culture and Characterization

Uveal melanoma cell lines were acquired (OCM1, OCM3, and OCM8 from June Kan-Mitchel, University of Southern California;

TABLE 1
In Vitro Serum Stability of ^{225}Ac-DOTA-MC1RL

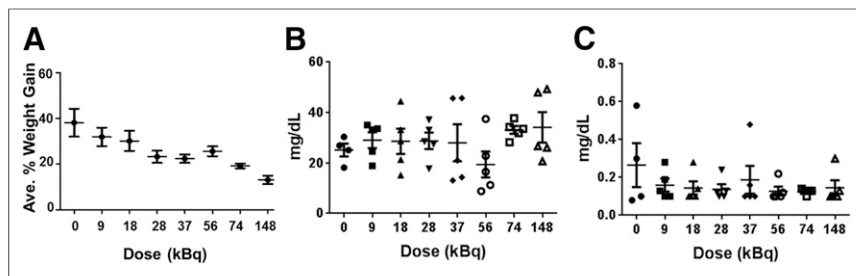| Day	% intact	
	Thin-layer chromatography scanner	γ-counter
0	100	100
2	97.3 ± 0.5	96.9 ± 0.4
4	95.6 ± 1.1	95.1 ± 0.8
6	93.5 ± 0.8	93.2 ± 1.3
8	91.4 ± 1.2	91.0 ± 0.9
10	90.2 ± 0.7	89.9 ± 1.3

FIGURE 2. MTD study for non–tumor-bearing mice: percentage weight gain (A), blood urea nitrogen (B), and blood creatinine (C).

OMM1 from Gregorius P. Luyten, University Hospital at Rotterdam; and MEL270, MEL290, and OMM2.3 from Timothy Murray, Bascom Palmer Eye Institute) and grown in RPMI medium, 10% fetal bovine serum, a 100 units/mL concentration of penicillin, a 100 mg/mL concentration of streptomycin, 1% 200 mM L-glutamine, 1% 100 mM sodium pyruvate, 1% minimal essential medium essential vitamin mixture (×100), 1% nonessential amino acid mixture (×100), and 1% 1 M (4-(2-hydroxyethyl)-1-piperazineethanesulfonic acid) in 5% CO_2 at 37°C. A375, A375/MC1R human cutaneous melanoma cells, and Hek293/MC1R cells were obtained and grown as before (12,20). Cells were authenticated per American Type Culture Collection guidelines (21), monitored for original morphology, and tested for *Mycoplasma* (MycoAlert kit; Lonza), and only passage numbers of less than 25 cells were used. MC1R expression and receptor number were determined as previously described (12,13) except that europium-DTPA-MC1RL was used for saturation binding. Cytotoxicity was determined as described in Supplemental Figure 2.

Radiochemical Synthesis and Characterization

DOTA-MC1RL or DOTA-SP (10 μg/10 μL of water), $^{225}Ac(NO_3)_3$ (3.4 MBq), 90 μL of water, and 10 μL of 20% L-ascorbic acid were added to a 1.5-mL tube followed by pH adjustment to 5.5–6 (1 M Tris buffer;10–12 μL) and incubation at 60°C for 1 h (Fig. 1). Specific activity was calculated using a standard method (22). Radiochemical purity was assessed 24 h after collection by a γ-counter, and in vitro serum stability was determined by adding 50 μL of ^{225}Ac-DOTA-MC1RL (2,072 kBq) to 1 mL of human serum (n = 4), incubated at 37°C for 10 d, and quantified at multiple time points by thin-layer chromatography and γ-counting using established methods (23).
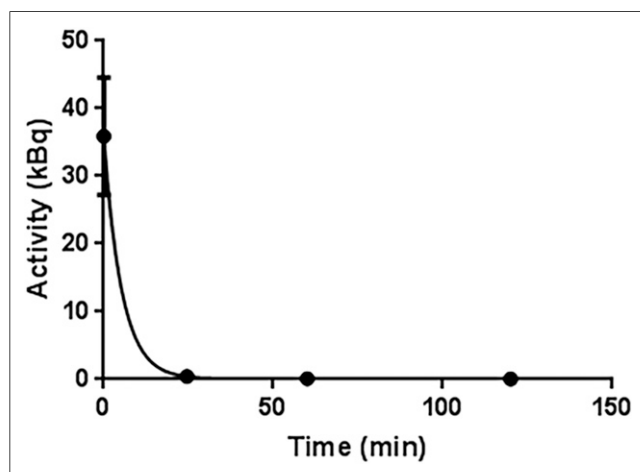

FIGURE 3. Plot of rat blood clearance: exponential decay nonlinear regression line fit of ^{225}Ac α-activity in rat blood over time, after intravenous administration of ^{225}Ac-DOTA-MC1RL (n = 4 rats).

Animal Studies

All protocols were approved (University of South Florida Institutional Animal Care and Use Committee protocol IS00000805 and Wake Forest University Health Sciences Institutional Animal Care and Use Committee protocol A11-144). Male and female animals were used. Sprague–Dawley rats, 10–12 wk old and weighing 200–250 g, were purchased with jugular vein catheters installed (Charles River). Nontumor studies used BALB/c mice (10–12 wk old, 18–22 g; Charles River). Severe combined immunodeficient (SCID) mice (6–8 wk old, 15–20 g; Charles River) were used for xenografting cell lines. Tail vein catheters were used for agent administration to mice.

For xenografting, 10×10^6 cells in 80 μL of phosphate-buffered saline and 20 μL of Matrigel (phenol red–free; Corning) were injected subcutaneously into the flank. Tumor volumes were determined by caliper using the following formulas: volume = (length × width²)/2 for A375 and A375/MC1R, and volume = (length × width × height)/2 for MEL270 tumors, which were initially flat with a gradual shift to a rounded shape.

Histology and Immunohistochemistry

Excised tissues were prepared for histology, hematoxylin and eosin staining, MC1R immunohistochemistry staining, and slide scanning as previously described (12). Metastasis burden was determined using images of 3 sections (25%, 50%, and 75%) through each liver and lung. Metastasis area was determined by segmentation using intensity and size threshold classifiers on the triple-red channel (Visiopharm software, version 6.7.0.2590). Total tissue area was determined with an intensity threshold classifier on the immunohistochemistry intensity channel, and the percentage metastasis was calculated.

To quantify MC1R expression in tumors, images from serial hematoxylin and eosin and immunohistochemistry sections were analyzed using Visiopharm, version 2017.7. Each serial section pair (hematoxylin and eosin and immunohistochemistry) was aligned using the tissue align module, and viable tumor was segmented by thresholding the hematoxylin channel. A multithreshold-marker-area analysis was then performed within the viable tumor region on each immunohistochemistry image. Each pixel was categorized as negative, weak, moderate, or strong on the basis of thresholds set by a pathologist, and the percentages of each category were normalized by total area of interest.

Maximum Tolerated Dose (MTD)

The MTD study was performed as previously described (23).

Measurement of Activity

Because α-particles from ^{225}Ac cannot be directly measured in tissue because of the short mean free path (18), ^{225}Ac α-activities were estimated using measurements of related γ-emissions. For the initial MTD study, syringes were prepared with a range of activities as determined by the γ-counter (Wallac 1470 Wizard; Perkin-Elmer). For subsequent studies, a dose calibrator (Atomlab 500; BioDex) was used to prefill syringes with 148 kBq ± 10% (per Appendix E of the BioDex manual) of ^{225}Ac-conjugate activity. Activities were measured for 2 min using dial number 38.2 as recommended by Biodex. Activities of ^{225}Ac, and the ^{221}Fr and ^{213}Bi daughter products (18), were measured by acquiring isomeric γ-spectra (Supplemental Fig. 3) before administration using a 4π well-type wipe-test γ-counter (Atomlab 500). Activities (^{225}Ac) were calculated using factors for γ-ray abundance per α-decay using calibration parameters and correction coefficients from Appendices A and E of the instrument manual. A full energy window
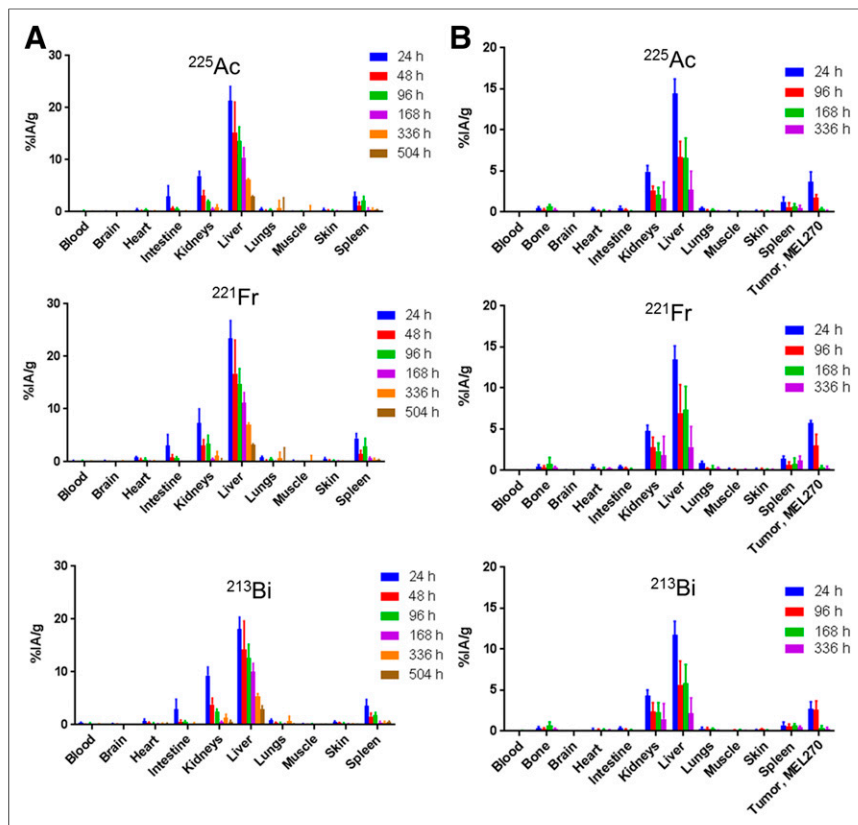
FIGURE 4. Biodistribution of ^{225}Ac-DOTA-MC1RL: ^{225}Ac, ^{221}Fr, and ^{213}Bi activities in tissues from non–tumor-bearing BALB/c mice (n = 6 per time point) (A) and SCID mice bearing MEL270 human uveal melanoma tumors (n = 5 per time point) (B).

(0–800 keV) was used for spectra acquisition that included γ-counts from ^{225}Ac (99.8-keV peak, 1% abundance) and 2 γ-emitting daughters, ^{221}Fr (218.1-keV peak, 11.4% abundance) and ^{213}Bi (440.5-keV peak, 25.9% abundance) (24). The α-activities were determined by fitting each peak with a multigaussian fit and integrating to determine the net

FIGURE 5. Biodistribution of ^{225}Ac-DOTA-MC1RL (A) and ^{225}Ac-DOTA-SP (B) in bilateral A375 and A375/MC1R tumors (n = 5 per time point).

number of counts while incorporating the acquisition time. Spectra were acquired at least 24 h after radiosynthesis or tissue rendering, ensuring that ^{225}Ac and daughters were in secular equilibrium (25). Activity remaining in the syringe and catheter after injection was calculated and subtracted to determine net administered activity.

Blood Pharmacokinetics

Sprague–Dawley rats were weighed before injection with radioactivity and injected with 148 kBq (±10%) of ^{225}Ac-DOTA-MC1RL in the syringe. Serial blood draws (45 μL) were taken from 5 min to 24 h after injection. ^{225}Ac α-activity was calculated as described above. Data were fitted using an exponential decay nonlinear regression.

Biodistribution

Non–tumor-bearing BALB/c mice, or SCID mice bearing MEL270 xenografts (160–650 mm³) or A375 and A375/MC1R bilateral xenografts (189–1,680 mm³), were intravenously administered 148 kBq (±10%) of ^{225}Ac α-activity in the syringe. Tissues were rendered and weighed at multiple time-points between 24 h and 3 wk after injection. For each tissue, ^{225}Ac, ^{221}Fr, and ^{213}Bi α-activities were calculated as described above and reported as percentage injected activity per gram (%IA/g).

Radiation Dosimetry

Biodistribution data for the different tissues were fitted using an exponential decay nonlinear regression, and dosimetry calculations were performed for ^{225}Ac, ^{221}Fr, ^{217}At, ^{213}Bi, and ^{213}Po using the generalized internal dosimetry schema of the MIRD Committee for α-particle emitters (26,27). The β⁻ decay branching ratio for ^{217}At to ^{217}Rn is only 0.01%; therefore, it was assumed that all decays of ^{217}At were by α-emission to ^{213}Bi. The branching ratios for decay of ^{213}Bi to ^{213}Po (98%) or ^{209}Tl (2%) were included in the calculation. Because of the relatively low linear-energy transfer and the small dimensions of the target tissues, the β⁻ emissions from ^{217}At, ^{213}Bi, ^{209}Tl, and ^{209}Pb were assumed negligible and were not included in the calculations (28). The following assumptions were made: uniform distribution of activity in the tissue volume; no α-particles escaping from the source tissue due to the short range; and electron and photon contributions that were negligible compared with α-particle energy deposition (28). It was also assumed that α-particles from ^{221}Fr (4.9-min half-life), ^{217}At (32.2-ms half-life), ^{213}Bi (46-min half-life), and ^{213}Po (4.2-μs half-life) were deposited in the same location as ^{225}Ac (10-d half-life) because of the relatively shorter half-lives of these daughter isotopes. Although ^{217}At and ^{213}Po do not have detectable γ-emissions, under the assumption that the decay chain had reached secular equilibrium, the accumulated activity of these 2 daughters would equal that of ^{221}Fr
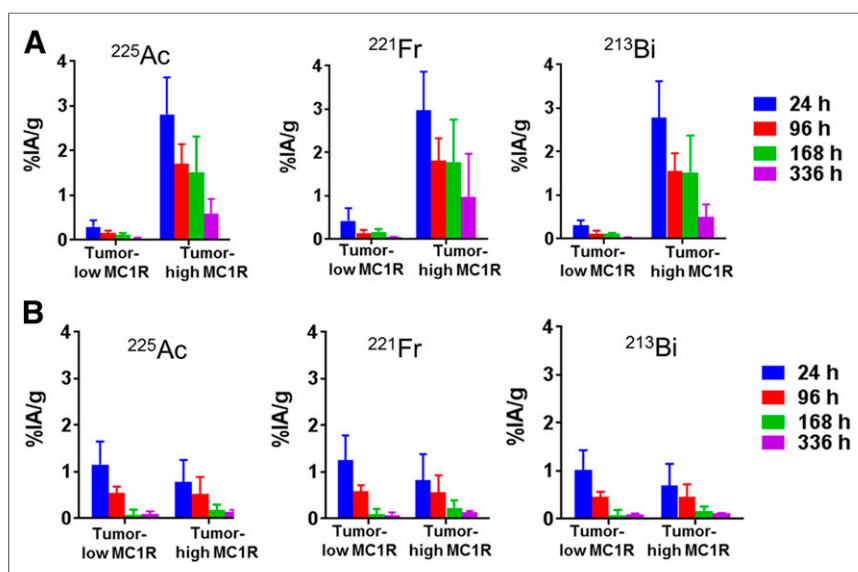
TABLE 2
Radiation Dosimetry and Clearance Kinetics Parameters for ^{225}Ac-DOTA-MC1RL in Non–Tumor-Bearing BALB/c Mice

Parameter	Blood	Brain	Heart	Intestine	Kidney	Liver	Lung	Muscle	Skin	Spleen
^{225}Ac										
Initial activity/organ (kBq)	ND	0.0065	0.0161	1.9113	0.7647	7.6597	0.0512	0.0044	0.0483	0.0426
Effective decay rate constant (h^{-1})	ND	0.0070	0.0030	0.0060	0.0060	0.0040	0.0030	0.0030	0.0050	0.0030
Effective decay half-life (d)	ND	4.1259	9.6270	4.8135	4.8135	7.2203	9.6270	9.6270	5.7762	9.6270
Accumulated activity/organ (kBq × h)	ND	0.7621	3.8089	260.3419	104.1599	1484.6038	12.1242	1.0529	7.7927	10.0784
Absorbed dose/injected activity (Gy/kBq)	ND	0.0002	0.0023	0.0102	0.0300	0.1485	0.0042	0.0004	0.0024	0.0092
^{221}Fr										
Initial activity/organ (kBq)	0.0153	0.0222	0.0349	1.9927	1.3795	8.4464	0.0723	0.0211	0.0705	0.0647
Effective decay rate constant (h^{-1})	0.0010	0.0030	0.0050	0.0070	0.0080	0.0040	0.0020	0.0030	0.0040	0.0040
Effective decay half-life (d)	28.8811	9.6270	5.7762	4.1259	3.6101	7.2203	14.4406	9.6270	7.2203	7.2203
Accumulated activity/organ (kBq × h)	5.6907	5.2622	5.6292	232.2869	139.2517	1637.0734	21.2642	4.9899	13.6614	12.5317
Absorbed dose/injected activity (Gy/kBq)	0.0022	0.0013	0.0037	0.0098	0.0434	0.1770	0.0080	0.0018	0.0045	0.0124
^{217}At										
Initial activity/organ (kBq)	0.0153	0.0222	0.0349	1.9927	1.3795	8.4464	0.0723	0.0211	0.0705	0.0647
Effective decay rate constant (h^{-1})	0.0010	0.0030	0.0050	0.0070	0.0080	0.0040	0.0020	0.0030	0.0040	0.0040
Effective decay half-life (d)	28.8811	9.6270	5.7762	4.1259	3.6101	7.2203	14.4406	9.6270	7.2203	7.2203
Accumulated activity/organ (kBq × h)	5.6907	5.2622	5.6292	232.2869	139.2517	1637.0734	21.2642	4.9899	13.6614	12.5317
Absorbed dose/injected activity (Gy/kBq)	0.0025	0.0014	0.0042	0.0110	0.0486	0.1983	0.0090	0.0021	0.0050	0.0139
^{213}Bi										
Initial activity/organ (kBq)	0.0236	0.0195	0.0309	1.8886	1.0318	6.5122	0.0717	0.0152	0.0627	0.0511
Effective decay rate constant (h^{-1})	0.0010	0.0010	0.0020	0.0050	0.0040	0.0040	0.0020	0.0020	0.0030	0.0030
Effective decay half-life (d)	28.8811	28.881	14.4406	5.7762	7.2203	7.2203	14.4406	14.4406	9.6270	9.6270
Accumulated activity/organ (kBq × h)	8.7917	7.2573	9.0914	304.6111	199.9839	1262.1858	21.0948	4.4603	14.8376	12.1064
Absorbed dose/injected activity (Gy/kBq)	0.0001	0.0000	0.0001	0.0002	0.0012	0.0025	0.0001	0.0000	0.0001	0.0002
^{213}Po										
Initial activity/organ (kBq)	0.0236	0.0195	0.0309	1.8886	1.0318	6.5122	0.0717	0.0152	0.0627	0.0511
Effective decay rate constant (h^{-1})	0.0010	0.0010	0.0020	0.0050	0.0040	0.0040	0.0020	0.0020	0.0030	0.0030
Effective decay half-life (d)	28.8811	28.881	14.4406	5.7762	7.2203	7.2203	14.4406	14.4406	9.6270	9.6270
Accumulated activity/organ (kBq × h)	8.7917	7.2573	9.0914	304.6111	199.9839	1262.1858	21.0948	4.4603	14.8376	12.1064
Absorbed dose/injected activity (Gy/kBq)	0.0044	0.0023	0.0079	0.0168	0.0811	0.1778	0.0103	0.0021	0.0063	0.0156
Total absorbed dose/injected activity (Gy/kBq)	0.0092	0.0053	0.0183	0.0481	0.2042	0.7042	0.0317	0.0064	0.0182	0.0512

ND = not detected.

and ^{213}Bi, respectively. The total absorbed α-particle dose was calculated from the summation of doses from ^{225}Ac, ^{221}Fr, ^{217}At, ^{213}Bi, and ^{213}Po.

Antitumor Efficacy

Tumor-bearing mice ($n = 11$/group) were injected with activities of ^{225}Ac-DOTA-MC1RL or ^{225}Ac-DOTA-SP, cold lanthanum-DOTA-MC1RL, or saline solution (0.9%, Cardinal Pharmaceuticals). Surpassing a 2,000 mm^3 tumor volume was the experimental endpoint unless clinical endpoints, such as 20% weight loss, tumor ulceration, hunched back, lack of grooming, or lethargy, were observed. Metastasis formation was identified by necropsy.

Statistical Analysis

The t test was used for the MTD study. The following analyses were used for comparison of the efficacy study groups: Kaplan–Meier for time to endpoint, a mixed-model analysis for tumor growth change, a paired Wilcoxon signed-rank test for initial decrease in tumor volume, a Fisher exact test with corrections for multiple testing using the Holm stepdown method for metastasis burden, and a nonparametric Kruskal–Wallis test for immunohistochemistry staining.

RESULTS

Synthesis and Characterization of Parent Compound and Lanthanide Chelates

The unmetallated DOTA-MC1RL was synthesized and, since there are no nonradioactive isotopes of actinium, the analogous lanthanum-DOTA-MC1RL chelate was prepared for use as a nonradioactive control (Supplemental Figs. 4–8) (23,29). Both DOTA-MC1RL and lanthanum-DOTA-MC1RL had high binding affinity for human MC1R, 0.24 ± 0.20 and 0.23 ± 0.18 nM inhibition constants, respectively (Supplemental Fig. 9A). The binding affinity of europium-DTPA-MC1RL to human MC1R was determined to be a 4.4 ± 2.3 nM dissociation constant (Supplemental Fig. 9B). Lower, 1.3 μM, dissociation constant affinity was observed for europium-DTPA-MC1RL binding to murine MC1R (Supplemental Fig. 9C). The scrambled peptide controls, lanthanum-DOTA-SP and europium-DOTA-SP, did not bind (Supplemental Figs. 9D and 9E).

TABLE 3
Radiation Dosimetry and Clearance Kinetics for ^{225}Ac-DOTA-MC1RL in SCID Mice Bearing MEL270 Tumors

| Parameter	Blood	Bone	Brain	Heart	Intestine	Kidney	Liver	Lung	Muscle	Skin	Spleen	Tumor
^{225}Ac												
Initial activity/organ (kBq)	0.0010	0.0172	0.0031	0.0151	0.3026	0.6417	4.8193	0.0265	0.0042	0.0242	0.0228	0.0518
Effective decay rate constant (h^{-1})	0.0010	0.0030	0.0020	0.0050	0.0130	0.0050	0.0060	0.0050	0.0020	0.0020	0.0040	0.0080
Effective decay half-life (d)	28.8811	9.6270	14.4406	5.7762	2.2216	5.7762	4.8135	5.7762	14.4406	14.4406	7.2203	3.6101
Accumulated activity/organ (kBq × h)	0.2726	3.2443	0.6873	2.1154	16.7417	89.9040	588.513	3.7089	0.9236	5.3441	3.6979	4.9055
Absorbed dose/injected activity (Gy/kBq)	0.0001	0.0041	0.0003	0.0020	0.0012	0.0273	0.0662	0.0025	0.0007	0.0010	0.0107	0.0045
^{221}Fr												
Initial activity/organ (kBq)	0.0036	0.0185	0.0059	0.0192	0.2655	0.6167	4.4828	0.0495	0.0071	0.0362	0.0257	0.0806
Effective decay rate constant (h^{-1})	0.0017	0.0030	0.0010	0.0030	0.0090	0.0040	0.0060	0.0040	0.0020	0.0020	0.0010	0.0070
Effective decay half-life (d)	16.9889	9.6270	28.8811	9.6270	3.2090	7.2203	4.8135	7.2203	14.4406	14.4406	28.881	4.1259
Accumulated activity/organ (kBq × h)	0.8370	3.4960	1.5396	3.6259	22.3311	99.8475	547.425	8.0162	1.5699	8.0166	6.7303	8.6407
Absorbed dose/injected activity (Gy/kBq)	0.0002	0.0047	0.0007	0.0037	0.0017	0.0328	0.0666	0.0058	0.0014	0.0017	0.0211	0.0086
^{217}At												
Initial activity/organ (kBq)	0.0036	0.0185	0.0059	0.0192	0.2655	0.6167	4.4828	0.0495	0.0071	0.0362	0.0257	0.0806
Effective decay rate constant (h^{-1})	0.0017	0.0030	0.0010	0.0030	0.0090	0.0040	0.0060	0.0040	0.0020	0.0020	0.0010	0.0070
Effective decay half-life (d)	16.9889	9.6270	28.8811	9.6270	3.2090	7.2203	4.8135	7.2203	14.4406	14.4406	28.881	4.1259
Accumulated activity/organ (kBq × h)	0.8370	3.4960	1.5396	3.6259	22.3311	99.8475	547.425	8.0162	1.5699	8.0166	6.7303	8.6407
Absorbed dose/injected activity (Gy/kBq)	0.0003	0.0053	0.0007	0.0041	0.0019	0.0367	0.0746	0.0065	0.0015	0.0019	0.0236	0.0097
^{213}Bi												
Initial activity/organ (kBq)	0.0016	0.0133	0.0027	0.0082	0.2160	0.5664	3.9089	0.0175	0.0017	0.0240	0.0131	0.0381
Effective decay rate constant (h^{-1})	0.0013	0.0020	0.0007	0.0040	0.0100	0.0040	0.0060	0.0060	0.0020	0.0050	0.0030	0.0060
Effective decay half-life (d)	22.2163	14.4406	41.2588	7.2203	2.8881	7.2203	4.8135	4.8135	14.4406	5.7762	9.6270	4.8135
Accumulated activity/organ (kBq × h)	0.4096	2.9358	0.7531	1.3342	16.2384	91.7024	477.346	2.1354	0.3859	3.3617	2.4736	4.6565
Absorbed dose/injected activity (Gy/kBq)	2.20E-06	7.39E-05	5.96E-06	2.51E-05	2.32E-04	5.61E-04	1.08E-03	2.88E-05	6.19E-06	1.32E-05	1.44E-04	8.68E-05
^{213}Po												
Initial activity/organ (kBq)	0.0016	0.0133	0.0027	0.0082	0.2160	0.5664	3.9089	0.0175	0.0017	0.0240	0.0131	0.0381
Effective decay rate constant (h^{-1})	0.0013	0.0020	0.0007	0.0040	0.0100	0.0040	0.0060	0.0060	0.0020	0.0050	0.0030	0.0060
Effective decay half-life (d)	22.2163	14.4406	41.2588	7.2203	2.8881	7.2203	4.8135	4.8135	14.4406	5.7762	9.6270	4.8135
Accumulated activity/organ (kBq × h)	0.4096	2.9358	0.7531	1.3342	16.2384	91.7024	477.346	2.1354	0.3859	3.3617	2.4736	4.6565
Absorbed dose/injected activity (Gy/kBq)	0.0002	0.0052	0.0004	0.0018	0.0016	0.0392	0.0756	0.0020	0.0004	0.0009	0.0101	0.0061
Total absorbed dose/injected activity (Gy/kBq)	0.0007	0.0193	0.0021	0.0115	0.0065	0.1366	0.2842	0.0168	0.0040	0.0056	0.0656	0.0290
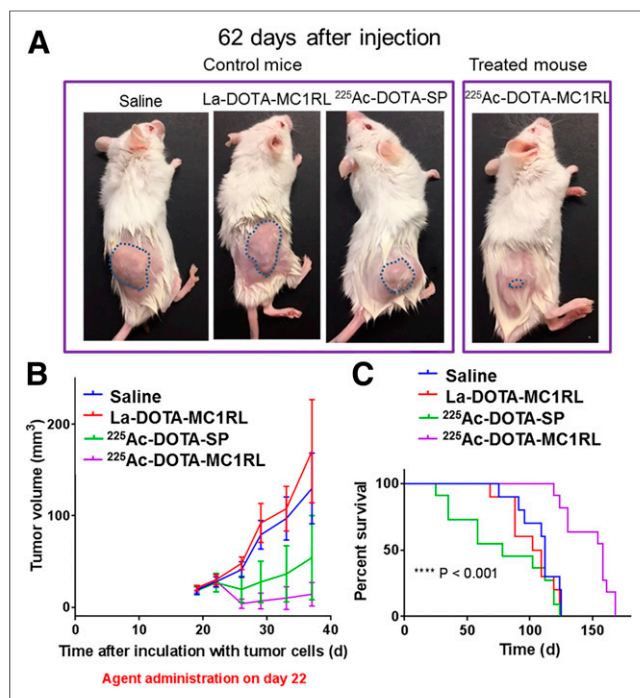
FIGURE 6. Efficacy study in mice bearing MEL270 tumors: representative images of tumors (outlined) (A); initial tumor growth volumes (B); and Kaplan–Meier plots (C).

Radiosynthesis and Characterization of ^{225}Ac Radiopharmaceutical

Radiochemical purity of 99.8% and specific activity of 181.3 ± 92.5 kBq/μg and 140.6 ± 55.5 kBq/μg for ^{225}Ac-DOTA-MC1RL and ^{225}Ac-DOTA-SP, respectively, were observed (Supplemental Fig. 10). In vitro serum stability was high, with 90% intact after 10 d (Table 1).

MC1R Expression on Uveal Melanoma Cell Lines and Xenograft Tumors

MC1R messenger RNA and protein expression were confirmed in a set of uveal melanoma cell lines (Supplemental Fig. 11). Only MEL270, OMM2.3, and OMM1 cells carry the GNAQ or GNA11 mutations found in nearly all uveal melanomas (*30*). The MEL270 and OMM1 cells formed tumors in immunocompromised mice, and all xenografts had high and uniform MC1R protein expression.

Receptor Number for Tumor Cell Lines

MEL270 cells were selected for the in vivo studies, and it was determined that MEL270 cells have 410,000 receptors per cell (Supplemental Fig. 12), which is a higher level of endogenous expression than that of the engineered A375/MC1R cells, which have 75,000 receptors per cell (*12*). The parental A375 melanoma cell line has extremely low expression, at 400 ± 93 MC1Rs per cell (*31*).

In Vitro MC1R-Specific Cytotoxicity

Cytotoxicity assays were performed with the goal of demonstrating target-specific cytotoxicity. Assay conditions were not optimized to demonstrate maximal toxicity. Significantly reduced proliferation ($P < 0.0001$) was observed in uveal melanoma cells and the engineered A375/MC1R cells treated with ^{225}Ac-DOTA-MC1RL relative to the untargeted ^{225}Ac-DOTA-SP or phosphate-buffered saline controls (Supplemental Fig. 2). All cell lines also had a significant ($P < 0.001$) response to incubation with ^{225}Ac-DOTA-SP relative to phosphate-buffered saline. However, there was no significant difference in A375 cell proliferation (extremely low MC1R) when treated with either the targeted or the untargeted radiopharmaceutical. These results demonstrate MC1R-specific cytotoxicity. Assay replicates yielded comparable results.

MTD

The MTD was evaluated in immune-competent non–tumor-bearing BALB/c mice ($n = 5$/cohort). Cohorts received a single intravenous injection of ^{225}Ac-DOTA-MC1RL over the range of 0–148 kBq in the syringe. At completion of the study (>11 ^{225}Ac half-lives, 118 d after injection), serum and tissues (adipose, bone, cecum, colon, duoden, esophageal, heart, ileum, kidney, liver, lung, lymph nodes, muscle, pancreas, small intestine, spleen, and stomach) were collected for histology and then examined in a masked manner by a veterinary pathologist to assess radiation-induced tissue damage. No remarkable damage was observed in any of the tissues (Supplemental Figs. 13–16). For example, the control kidneys had minimal multifocal interstitial fibrosis and minimal medullary protein in tubules, which were both considered to be incidental findings. The incidental minimal medullary protein was also found in some kidneys from the groups that received treatment activities, but each treatment group also included kidneys that were within normal limits for all types of damage. The cortex of one kidney from the group with the highest administered activity had a focal extracellular cortical hyaline substance that was healing and was considered to be an incidental finding (Supplemental Fig. 14D). Blood urea nitrogen and creatinine, which are important indicators of renal function, were also determined and were not significantly elevated among the groups (Figs. 2B and 2C). All animals had gained weight by the end of the study, albeit less weight was gained by animals at the highest dose level than in the lowest (Fig. 2A).

Pharmacokinetics and Biodistribution

In rats, ^{225}Ac-DOTA-MC1RL rapidly cleared (<15 min after injection) from blood circulation (Fig. 3). After administration to non–tumor-bearing BALB/c mice, ^{225}Ac activities were observed primarily in clearance tissues. At 24 h after injection of ^{225}Ac-DOTA-MC1RL, the liver, kidneys, spleen, and intestine had 21.2 ± 2.8, 6.9 ± 0.9, 2.9 ± 0.8, and 2.9 ± 2.0 %IA/g, whereas negligible activity was observed in the other tissues measured. Activity had largely cleared from the tissues at 1–3 wk (Fig. 4A). For tumor-bearing animals, activity was retained in MC1R-positive tumors, that is, MEL270 (Fig. 4B) and A375/MC1R tumors (Fig. 5A), which had 3.6 ± 1.2 and 2.8 ± 0.8 %IA/g, respectively, compared with the nominal 0.30 ± 0.1 %IA/g in the MC1R-negative A375 tumors at 24 h after injection. The clearance tissues in tumor-bearing animals had lower activities than in non–tumor-bearing mice: for example, 14.4 ± 1.7 %IA/g in the livers of MEL270 tumor-bearing mice at 24 h (Fig. 4B), compared with the 21.2 ± 2.8 %IA/g in the non–tumor-bearing mice (Fig. 4A). The ^{225}Ac-DOTA-SP tumor distribution in the bilateral A357 and A375/MC1R model was also determined, and as expected, uptake was minimal and did not differ between the positive and negative A375 tumors (Fig. 5B). The distribution of ^{221}Fr and ^{213}Bi was also determined (Figs. 4 and 5). However, since ^{225}Ac and daughters are at secular equilibrium by 24 h after injection and the ^{221}Fr and ^{213}Bi atoms
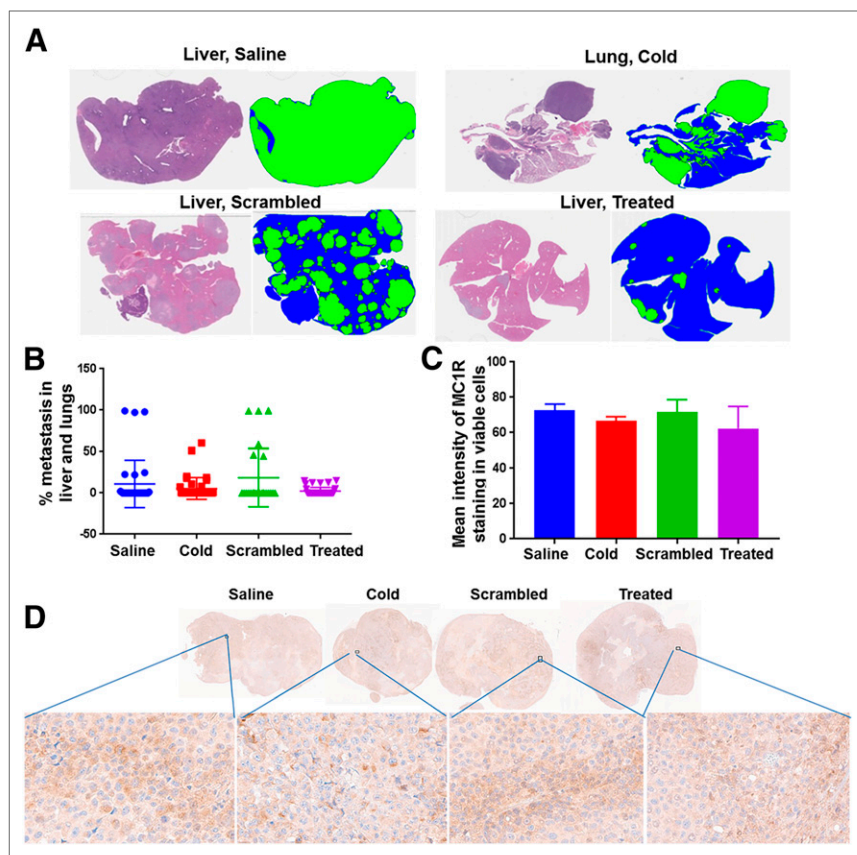
FIGURE 7. Metastasis study in MEL270 uveal melanoma mouse model and MC1R expression in tumors reaching endpoints from each treatment group: representative hematoxylin and eosin staining and corresponding threshold segmentations of sections containing liver and lung metastases (cold = lanthanum-DOTA-MC1RL; scrambled = untargeted; treated = ^{225}Ac-DOTA-MC1RL; blue = normal tissue; green = metastasis) (A); quantified metastasis burden (B); graph (C) and sections (D) for MC1R immunohistochemistry staining of MEL270 tumors after reaching endpoints.

Antitumor Efficacy

SCID mice bearing MEL270 tumors (124 $\pm$ 36 mm^3 pretreatment tumor volumes) were injected with a single administration of ^{225}Ac-DOTA-MC1RL (92.5 $\pm$ 9.3 kBq), ^{225}Ac-DOTA-SP (99.9 $\pm$ 9.9 kBq), lanthanum-DOTA-MC1RL (1 pmol/mouse), or saline. Representative images show much smaller tumors in treated mice than in controls (Fig. 6A), and tumor volumes decreased immediately after treatment relative to controls ($P = 0.001$) before eventual regrowth (Fig. 6B). Treated mice had a significantly delayed time to experimental or clinical endpoint ($P < 0.001$), with a median survival of 148 d, compared with the median survival of control groups (79–108 d), and differences among the controls were not significant (Fig. 6C). In this study, some animals were euthanized because of reaching clinical endpoints instead of the experimental endpoint (Supplemental Table 1). Some of the animals that reached clinical endpoints had metastases in the liver or lungs, and metastasis burden was significantly lower in the ^{225}Ac-DOTA-MC1RL treated group than in the controls ($P = 0.024$) (Figs. 7A and 7B). Mice bearing A375/MC1R tumors (240 $\pm$ 110 mm^3 pretreatment volume) were also injected with either sterile saline, lanthanum-DOTA-MC1RL, 107.3 $\pm$ 11.1 kBq of ^{225}Ac-DOTA-SP, or 59.2 $\pm$ 5.9 kBq of ^{225}Ac-DOTA-MC1RL, and significant decreases in tumor volume ($P = 0.005$) and tumor growth delay ($P < 0.0001$) were observed. Some tumors that disappeared did not recur, and those mice lived their natural life span (Supplemental Figs. 18A–18C). After tumors reached an endpoint, MC1R staining was quantified, and the level of MC1R expression was not significantly different in treated tumors that responded by shrinking before regrowth relative to control tumors ($P = 0.60$ for MEL270 and $P = 0.82$ for A375/MC1R) (Figs. 7C and 7D; Supplemental Fig. 18D).

DISCUSSION

We have developed and evaluated a novel MC1R-targeted radiopharmaceutical, ^{225}Ac-DOTA-MC1RL, for TAT of metastatic uveal melanoma. The choice of using a peptide-targeting ligand is reinforced by the recent preclinical and clinical successes of TAT radiopeptides (14,15,32–34). Another group has also reported the development of a peptide-based TAT, ^{212}Pb-CCMSH, that is targeted to melanocortin receptors for treatment of melanoma (35). However, ^{212}Pb-CCMSH was associated with renal toxicity. This is likely due to the use of an α-MSH derivative–targeting ligand, as α-MSH has specificity for multiple melanocortin receptor isoforms, including MC5R, which is expressed in the human kidney and lungs (6). The MC1RL-targeting moiety used in the current work has specificity for the MC1R isoform (13), greatly reducing the potential for renal toxicity. Another advantage of ^{225}Ac-DOTA-MC1RL over the ^{212}Pb-TAT agent is that ^{225}Ac has greater cell-killing potential through

present during injection will be mostly decayed, the ^{221}Fr and ^{213}Bi detected in the samples are from decay of the ^{225}Ac taken into the tissues.

Radiation Dosimetry

Biodistribution data were fitted (Supplemental Fig. 17), and clearance kinetics, tissue biologic half-life, accumulated activity, and absorbed dose/injected activity (Gy/kBq) were estimated for each radionuclide in each tissue for non–tumor-bearing and MEL270 tumor-bearing mice (Tables 2 and 3). The effective decay half-lives calculated for ^{225}Ac in tissues—for example, 7.2 d in liver—were shorter than the radiodecay half-life of ^{225}Ac (10 d), indicating biologic clearance. The calculated total absorbed dose per injected activity (Gy/kBq) for ^{225}Ac-DOTA-MC1RL was minimal in all tissues except clearance organs and positive tumor. Since the positive tumors shrank rapidly in response to the treatment and the total absorbed doses were extrapolated from data collected over a 2-wk period, the dose values for the tumors are likely subdued relative to the clearance organs, which did not have appreciable cellular toxicity at the administered activities. The total absorbed dose in the liver was generally lower in mice with tumors than in nontumor mice: for example, 0.284 and 0.704 Gy/kBq, respectively.

generation of 4 α-particle emissions per radionuclide, compared with the single α-emission of ^{212}Pb, in their relative decay chains (*35,36*).

^{225}Ac-DOTA-MC1RL has high affinity for MC1R, high radiochemistry yield and purity, high biostability, and MC1R-specific cytotoxicity in vitro. In vivo studies demonstrated low toxicity, rapid blood clearance, and uptake into MC1R-positive tumors and clearance organs. Biodistribution studies demonstrated that ^{225}Ac remains in the compartments where ^{225}Ac-DOTA-MC1RL was initially distributed, that is, tumors and clearance organs, and the corresponding clearance kinetics parameters and radiation dose delivered by all α-particle–emitting radioisotopes in the decay chain were calculated. Considering the 10-d half-life of ^{225}Ac, most of the administered ^{225}Ac-DOTA-MC1RL will have either been taken into tumor cells (*7*) or cleared from the blood before decay. Hence, ^{225}Ac-DOTA-MC1RL likely functions as an in vivo α-particle generator, concentrating α-emissions in the target tumor tissues, with limited translocation of daughter isotopes (*32*). This is consistent with the recent observations of efficacy with low toxicity observed for an ^{225}Ac-PSMA–targeting small-molecule conjugate (*37*).

In vivo efficacy studies demonstrated significant tumor and metastasis growth delay and prolonged survival in human uveal and cutaneous melanoma xenograft models in mice after a single treatment of ^{225}Ac-DOTA-MC1RL, including some cures. Tumors that shrank and regrew after treatment had the same MC1R expression levels as controls, suggesting that multiple treatment regimens would increase efficacy.

CONCLUSION

We have developed and evaluated a novel MC1R-targeted radiopharmaceutical for TAT of metastatic uveal melanoma. In vivo studies demonstrated low toxicity, rapid blood clearance, uptake into MC1R-positive tumors and clearance organs, significant tumor and metastasis growth delay, and prolonged survival in human uveal melanoma xenograft models in mice after a single treatment of ^{225}Ac-DOTA-MC1RL. This novel radiopharmaceutical has strong potential to benefit patients with metastatic uveal melanoma, which has had no significant improvement in treatment in the last 20 y.

DISCLOSURE

ACKNOWLEDGMENTS

REFERENCES

1. Chattopadhyay C, Kim DW, Gombos DS, et al. Uveal melanoma: from diagnosis to treatment and the science in between. *Cancer.* 2016;122:2299–2312.
2. Krantz BA, Dave N, Komatsubara KM, Marr BP, Carvajal RD. Uveal melanoma: epidemiology, etiology, and treatment of primary disease. *Clin Ophthalmol.* 2017;11:279–289.
3. Komatsubara KM, Carvajal RD. Immunotherapy for the treatment of uveal melanoma: current status and emerging therapies. *Curr Oncol Rep.* 2017;19:45.
4. López MN, Pereda C, Ramirez M, et al. Melanocortin 1 receptor is expressed by uveal malignant melanoma and can be considered a new target for diagnosis and immunotherapy. *Invest Ophthalmol Vis Sci.* 2007;48:1219–1227.
5. Yang Y. Structure, function and regulation of the melanocortin receptors. *Eur J Pharmacol.* 2011;660:125–130.
6. Chhajlani V. Distribution of cDNA for melanocortin receptor subtypes in human tissues. *Biochem Mol Biol Int.* 1996;38:73–80.
7. Tafreshi NK, Silva A, Estrella VC, et al. In vivo and in silico pharmacokinetics and biodistribution of a melanocortin receptor 1 targeted agent in preclinical models of melanoma. *Mol Pharm.* 2013;10:3175–3185.
8. Ainger SA, Jagirdar K, Lee KJ, Soyer HP, Sturm RA. Skin pigmentation genetics for the clinic. *Dermatology.* 2017;233:1–15.
9. Ezzedine K, Eleftheriadou V, Whitton M, van Geel N. Vitiligo. *Lancet.* 2015;386:74–84.
10. Salazar-Onfray F, Lopez M, Lundqvist A, et al. Tissue distribution and differential expression of melanocortin 1 receptor, a malignant melanoma marker. *Br J Cancer.* 2002;87:414–422.
11. Tagliabue E, Fargnoli MC, Gandini S, et al. MC1R gene variants and non-melanoma skin cancer: a pooled-analysis from the M-SKIP project. *Br J Cancer.* 2015;113:354–363.
12. Tafreshi NK, Huang X, Moberg VE, et al. Synthesis and characterization of a melanoma-targeted fluorescence imaging probe by conjugation of a melanocortin 1 receptor (MC1R) specific ligand. *Bioconjug Chem.* 2012;23:2451–2459.
13. Barkey NM, Tafreshi NK, Josan JS, et al. Development of melanoma-targeted polymer micelles by conjugation of a melanocortin 1 receptor (MC1R) specific ligand. *J Med Chem.* 2011;54:8078–8084.
14. Morgenstern A, Apostolidis C, Kratochwil C, Sathekge M, Krolicki L, Bruchertseifer F. An overview of targeted alpha therapy with 225actinium and 213bismuth. *Curr Radiopharm.* 2018;11:200–208.
15. Makvandi M, Dupis E, Engle JW, et al. Alpha-emitters and targeted alpha therapy in oncology: from basic science to clinical investigations. *Target Oncol.* 2018;13:189–203.
16. Baidoo KE, Yong K, Brechbiel MW. Molecular pathways: targeted alpha-particle radiation therapy. *Clin Cancer Res.* 2013;19:530–537.
17. Deblonde GJ, Abergel RJ. Active actinium. *Nat Chem.* 2016;8:1084.
18. Ma D, McDevitt MR, Finn RD, Scheinberg DA. Breakthrough of ^{225}Ac and its radionuclide daughters from an ^{225}Ac/^{213}Bi generator: development of new methods, quantitative characterization, and implications for clinical use. *Appl Radiat Isot.* 2001;55:667–678.
19. Josan JS, De Silva CR, Yoo B, et al. Fluorescent and lanthanide labeling for ligand screens, assays, and imaging. *Methods Mol Biol.* 2011;716:89–126.
20. Handl HL, Vagner J, Yamamura HI, Hruby VJ, Gillies RJ. Lanthanide-based time-resolved fluorescence of in cyto ligand-receptor interactions. *Anal Biochem.* 2004;330:242–250.
21. Reid Y, Storts D, Riss T, Minor L. Authentication of human cell lines by STR DNA profiling analysis. In: Sittampalam GS, Coussens NP, Brimacombe K, et al. *Assay Guidance Manual.* Bethesda, MD: Eli Lily & Company and the National Center for Advancing Translational Science; 2004:1–21.
22. Bonardi ML, de Goeij JJM. How do we ascertain specific activities in no-carrier-added radionuclide preparations? *J Radioanal Nucl Chem.* 2005;263:87–92.

23. Pandya DN, Hantgan R, Budzevich MM, et al. Preliminary therapy evaluation of [225]Ac-DOTA-c(RGDyK) demonstrates that Cerenkov radiation derived from [225]Ac daughter decay can be detected by optical imaging for in vivo tumor visualization. *Theranostics.* 2016;6:698–709.

24. Apostolidis C, Molinet R, Rasmussen G, Morgenstern A. Production of Ac-225 from Th-229 for targeted alpha therapy. *Anal Chem.* 2005;77:6288–6291.

25. Robertson AKH, Ramogida CF, Rodriguez-Rodriguez C, et al. Multi-isotope SPECT imaging of the [225]Ac decay chain: feasibility studies. *Phys Med Biol.* 2017;62:4406–4420.

26. Song H, Hobbs RF, Vajravelu R, et al. Radioimmunotherapy of breast cancer metastases with alpha-particle emitter [225]Ac: comparing efficacy with [213]Bi and [90]Y. *Cancer Res.* 2009;69:8941–8948.

27. Bolch WE, Eckerman KF, Sgouros G, Thomas SR. MIRD pamphlet no. 21: a generalized schema for radiopharmaceutical dosimetry–standardization of nomenclature. *J Nucl Med.* 2009;50:477–484.

28. Kratochwil C, Bruchertseifer F, Rathke H, et al. Targeted alpha therapy of mCRPC with [225]actinium-PSMA-617: dosimetry estimate and empirical dose finding. *J Nucl Med.* 2017;58:1624–1631.

29. Thiele NA, Wilson JJ. Actinium-225 for targeted alpha therapy: coordination chemistry and current chelation approaches. *Cancer Biother Radiopharm.* 2018;33:336–348.

30. Griewank KG, Yu X, Khalili J, et al. Genetic and molecular characterization of uveal melanoma cell lines. *Pigment Cell Melanoma Res.* 2012;25:182–187.

31. Cheng Z, Xiong Z, Subbarayan M, Chen X, Gambhir SS. ^{64}Cu-labeled alpha-melanocyte-stimulating hormone analog for microPET imaging of melanocortin 1 receptor expression. *Bioconjug Chem.* 2007;18:765–772.

32. Miederer M, Henriksen G, Alke A, et al. Preclinical evaluation of the alpha-particle generator nuclide [225]Ac for somatostatin receptor radiotherapy of neuroendocrine tumors. *Clin Cancer Res.* 2008;14:3555–3561.

33. Nayak TK, Norenberg JP, Anderson TL, Prossnitz ER, Stabin MG, Atcher RW. Somatostatin-receptor-targeted alpha-emitting [213]Bi is therapeutically more effective than beta(−)-emitting ^{177}Lu in human pancreatic adenocarcinoma cells. *Nucl Med Biol.* 2007;34:185–193.

34. Drecoll E, Gaertner FC, Miederer M, et al. Treatment of peritoneal carcinomatosis by targeted delivery of the radio-labeled tumor homing peptide bi-DTPA-[F3]2 into the nucleus of tumor cells. *PLoS One.* 2009; 4:e5715.

35. Miao Y, Hylarides M, Fisher DR, et al. Melanoma therapy via peptide-targeted α-radiation. *Clin Cancer Res.* 2005;11:5616–5621.

36. McDevitt MR, Ma D, Lai LT, et al. Tumor therapy with targeted atomic nanogenerators. *Science.* 2001;294:1537–1540.

37. Kratochwil C, Bruchertseifer F, Rathke H, et al. Targeted alpha-therapy of metastatic castration-resistant prostate cancer with [225]Ac-PSMA-617: swimmer-plot analysis suggests efficacy regarding duration of tumor control. *J Nucl Med.* 2018;59:795–802.

The Journal of NUCLEAR MEDICINE

Melanocortin 1 Receptor−Targeted α-Particle Therapy for Metastatic Uveal Melanoma

Narges K. Tafreshi, Christopher J. Tichacek, Darpan N. Pandya, Michael L. Doligalski, Mikalai M. Budzevich, HyunJoo Kil, Nikunj B. Bhatt, Nancy D. Kock, Jane L. Messina, Epifanio E. Ruiz, Nella C. Delva, Adam Weaver, William R. Gibbons, David C. Boulware, Nikhil I. Khushalani, Ghassan El-Haddad, Pierre L. Triozzi, Eduardo G. Moros, Mark L. McLaughlin, Thaddeus J. Wadas and David L. Morse

This article and updated information are available at:
http://jnm.snmjournals.org/content/60/8/1124

Information about reproducing figures, tables, or other portions of this article can be found online at:
http://jnm.snmjournals.org/site/misc/permission.xhtml

Information about subscriptions to JNM can be found at:
http://jnm.snmjournals.org/site/subscriptions/online.xhtml

SNMMI | SOCIETY OF NUCLEAR MEDICINE AND MOLECULAR IMAGING

Development of Targeted Alpha Particle Therapy for Solid Tumors

Narges K. Tafreshi [1], **Michael L. Doligalski** [1], **Christopher J. Tichacek** [1], **Darpan N. Pandya** [4], **Mikalai M. Budzevich** [5], **Ghassan El-Haddad** [6], **Nikhil I. Khushalani** [7], **Eduardo G. Moros** [1,2,3,8], **Mark L. McLaughlin** [9], **Thaddeus J. Wadas** [4] **and David L. Morse** [1,3,5,8,*]

[1] Department of Cancer Physiology, H. Lee Moffitt Cancer Center & Research Institute, Tampa, FL 33612, USA; Narges.Tafreshi@moffitt.org (N.K.T.); mldoligalski@gmail.com (M.L.D.); Christopher.Tichacek@moffitt.org (C.J.T.); Eduardo.Moros@moffitt.org (E.G.M.)

[2] Department of Radiation Oncology, H. Lee Moffitt Cancer Center & Research Institute, Tampa, FL 33612, USA

[3] Department of Physics, University of South Florida, Tampa, FL 33612, USA

[4] Department of Cancer Biology, Wake Forest University Health Sciences, Winston-Salem, NC 27157, USA; dapandya@wakehealth.edu (D.N.P.); twadas@wakehealth.edu (T.J.W.)

[5] Small Animal Imaging Laboratory, H. Lee Moffitt Cancer Center & Research Institute, Tampa, FL 33612, USA; Mikalai.Budzevich@moffitt.org

[6] Depts. of Diagnostic Imaging and Interventional Radiology, H. Lee Moffitt Cancer Center & Research Institute, Tampa, FL 33612, USA; Ghassan.ElHaddad@moffitt.org

[7] Department of Cutaneous Oncology, H. Lee Moffitt Cancer Center & Research Institute, Tampa, FL 33612, USA; Nikhil.Khushalani@moffitt.org

[8] Department of Oncologic Sciences, University of South Florida, Tampa, FL 33612, USA

[9] Department of Pharmaceutical Sciences, West Virginia University, Health Sciences Center, Morgantown, WV & Modulation Therapeutics Inc., 64 Medical Center Drive, Morgantown, WV 26506, USA; mark.mclaughlin@hsc.wvu.edu

* Correspondence: David.Morse@Moffitt.org; Tel.: +1-813-745-8948; Fax: +1-813-745-8375

Abstract: Targeted alpha-particle therapy (TAT) aims to selectively deliver radionuclides emitting α-particles (cytotoxic payload) to tumors by chelation to monoclonal antibodies, peptides or small molecules that recognize tumor-associated antigens or cell-surface receptors. Because of the high linear energy transfer (LET) and short range of alpha (α) particles in tissue, cancer cells can be significantly damaged while causing minimal toxicity to surrounding healthy cells. Recent clinical studies have demonstrated the remarkable efficacy of TAT in the treatment of metastatic, castration-resistant prostate cancer. In this comprehensive review, we discuss the current consensus regarding the properties of the α-particle-emitting radionuclides that are potentially relevant for use in the clinic; the TAT-mediated mechanisms responsible for cell death; the different classes of targeting moieties and radiometal chelators available for TAT development; current approaches to calculating radiation dosimetry for TATs; and lead optimization via medicinal chemistry to improve the TAT radiopharmaceutical properties. We have also summarized the use of TATs in pre-clinical and clinical studies to date.

Keywords: targeted alpha-particle therapy; solid tumors; mechanism of cell death; targeting moieties; chelation; radiation dosimetry; medicinal chemistry; clinical studies

---

1. Introduction

Over the past two decades, radioimmunotherapy (RIT) has proven to be an effective treatment for non-solid tumors (reviewed in [1,2]); e.g., radiolabeled anti-CD20 monoclonal antibodies for the

treatment of lymphoma. These antibody-radionuclide conjugates have typically used beta (β)-particle emitting radionuclides; e.g., ^{131}I, [67]Cu, ^{177}Lu or [90]Y. However, due to the relatively long range of the associated β-emissions and the poor tumor penetration of antibodies, there has been concern regarding the use of RIT for treatment of solid tumors, where much of the energy is deposited in the surrounding normal tissues relative to the tumor, particularly in the case of small tumor cell foci or metastases [1]. Alpha (α)-particle-emissions have a much shorter range and greater linear energy transfer (LET) relative to β-emissions, depositing more energy into smaller volumes [3]. Hence, there has been significant interest in the development of targeted alpha-particle therapy (TAT) for the treatment of solid tumors. Recently, the FDA approved the use of [223]RaCl$_2$ (Xofigo®) for the palliative care of prostate bone metastases, and the efficacy of [223]RaCl$_2$ and [225]Ac–PSMA–617 have been demonstrated in the treatment of prostate bone metastases (Figure 1) [4–6]. These developments have further elevated interest in the development of novel α-emission cancer treatments [7,8]. Typically, TAT for solid tumors involves attaching an α-particle-emitting radionuclide to a tumor targeting scaffold, followed by the intravenous administration and systemic targeting of tumors and metastases. The α-particle range is only a few cell diameters, ensuring that the greatest effect of tumor TAT remains within the tumor volume [3]. Herein we discuss the current progress, challenges and approaches toward the development of novel TATs for the treatment of solid tumors.
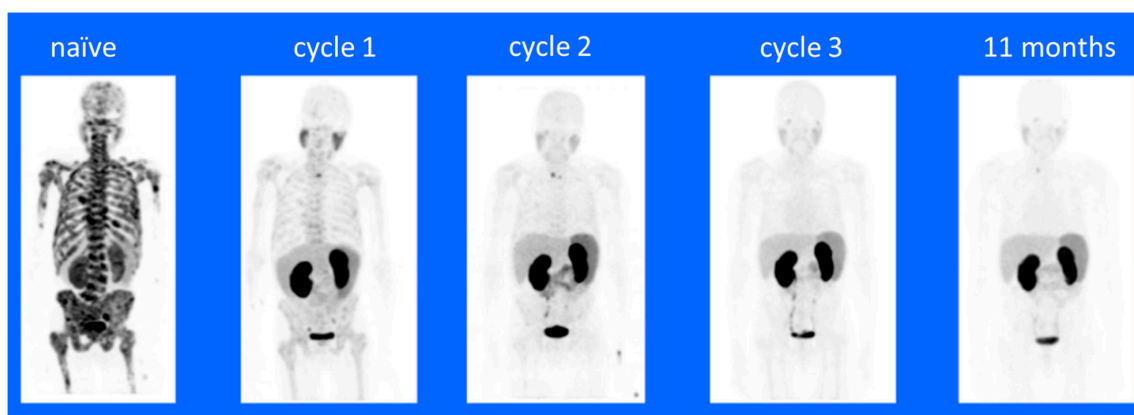
Figure 1. ^{68}Ga-PSMA-11 PET/CT images of a treatment-naïve patient with extensive bone metastasis at primary diagnosis. A complete remission was observed after three cycles of [225]Ac-PSMA-617 with de-escalating activities of 8/7/6 MBq. The patient remained symptom-free with undetectable serum PSA and a negative ^{68}Ga-PSMA-11 PET/CT at 11-month follow-up evaluation. This figure and legend were reproduced from Sathekge, et al. [6].

There are differences in the mechanism of tumor cell killing when comparing β-emission to α-emission therapies. β-particles scale to the size of electrons, travel over a relatively longer range (0.5–12 mm) in tissues in comparison to α-particles, have relatively lower LET and generate hydroxyl free-radicals by breaking covalent bonds of water molecules in the tissue [9]. These free radicals result in oxidative damage to the cellular DNA macromolecules, causing double-strand breaks [10]. In contrast, α-particles are heavier (size of He atom), travel over a much shorter range (40–90 μm), and thus, have hundreds fold higher LET (α = 100 keV/μm versus β = 0.2 keV/μm) [11–14]. Hence, α-emissions deposit large amounts of energy in a smaller volume relative to β-emissions and result in the direct breaking of covalent bonds; e.g., DNA double-strand breaks. In either case (α or β), the DNA damage can activate DNA damage checkpoints and double-strand break repair [15]. Where the damage is significant or if there are defects in the checkpoint or repair pathways such that repairs cannot be made, i.e., irreparable damage, programmed cell death (apoptosis) is initiated [16]. In apoptosis-deficient tumor cells, the resulting damage to the cellular machinery eventually results in necrotic cell death [16]. Hence, α-emission therapy potentially has several distinct advantages relative to β therapy. First, the shorter range of α-emissions result in lower off-target damage but will

still allow for killing of adjacent tumor cells. Since tumors are known to be heterogeneous in marker expression [17], nearby cells that do not express the target can also be damaged and killed, potentially eliminating a mechanism of resistance; i.e., killing of marker expressing cells with the clonal expansion of non-marker expressing cells. Second, the greater energy deposition will result in greater DNA damage and a correspondingly greater level of cell killing. Third, α-emission-mediated DNA damage does not rely on the generation of free radicals, potentially eliminating the development of a major mechanism of resistance to radiation therapy; e.g., upregulation of superoxide dismutase, etc. [3].

There are many α-emitting radionuclides available for use in the development of TAT, and factor, including nuclear characteristics, availability, chemistry, specific activity, synthesis yield, chemical and biological stability of conjugates, and costs, need to be considered. Choice of targeting scaffold is also a major consideration in TAT development. Antibodies, antibody fragments, peptides and passive targeting strategies have been employed and the type of targeting moiety chosen will have a bearing on the type of radionuclide attachment used, the route of clearance and blood pharmacokinetics (PK), tissue biodistribution (BD) and radiation dosimetry. The relative merits of available radionuclides, attachment chemistries and targeting moieties are discussed herein. Radiation dosimetry (RD) is an area of key importance in development of TATs. The discrete decay chains of some α-particle-emitting radionuclides involve the generation of daughter products with individual radioactive emission properties. Hence, the biological fate of the daughter products and resulting tissue exposure to ionizing radiation is a major concern that must be evaluated and the current status of RD studies in the context of TAT development are also discussed. Strategies for lead optimization via medicinal chemistry to improve the TAT radiopharmaceutical properties and methods of current good manufacturing practice (cGMP) production are discussed. Also included are brief reviews of preclinical and clinical TAT studies conducted to date.

2. Mechanism of Action/Tumor Cell Killing

Since the discovery of radioactive materials, the effect of radiation on the properties of matter has been of significant interest in the disciplines of material science, geology and astrophysics. For example, the first large-scale effect of radiation on solid material was observed by E.P. Wigner via exposure to a nuclear fission reactor, and that was thus named the Wigner effect, or "Wigner's disease" [1]. Since then, the large spread of medical technology involving sources of ionization radiation [2] and the development of nuclear weapons has caused a spike in studies on the effect of radiation on living tissue. That work increased our understanding of the concept of radiation risk and created new fields of scientific study; for example, radiation health safety, radiation dosimetry and radiation oncology.

Because of the high energy of α-particles and stochastic nature of ionization radiation, their effects may be observed on all levels of a biological system. Any molecule, cell, tissue or organ can display α-decay radiation damage, and such damage can be localized, or occur throughout the entire body of any multicellular organism [3].

The first step in producing radiation effects is the generation of a primary recoil atom and α-particles by a radioactive decay. Such events take place very rapidly in much less than 1 fs [4]. In the case of α-decay of radiopharmaceutical isotopes of interest, the average kinetic energy per recoil atom is ~100 keV, and the average kinetic energy deposited within the range of a single α-particle is 5 MeV. It is clear that the relatively high levels of energy deposited by the combination of the fast-moving heavy ions and high energy α-particles can cause large amounts of damage to solid matter. There are many methods to estimate the effect of radiation in solid materials; e.g., the stopping theory based on coulombic interactions, molecular dynamics and transport theory. However, unlike solid materials, biological tissues do not consist of solid crystalline structures, and this significantly increases the complexity of estimating the effects of α-decay (as well as other ionization radiation), making the application of the aforementioned methods impossible or extremely difficult numerically. To overcome such limitations, a semi-quantitative approach has been applied. First, the biological effects observed in irradiated subjects were separated into one of two categories [3,6]: deterministic effects, which have

a practical threshold absorption dose below which effects are negligible or not evident; and stochastic effects, where the relationship between dosage and severity of effect is either less evident or absent.

Maintaining the integrity of many different types of macromolecular structures is important to cell viability and all cellular organic molecules are subject to damage by ionizing radiation. However, the genomic DNA molecules are considered to be the most critical targets for the biological effects of ionizing radiation because intact DNA is required for cellular replication and damaged but repaired DNA can result in the fixation of genetic mutations that can affect normal cellular function and viability [18]. Ionizing radiation interacts with DNA either by directly transferring energy to the biological material or indirectly by creating reactive free radicals from the radiolysis of water. These interactions result in damage to the DNA's structure via broken covalent bonds. Linear energy transfer (LET) is an approach to describe the spatial distribution of ionization and excitation produced by direct or indirect effects of different types of radiation along a linear path [15]. Alpha (α) particles have high LET radiation because they create dense ionizations and excitations in matter due to coulombic interactions with atoms. Being a heavy charged particle, an α-particle will continuously slow down along its track with minimal deflection. Through the process of slowing down, the interaction cross-section towards the end of travel increases, resulting in increased LET, which is known as the Bragg Peak (Figure 2) [19,20].

Relative biological effectiveness (RBE) is the ratio of the dose of a reference radiation and the dose of a test radiation that produces the same biological effect. Some of the most common biological effect measurements are necrotic and apoptotic (programmed) cell death, DNA damage, chromosomal aberrations and genetic mutations. The RBE of α-particles can range from 3.5 to 4 for cell killing or 6 to 12 for mutation, and be up to 10 for cell transformation [15]. As a comparison, the RBE for low LET electrons and photons is 1.

An important biological endpoint is cell killing. Damage to cells can be classified as either sub-lethal events or lethal events. Sub-lethal events are due to the accumulation of damage that has the potential to be repaired, typically as a result of exposure to lower doses, and lethal events typically result from irreparable damage due to exposure to higher doses [3]. The ability to repair these events is seen as a shoulder on the cell survival curve and is characteristic of low LET radiation (Figure 3) [21]. A single event of high LET radiation can be lethal. The cell survival curve for a lethal event does not have a shoulder, indicating the inability to repair [22].

The DNA double-strand break is the most biologically significant type of damage, which occurs as a result of two single strand breaks in close proximity or a rupture of the double-strand at the site of interaction [23]. Cell survival is highly dependent on the spatial distribution of double-strand breaks [15]. Given the same dose, high LET radiation can create up to four times more double-strand breaks of low LET radiation. Additionally, the formation of high LET double-strand breaks are more complex compared to low LET in that they are less randomly distributed and form clustered DNA damage to multiple base-pairs [19]. It has been widely accepted that high oxygen levels play a large role in a cell's sensitivity to ionizing radiation, and hence, tumor hypoxia is an established factor in resistance to radiation therapy [24]. This is due to enhancement of free radical production by the presence of oxygen. Free radical production occurs as a result of indirect action, or low LET interactions. Since α-particles interact directly with the DNA, the level of oxygen becomes irrelevant; hence, eliminating a major mechanism of resistance to therapy [3].

produced by direct or indirect effects of different types of radiation along a linear path [15]. Alpha (α) particles have high LET radiation because they create dense ionizations and excitations in matter due to coulombic interactions with atoms. Being a heavy charged particle, an α-particle will continuously slow down along its track with minimal deflection. Through the process of slowing down, the interaction cross-section towards the end of travel increases, resulting in increased LET, which is known as the Bragg Peak (Figure 2) [19,20].

(A)

(B)
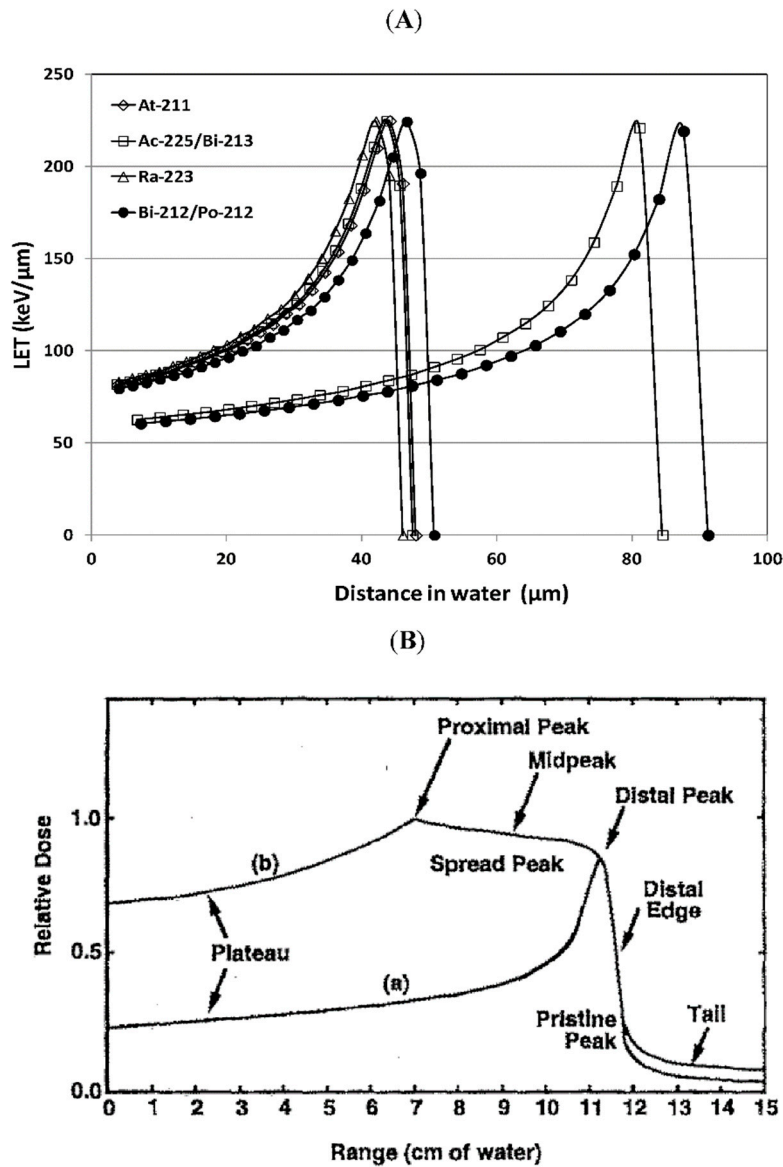
Figure 2. (**A**) Linear energy transfer (LET) versus distance in water traveled by typical α-particles emitted by radionuclides in development for α-particle radioimmunotherapy: [225]Ac (5.829 MeV)/[213]Bi (8.375 MeV), [211]At (5.867 MeV), [212]Bi (6.08 MeV)/[212]Po (8.78 MeV), [223]Ra (5.716 MeV). The range of the α-particle and the position of the Bragg peaks are correlated with the initial energy of the α-particles. LET of α-particles in water was calculated using stopping-power and range tables (continuous slowing down approximation range) for electrons, protons and helium ions from the National Institute of Standards and Technology (NIST). (**B**) The deposition of heavy ion energy as a function of penetrating depth of (a) a pristine beam and (b) a modulated beam with widened stopping region (spread out Bragg peaks). This figure and legend were reproduced from [19].
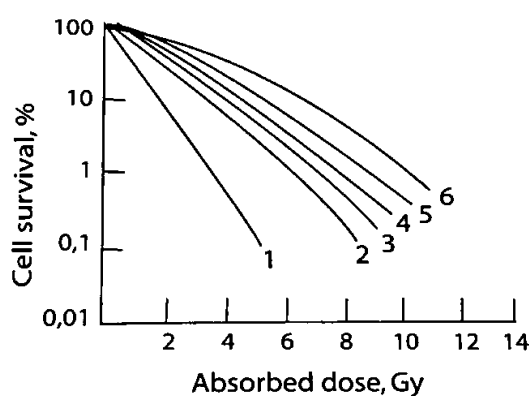
Figure 3. Survival of a human kidney T-cell culture irradiated with ionizing particles of different kinds: (1) particles with E = 2.5 MeV, LET = 165 keV/m; (2) particles with E = 27 MeV, LET = 25 keV/m; (3) deuterons with E = 3.0 MeV, LET = 20 keV/m; (4) X-rays with E = 20 keV and LET = 6 keV/m; (5) X-rays with E = 250 keV and LET = 2.5 keV/m; and (6) particles with E = 2.2 MeV, LET = 0.3 keV/m. This figure and legend were reproduced from [21].

After exposure to radiation that results in DNA damage, the cell cycle can be stopped at cell-cycle checkpoints which allow the cell to repair the damage via multiple repair mechanisms in order to preserve genomic integrity [23]. In the case of irreparable damage, the cell will eventually undergo cell death by apoptosis or necrosis. The two main repair mechanisms of double-strand breaks are homologous recombination and non-homologous end joining. Homologous recombination occurs in the late S and G2 phases of DNA synthesis where an intact DNA template is available, resulting in more efficient and higher-fidelity repair. Non-homologous end joining occurs throughout the cell cycle but is the only means of repair in G1 and early S phases. In this error prone repair method, DNA ends are rejoined with no sister templates [22]. In this case, chromosomal aberrations can occur as a result of recombining incorrect DNA ends; i.e., combining a loose end to some other molecule, and the truncation of ends. If incorrect repair occurs prior to DNA replication, these errors can be replicated in daughter DNA which can lead to mitotic cell death or can lead to the generation of genomic mutations without cell death [22]. There is also the situation where double-strand breaks are not repaired and the dividing cell enters mitosis, leading to mitotic catastrophe and eventual cell death. A higher proportion of double-strand breaks remain un-rejoined after exposure to high LET radiation [15]. When it comes to damage from high LET α-particles in close proximity to the cells being irradiated, the main radiobiological effect is complex and irreparable DNA damage resulting in cell death by either apoptosis or necrosis.

In the last few years, successful attempts have been made to explain the bystander effect [24,25]. The bystander effect is defined as a group of effects that are observed in cells that have not been directly irradiated following the irradiation of other nearby cells. Two mechanisms were proposed. One is the transfer of genomic instability through p53-mediated pathways, and the other suggests that irradiated cells secrete cytokines or other factors that transit to other cells that are not irradiated and signal for increased levels of intracellular reactive oxygen species [26]. One of the defined sub-classes of the bystander effect is the "abscopal effect," in which radiation treatment of a tumor propagates to tumors outside the irradiated volume [26]. A more recent publication demonstrated an effect that might explain the abscopal effect [27]. It was demonstrated that α-particle treatment of prostate cancer cells generated an adaptive antitumoral immune response, as has been previously reported for other forms of radiation. Combinations of bystander effects and the abscopal (likely immune) response in vivo are potential mechanisms of the efficacy for tumors that are not venerable to the targeted α-emitter radiotherapy in a patient with heterogeneous target expression.

3. Alpha-Particle Emitting Radionuclides

Using radiation as a method of cancer therapy requires delivering the maximum dose to the tumor while minimizing the dose to healthy tissues. Targeted radionuclide therapy is advantageous in that it seeks molecular and functional targets within patient tumor sites [28]. Beta (β)-emitting radionuclides (^{90}Y, ^{131}I, ^{177}Lu and ^{186}Re) are used for cancer-targeted therapy but have problems with cross-fire irradiation of normal tissues due to their relatively long range in tissue, which is 0.5–12 mm. In contrast, α-particles deposit higher energy over a much shorter range (40–90 μm), potentially causing higher cytotoxicity to tumor cells while delivering a lower dose to normal, adjacent tissues [29]. Alpha (α)-emission is the process by which an unstable nucleus ejects a highly-energetic, heavy, charged particle consisting of two protons and two neutrons. Alpha (α)-particles have a higher LET (100 keV/μm) compared to β-particles (0.2 keV/μm) which results in a dense ionization track in matter. The short range of α-emission provides specificity to the target cell population with a minimal effect on surrounding normal cells, and the high LET leads to a high frequency of irreparable DNA double-strand breaks [18]. This limits cytotoxic effects to within a small distance from the location of decay. It has been estimated that only one cell traversal by an α-particle track is necessary to kill a cell while, thousands of β-particle traversals are required for the same effect [30]. Because of the long range of β-particles and the need of a high number of hits for cell killing, a large portion of the dose deposited is outside of the intended target. In addition to treatment of solid tumors, the use of α-particles for targeted treatment of circulating disease could be an improvement due to the potentially reduced damage to normal tissues. Use of TAT has been considered for killing isolated cancer cells in transit in the vascular and lymphatic systems, in regressing tumors by disruption of tumor capillary networks and in treatment of micrometastatic foci [31]. In particular, TAT may be ideal for treatment of solid metastases, as the short range will primarily kill tumor cells, with little deleterious impact on surrounding normal tissue. Additionally, heterogeneity of target expression has been observed within a given tumor or metastasis [32] and this is thought to be a mechanism of developing resistance to targeted therapies; non-target expressing cells survive treatment and clonally expand into a resistant population. In this case, α or β-emissions from a targeted cell will serve to kill surrounding untargeted cells within the effective range, potentially reducing the development of resistance.

A number of factors need to be considered when choosing an α-emitting radionuclide for therapy. These include proper nuclear characteristics, ease of radiochemical incorporation, specific activity, synthesis yields, chemical and biological stability, availability and cost [29].

The physical half-life of the radionuclide should be long enough to allow for radiosynthesis preparation and be compatible with the pharmacokinetics of tumor localization [33]. The decay pathway of the α-emitter should be carefully analyzed. Due to the conservation of energy and linear momentum, a daughter nuclide which subsequently decays by α-emission could detach from the radioimmunoconjugate; see for example [34]. These free products could travel away and deposit doses to healthy tissues. A decay chain that is long and complicated, having many different decay types, could also present an issue dosimetrically, especially if the daughter products are metabolized differently than the parent. A possible way to overcome this issue is to use ^{225}Ac as an in vivo generator in which the delivery system is designed to be internalized into the target cell where the toxic daughter elements may detach from the targeting vector but remain trapped in the cell [35].

Another important nuclear characteristic is having a large number of α-emissions per decay. The radiotoxicity associated with having multiple emissions could be high enough to kill a tumor cell in a single decay. An accompanying gamma (γ) photon emission with energy suitable for in vivo imaging is also beneficial for assisting with pharmacokinetic and dosimetric evaluations [33].

Another important element for radionuclide selection is availability. Alpha (α)-emitters are produced either by cyclotron bombardment or by reactor irradiations, are incorporated into a generator and are eluted from a parental source. Obtaining radionuclides in pure form with high specific activity and large quantities is essential for adequate therapeutic evaluation. High specific activity is important to avoid receptor saturation by the unlabeled targeting agent [36]. If membrane antigenic density is

low, insufficient binding to tumor cells will occur [36]. Transportation of these radionuclides safely and economically is also a key issue in selection.

While there are over 100 α-emitting radionuclides, only several have been investigated in preclinical and clinical studies. This is mostly due to radionuclides lacking nuclear properties, the absence of viable chemistry, complicated decay chains and production and economic issues [37]. Therefore, radionuclides meeting the criteria for therapeutic use have been limited to ^{225}Ac, ^{211}At, ^{212}Bi, ^{213}Bi, ^{212}Pb, ^{223}Ra, ^{224}Ra, ^{149}Tb and ^{227}Th. The physical characteristics of these isotopes can be seen in Table 1.

Table 1. Physical characteristics of α-emitting radioisotopes investigated for clinical use.

Isotope	Half-Life	Max Energy	Emissions Per Decay
^{225}Ac	10.1 d	5.83	4 α, 2β-
^{211}At	7.2 h	5.87	1 α, 1 EC
^{212}Bi	1.01 h	6.09	1 α, 1β-
^{213}Bi	45.6 min	5.87	1 α, 2β-
^{212}Pb	10.6 h	6.09	1 α, 2β-
^{223}Ra	11.4 d	5.87	4 α, 2β-
^{224}Ra	3.6 d	8.8	5 α, 2 β-
^{149}Tb	4.1 h	3.96	1 α, 1 β+
^{227}Th	18.7 d	6.04	5 α, 2β-

The first α-emitter to be used in human clinical trials for therapy was ^{213}Bi in 1997, when it was labeled to the anti-leukemia antibody HuM195 [38]. ^{213}Bi is available through generator based ^{225}Ac and decays with a 45.6 min half-life by emission of one α (8.37 MeV) and two β-particles. The generator is produced at Oak Ridge National Laboratory in the US and at the Institute for Transuranium Elements in Karlsruhe Europe. In the decay of ^{213}Bi, there is an emission of a 440 keV isomeric γ, which is beneficial for imaging studies.

^{211}At decays with a half-life of 7.2 h and emits two α-particles through a split decay pathway with energies of 5.87 and 7.45 MeV. One path is to ^{207}Bi by α-emission followed by electron capture to ^{207}Pb and the other is by electron capture to ^{211}Po followed by α-emission to ^{207}Pb. An advantage of this decay path is that ^{211}Po emits 77–92 keV characteristic X-rays which can be used for imaging [37]. The main disadvantages are availability and purity. Conventionally, the production of ^{211}At requires α-particle cyclotrons, which are only available in a few places worldwide, to produce the ^{209}Bi(α,2n)^{211}At reaction with minimal ^{210}At contamination [39]. Astatine has significant metallic characteristics that lead to complications in standard antibody labeling and results in a rapid release of free ^{211}At [37,40,41]. To resolve this problem, approaches have been developed by several research groups based on small linker molecules that create an aryl carbon–astatine bond involving an astatodemetallation reaction using tin, silicon or mercury precursors [42]. Other alternative methods for astatination, e.g., boron-astatine, rhodium-astatine or nanoparticle encapsulation, are also being pursued [43].

^{225}Ac is a radiometal with a half-life of 10.1 days and produces six radionuclide daughters in the decay path to stable ^{209}Bi. For each decay event of ^{225}Ac, there are successively, four α and two β emissions with high energy (α 8.38 MeV, β 1.42 MeV). In the decay of ^{225}Ac and its daughters there are several isomeric γ emissions with energy suitable for imaging studies. The relatively long half-life allows for a centralized production site that can ship ^{225}Ac to users [44]. The main method for generating ^{225}Ac for clinical studies is through the decay of ^{229}Th which originates from ^{233}U. In the world there are three main sources of ^{229}Th: Oak Ridge National Laboratory (USA), The Institute of Physics and Power Engineering (Russia) and The Institute for Transuranium Elements (Germany). The quantities produced are not enough for a global application of ^{225}Ac. To keep up with the increasing demand for ^{225}Ac for clinical applications, it has been found that large scale quantities can be produced through high-energy proton irradiation of ^{232}Th [45,46]. To address the shortage, the US Department of Energy formed a Tri-lab collaboration of Los Alamos (LANL), Brookhaven (BNL) and Oak Ridge (ORNL) National Laboratories with the goal of developing an alternative route for production of Ac [47].

Another limitation for this radionuclide has been with the radiochemical stability of the attachment to immunoconjugate. McDevitt et al. [34], state that the instability of these attachments is due to the high classical recoil energy (100–200 keV) of the daughter product which breaks the molecular bonds of the chelator. Significant advances have been made in developing chelators that form thermodynamically stable and kinetically inert complexes with ^{225}Ac. Khabibullin et al., recently calculated the chelation stability of ^{225}Ac and daughters in the 1,4,7,10-tetraazacyclododecane-1,4,7,10-tetraacetic acid (DOTA) chelator [48].

As one potentially abundant starting material, ^{212}Bi (1.01 h half-life) can be obtained from ^{228}Th and decays via a branched pathway to ^{208}Tl (36% α) and ^{212}Po (64% β); then, both decay to stable ^{208}Pb [33]. However, ^{212}Bi has several disadvantages that potentially limit its use. First, its short half-life can be problematic if the production and shipping processes are lengthy. This issue can be solved by using ^{224}Ra as a generator to locally produce ^{212}Bi. Another complication is the high energy γ emission (2.6 MeV) which requires a considerable amount of shielding to minimize exposure. This, along with the short half-life, makes shipping difficult, resulting in an availability problem.

^{223}Ra is found naturally in trace amounts following the decay of ^{235}U, but it is mainly produced artificially by the decay of ^{227}Th ($T_{1/2}$ = 18.7 days), which is produced from ^{227}Ac ($T_{1/2}$ = 21.77 years). Since ^{227}Ac is found only in traces in uranium and thorium ores, it is mainly synthesized by ^{226}Ra ($T_{1/2}$ = 1600 years) irradiation in a nuclear reactor [49]. ^{223}Ra has a half-life of 11.4 days and emits four α-particles, two β-particles and γ rays on the path to stable ^{207}Pb [34]. While the emission of four α-particles is advantageous for tumor toxicity, ^{219}Rn in gaseous form is also emitted, which can redistribute in the body and dose non-targeted cells. See Figure 3 for comparable energies of α-particles.

The major challenge using ^{223}Ra is finding a suitable ligand for in vivo sequestration. However, similarly to cations of the alkaline earth elements, radium has natural bone-seeking properties without the need for a carrier agent. As radium mimics calcium, when ^{223}Ra dichloride (Xofigo®) is injected intravenously, it forms complexes with the bone mineral hydroxyapatite at areas of increased metabolic bone activity, such as bone metastases, thereby exerting a highly localized antitumoral effect [7]. In addition, the ^{223}Ra daughter isotopes are also retained in the bone matrix [50].

Thanks to this characteristic, ^{223}Ra dichloride (^{223}RaCl$_2$) has demonstrated improvement in overall survival for the treatment of bone metastases in castration-resistant prostate cancer and has received FDA approval for this application [34], making it the first FDA approved TAT.

^{227}Th can be produced continuously from ^{227}Ac and decays with a half-life of 18.7 days to ^{223}Ra [51]. The long half-life is beneficial for radiolabeling and targeting. ^{227}Th also decays with accompanying γ emissions of 236 keV and 50 keV, which can be used for imaging but are low enough to avoid the need for patient shielding.

^{212}Pb has a 10.6 h half-life and is produced either from the decay chain of ^{228}Th or by the ^{224}Ra generator [39]. Because of its long half-life and the fact that ^{212}Pb is a β-emitter that decays to ^{212}Bi, one approach has been to use this radionuclide as an in vivo generator to compensate for the short half-life of ^{212}Bi [52]. ^{212}Pb can deliver over ten times the dose per unit of administered activity compared to ^{212}Bi or ^{213}Bi [53]. The major issue with ^{212}Pb is the electron capture and auger electron emissions which can cause significant recoil of the ^{212}Bi daughter [54]. The free ^{212}Pb has been shown to cause severe bone marrow toxicity [55], while the free Bi has shown to cause kidney toxicity. By co-injecting DTPA or EDTA chelating agents, rapid release of free ^{212}Bi can be achieved [56].

4. Targeting Moieties

In the burgeoning field of targeted radiopharmaceuticals, there is no universal answer to the question: what is the best targeting molecule? Rather, the abundance of target molecule classifications allow for a more customized approach to developing TATs. Globally, the requirements of a targeting ligand include the ability to concentrate at and bind to extracellular targets and the availability of chemical functional groups amenable to the attachment of linkers and chelators. A balance of many other factors like off-target binding, biodistribution and pharmacokinetics (particularly with

respect to the decaying half-life of the chosen radionuclide) are all critical factors for the selection of a proper targeting ligand. Recently, small molecules, peptides, antibodies, antibody fragments and even some passive targeting strategies have been investigated to deliver radioisotope payloads. See Tables 2 and 3 for examples of TAT conjugates that have been studied in the pre-clinical and clinical environments. This section will explore the advantages and challenges of the aforementioned targeting ligand categories.

4.1. Small Molecules

An advantage of using low molecular weight ligands as targeting moieties for α-therapy include rapid penetration into the tumor and rapid clearance of unbound conjugates from circulation; thus, reducing toxicity. Internalizing ligands are particularly beneficial for ^{225}Ac's application in order to harness the multiple α-particles emitted in its decay chain. A successful example of using small molecules in TAT is ^{225}Ac-PSMA-617 for the therapy of metastatic, castration-resistant prostate cancer [57,58]. The favorable pharmacokinetics properties of the PSMA-617 small molecule include its fast tumor uptake, high internalization rate, extended tumor retention and rapid clearance of unbound ligand [58]. These features make the molecule highly desirable for labeling with an α-emitter with a half-life of several days and multiple α-emissions in its decay chain, like ^{225}Ac. The first report of the significant therapeutic efficacy of ^{225}Ac-PSMA-617 involved two patients with late-stage, metastatic, castration-resistant prostate cancer (mCRPC) and complete remissions [59]. Additional clinical studies have further revealed the remarkable anti-tumor activity and the promising duration of tumor-control of treatment with ^{225}Ac-PSMA-617 [6,59,60]. These studies have further demonstrated the significant potential of TAT (Table 3, Figure 1). Xerostomia (dry mouth syndrome) was the main side effect, indicating that further modifications in clinical trial design might be necessary to further enhance the therapeutic range.

4.2. Peptides

Peptides are oligomers of amino acids that may sometimes exhibit secondary structure; they may have branched or linear frameworks, and may be composed of varying amounts of non-canonical monomers. The polypeptide chains of peptides can have anywhere from 2 to 70 amino acids but more typical examples of targeting peptides are made of less than 10–15 amino acids (1000–1500 MW). Owing to this molecular weight and their capacity to be synthesized and modified with conventional organic synthesis techniques, peptides have long been utilized as targeting agents for radionuclide therapies and diagnostic applications.

Since the 1980s, analogs of the endogenous peptide hormone somatostatin have been developed as therapeutics for neuroendocrine disorders [61]. The FDA approved octreotide (OC, Figure 4), the cyclic octapeptide, upon which much of the early peptide receptor radionuclide therapy (PRRT) was based. Chelating molecules attached and various radionuclides for β and α-emission therapies have been reported. Figure 4 details the structure of OC and two of its commonly-used PRRT ligand analogs, DOTATOC and DOTATATE.

Nephrotoxicity is often one of the highest concerns in PRRT due to tubular reabsorption of the labeled peptide after glomerular filtration [62]. Seventy-four human patients were followed (>1 year) after PRRT with the β-emitter ^{177}Lu-Octreotate. Renal function was monitored by accessing glomerular filtration rate (GFR). Somewhat surprisingly, renal impairment was minimal, with only 43% of patients experiencing a decrease in GFR (<2 mL/min/m2 per year) and 11 patients actually saw increased GFR (>10 mL/min/m2 per year) [63]. The first published account of the α-emitter ^{213}Bi in an OC analog (DOTATOC, Figure 4) was reported in 2006. The radio-peptide ligand was shown to retain its affinity for the somatostatin receptor and inhibited tumor growth in a somatostatin receptor-positive rat pancreatic tumor model (CA20948) [64]. Importantly, the study followed major organ toxicities in rodents. Little to no nephrotoxicity was observed at the various administered activities (13–22.2 Mbq).

More recently, even tumors that had become radioresistant to β-therapy (^{90}Y and ^{177}Lu–DOTATOC) responded to ^{213}Bi–DOTATOC in a clinical model of eight human patients [65]. The treatment for each patient was individualized according to each particular disease state and each patient had substantially positive outcomes in terms of tumor regression and survival. Critically, the acute hematological toxicity normally associated with the analogous β-therapies was only moderate. This limited report suggested only a mild reduction in acute renal function. No other major acute toxicities were reported. This first-in-human report of this peptide-targeted alpha therapeutic may lay the ground work for future human TAT using peptide-targeted systems.
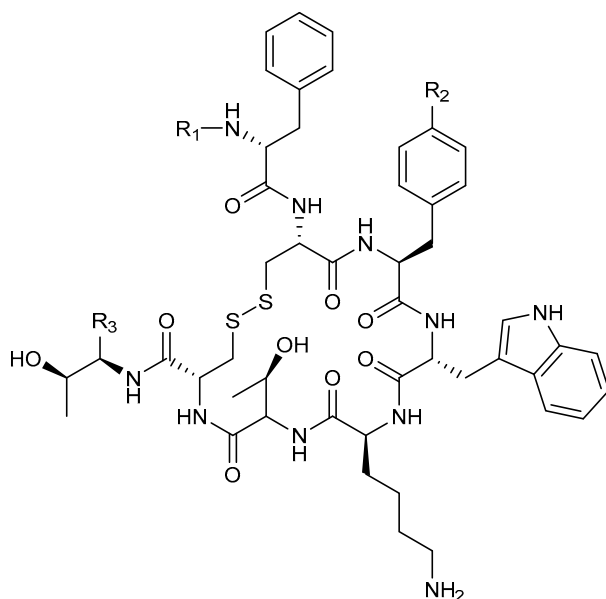

Figure 4. The somatostatin mimetic octreotide and its DOTA-containing analogs. Octreotide: R_1 = H, R_2 = H and R_3 = CH$_2$OH; DOTATOC (endotreotide): R_1 = DOTA, R_2 = OH and R_3 = CO$_2$H; DOTATATE (Octreotate): R_1 = DOTA, R_2 = OH and R_3 = CH$_2$OH.

It has been the common supposition that TAT would work well for small, disseminated tumors but not as well for large, solid tumors. Recently, DOTATATE (Figure 4) was labeled with ^{213}Bi and used to investigate efficacy differences in tumor size among two tumor models, rat pancreatic (CA20948) and human small cell carcinoma (H69) with each containing a small (50 mm^3) and large (200 mm^3) tumor group [66]. Both tumor lines maintained high expression of SSTR$_2$ and all tumor groups saw delayed tumor growth and higher survival over controls. Three mice from the smaller tumor groups were effectively put into remission through the end of the study. This report has implications for TAT in regard to tumor receptor heterogeneity, tumor size and perfusion. More recently, α-emitting radionuclides have been conjugated to melanocortin 1 receptor targeting peptides and efficacy determined in the pre-clinical treatment of mouse xenograft models of cutaneous and uveal melanomas [67–69].

4.3. Antibodies

Full length immunoglobulins (IgGs) are typically in the 150 kDa molecular weight range, and have been proven to have high binding affinity and specificity to a broad range of extracellular receptors. Developments in hybridoma cell line technology have opened the door to the production of monoclonal antibodies (mAbs) which can be labeled with chelating molecules, to which radionuclides can be added. This approach to specifically deliver ionizing radiation payloads is termed radioimmunotherapy (RIT). While many of the examples here will involve radioactive payloads directly conjugated to the protein, antibodies have also been employed to target macromolecular payloads, such as nanoparticles and liposomes, to cellular targets [70–72].

A research group based in the Memorial Sloan-Kettering Cancer Center (MSKCC) has reported several accounts of their work labeling trastuzumab with actinium 225. This mAb is the well-known and FDA approved *HER2/ERRB2*-targeting agent. Initially, they showed through a three cell line, spheroid in vitro model that their α-RIT scheme could penetrate spheroids, retard growth and prevent regrowth of colonies in a dose dependent manner [73]. While a promising start, this work underscored the importance of target expression and also suggested challenges of RIT due to extravasation of targeting agents in normal tissues and toxicities of released/free decaying daughter products [74,75].

The MSKCC Scheinberg group's work eventually led to the first clinical trial of an actinium 225 chelated targeting antibody (Clinical Trials.gov Identifier: NCT00672165). This α-RIT scheme utilized the previously-explored humanized anti CD33 antibody, limtuzumab, to target acute myeloid leukemia cells. Subsequently, that preliminary work led to the birth of Actinium Pharmaceuticals, Inc. and a portfolio of targeted ^{225}Ac conjugated constructs in both preclinical and clinical pipelines.

Astatine-211 has also been utilized for α-RIT. In 2013, Orozco and coworkers coupled a decaborate cage structure (B10, Figure 5) with ^{211}At to anti-CD45 antibody in an attempt to target acute myeloid leukemia [76]. More recently Green and coworkers reported an example using anti-CD20 mAb conjugated with a ^{211}At with a similar B10 labeling scheme [77]. This study sought to eliminate minimal residual disease (MRD) in a mantle cell lymphoma animal model. Their remarkable results showed 70% eradication of the MRD in animals bearing a disseminated model. However, the subcutaneous lymphoma xenograft group treated with the same agents only saw prolonged survival (two to three-fold) without any cured animals. This study is clear evidence of the need for tumor perfusion of the TAT.
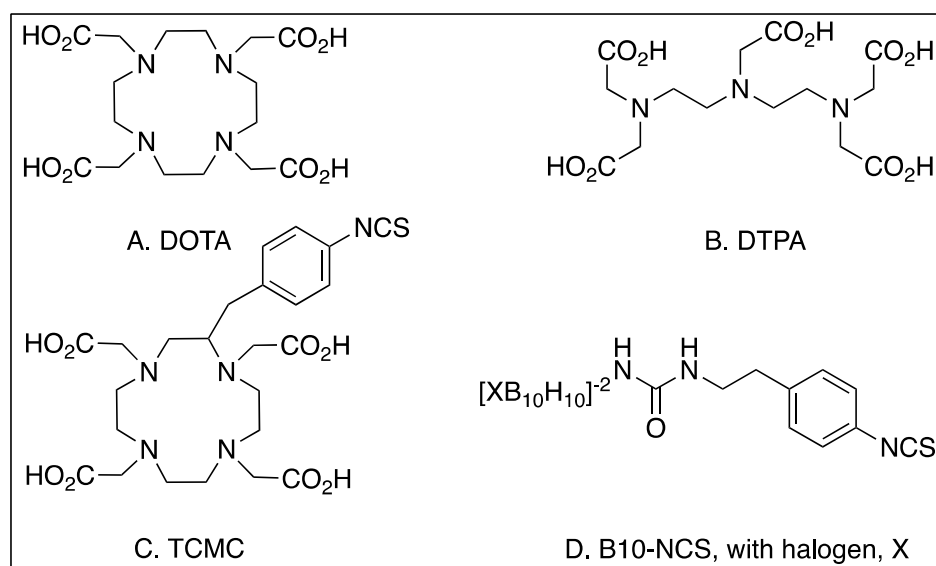
Figure 5. Common metal chelators and binders used to attach radionuclides to targeting ligands.

4.4. Antibody Fragments

A limitation of full-size IgGs is their typical 1–3 week serum stability. While this kind of circulation may be advantageous for certain therapeutic applications, for radioimmunotherapy (RIT) it presents a serious liability. Excess antibody can continue to circulate, lowering the tumor-to-nontumor (T/NT) ratio, particularly with respect to the tumor-to-blood (T/B) ratio. Finally, high levels of continuously-circulating α-emitters result in hematological toxicities, as well as extravasation in normal tissues.

In attempts to shorten the long plasma half-life of full-length antibodies, many groups have sought to reduce the sizes of the mAbs while retaining their remarkable binding characteristics. To those ends, antibodies have been cleaved into smaller sections through enzymatic digestion and also engineered

ab initio [78,79]. For comparison, the engineered antibody fragments of diabodies (Db) and minibodies (Mb) have typical circulating half-lives of 2–5 and 5–12 h, respectively, while the circulating half-life of full-length IgGs is more typically 1–3 weeks. Monovalent and bivalent affibodies (7 and 15 kDa respectively) have been developed with targeting specificity to *HER-2* and they have plasma half-lives of roughly 45 min [80]. The science of antibodies is ever progressing and new classes are still being observed in nature; nanobodies (13–14 kDa) are heavy chain-only antibodies, that have been isolated from *Camelidae* and have lately been conjugated with theranostic radionuclides [81]. These new categories of targeting constructs are adding to the growing body of evidence that there may be a so-called 'Goldilocks' zone in terms of the size of targeting constructs.

4.5. Passive Targeting

Another strategy often employed for TAT is based on the natural selective uptake and accumulation of certain elements. For instance, the actively restructuring environment of osteoblastic bone metastases is conducive to calcium accumulation in the form of hydroxyapatite. Due to the resemblance of radium-223 to calcium, it can act as a surrogate and be incorporated into the rapidly-growing matrix [7,29]. Indeed, the recent approval of ^{223}Ra dichloride therapies for metastatic castrate-resistant prostate cancer has been followed in patients for over twelve months with moderately successful outcomes [82]. Other studies have looked to ^{223}Ra dichloride for the treatment of the bone metastases from hormone-refractory breast cancer [83,84].

The enhanced permeability and retention (EPR) effect is often regarded as a rationale for the passive targeting of large macromolecules like nanoparticles and liposomes. This accumulation of macromolecules through the leaky vasculature of quickly-dividing tumor cells also provides the opportunity to incorporate multiple radionuclides into the framework of a targeting molecule. Additionally, it has been proposed that nanoparticles or liposomes could be used to sequester decaying daughter products that would otherwise be released to freely circulate in the blood because of damage to molecular bonds due to α-decay or metabolism of the radiopharmaceutical [85,86].

5. Chelation/Attachment

5.1. Radiosynthesis

The recent approval of ^{223}RaCl$_2$ has reinvigorated research into TAT development [87]. Several α-particle-emitting radionuclides have been described in the literature, and these include ^{211}At, $^{212/213}$Bi, ^{212}Pb and ^{225}Ac [44,88,89]. With the exception of ^{211}At [41,42,90], all are radiometals that require a bifunctional chelator for the attachment of the therapeutic radioisotope to the targeting moiety. The chemistries of $^{212/213}$Bi and ^{212}Pb have been covered extensively elsewhere [91–94]. The radiochemistry of radium has recently been reviewed [95]. This section will cover recent advances in ^{225}Ac chelation chemistry that have occurred since the publication of the excellent review by Scheinberg and McDevitt in 2011 [96].

^{225}Ac, whose decay chain was not finally resolved until the middle of the 20th century is one of 29 radioactive isotopes of actinium, which is the first element of the actinide series [97]. Although the lack of non-radioactive actinium isotopes has hindered the exploration of ^{225}Ac chemistry, the pioneering work of Seaborg and others has provided an important understanding of the basic reaction chemistry of this element [97–99]. Actinium chemistry has been observed to closely follow that of lanthanum chemistry, since both exist as trivalent ions in solution. These observations have led to the belief that La^{3+} can be an important non-radioactive surrogate for Ac^{3+}, with the caveat that the differences in ionic radii must be considered carefully [100].

Despite the relatively limited knowledge of actinium chemistry, the medical community has seized upon its therapeutic potential in TAT. Using lanthanide chemistry as a guide, many attempts to attach this radioisotope to targeting molecules have been reported with a variety of acyclic and cyclic ligands that would effectively chelate this radioisotope [101–106]. To date, however,

only 1,4,7,10-tetraazacyclododecane-1,4,7,10-tetraacetic acid (DOTA) has found widespread acceptance as an ^{225}Ac chelator in both preclinical and clinical applications [96], despite the low radiochemical yields and specific activities that have been reported [73,104,107]. Maguire et al. have described an improved, one-step ^{225}Ac radiolabeling procedure of monoclonal antibodies that resulted in a 10-fold increase in radiolabeling yield and a 30-fold increase in specific activity [108]. The authors concluded that the improvements in yield and specific activity resulted from greater control over the DOTA–mAb conjugation reaction and the improved chelation of ^{225}Ac during radiosynthesis. Additionally, the new procedure did not alter antibody activity or therapeutic efficacy in vivo, which further suggests the usefulness of this strategy. More recently, Poty et al. reported a single-step click chemistry approach to ^{225}Ac-radioimmunoconjugate synthesis [109]. The click approach generated superior radiochemical yields compared to the standard two-step strategy, suitable specific activities, good in vitro stability and excellent biodistribution profiles. The authors proposed that said novel click strategy could be applied when the targeting vector is unstable under the conditions used for the standard method.

Despite improving the radiochemical yield and specific activity of ^{225}Ac radiopharmaceuticals, important challenges, which include minimizing the detrimental effects of recoil energy and effectively sequestering the cytotoxic daughter products ^{221}Fr and ^{213}Bi after ^{225}Ac decay, remain to be overcome. While several reports have described cellular internalization as an effective method of sequestering ^{225}Ac and its daughter products [35], scientists are increasingly turning to nanotechnology to resolve this issue, and a variety of nanoparticles, including liposomes and carbon-based nanoparticles, have been explored [96,110–115]. Recent reports have demonstrated that LaPO$_4$ nanoparticles hold promise as safe and effective nanocarriers for ^{225}Ac [71]. In these studies, the authors synthesized LaPO$_4$ (monazite) nanoparticles doped with ^{225}Ac. These particles were prepared with functionalized surfaces that facilitated the attachment of 201B mAb, which targets murine thrombomodulin on lung epithelium. Upon in vivo injection, targeted particles accumulated rapidly in the lung through specific interactions between the 201B mAb and its antigen. Moreover, retention of ^{225}Ac and half of the ^{221}Fr and ^{213}Bi daughter nuclei within the particles demonstrated the potential for trapping radionuclides after high energy emissions. McLaughlin et al. improved upon this work by examining ^{225}Ac-doped LaPO$_4$ nanoparticles that were encapsulated by GdPO$_4$ and Au shells [86]. These particles had an average diameter of 27 nm, and were easily conjugated to the 201b mAb using standard bioconjugation techniques. Biodistribution and small animal single-photon emission computed tomography (SPECT) studies revealed the specific targeting of murine thrombomodulin within the lung epithelium that was reduced upon the administration of non-radioactive 201b mAb. Interestingly, the multi-layered nanoparticle design seemed to increase the retention of ^{225}Ac, ^{221}Fr and ^{213}Bi within the particle, which reduced the radiation dose experienced by the kidney. Approximately four and five-fold reductions were observed at 1 and 24 h post-injection, respectively. These data demonstrate that multi-functional, layered nanoparticles have the potential to deliver and retain ^{225}Ac and its daughter radionuclides at the target site, while minimizing off-target toxicities that can occur from errant daughter products in the ^{225}Ac decay chain.

5.2. Linkers/Rational Design

The most utilized chelating molecules for targeted radionuclide therapies using biological molecules are 1,4,7,10-tetraazacyclododecane-1,4,7,10-tetraacetic acid (DOTA) and diethylene triamine pentaacetic acid (DTPA), and their related analogs (Figure 5). Depending on the how the compound is linked to the targeting ligand, these organic structures feature 3 or 4 carboxylates that are negatively charged at physiological pH, and along with the lone pair electrons from each of the 3 or 4 nitrogens, they can coordinate metal ions like α and β-emitting radionuclides. Often, these chelating molecules are linked to the targeting molecule by forming a new amide bond between an amine on the targeting molecule and a carboxylate on the DOTA/DTPA. This strategy is particularly advantageous in the case of peptide synthesis since the reaction, characterization and purification of the linker addition can be part of the overall synthesis of the targeting ligand.

When DOTA or DTPA are linked to proteins like antibodies, amide bonds are typically created between a primary amine of surface-exposed lysine residue and an activated carboxylate on the DOTA or DTPA (Figure 6). Another widespread chemistry available to link protein lysines with DOTA or DTPA is through an isothiocyanate which yields a stable thiourea (Figure 6) [53,116]. While these newly formed amide bonds create the same covalent structure as the peptide-synthesized version, there are important distinctions. In the stochastic reaction of any accessible lysine, many different combinations are possible, and there is little to no control over the regioselectivity of the conjugation. It is unlikely, but possible, that targeting ligands could block or hinder the
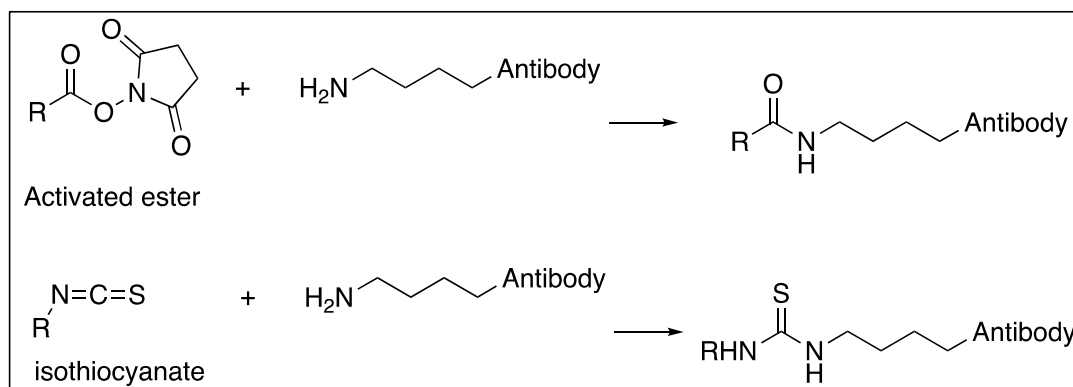

Figure 6. Common conjugation chemistries used to functionalize biomolecules. Countless other schemes have been well characterized and the reader is directed to Bioconjugates Techniques for a review and protocols [117].

The importance of site-specific modifications to biologic targeting motifs is only recently becoming clear. In a 2014 paper from UCLA [118], diabodies (Dbs) were conjugated both site-specifically through reduced cysteines and non-specifically through accessible lysine ε-amines to DOTA chelators. While the tumor-to-blood ratio of the specifically labeled protein was moderately higher than the more heterogeneous product, the more striking result was the renal and hepatic distribution. Kidney uptake levels were almost doubled for the cysteine-labeled Db, and liver uptake levels were reduced for the non-specific amine-labeled Dbs.

Other important research regarding linkers has uncovered different methods to reduce kidney toxicity, via the renal reabsorption of radiolabeled peptides and antibody fragments, as they are filtered by the glomerulus. By taking advantage of renal brush border enzymes, the radionuclide can be cleaved from targeting ligand and excreted. By engineering an antibody fragment with a C-terminal lysine, and subsequently modifying the ε-amine with DOTA:indium-111, Li and coworkers demonstrated a 50%-60% reduction in the kidney uptake of the radionuclide [119]. More recently, a Japanese group probed the brush border enzymes to understand more about their specificity and they were able to pinpoint a glycine-tyrosine linkage that specifically cleaved a radio-iodinated benzoate derivative from an antibody Fab fragment [120]. Presumably, a similar strategy could be used for the α-emitting halogen, ^{211}At.

Polyethylene glycol (PEG) linkers are made of repeating $-CH_2CH_2O-$ monomers and are commonly employed by chemists to alter biodistribution and pharmacokinetics. PEGs can be prepared in two categories, polymeric and discrete oligomers. Bifunctionalized versions of these polymers can link targeting molecules with the chelating agent or just add bulk/solubility to lower molecular weight entities. Researchers wishing to reduce immunologic response to nanoparticles have been known to decorate their macromolecules with PEG [70], as was the case with McLaughlin and coworkers with PEG12 linker used to link ^{225}Ac containing nanoparticles to mAb [86].

6. Radiation Dosimetry

Dosimetry provides means for evaluating the efficacy of a radiation therapy modality [3]. Because the goal is to a deliver high dose to tumor cells with a minimal dose to normal tissues, it is of great importance to quantify accurately where, when and how a dose is being deposited. The Medical Internal Radiation Dose Committee (MIRD) developed an approach to determine the

6. Radiation Dosimetry

Dosimetry provides means for evaluating the efficacy of a radiation therapy modality [3]. Because the goal is to a deliver high dose to tumor cells with a minimal dose to normal tissues, it is of great importance to quantify accurately where, when and how a dose is being deposited. The Medical Internal Radiation Dose Committee (MIRD) developed an approach to determine the average absorbed dose from internal radionuclides [121]. The absorbed dose method accounts for low LET radiation where thousands of statistically independent deposition events across a cell are required to induce a biological effect [3]. With respect to an α-particle's interactions, the averaged absorbed dose will fail to characterize biological outcome. Because the α-particle range is only a few cell lengths, some cell nuclei will receive multiple traversals while others will receive zero traversals. Additionally, the location of the α-particle track will determine the energy absorption by the cell. These factors result in large statistical variability of energy deposition and stochastic effects become important. To account for those effects, Roeske developed a microdosimetric methodology based on the mean dose to target cells, probability distribution of specific energy absorbed by target cells, and the fraction of cells receiving zero hits [122]. Kellerer and Chmelevsky described the requirement that microdosimetry must be used when the relative deviation of local dose is greater than 20% [122]. Following this criterion, microdosimetric techniques are more important in analyzing non targeted cells where the local average dose is small, resulting in larger variations than targeted cells.

In most cases, the activity level and mean absorbed doses to the target are large, resulting in a low expected stochastic deviation, and therefore, there is no need to use microdosimetric techniques. The MIRD Pamphlet No. 22: Radiobiology and Dosimetry of Alpha-Particle Emitters for Targeted Radionuclide Therapy recommends using the conventional MIRD formalism [3]. The mean absorbed dose to the target region, r_T, from a source region, r_S, due to a particular emission type, x, over a dose integration period, T_D, is given by:

$$D_x(r_T, T_D) \; = \; \widetilde{A}(r_S, T_D) \frac{\sum_i \Delta_i^x \varphi\big(r_T \leftarrow r_S; E_i^x\big)}{M(r_T)} \tag{1}$$

where $\widetilde{A}(r_S, T_D)$ is the total number of nuclear transitions in the target region; Δ_i^x is the mean energy emitted per disintegration for the i-th emission of type x; $\varphi\big(r_T \leftarrow r_S; E_i^x\big)$ is the fraction of energy emitted per nuclear transition in the source region that is absorbed in the target region by the i-th emission of type x that is emitted with initial energy E; and $M(r_T)$ is the mass of the target region. The total number of nuclear transitions is determined by measuring activity levels in tissue samples at several points in time post administration. The activity levels plotted against time gives a time-activity curve which is integrated to obtain the total number of nuclear transitions. The mean energy emitted per emission Δ_i is a physical property of the radionuclide and can be obtained from nuclear decay tables. The absorbed fraction for each decay type is dependent on the reference phantom geometry and obtained through Monte Carlo calculation. The dose contribution from each emission type is then weighted by its relative biological effectiveness, and then summed:

$$D_{RBE}(r_T, T_D) \; = \; RBE_\alpha D_\alpha(r_T, T_D) + RBE_e D_e(r_T, T_D) + RBE_{ph} D_{ph}(r_T, T_D) \tag{2}$$

Several assumptions are made when using this formalism of dose calculation. It is assumed that the activity is uniformly distributed in the organ and that α-energy deposition is also uniformly distributed in the organ. It is also assumed that dose from both α and β-emissions are locally deposited. The calculation of the absorbed fractions is based on idealized phantoms that have standard geometries which cannot account for the individual anatomy of a patient. It is also important to note that radioactive daughters are not taken into account. Therefore, daughter decays must also be calculated, as well as accounting for daughters' biodistribution. The formalism was developed as an adequate

method for the dosimetry of internal radionuclides used for diagnostic purposes and lacks the accuracy needed for therapeutic applications.

As a first method to improve on the original MIRD formalism, phantoms were developed to better match the standard human anatomy. For example, Christy and Eckerman developed phantoms that represented a male, a female and children [123]. Later, as computational power increased, voxelized phantoms like VoxelMan were created based off 3D imaging [124]. MIRD Pamphlet No. 17 describes a method to extend the S value formalism to the voxel level to account for nonuniform distributions of activity [125]. The most extensive software that has adapted the MIRD S factors is OLINDA/EXM, which has calculated an internal dose for over 200 radionuclides, including α-emitters, in 10 different phantoms [126].

The voxel S method is still a model-based approach to dosimetry. There is much less tolerance for inaccuracies in therapeutic applications, which calls upon the need for patient-specific dosimetry. In order to accomplish this, the patient's own anatomy, obtained from CT, is used in combination with SPECT imaging to obtain 3D spatial distribution of activity. It is advantageous for the α-emitting radionuclide to also have γ photon emission as it decays so that SPECT imaging can provide information about regional uptake. The method to calculate a 3D, imaged-based dose is as follows [127]. Serial SPECT studies taken over time post administration of the radiopharmaceutical can determine the pharmacokinetic variations within an organ on the voxel level. The SPECT/CT images are registered together and integrated voxel by voxel over time to obtain the 3D, time-integrated activity. The CT provides a map of tissue electron density for each voxel, which is necessary for dosage calculations. A Monte Carlo package is then employed using the activity distribution as the source definition and energy deposition is tallied in each voxel. Several software packages are available for 3D, patient-specific dosimetry, including MCID [128], OEDIPE [129] and SCMS [130] which are based on MCNP, 3D-RD [131] and DOSIMG [132] which are based on EGS [133], RAYDOSE [134] and RAPID [135] which are based on GEANT4 [136], and DPM [137], which is not a public domain code. Both MCNP and GEANT4 can simulate α-particles, while EGS can only transport photons and electrons.

While imaging-based dosimetry can account for non-uniformity and calculate dose at the voxel level, it is still a macroscopic quantity. The spatial resolution of current SPECT imaging ranges from 5 to 25 mm [31]. These dimensions are much larger than the 40–90 μm range of an α-particle. This results in the stochastic variations due to α-particle energy depositions not being taken into account and the voxel dose could be misleading. For α-particles, the ideal dosimetric targets are isolated cancer cells in transit in the vascular and lymphatic systems, micro-metastases and tumor capillary networks [31]. The only way to study the dosimetry of α-particles on a small scale is pre-clinically. These have been limited to in vitro measurements and microdosimetric Monte Carlo models. However, recently, several groups have developed alpha cameras, such as the Ionizing-Radiation Quantum Imaging Detector, which provides images of the ex vivo activity distribution with a spatial resolution on the order of tens of microns μm [138,139]. Monte Carlo methods can then be employed to calculate the dose absorbed on that scale. This is viewed as an important advancement in alpha dosimetry because no further modeling was needed to obtain the spatial and temporal activity distribution.

Table 2. Preclinical targeted alpha-particle therapy (TAT) studies.

Isotope	Study	Molecular Target	Targeting Moiety	Drug(s) & Route	Cancer Type & Animal Model	Key Results	Ref
^{225}Ac	Efficacy, toxicity	PSMA, CD19	J591 & B4 mAbs	^{225}Ac–DOTA–J591, ^{225}Ac-B4, i.v.	Human LNCaP prostate s.c. xenografts & disseminated Daudi lymphoma in male nude mice.	Both effective without toxicity.	[35]
^{225}Ac	Efficacy, toxicity	HER-2/neu	Trastuzumab	^{225}Ac–DOTA–trastuzumab, i.p.	SKOV3 human ovarian cancer s.c. xenografts in female nude mice.	Effective with no toxicity.	[148]
^{225}Ac	PK, RD, toxicity	CD33	HuM195 Ab	^{225}Ac–DOTA–HuM195, i.v.	Cynomolgus monkey leukemia (does not express the human CD33 target).	12 d blood $T_{1/2}$, dosimetry kinetics estimated, efficacy without renal toxicity.	[149]
^{225}Ac	BD, efficacy, toxicity	Ganglioside GD2	3F8 Ab	^{225}Ac–DOTA–3F8, i.v.	NMB-7 human neuroblastoma xenografts in nude mice (BD), meningeal carcinomatosis xenografts in nude rats (efficacy) & cynomolgus monkeys (toxicity).	Tumor specificity, increased survival, no toxicity.	[150]
^{225}Ac, ^{177}Lu	BD, efficacy, toxicity	Somatostatin receptors	DOTATOC peptide	^{225}Ac and ^{177}Lu–DOTATOC, i.v.	AR42J rat pancreatic exocrine s.c. xenografts in nude mice.	^{225}Ac-TAT had greater efficacy relative to ^{177}Lu-TBT with low toxicity.	[151]
^{225}Ac, ^{213}Bi, ^{90}Y	BD, dosimetery, efficacy, toxicity	HER-2/neu	7.16.4 mAb	^{225}Ac, ^{213}Bi and ^{90}Y-7.16.4, i.v.	neu-N transgenic mouse model with rat HER-2/*neu* expression and spontaneous lung metastases & NT2.5 mouse mammary fat pad xenografts with rat HER-2/*neu*.	^{225}Ac-TAT had greater efficacy but with renal toxicity relative to ^{213}Bi-TAT & ^{90}Y-TBT.	[152]
^{225}Ac, ^{213}Bi	BD, efficacy, toxicity	nucleolin	F3 peptide	^{225}Ac–DOTA–F3, ^{213}Bi–DTPA–F3, i.p.	MDA-MB-435 human peritoneal carcinomatosis in SCID mice.	^{225}Ac-TAT had greater efficacy relative to ^{213}Bi-TAT with specific tumor uptake and minor renal toxicity.	[153,154]
^{225}Ac	Safety and efficacy	IL13RA2	Pep-1L peptide	[^{225}Ac]Pep-1L, stereotactic intracranial injection	U8251 human glioblastoma orthotopic xenografts in male nude mice.	Efficacy with no significant toxicity.	[155]
^{225}Ac	Vascular normalization & efficacy	Vascular endothelial (VE)-cadherin	E4G10 Ab	^{225}Ac–DOTA–E4G10, i.v.	LS174T human colon s.c. xenografts in female nude mice.	Improved tumor vascular architecture & increased efficacy when combined with chemotherapy.	[107]

Table 2. *Cont.*

Isotope	Study	Molecular Target	Targeting Moiety	Drug(s) & Route	Cancer Type & Animal Model	Key Results	Ref
^{225}Ac	BBB and BTB permeabili-zation	Integrin $\alpha_v\beta_3$	small-molecule antagonist	^{225}Ac-labeled targeted liposomes (^{225}Ac-TL), intracranial injection	U87 MG human glioblastoma orthotopic xenografts in male nude mice.	Enhanced blood-brain barrier (BBB) and bood-tumor barrier (BTB) permeability.	[156]
^{225}Ac	BD, Efficacy	Thrombo-modulin	201b mAb	LnPO$_4$ nanoparticles (NPs) doped with ^{225}Ac-201b, i.v.	Syngeneic EMT6 mouse breast epithelial cell metastases in BALB/c mouse lung following i.v. injection of cells	Retention of ^{225}Ac and daughters in lung tissue, metastasis burden reduced.	[157]
^{225}Ac	Micro BD, RD	PD-L1	anti-PD-L1-BC Ab	^{225}Ac–DOTA–anti-PD-L1-BC, i.v.	NT2.5 mouse mammary xenografts in female nude mice.	Uniform distribution in liver, non-uniform in kidney and tumor, liver RD was limiting.	[158]
^{225}Ac	BD and toxicity	Bone metastasis	Zoledronic acid (ZOL)	^{225}Ac–DOTAZOL, i.v.	Wistar rats.	High bone:blood ratio. Kidney toxicity.	[159]
^{225}Ac	BD, RD and dose response	PSMA	PSMA ligands with albumin-binding moiety	^{225}Ac-RPS-074, i.v.	LNCaP human prostate cancer s.c. xenografts in BALB/c mice.	Decreased clearance rate, single administration had complete response in 86% of tumors.	[160]
^{225}Ac	PK, BD, specificity, RD, toxicity, efficacy	MC1R	MC1RL peptide	^{225}Ac–DOTA–MC1RL, i.v.	PK (Sprague-Dawley rats), BALB/c mice (toxicity and BD) and MEL270 human uveal melanoma s.c. xenografts in SCID mice (BD and efficacy).	Renal and hepatobiliary excretion, rapid blood clearance, low toxicity, prolonged survival and decreased metastasis after single injection.	[67]
^{225}Ac	Efficacy, toxicity	CA19.9	5B1 human mAb	^{225}Ac-labeled tetrazine radioligand and a transcyclooctene5B1 for pretargeting, i.v.	Bilateral MIAPaCa-2 (CA19.9-negative) and BxPC3 (CA19.9-positive) pancreatic cancer s.c. xenografts, and BxPC3 orthotopic xenografts in nude mice.	Pretargeting has similar efficacy compared to conventional TAT with reduced hematotoxicity.	[144]
^{225}Ac	Vascular normalization & efficacy	Vascular endothelial (VE)-cadherin	E4G10 Ab	^{225}Ac–DOTA–E4G10, i.v.	LS174T human colon s.c. xenografts in female nude mice.	Improved tumor vascular architecture & increased efficacy when combined with chemotherapy.	[107]

Table 2. *Cont*.

Isotope	Study	Molecular Target	Targeting Moiety	Drug(s) & Route	Cancer Type & Animal Model	Key Results	Ref
^{211}At	BD, RD, specificity, efficacy, toxicity	Tenascin glycoprotein	81C6 mAb	^{211}At-81C6, subarachnoid catheter or i.v.	Female athymic rat model of neoplastic meningitis by inoculation of human rhabdomyosarcoma cells via subarachnoid catheter.	Efficacy without significant toxicity. RD estimates.	[161,162]
^{211}At	PK, BD, efficacy, toxicity	gp38	MOv18 mAb	^{211}At- & ^{131}I-MOv18, i.p. or i.v.	Peritoneal OVCAR-3 human ovarian xenografts in BALB/c ν/ν or nude mice following IP injection of cells.	^{211}At-TAT had greater efficacy relative to ^{131}I-TBT.	[163–166]
^{211}At	Tumor neo-vasculature targeting	Fibronectin ED-B domain	Human scFv(L19)	^{211}At-scFv(L19), i.v.	Murine F9 teratocarcinoma & rat FE8 sarcoma in female nude mice.	Retained at tumor blood vessels resulting in increased tumor to blood ratios.	[140]
^{211}At	BD, tumor dosimetry, efficacy, toxicity	95-kDa glycoprotein	MX35 mAb	^{211}At-MX35, i.p. or i.v.	OVCAR-3 human ovarian cancer micrometastases in nude mice.	Fractionated treatment increased efficacy without significant toxicity.	[23,167,168]
^{211}A, ^{90}Y	Efficacy	CD30	HeFi-1 mAb	^{211}At-, ^{90}Y HeFi-1, i.v.	Human anaplastic large cell lymphoma cells in SCID/NOD mice. Karpas 299 cell i.v. injection for leukemia & SUDHL-1 xenografts for lymphoma.	^{211}At-HeFi-1 increased survival in the leukemia model & combination with unlabeled HeFI-1 further improved efficacy. ^{90}Y-HeFi-1 TBT increased survival in the lymphoma model.	[169]
^{211}At	BD, efficacy, toxicity	CD44v6	U36 chimeric mAb	^{211}At-U36, i.v.	UT-SCC7 human head and neck squamous cell carcinoma s.c. xenografts in nude mice.	Reduced tumor growth with no significant toxicity. BD consistent with targeting.	[170]
^{211}At	BD, efficacy, toxicity	HER2/neu	C6.5 diabody	^{211}At-SAPS-C6.5, i.v.	HER2/neu-positive MDA-MB-361/DYT2 breast xenografts in nude mice.	Tumor growth delay with low renal toxicity.	[142]
^{211}At	Efficacy	NIS-transduced tumor cells	Astatide (HAt) peptide	^{211}At-astatide, i.p.	NIS transduced LNCaP human prostate (NP-1) and parental (P-1) s.c. xenografts in male nude mice.	Accumulation similar to iodine with efficacy against NP-1 tumors relative to control P-1 tumors.	[147]

<div align="center">

Table 2. *Cont.*

</div>

Isotope	Study	Molecular Target	Targeting Moiety	Drug(s) & Route	Cancer Type & Animal Model	Key Results	Ref
^{211}At, ^{213}Bi	BD, myelo suppression, toxicity	CD45	30F11 Ab	^{211}At-30F11-ADTM, ^{213}Bi-30F11-CHX-A″, i.v.	Female BALB/c mice.	^{211}At-TAT induced myeloablation in haematopoietic tissues with greater efficacy and less toxicity relative to the ^{213}Bi conjugate.	[171]
^{211}At	Efficacy	HER-2/neu	Trastuzumab	^{211}At-trastuzumab, i.p.	SKOV3 human ovarian i.p. xenografts in nude mice.	Combination of trastuzumab and ^{211}At-trastuzumab resulted in complete tumor eradication.	[172]
^{211}At	Dosimetry, toxicity, efficacy	Lewis Y epitope	BR96, chimeric IgG1 mAb	^{211}At-BR96, i.v.	BN7005-H_1D_2 rat syngeneic sub-peritoneal colon engraftments.	Resulted in undetectable tumors with tolerable toxicity.	[173]
^{211}At	Efficacy	CD20	1F5 mAb	^{211}At-1F5, i.v.	Human Ramos (Burkitt lymphoma) s.c. xenografts in nude mice and i.v. injection of Ramos cells in SCID mice for disseminated lymphoma.	Highly effective in minimal residual disease mouse model.	[77]
^{211}At	BD, dosimetry	Sigma-2 receptor	MM3 ligand	^{211}At-MM3, i.v.	EMT6 murine breast syngeneic tumor in female BALB/c mice.	Tumor specific targeting.	[146]
^{211}At	Efficacy	Norepineph-erine transporter	Benzyl-guanidine	meta-[^{211}At]-astatobenzyl-guanidine, i.v.	PC12 rat pheochromocytoma s.c. xenograft in nude mice.	Reduced tumor size without weight loss.	[174]
^{211}At	BD, efficacy	MICA/B	anti MICA/B Ab	^{211}At-anti MICA/B Ab, i.v.	HCT116 (p53$^{-/-}$ & MICA/B positive) human colon cancer s.c. xenograft in nude mice.	Significant reduction in tumor growth, no weight loss, erythrocytopenia with recovery in 3-4 wks.	[175]
^{213}Bi, ^{90}Y	Toxicity and efficacy	CO17-1A	CO17-1A Fab′	^{213}Bi-Fab′ and ^{90}Y-Fab′, i.v.	GW-39 human colon cancer s.c. xenograft in nude mice.	TAT had greater efficacy and lower toxicity than TBT.	[176]
^{212}Bi	Specificity, efficacy, toxicity	gp70	103A mAb	^{212}Bi–CHX-A-DTPA–103A, i.v.	RLV induced erythroleukemia in BALB/c mice.	Clinical and histological remission of erythroleukemia and prolonged survival with low toxicity.	[177]

Table 2. *Cont.*

Isotope	Study	Molecular Target	Targeting Moiety	Drug(s) & Route	Cancer Type & Animal Model	Key Results	Ref
^{212}Bi	BD, efficacy, toxicity	CD25	Anti-Tac, humanized mAb	^{212}Bi–CHX-A-anti-Tac, i.v.	SP2 and SP2/Tac syngeneic murine lymphoma in nude mice.	Effective in treatment of bulky solid tumors.	[178]
^{213}Bi	Stability, PK, toxicity	CD33	HuM195 mAb	^{213}-Bi-CHX-A-DTPA–HuM195, i.p. or i.v.	Normal BALB/c mice without leukemia.	Favorable stability, PK and toxicity.	[179]
^{213}Bi, ^{90}Y	Pretargeting efficacy	CD25 (Tac)	Humanized anti-Tac mAb (HAT)	^{213}Bi- & ^{90}Y-DOTA–HAT; & HAT–streptavidin & ^{213}Bi-DOTA–biotin or ^{90}Y-DOTA–biotin, i.v.	Intraperitoneal MET-1 human adult T-cell leukemia in SCID/NOD mice.	Pre-targeted ^{213}Bi TAT increased survival relative to ^{213}Bi–DOTA–HAT, ^{90}Y TBT & pre-targeted TBT.	[143]
^{213}Bi, ^{131}I	Efficacy	TAG-72	Humanized, domain-deleted CC49 mAb (HuCC49ΔCH2)	^{213}Bi- or ^{131}I-HuCC49ΔCH2, i.p.	TAG-72+ LS-174T & TAG-72 negative MIP human colon i.p. xenografts in nude mice.	^{213}Bi-TAT had greater growth inhibition or regression relative to ^{131}I-TBT.	[180]
^{213}Bi	Efficacy, toxicity	d9-E-cad	d9-E-cad mAb	^{213}Bi-d9-E-cad mAb, i.p.	HSC45-M2 human gastric i.p. xenografts with d9-E-cad mutation in female nude mice.	Double administration had greater efficacy relative to single administration, with no toxicity.	[181]
^{213}Bi	BD, efficacy, toxicity	Somatostatin receptors	DOTATOC peptide	^{213}Bi–DOTATOC, i.v.	CA20948 rat pancreatic adenocarcinoma tumors in Lewis rats.	Antitumor efficacy with low toxicity.	[64]
^{213}Bi	Specificity, BD	CD87	P-P4D peptide	^{213}Bi-P-P4D, i.p.	OV-MZ-6 human ovarian i.p. xenografts in female nude mice.	Specific tumor uptake, kidney uptake reduced by co-injection of gelofusine.	[182]
^{213}Bi	Efficacy, toxicity	MUC1, uPAR and BLCA-38	C595 & BLCA-38 mAbs, & PAI2 protein	^{213}Bi-C595, -BLCA-38 & -PAI2, i.p.	PC-3 human prostate orthotopic, intratibial and s.c. xenograft tumors in NOD SCID mice.	Multiple TAT can overcome heterogeneous antigen expression with efficacy against micrometastases.	[145]
^{213}Bi	Efficacy, toxicity	EGFR	Matuzumab	^{213}Bi-matuzumab, intravesical	EJ28 human orthotopic bladder xenografts in nude mice.	Increased survival without toxicity. Combination with mitomycin C increased efficacy with nephrotoxicity.	[183]
^{213}Bi	Efficacy	TAG-72	Humanized CC49 mAb (HuCC49DCH2)	^{213}Bi- HuCC49DCH2, i.p.	LS-174T human colon i.p. xenografts in female nude mice.	Combination trastuzumab and i.p. TAT increased efficacy and was well tolerated.	[184]
^{213}Bi	Pretargeting efficacy	CD20	scFv-1F5-SA (streptavidin fusion protein)	1F5-SA & ^{213}Bi–DOTA–biotin, i.v.	Ramos human lymphoma xenografts in nude mice.	Tumor regression and increased survival in mice with small tumors via pretargeting.	[141]

Table 2. *Cont.*

Isotope	Study	Molecular Target	Targeting Moiety	Drug(s) & Route	Cancer Type & Animal Model	Key Results	Ref
^{213}Bi, ^{177}Lu	BD, dosimetry, efficacy, toxicity	GRP	PESIN and AMBA peptides	^{177}Lu–DOTA–PESIN, ^{213}Bi–DOTA–PESIN, or ^{213}Bi-AMBA, i.v.	PC-3 human prostate s.c. xenografts in female nude mice.	^{213}Bi-TAT had greater efficacy compared to ^{177}Lu-TBT. ^{213}Bi–DOTA–PESIN had lower renal toxicity relative to ^{213}Bi-AMBA.	[185]
^{213}Bi, ^{177}Lu	Efficacy	CD138	9E7.4 mAb	^{213}Bi-9E7.4 and ^{177}Lu-9E7.4, i.v.	5T33 murine multiple myeloma cell syngeneic i.v. injection into C57/BL6 mice.	^{213}Bi-9E7.4 increased survival and cured 45%, ^{177}Lu-9E7.4' increased survival, no cures.	[186]
^{213}Bi, ^{177}Lu	Efficacy, toxicity	Mutant d9-E-cadherin	d9MAb	^{213}Bi-d9Mab & ^{177}Lu-d9Mab, i.p.	HSC45-M2 human gastric cancer cell i.p. injection in nude mice.	^{213}Bi had comparable efficacy with lower toxicity.	[187]
^{213}Bi	BD, efficacy, toxicity	CD138	Anti-mouse CD138 Ab	^{213}Bi-CD138, i.v.	5T33 mouse multiple myeloma cell engraftment into syngeneic C57BL/KaLwRij mice.	Increased survival with only moderate and transient toxicity.	[188]
^{213}Bi	Efficacy, toxicity	EGFR	Matuzumab	^{213}Bi-matuzumab, intravesical.	EJ28 human orthotopic bladder xenografts in nude mice.	Increased survival with low toxicity.	[189]
^{213}Bi	PK, efficacy, dosimetry, toxicity	SSTR2	DOTATATE peptide	^{213}Bi–DOTATATE, i.v.	Neuroendocrine H69 human small cell lung carcinoma and CA20948 rat pancreatic s.c. xenografts in nude mice.	Effective in small and large tumors (both types), with dose limiting renal toxicity.	[66]
^{212}Pb	Efficacy	HER-1	Cetuximab	^{212}Pb-cetuximab, i.p.	ILS174T human colon i.p. xenografts in nude mice.	Extended survival and combined with gemcitabine & carboplatin increased efficacy.	[190]
^{212}Pb	Efficacy	MC1R	DOTA-Re (Arg^{11})CCMSH peptide	^{212}Pb[DOTA]–Re (Arg11)CCMSH, i.v.	B16/F1 murine melanoma syngeneic s.c. engraftments in C57BL/6 mice.	Tumor eradication at higher activities.	[191]
^{212}Pb	Efficacy	HER-2 and CEA	Trastuzumab & 35A7	^{212}Pb-trastuzumab & ^{212}Pb-35A7, i.p.	A-431 HER-2 positive and CEA transfected vulvar squamous carcinoma cells i.p in nude mice.	Internalizing anti-HER2 labeled Ab had greater efficacy than non-internalizing anti-CEA labeled Ab.	[192]
^{212}Pb	Efficacy, toxicity	HER-2/neu	Trastuzumab	^{212}Pb-trastuzumab, i.p.	LS174T human colon & Shaw human pancreatic i.p. xenografts in nude mice.	Increased survival with low toxicity.	[193]

Table 2. *Cont.*

Isotope	Study	Molecular Target	Targeting Moiety	Drug(s) & Route	Cancer Type & Animal Model	Key Results	Ref
^{212}Pb	Efficacy	HER-2/neu	Trastuzumab	^{212}Pb-trastuzumab, i.p.	LS-174T human colon i.p. xenografts in nude mice.	Combination with gemcitabine increased survival.	[194]
^{212}Pb	BD, efficacy	B7-H3	376.96 mAb	^{212}Pb-376.96, i.p.	ES-2 or A2780cp20 human ovarian cancer cells i.p. into nude mice.	High peritoneal retention, tumor tissue accumulation & increased survival.	[195]
^{212}Pb	BD, efficacy	B7-H3	376.96 mAb	^{212}Pb-376.96, i.v.	Panc039 pancreatic cancer orthotopic xenografts in nude mice.	High tumor uptake & tumor growth inhibition.	[196]
^{212}Pb	BD, efficacy	CSPG4	225.28 mAb	^{212}Pb-225.28, i.v.	SUM159 & 2LMP human triple negative breast cancer (TNBC) orthotopic mammary fat pad xenografts in nude mice.	Dose-dependent growth inhibition.	[197]
^{212}Pb	Administration route, toxicity, efficacy	EGFR	Panitumumab F(ab')$_2$ fragment	^{212}Pb-panitumumab F(ab')$_2$, i.p. & i.v.	ILS-174T human colon i.p. xenografts in nude mice.	Increased survival with tolerated toxicity via i.p. or i.v. injection.	[198]
^{212}Pb	Efficacy, combination therapy	MC1R	ee-cyclized α-MSH peptide	^{212}Pb–DOTA–MC1L, BRAFi & HDACi	A2058 & MEWO human melanoma xenografts in nude mice.	Improved tumor response by combination therapy.	[69]
^{227}Th	BD, efficacy, toxicity	CD20	Rituximab	^{227}Th–DOTA–p-benzyl-rituximab, i.v.	BALB/c mice & Raji human B-cell lymphoma s.c. xenografts in nude mice.	Increased efficacy with managable toxicity.	[199]
^{227}Th	BD, efficacy, toxicity	HER-2/neu	Trastuzumab	^{227}Th–DOTA–trastuzumab, i.v.	SKBR-3 human breast cancer xenografts in nude mice.	Tumor growth inhibition with no toxicity.	[200]
^{227}Th	BD, efficacy, toxicity	CD70	Anti-human CD70 mAb	CD70-TTC, i.v.	786-O human renal cancer s.c. xenografts in nude mice	Well tolerated with inhibition of tumor growth.	[201]
^{224}Ra	Efficacy, toxicity	peritoneal metastases	Injection into peritoneum	^{224}Ra-labeled calcium carbonate microparticles, i.p.	ES-2 and SKOV3 human ovarian cancer i.p. xenografts in nude mice.	Well tolerated with antitumor effect.	[202]

7. Pre-Clinical Studies

7.1. Preclinical Therapeutics Studies

In recent years, a number of pre-clinical studies have been reported that provide strong evidence of the potential for use of TAT in the treatment of cancers. See Table 2 for a summary of the published in vivo preclinical TAT studies (n = 48) that have used animal models of cancer. Most of these studies (81%) have involved the use of immunoconjugates where monoclonal antibodies serve both as the targeting moiety and as the attachment scaffold for the α-emitting radionuclide. Two of these immunoconjugates involved the use of antibody fragments (scFv) [140,141] and one used a diabody [142]. Three studies involved pretargeting, where a cancer targeting antibody–streptavidin construct, or antibody–TCO (*trans*-cyclooctene) construct for click chemistry, was injected prior to delivery of an α-emitting radionuclide attached to biotin [141,143,144]. In this study, pre-targeting demonstrated increased efficacy over TAT using the targeting antibody alone. Peptide-based targeting moieties were used in 15% of these studies. In other individual studies, a protein [145], a small molecule ligand [146] and an inorganic compound [147] were used as targeting groups.

As is the case for most radioimmunotherapies in current use, that typically deliver β-emitting radionuclides, a number of the reported TAT studies (23%) targeted non-solid tumors; i.e., leukemias, lymphomas and multiple myeloma. A majority of these non-solid tumor studies reported significant efficacy and/or decreased systemic toxicity relative to controls. Since α-emissions have higher LET over a shorter range, there is significant interest in the use of TAT for treatment of solid tumors. This is evident in the preclinical studies reported, as 79% involved targeting of solid tumors and nearly all of these studies reported significant efficacy against solid tumors relative to controls, with nearly half also reporting low or manageable systemic toxicity. Four of these studies demonstrated increased efficacy using TAT relative to targeted beta (β)-emission therapy (TBT) using the same targeting moiety and tumor model [143,151,152,163–166,180,185].

7.2. Preclinical Imaging

Whether developing a small molecule or antibody-based therapeutic, pharmaceutical companies traditionally rely upon molecular imaging to assist them in identifying the most promising molecules in the research pipeline to be carried forward into clinical trials [203–206]. Furthermore, this strategy has been particularly effective in developing targeted, systemic β-based radiotherapies when the β-emitting radioisotope can be paired with a diagnostic surrogate for SPECT or PET imaging. Several of these pairs include $^{64/67}$Cu, $^{86/90}$Y and $^{124/131}$I [207]. However, with the exception of the $^{203/212}$Pb system [68,191,208], researchers developing TATs with other α-emitters such as ^{213}Bi, ^{211}At and ^{225}Ac, have not been able to capitalize on this strategy. This limitation has hindered TAT development, but also stimulated attempts by the scientific community to observe the pharmacokinetics of TAT therapies using the decay of TAT radioisotopes in preclinical or clinical settings. For example, Sgouros et al. attempted to use the 440 keV γ emission of ^{213}Bi to monitor the biodistribution of ^{213}Bi-HuM195 in patients with leukemia [209]. Due to the short half-life of the radioisotope, data acquisition was limited to sixty minutes after patient injection, but this was sufficient to detect elevated levels of radioactivity in the red marrow, liver and spleen. While the data suggested that it would be possible to derive important pharmacokinetic and dosimetric data from the in vivo imaging of the ^{213}Bi emissions, the large amount of activity necessary for imaging has precluded its routine use in a clinical setting.

The decay scheme and extreme cytocidal potency of ^{225}Ac further complicates the TAT community's ability to develop preclinical and clinical imaging methodologies to monitor pharmacokinetics and estimate dosimetry. Since the 440 keV emission derived from ^{213}Bi decay is considered too energetic for preclinical imaging applications, attention has focused on the less energetic 218 keV γ ray emission of ^{221}Fr, which has been used to monitor the biodistribution of ^{225}Ac-doped nanoparticles in mice [71,86], and this approach has shown promise. However, in this imaging paradigm, animals are typically euthanized 1 h after receiving the radiopharmaceutical and imaged 24 h after euthanasia to ensure

isotopic equilibrium. Hence, these experiments do not address the potential of longitudinal SPECT studies to inform development of ^{225}Ac-radiopharmaceuticals. Clearly, new approaches are needed, since the ability to image and visualize ^{225}Ac-based radiopharmaceutical biodistribution, metabolism, and clearance in animal models through longitudinal imaging studies would be advantageous [210,211].

Cerenkov luminescence imaging has emerged as an alternative to traditional nuclear medicine techniques for visualizing the delivery and biodistribution of TATs. Cerenkov luminescence is derived from the emission of ultraviolet light when certain charged particles exceed the phase velocity of light in a given medium [212,213], and this effect can be observed using standard optical imaging systems originally designed to detect bioluminescence and fluorescence. Recently, Cerenkov emissions were observed with the decay of several medically relevant isotopes, including ^{225}Ac, which was reported to yield the largest optical signal among all isotopes examined [211,214]. Alpha (α) particles however, do not travel with sufficient velocity to generate Cerenkov emissions, which led researchers to postulate that the emissions observed resulted from the β-decay of the ^{213}Bi, ^{209}Tl and ^{209}Pb daughter products. Subsequent publications, using theoretical and experimental means, described the association between Cerenkov radiation and ^{225}Ac decay [214,215]. While both research groups determined that Cerenkov luminescence imaging (CLI) could be accomplished with ^{225}Ac and other α-particle emitting radionuclides, it was determined that radionuclides' decays solely by α-particle emission do not produce sufficient Cerenkov radiation to be useful for imaging. Secondly, a time delay would be needed for equilibrium to be established between the parent radionuclide and its daughter products. For ^{225}Ac, this delay was determined to be ten hours. This precludes the imaging of small molecules and peptides at early time points, but allows one to monitor the biodistribution of ^{225}Ac-labeled antibodies and nanoparticles, which require extended circulation time for effective tumor targeting and blood clearance. Finally, the high recoil energy associated with ^{225}Ac and daughter product release from the original conjugate must be considered. The emission of Cerenkov radiation may not reflect the actual biodistribution of the radiopharmaceutical in question, but of the daughter products producing the Cerenkov emissions [216]. Sequestering the daughter products with the original conjugate is important if this technique is to provide any benefit to the TAT community. In proof of principle studies, Pandya and coworkers seized upon these recommendations and further tested the association between ^{225}Ac decay and Cerenkov radiation in living animals [217]. The authors synthesized ^{225}Ac–DOTA–c(RGDyK) and evaluated its stability, biodistribution and potential use as an imaging agent in CLI in a murine model expressing human glioblastoma U87mg tumors, which overexpress the $\alpha_v\beta_3$ integrin. Additionally, they exploited the well-documented ability of RGD-containing ligands to be internalized on integrin binding to sequester the ^{225}Ac and the daughter products within the tumor. This technique, often referred to as the nanogenerator approach, has been used successfully to sequester ^{225}Ac-based radiotherapeutics and daughter decay products within a cell to increase their therapeutic effectiveness [35,149,150]. Surprisingly, all animals demonstrated no signs of distress during these experiments. When compared to $\alpha_v\beta_3^-$ tissues, in vivo CLI revealed five-fold more luminescence from the $\alpha_v\beta_3^+$ tumors. Luminescence was also observed in the liver and kidney tissues, which have been shown in related biodistribution studies to be involved in the clearance and excretion of this radiopharmaceutical [218–220]. Ex vivo image analysis also revealed a similar trend as the in vivo results, and the addition of a blockade reduced the luminescence emitted from the tumors by 80%, which suggested to the authors that activity delivered by the radiopharmaceutical and internalized through specific receptor-interactions was being retained in the tumor. To further validate the theranostic potential of their approach, they also performed preliminary therapy studies in U87mg tumor-bearing mice, which illustrated the cytocidal potency of their α-emitting radiotherapeutic [221]. While more studies are needed, these promising results suggest that this area of research may have broader implications for molecular imaging and may help to facilitate TAT development.

8. Medicinal Chemistry

8.1. Lead Optimization

As previously touched upon, the characteristics of various targeting ligands, like lipophilicity, molecular weight and ionization potential are all critical variables that help modulate radiopharmaceutical properties. For example, small, polar compounds may undergo rapid renal excretion. The addition of a PEG linker will add water solubility, bulk, and may help avoid kidney toxicities. Conversely, the removal of an ionizable group (e.g., sulfonate or protonated amines at physiologic pH) during medicinal chemistry design may make the targeting ligand more hydrophobic and shift clearance toward initial liver processing. Therefore, when working to reduce targeting ligand complexity or increase the ease of synthesis, these physical attributes of the compound must be taken into consideration.

Antibodies and engineered fragments can also benefit from medicinal chemistry optimization. Many chelators and linkers covalently attached to antibodies and their fragments produce heterogeneous products. In the most typical fashion of linker attachment, surface accessible lysine side chains are utilized to form covalent bonds with radionuclide chelating molecules (Figure 6). Site-specific antibody modifications can yield more homogeneous products. The Rader group at Scripps Florida has made such progress by engineering a selenocysteine residue into targeting antibodies, allowing for complete control of regiochemistry during functionalization [222].

Another route to increasing T/NT ratios is through the notion of pretargeting. These strategies operate under the premise that nonradiolabeled, bifunctional targeting agents can be administered to the patient and allowed to converge to their target. Once the unbound portion has cleared, a fraction of radiolabeled molecule with a binding affinity for the bifunctional targeting agent is administered. Typically, the radiolabeled agent is designed to clear quickly if unavailable for binding; thus, lowering off-target radiation. Typical binding partners amenable to pretargeting schemes include avidin/streptavadin–biotin, DNA–DNA or antibody–hapten [223]. For a more in-depth analysis of pretargeting strategies please see the recent review article from Frampas and coworkers [224].

Novel combination therapies are also now being investigated. Combination therapies can be particularly useful in heterogeneous diseases like multiple myeloma. Anti CD138 mAb conjugated with ^{213}Bi has been tested synergistically with the chemotherapeutic melphalan to help eliminate residual disease in a multiple myeloma model [116]. Interestingly, this study saw no benefit to the combination therapy when compared with RIT alone. The speculation was that the follow-up treatment with CD138-targeted mAb was less successful due a swift reduction in CD138 antigen in cells progressing through apoptosis [225], illustrating the importance of the orthogonality in study design as it relates to combination treatments and target expression.

8.2. cGMP Production

Current good manufacturing practice (cGMP) standards for the production of the targeting ligand precursors before the incorporation of the α-emitting radioisotopes are similar to those used for the manufacturing of peptide, antibody or antibody fragment drug and drug candidates. There are numerous cGMP-compliant peptide synthesis companies, and often the preclinical grade peptides will be prepared by standard solid-phase synthesis and purified to $\geq$ 95% purity, but cGMP-grade peptides will often be prepared via routes that allow greater control over the purity and reliability of the synthesis. For instance, cGMP peptides are more likely to be prepared using a greater reliance on solution phase-synthesis procedures than preclinical grade peptides because the costs can be much lower on scaled-up batches of peptide, and more importantly, impurities can be removed as they build up during a solution-phase synthesis, whereas impurities just build up during standard solid-phase synthesis procedures. The recent development of a fully solid-phase synthesis of cGMP-quality Fuzeon® is an exception to this trend that may lead to a greater reliance on fully solid-phase synthesis procedures for the production of cGMP peptides. Frequently, solid phase methods are used in

combination with solution phase synthesis methods. As an example, preclinical grade linear peptides can be prepared and cyclized to the final product on resin, whereas cGMP grade peptides will often be prepared on resin and purified and then cyclized in solution, due to the easier analysis of reactions in solution.

The cGMP production of antibody and antibody fragments will be focused on for the development of robust methods of production often using hybridoma technologies and purification by at least two orthogonal separation methods, usually involving an affinity column purification step followed by a size exclusion type purification system. Often these biotechnology-based manufacturing methods produce antibody or antibody fragments that are chemically programmed to provide specific sites for metal chelate attachment. For a recent review of this topic please, see the two-part article from Adumeau et al. [226,227].

The results of these manufacturing processes are lyophilized powders or relatively-concentrated, sterile, aqueous buffer solutions of the targeting moieties that are ready to chelate the α-emitters. The main difference between cGMP radiosynthesis for clinical trials and research grade radiosynthesis in the United States is the implementation of an FDA-compliant audit trail. Since the development of α-emitting radiopharmaceuticals is happening globally, another major issue concerning production and distribution of these novel therapies is the consideration of the local regulatory environment. A discussion of the potential for harmonization of the various international regulations has recently been published [228].

Table 3. Clinical TAT studies.

Isotope	Molecular Target	Targeting Moiety	Drug	Cancer Type	Trial/# of Patients	Administration Route	Key Results	Ref
[225]Ac	CD33	HuM195	[225]Ac–DOTA–HuM195	AML	Phase I/20, Ongoing multicentric phase I, II	Intravenous	Safe at doses ≤ 3 µCi/kg, anti-leukemic activity across all dose levels studied, no acute toxicities, myelosuppression	[235]
[225]Ac	PSMA	PSMA-617 ligand	[225]Ac–PSMA-617	Prostate cancer	NA/40	Intravenous	Remarkable anti-tumor response was observed in the patients. Xerostomia in salivary gland was the main side effect.	[5,6,60,233,236,237]
[225]Ac	Somatostatin receptors	DOTATOC peptide	[225]Ac–DOTATOC	Neuroendocrine tumors	NA/34	Not mentioned	Well-tolerated with promising treatment efficacy	[234]
[211]At	Tenascin-C	chimeric 816 antibody	[211]At-ch81C6	Glioblastoma	Phase I/18	surgically created resection cavity	Increased Median survival (54 weeks), No dose-limiting toxicity, No-grade 3 toxicity	[238]
[211]At	NaPi2b	MX35 F(ab')2	[211]At-MX35 F(ab')2	Ovarian carcinoma	Phase I/9	Intraperitoneal	No adverse effects, grade I toxicity, no bone marrow toxicity	[239]
[213]Bi	CD33	HuM195	[213]Bi–CHX-A-DTPA–HuM1 95	AML	Phase I/18	Intravenous	14 patients had reductions in marrow blasts	[240]
[213]Bi	CD33	HuM195	[213]Bi–CHX-A-DTPA–HuM1 95	AML	Phase I, II/31	Intravenous	dose-response relationship with remission at the highest doses	[241]
[213]Bi	CD20	Rituximab	[213]Bi–CHX-A''- Rituximab	Non-Hodgkin lymphoma	Phase I/9	Intravenous	Myelosuppression and no other toxic side, two patients responded	[242]
[213]Bi	Neurokinin type-1 receptor	Substance P	[213]Bi–DOTA–[Thi8, Met (O2) 11]–substance P	Glioblastoma	NA/2, 9, 20	Intrathecal	Well-tolerated, favorable response	[229,230,243]
[213]Bi	NG2 proteoglycan	9.2.27 antibody	[213]Bi–cDTPA–9.2.27	Melanoma	Phase I/38	Intralesional	TAT was safe up to 450 mCi and effective at 200 mCi	[244,245]
[213]Bi	Somatostatin receptors	DOTATOC peptide	[213]Bi–DOTATOC	Neuroendocrine tumors	NA/7	Intraarterial infusion	responses were observed in all patients	[65]
[213]Bi	EGFR	Cetuximab	[213]Bi–CHX-A-DTPA–anti-EGFR	carcinoma in situ (CIS) of the bladder	Pilot studies/9 and 12	Intravesical	TAT well tolerated and showed therapeutic efficacy	[231,232]
[212]Pb	HER2	Trastuzumab	[212]Pb–TCMC–trastuzumab	Ovarian Cancer	Phase I/3	Intraperitoneal	Dose escalation showed a little agent-related toxicity, consistent with the dosimetry data	[246,247]
[223]Ra	Hydroxy-apatite	NA	[223]Ra–chloride	Prostate cancer mets	Phase I-III/921	Intravenous	radium-223 improved overall survival	[7,8,82,248–251]

9. Clinical Studies

9.1. Recent TAT Clinical Trials

Despite the potential therapeutic benefits of the α-particle emitting radioisotopes over β-particle emitters, the restricted availability of relevant radionuclides and limited number of phase III clinical trials has so far limited the clinical use of TAT. Table 3 summarizes the TAT clinical studies conducted to date. Clinical trials prior to 2014 were reviewed by Elgqvist et al. [34] and we will focus on the more recent trials herein. The use of short-lived α-emitters like ^{211}At ($T_{1/2}$ = 7.2 h), ^{212}Bi ($T_{1/2}$ = 60 min) and ^{212}Pb ($T_{1/2}$ = 10.6 h) has been subdued so far, due to production and distribution limitations. However, this is not the case for ^{213}Bi ($T_{1/2}$ = 46 min), which, going back over the past two decades, has been used in the largest number of TAT clinical trials to date. Recent ^{213}Bi studies have included the targeting of peptides for the treatment of glioblastoma [229,230] and neuroendocrine tumors [65], and the targeting of monoclonal antibodies for the treatment of bladder cancer [231,232]. Since the approval of ^{223}Ra-dichloride for the treatment of CRPC in 2013, ^{225}Ac has also emerged as a targeted therapeutic radionuclide of interest that has been used for targeting a small molecule [5,6,233], peptide [234] and monoclonal antibody [235] for the targeting of prostate cancer, neuroendocrine tumors, and acute myeloid leukemia (AML), respectively. Clinical studies of TATs using ^{225}Ac or ^{213}Bi as the therapeutic radionuclide have recently been reviewed [58]. Although the responses have been impressive for some, ^{225}Ac–PSMA-617 in particular, the completion of more randomized clinical trials comparing TAT to standard of care will be essential to determine the clinical utility of these new therapeutic approaches.

9.2. Radium-223 Dichloride (^{223}RaCl$_2$) Trials

In the following section, we will discuss the first and only clinically-approved TAT in the United States so far. After more than a 100 years since the discovery of the radium element in 1898 by Marie and Pierre Curie, on May 15, 2013, one of its radioisotopes, radium-223 (Ra-223) became the first α-emitting radionuclide to be approved by the Food and Drug Administration (FDA) in the form of radium-223 dichloride (^{223}RaCl$_2$, Xofigo® formerly Alpharadin, made by Bayer HealthCare Pharmaceuticals Inc.) for the treatment of patients with castration-resistant prostate cancer (CRPC), with symptomatic bone metastases, and no known visceral metastatic disease [252]. This was based on the improvement in overall survival following intravenous administration of ^{223}RaCl$_2$ in patients with advanced prostate cancer with metastases to the bone, demonstrated in a double-blind randomized placebo-controlled trial called the ALSYMPCA (alpharadin in symptomatic prostate cancer) trial [7].

The role of systemic radionuclide therapy to the bone is to deliver therapeutically-effective radiation doses to multiple foci, including microscopic disease, as opposed to external beam radiotherapy, that gives more focal treatment and affects both normal bone marrow and metastases [253]. The two most commonly used radionuclide bone seeking agents for bone pain palliation are ^{89}Sr (Metastron) and ^{153}Sm-ethylene diamine *N*,*N'*-tetra(methylene) phosphonic acid (^{153}Sm-EDTMP; Quadramet) [254], but these β-particle therapies, although effective for pain palliation, frequently cause myelosuppression and have not been shown to affect patient survival [255].

Cations of the alkaline earth elements (strontium, barium, and radium) have natural bone-seeking properties without the need for a carrier agent. As radium mimics calcium, when Ra-223 dichloride is injected intravenously, it forms complexes with the bone mineral hydroxyapatite at areas of increased metabolic bone activity, such as bone metastases, thereby exerting a highly localized antitumoral effect [7,256]. In addition, the Ra-223 daughter isotopes are also retained in the bone matrix [50]. The shorter penetration range of Ra-223 causes less bone marrow toxicity than bone-seeking β-particles [256]. The peak skeletal uptake of Ra-223 occurs within 1 h of injection, and blood radioactivity levels are <1% after 24 h with almost no redistribution of daughter nuclides from bone [256]. The total skeletal uptake ranges between 40% and 60% of the administered activity [257], and the excretion is predominantly via the gastrointestinal tract, with much less renal clearance [258]. Due to their significantly higher potency, the activities administered of α-emitters are much lower

than β emitters, with significantly less radiation exposure to hospital staff and family members [259]. Merely basic hygiene measures and routine contamination protection barriers, such as latex gloves, are enough to protect both health care personnel involved in the patient's radionuclide administration and the patient's family.

In the first-in-human single dosage phase I trial for patients with breast and prostate cancer skeletal metastases, single dose Ra-223 was well tolerated at all therapeutically relevant doses (46–250 kBq/kg intravenously [IV]) [257]. There was no dose-limiting hematological toxicity, only mild, transient myelosuppression (nadir 2 to 4 weeks after the injection) and mild transient diarrhea, with nausea and vomiting more frequently observed in the highest dosage group [257]. Subsequently, the phase I dose-escalation study in advanced prostate cancer with bone metastases, showed that repeated Ra-223 dosing was well tolerated to a total dose of 250 kBq/kg [50].

In the following phase II study of CRPC patients with symptomatic bone metastases, Ra-223 given at different doses (5, 25, 50 and 100 kBq/kg) was well tolerated with a positive effect on pain assessments (visual analogue scale [VAS] and analgesic use). At week 8, 56% and 71% of patients had reduced pain and stable analgesic consumption in the 50 and 100 kBq/kg groups, respectively. A statistically significant decrease in bone turnover markers, including alkaline phosphatase, was noted in the highest dose-group ($p = 0.0067$) [260].

The phase III, double-blind, randomized, placebo-controlled, multicenter, multinational ALSYMPCA trial enrolled patients from June 2008 through February 2011 [7]. Eligible patients had progressive metastatic symptomatic disease and regular use of analgesic medication or treatment with external beam radiation therapy (EBRT) for cancer-related bone pain within the previous 12 weeks. Patients were randomized 2:1 to receive six injections of radium-223 (50 kBq/kg IV) or a saline placebo infusion; a cycle was comprised of one injection every 4 weeks. The primary endpoint was overall survival (OS). Various secondary endpoints included time to first symptomatic skeletal events (SSE), time to alkaline phosphatase increase and time to PSA progression. A planned interim analysis was conducted, and on June 3, 2011, the Independent Data Monitoring Committee recommended stopping the trial early due to evidence of a significant treatment benefit. Median OS was 14.0 months for Ra-223 (95% CI (confidence interval): 12.1–15.8) versus 11.2 months for placebo (95% CI: 9.0–13.2) ($p = 0.00185$; HR (hazard ratio) = 0.695; 95% CI: 0.552–0.875).

An updated analysis included 528 events from 921 randomized patients prior to placebo patients crossing over to Ra-223 [7,261]. For this analysis, median OS was 14.9 months for Ra-223 arm (95% CI: 13.9–16.1) and 11.3 months for patients receiving placebo (95% CI: 10.4–12.8) (HR = 0.695; 95% CI: 0.581–0.832). OS favored Ra-223, with a 30% reduction in the risk of death compared with placebo. The OS benefit with Ra-223 was supported by a delay in time to first SSE compared to the placebo (15.6 versus 9.8 months; HR = 0.66; 95% CI, 0.52–0.83; $p < 0.001$). Improvement in survival was independent of both prior exposure to docetaxel [250] and the use of bisphosphonates [261]. Ra-223 significantly prolonged time to total ALP progression (HR = 0.167; 95% CI: 0.129–0.217; $p < 0.00001$); and time to PSA progression (HR = 0.643; 95% CI: 0.539–0.768; $p < 0.00001$) was associated with a beneficial effect on pain and quality of life (QOL) [262], and was associated with a highly favorable safety profile with a low rate of adverse hematological events. The most common (at least two percent) of the adverse reactions in patients receiving Ra-223 were nausea, diarrhea, vomiting, renal impairment and peripheral edema.

Based on these data, the National Comprehensive Cancer Network (NCCN) supports the use of $^{223}RaCl_2$ (Xofigo®) as a first-line therapy for patients with symptomatic metastatic CRPC and no visceral metastases with a Category 1 recommendation [227]. The recommended dose for $^{223}RaCl_2$ is 50 kBq/kg (1.35 microcuries/kg) administered by slow intravenous injection, over 1 min, every 4 weeks, for a total of six cycles.

Since completion of the ALSYMPCA trial, Ra-223 has been studied in combination with other, newly-approved CRPC therapies, such as abiraterone, enzalutamide, docetaxel, cabazitaxel, sipuleucel-T, olaparib and pembrolizumab [263–265]. A phase 3, randomized, double-blind study of

radium-223 or placebo, each in combination with abiraterone plus prednisone in chemotherapy-naive patients with asymptomatic or mildly symptomatic mCRPC with bone metastases (ERA 223; NCT02043678) [266], was recently prematurely unblinded. The independent data monitoring committee (IDMC) recommended unblinding the trial due to the observation of more fractures and deaths in the combination treatment arm. The European Medicines Agency (EMA)'s Pharmacovigilance Risk Assessment Committee (PRAC) has reviewed the preliminary data from the ongoing clinical study. In the study 34.7%, of patients treated with Xofigo, Zytiga and prednisone/prednisolone have died so far, compared with 28.2% of patients given placebo, Zytiga and prednisone/prednisolone. Fractures have also occurred more frequently with the Xofigo combination than the placebo combination (26% versus 8.1%). Unblinded data from the study are currently being analyzed to confirm the preliminary findings of the IDMC. Given these results from ERA 223 trial, the current recommendation is not to combine radium-223 with concomitant abiraterone acetate and prednisone (https://www.ema.europa.eu/news/prostate-cancer-medicine-xofigo-must-not-be-used-zytiga-prednisoneprednisolone). Hence, the administration of concomitant chemotherapy with Xofigo is not recommended due to an increased risk of adverse reactions [267].

Immune modulation has been examined in vitro in human prostate, breast and lung carcinoma cells following exposure to sub-lethal doses of ^{223}Ra. Malamas and his colleagues showed that ^{223}Ra significantly enhanced T cell-mediated lysis of each tumor type by CD8+ cytotoxic T lymphocytes (CTLs) specific for MUC-1, brachyury, and CEA tumor antigens. Therefore, ^{223}Ra may be more effective in combination with immunotherapies [268].

In view of the increased long term risk of secondary malignancies, such as sarcomas and leukemias, that were seen in patients who were treated with high doses of another radium isotope, radium-224 ($T_{1/2} = 3.7$ days) (primarily used in Europe) for bone pain associated with ankylosing spondylitis, there is concern for development secondary malignancy with the use of Ra-223. So far there has been no evidence of secondary malignancies following Ra-223 therapy [7,269]. However, it is important to note that patients with metastatic CRPC have a much shorter overall survival than patients with ankylosing spondylitis. Care should be taken when expanding the use of Ra-223 to other patient groups with longer expected overall survival times, since the rate of secondary tumor development may increase.

Ra-223 trials have been performed for patients with diseases other than CRPC. Ra-223 was found to be safe and well tolerated when studied in a phase II, open-label trial investigating the safety and short-term efficacy in patients with breast cancer who had bone-dominant disease [270], but the data are still limited. In contrast to prostate cancer, multiple myeloma bone lesions are predominantly lytic. It is not yet know if Ra-223 will have any role in this category of patients, but based on previous clinical trials using ^{153}Sm-EDTMP plus chemotherapy, the combination showed efficacy in some patients with far-advanced myeloma [271], so theoretically, these results could be replicated with Ra-223, with potentially fewer side effects. In view of the limited but positive experience in ^{153}Sm-EDTMP for osteosarcoma due to its osteoblastic nature [272], there is currently a phase I dose trial for the use of Ra-223 in patients with osteosarcoma at the M.D. Anderson Cancer Center (www.clinicaltrials.gov; NCT01833520).

10. Conclusions

There has recently been significant interest and progression toward the development of targeted alpha-particle therapy (TAT) for the treatment of solid tumors. Many pre-clinical and clinical studies have demonstrated promising anti-tumor efficacy results (Tables 2 and 3). The success of ^{223}RaCl$_2$ in the care of patients with bone metastases and the apparent efficacy of additional TAT agents in recent clinical studies, e.g., ^{213}Bi–DOTATOC and ^{225}Ac-PSMA, has brought attention to this area of radiopharmaceutical development and increased the potential for successful translation of TAT for treatment of solid tumors and metastases [65,233]. Three radioisotopes have seen the most use in preclinical and clinical studies, ^{213}Bi, ^{225}Ac and ^{211}At. Each of these radionuclides has distinct advantages and disadvantages regarding availability, cost, decay chain attributes, tissue distribution

and stability of attachment. Of these, ^{225}Ac is readily available and has the distinct advantage of having a long, 10 d half-life, which allows for centralized production and distribution compared to the requirement of local production for the other radionuclides with shorter half-lives. Since TAT does not rely on the generation of free-radicals for the generation of DNA damage, as is the case for β-emission therapies, a major mechanism of resistance to radiation treatment can be bypassed; i.e., upregulation of superoxide dismutase. Some evidence of this was seen in a report stating that patients with tumors that have developed resistance to ^{90}Y/^{177}Lu–DOTATOC therapy were sensitive to subsequent treatment with ^{213}Bi–DOTATOC [65]. Additionally, the use of α-emitters enables solid-tumor targeted therapy with decreased peripheral tissue damage and the potential for decreased development of resistance due to the ability to kill surrounding tumor cells that do not express the target marker in a heterogeneous tumor microenvironment. Small molecules, peptides and monoclonal antibodies have been used for tumor targeting (Tables 2 and 3). However, due to the shorter clearance time (minutes to hours), small molecules and peptides may have an advantage over antibodies that can circulate for days in that they can accumulate in the target tumor and clear systemically prior to decay and deposition of energy, maximizing the beneficial effects of the ionizing radiation while minimizing the off-target exposure. This is especially true when using radionuclides with a long half-life; e.g., ^{225}Ac. Peptide-targeted agents may have a greater risk of generating renal toxicity [66], but there is evidence that lead optimization via medicinal chemistry could potentially improve the renal toxicity of a given peptide agent. For example, a recent preclinical study of two different gastrin-releasing peptide receptor (GRP-R)-targeting agents using two different ^{213}Bi-labeled GRP-R targeting peptides demonstrated differential renal toxicities [185]. TAT is currently emerging as a potentially new and effective approach toward the treatment of solid tumors, and the clinical translation of novel TAT radiopharmaceuticals appears to be on the near horizon. Since the abscopal effect has been observed in external beam therapy in animals, the ability to target internal radiation to tumors via TAT may have additional added value as a companion to the recently-successful immune checkpoint targeted therapies.

References

1. Pouget, J.P.; Navarro-Teulon, I.; Bardies, M.; Chouin, N.; Cartron, G.; Pelegrin, A.; Azria, D. Clinical radioimmunotherapy–the role of radiobiology. *Nat. Rev. Clin. Oncol.* **2011**, *8*, 720–734. [CrossRef] [PubMed]

2. Bodet-Milin, C.; Kraeber-Bodere, F.; Eugene, T.; Guerard, F.; Gaschet, J.; Bailly, C.; Mougin, M.; Bourgeois, M.; Faivre-Chauvet, A.; Cherel, M.; et al. Radioimmunotherapy for Treatment of Acute Leukemia. *Semin. Nucl. Med.* **2016**, *46*, 135–146. [CrossRef] [PubMed]

3. Sgouros, G.; Roeske, J.C.; McDevitt, M.R.; Palm, S.; Allen, B.J.; Fisher, D.R.; Brill, A.B.; Song, H.; Howell, R.W.; Akabani, G.; et al. MIRD Pamphlet No. 22 (abridged): Radiobiology and dosimetry of alpha-particle emitters for targeted radionuclide therapy. *J. Nucl. Med.* **2010**, *51*, 311–328. [CrossRef] [PubMed]

4. Dizdarevic, S.; Jessop, M.; Begley, P.; Main, S.; Robinson, A. (223)Ra-Dichloride in castration-resistant metastatic prostate cancer: Improving outcomes and identifying predictors of survival in clinical practice. *Eur. J. Nucl. Med. Mol. Imaging* **2018**, *45*, 2264–2273. [CrossRef] [PubMed]

5. Kratochwil, C.; Bruchertseifer, F.; Rathke, H.; Hohenfellner, M.; Giesel, F.L.; Haberkorn, U.; Morgenstern, A. Targeted alpha-Therapy of Metastatic Castration-Resistant Prostate Cancer with (225)Ac-PSMA-617:

Swimmer-Plot Analysis Suggests Efficacy Regarding Duration of Tumor Control. *J. Nucl. Med.* **2018**, *59*, 795–802. [CrossRef] [PubMed]

6. Sathekge, M.; Bruchertseifer, F.; Knoesen, O.; Reyneke, F.; Lawal, I.; Lengana, T.; Davis, C.; Mahapane, J.; Corbett, C.; Vorster, M.; et al. (225)Ac-PSMA-617 in chemotherapy-naive patients with advanced prostate cancer: A pilot study. *Eur. J. Nucl. Med. Mol. Imaging* **2019**, *46*, 129–138. [CrossRef]

7. Parker, C.; Nilsson, S.; Heinrich, D.; Helle, S.I.; O'Sullivan, J.M.; Fossa, S.D.; Chodacki, A.; Wiechno, P.; Logue, J.; Seke, M.; et al. Alpha emitter radium-223 and survival in metastatic prostate cancer. *N. Engl. J. Med.* **2013**, *369*, 213–223. [CrossRef]

8. Sartor, O.; Sharma, D. Radium and other alpha emitters in prostate cancer. *Transl. Urol.* **2018**, *7*, 436–444. [CrossRef]

9. Franchet-Beuzit, J.; Spotheim-Maurizot, M.; Sabattier, R.; Blazy-Baudras, B.; Charlier, M. Radiolytic footprinting. Beta rays, gamma photons, and fast neutrons probe DNA-protein interactions. *Biochemistry* **1993**, *32*, 2104–2110. [CrossRef]

10. Schulte-Frohlinde, D. Mechanism of radiation-induced strand break formation in DNA and polynucleotides. *Adv. Space Res.* **1986**, *6*, 89–96. [CrossRef]

11. Cox, R.; Masson, W.K. Mutation and inactivation of cultured mammalian cells exposed to beams of accelerated heavy ions. III. Human diploid fibroblasts. *Int. J. Radiat. Biol. Relat. Stud. Phys. Chem. Med.* **1979**, *36*, 149–160. [CrossRef] [PubMed]

12. Goodhead, D.T.; Munson, R.J.; Thacker, J.; Cox, R. Mutation and inactivation of cultured mammalian cells exposed to beams of accelerated heavy ions. IV. Biophysical interpretation. *Int. J. Radiat. Biol. Relat. Stud. Phys. Chem. Med.* **1980**, *37*, 135–167. [CrossRef] [PubMed]

13. Munson, R.J.; Bance, D.A.; Stretch, A.; Goodhead, D.T. Mutation and inactivation of cultured mammalian cells exposed to beams of accelerated heavy ions. I. Irradiation facilities and methods. *Int. J. Radiat. Biol. Relat. Stud. Phys. Chem. Med.* **1979**, *36*, 127–136. [CrossRef] [PubMed]

14. Thacker, J.; Stretch, A.; Stephens, M.A. Mutation and inactivation of cultured mammalian cells exposed to beams of accelerated heavy ions. II. Chinese hamster V79 cells. *Int. J. Radiat. Biol. Relat. Stud. Phys. Chem. Med.* **1979**, *36*, 137–148. [CrossRef]

15. Pouget, J.P.; Mather, S.J. General aspects of the cellular response to low- and high-LET radiation. *Eur. J. Nucl. Med.* **2001**, *28*, 541–561. [CrossRef]

16. Galluzzi, L.; Vitale, I.; Aaronson, S.A.; Abrams, J.M.; Adam, D.; Agostinis, P.; Alnemri, E.S.; Altucci, L.; Amelio, I.; Andrews, D.W.; et al. Molecular mechanisms of cell death: Recommendations of the Nomenclature Committee on Cell Death 2018. *Cell Death Differ.* **2018**, *25*, 486–541. [CrossRef]

17. Dagogo-Jack, I.; Shaw, A.T. Tumour heterogeneity and resistance to cancer therapies. *Nat. Rev. Clin. Oncol.* **2018**, *15*, 81–94. [CrossRef]

18. Sgouros, G. Alpha-particles for targeted therapy. *Adv. Drug Deliv. Rev.* **2008**, *60*, 1402–1406. [CrossRef]

19. Song, H.; Senthamizhchelvan, S.; Hobbs, R.F.; Sgouros, G. Alpha Particle Emitter Radiolabeled Antibody for Metastatic Cancer: What Can We Learn from Heavy Ion Beam Radiobiology? *Antibodies* **2012**, *1*, 124–148. [CrossRef]

20. Lawrence, J.H.; Tobias, C.A.; Born, J.L.; Linfoot, J.A.; Kling, R.P.; Gottschalk, A. Alpha and Proton Heavy Particles and the Bragg Peak in Therapy. *Trans. Am. Clin. Clim. Assoc.* **1964**, *75*, 111–116.

21. Kudryashow, Y.B. *Radiation Biophysics (Ionization Radiation)*; Nova Science Publishers Inc.: Hauppauge, NY, USA, 2006.

22. Hall, E.J.; Giaccia, A.J. *Radiobiology for the Radiologist*; Lippincott Williams & Wilkins: Philadelphia, PA, USA, 2006.

23. Elgqvist, J.; Andersson, H.; Back, T.; Hultborn, R.; Jensen, H.; Karlsson, B.; Lindegren, S.; Palm, S.; Warnhammar, E.; Jacobsson, L. Therapeutic efficacy and tumor dose estimations in radioimmunotherapy of intraperitoneally growing OVCAR-3 cells in nude mice with (211)At-labeled monoclonal antibody MX35. *J. Nucl. Med.* **2005**, *46*, 1907–1915.

24. Thomlinson, R.H.; Gray, L.H. The histological structure of some human lung cancers and the possible implications for radiotherapy. *Br. J. Cancer* **1955**, *9*, 539–549. [CrossRef] [PubMed]

25. Mothersill, C.; Seymour, C. Radiation-induced bystander effects: Evidence for an adaptive response to low dose exposures? *Dose Response* **2006**, *4*, 283–290. [CrossRef] [PubMed]

26. Sawal, H.A.; Asghar, K.; Bureik, M.; Jalal, N. Bystander signaling via oxidative metabolism. *Onco. Target* **2017**, *10*, 3925–3940. [CrossRef] [PubMed]

27. Ludgate, C.M. Optimizing cancer treatments to induce an acute immune response: Radiation Abscopal effects, PAMPs, and DAMPs. *Clin. Cancer Res.* **2012**, *18*, 4522–4525. [CrossRef]

28. Williams, L.E.; DeNardo, G.L.; Meredith, R.F. Targeted radionuclide therapy. *Med. Phys.* **2008**, *35*, 3062–3068. [CrossRef]

29. Jadvar, H.; Quinn, D.I. Targeted alpha-particle therapy of bone metastases in prostate cancer. *Clin. Nucl. Med.* **2013**, *38*, 966–971. [CrossRef]

30. Miederer, M.; Scheinberg, D.A.; McDevitt, M.R. Realizing the potential of the Actinium-225 radionuclide generator in targeted alpha particle therapy applications. *Adv. Drug Deliv. Rev.* **2008**, *60*, 1371–1382. [CrossRef]

31. Allen, B.J.; Huang, C.Y.; Clarke, R.A. Targeted alpha anticancer therapies: Update and future prospects. *Biologics* **2014**, *8*, 255–267. [CrossRef]

32. Marusyk, A.; Polyak, K. Tumor heterogeneity: Causes and consequences. *Biochim. Biophys. Acta* **2010**, *1805*, 105–117. [CrossRef]

33. Imam, S.K. Advancements in cancer therapy with alpha-emitters: A review. *Int. J. Radiat Oncol. Biol. Phys.* **2001**, *51*, 271–278. [CrossRef]

34. Elgqvist, J.; Frost, S.; Pouget, J.P.; Albertsson, P. The potential and hurdles of targeted alpha therapy—Clinical trials and beyond. *Front. Oncol.* **2014**, *3*, 324. [CrossRef] [PubMed]

35. McDevitt, M.R.; Ma, D.; Lai, L.T.; Simon, J.; Borchardt, P.; Frank, R.K.; Wu, K.; Pellegrini, V.; Curcio, M.J.; Miederer, M.; et al. Tumor therapy with targeted atomic nanogenerators. *Science* **2001**, *294*, 1537–1540. [CrossRef] [PubMed]

36. Pozzi, O.; Guatelli, S.; Allen, B.; Barbet, J.; Cherel, M.; Bardies, M.; Bruchertseifer, F.; Seidl, C.; Bombardieri, E.; Bilewicz, A.; et al. Report: Technical Meeting on "Alpha emitting radionuclides and radiopharmaceuticals for therapy". Available online: http://www-naweb.iaea.org/napc/iachem/working_materials/TM-44815-report-Alpha-Therapy.pdf (accessed on 25 September 2019).

37. Kim, Y.S.; Brechbiel, M.W. An overview of targeted alpha therapy. *Tumour Biol.* **2012**, *33*, 573–590. [CrossRef] [PubMed]

38. McDevitt, M.R.; Finn, R.D.; Ma, D.; Larson, S.M.; Scheinberg, D.A. Preparation of alpha-emitting 213Bi-labeled antibody constructs for clinical use. *J. Nucl. Med.* **1999**, *40*, 1722–1727.

39. Couturier, O.; Supiot, S.; Degraef-Mougin, M.; Faivre-Chauvet, A.; Carlier, T.; Chatal, J.F.; Davodeau, F.; Cherel, M. Cancer radioimmunotherapy with alpha-emitting nuclides. *Eur. J. Nucl. Med. Mol. Imaging* **2005**, *32*, 601–614. [CrossRef]

40. Corson, D.R.; MacKenzie, K.R.; Segre, E. Artificially Radioactive Element 85. *Phys. Rev. J.* **1940**, *58*, 672. [CrossRef]

41. Zalutsky, M.R.; Pruszynski, M. Astatine-211: Production and availability. *Curr. Radiopharm.* **2011**, *4*, 177–185. [CrossRef]

42. Zalutsky, M.R.; Vaidyanathan, G. Astatine-211-labeled radiotherapeutics: An emerging approach to targeted alpha-particle radiotherapy. *Curr. Pharm. Des.* **2000**, *6*, 1433–1455. [CrossRef]

43. Guerard, F.; Gestin, J.F.; Brechbiel, M.W. Production of [(211)At]-astatinated radiopharmaceuticals and applications in targeted alpha-particle therapy. *Cancer Biother. Radiopharm.* **2013**, *28*, 1–20. [CrossRef]

44. Wadas, T.J.; Pandya, D.N.; Solingapuram Sai, K.K.; Mintz, A. Molecular targeted alpha-particle therapy for oncologic applications. *AJR Am. J. Roentgenol.* **2014**, *203*, 253–260. [CrossRef] [PubMed]

45. Zhuikov, B.L.; Kalmykov, S.N.; Ermolaev, R.A.; Aliev, V.M.; Kokhanyuk, V.L.; Matushko, I.G.; Tananaev, B.F.; Myasoedov, B.F. Production of 225Ac and 223Ra by irradiation of Th with accelerated protons. *Radiochemistry* **2011**, *53*, 77–80. [CrossRef]

46. Griswold, J.R.; Medvedev, D.G.; Engle, J.W.; Copping, R.; Fitzsimmons, J.M.; Radchenko, V.; Cooley, J.C.; Fassbender, M.E.; Denton, D.L.; Murphy, K.E.; et al. Large scale accelerator production of (225)Ac: Effective cross sections for 78–192 MeV protons incident on (232)Th targets. *Appl. Radiat Isot.* **2016**, *118*, 366–374. [CrossRef] [PubMed]

47. John, K. Targeted Alpha Therapy: The US DOE Tri-Lab (ORNL, BNL, LANL) Research Effort to Provide Accelerator-Produced 225Ac for Radiotherapy. In Proceedings of the American Physical Society Annual Meeting, New Orleans, LA, USA, 28–31 January 2017.

48. Khabibullin, A.R.; Karolak, A.; Budzevich, M.M.; McLaughlin, M.L.; Morse, D.L.; Woods, L.M. Structure and properties of DOTA-chelated radiopharmaceuticals within the (225)Ac decay pathway. *Medchemcomm* **2018**, *9*, 1155–1163. [CrossRef] [PubMed]

49. Greenwood, N.N.; Earnshaw, A. *Chemistry of the Elements*, 2nd ed.; Butterworth-Heinemann: Oxford, UK, 1997; p. 946. ISBN 0-08-037941-9.

50. Bruland, O.S.; Nilsson, S.; Fisher, D.R.; Larsen, R.H. High-linear energy transfer irradiation targeted to skeletal metastases by the alpha-emitter 223Ra: Adjuvant or alternative to conventional modalities? *Clin. Cancer Res.* **2006**, *12*, 6250s–6257s. [CrossRef]

51. Henriksen, G.; Bruland, O.S.; Larsen, R.H. Thorium and actinium polyphosphonate compounds as bone-seeking alpha particle-emitting agents. *Anticancer Res.* **2004**, *24*, 101–105.

52. Mausner, L.F.; Straub, R.F.; Srivastava, S.C. The in vivo generator for radioimmunotherapy. *J. Label. Compd. Radiopharm.* **1989**, *26*, 498–500. [CrossRef]

53. Baidoo, K.E.; Milenic, D.E.; Brechbiel, M.W. Methodology for Labeling Proteins and Peptides with Lead-212 ((212)Pb). *Nucl. Med. Biol.* **2013**, *40*, 592–599. [CrossRef]

54. Mirzadeh, S.; Kumar, K.; Gansow, O.A. The Chemical Fate of ^{212}Bi-DOTA Formed by β^- Decay of ^{212}Pb(DOTA)$^{2-}$. *Radiochem. Acta* **1993**, *60*, 1–10. [CrossRef]

55. Ruble, G.; Wu, C.; Squire, R.A.; Ganswo, O.A.; Strand, M. The use of 212Pb-labeled monoclonal antibody in the treatment of murine erythroleukemia. *Int. J. Radiat. Oncol. Biol. Phys.* **1996**, *34*, 609–616. [CrossRef]

56. Su, F.M.; Beaumier, P.; Axworthy, D.; Atcher, R.; Fritzberg, A. Pretargeted radioimmunotherapy in tumored mice using an in vivo 212Pb/212Bi generator. *Nucl. Med. Biol.* **2005**, *32*, 741–747. [CrossRef] [PubMed]

57. Fendler, W.P.; Cutler, C. More alpha Than beta for Prostate Cancer? *J. Nucl. Med.* **2017**, *58*, 1709–1710. [CrossRef] [PubMed]

58. Morgenstern, A.; Apostolidis, C.; Kratochwil, C.; Sathekge, M.; Krolicki, L.; Bruchertseifer, F. An Overview of Targeted Alpha Therapy with (225)Actinium and (213)Bismuth. *Curr. Radiopharm.* **2018**, *11*, 200–208. [CrossRef] [PubMed]

59. Kratochwil, C.; Bruchertseifer, F.; Giesel, F.L.; Weis, M.; Verburg, F.A.; Mottaghy, F.; Kopka, K.; Apostolidis, C.; Haberkorn, U.; Morgenstern, A. 225Ac-PSMA-617 for PSMA-Targeted alpha-Radiation Therapy of Metastatic Castration-Resistant Prostate Cancer. *J. Nucl. Med.* **2016**, *57*, 1941–1944. [CrossRef]

60. Kratochwil, C.; Bruchertseifer, F.; Rathke, H.; Bronzel, M.; Apostolidis, C.; Weichert, W.; Haberkorn, U.; Giesel, F.L.; Morgenstern, A. Targeted alpha-Therapy of Metastatic Castration-Resistant Prostate Cancer with (225)Ac-PSMA-617: Dosimetry Estimate and Empiric Dose Finding. *J. Nucl. Med.* **2017**, *58*, 1624–1631. [CrossRef]

61. Bauer, W.; Briner, U.; Doepfner, W.; Haller, R.; Huguenin, R.; Marbach, P.; Petcher, T.J.; Pless, J. SMS 201–995: A very potent and selective octapeptide analogue of somatostatin with prolonged action. *Life Sci.* **1982**, *31*, 1133–1140. [CrossRef]

62. Maack, T.; Johnson, V.; Kau, S.T.; Figueiredo, J.; Sigulem, D. Renal filtration, transport, and metabolism of low-molecular-weight proteins: A review. *Kidney Int.* **1979**, *16*, 251–270. [CrossRef]

63. Sabet, A.; Ezziddin, K.; Pape, U.-F.; Reichman, K.; Haslerud, T.; Ahmadzadehfar, H.; Biersack, H.-J.; Nagarajah, J.; Ezziddin, S. Accurate assessment of long-term nephrotoxicity after peptide receptor radionuclide therapy with 177Lu-octreotate. *Eur. J. Nucl. Med. Mol. Imaging* **2013**, *41*, 505–510. [CrossRef]

64. Norenberg, J.P.; Krenning, B.J.; Konings, I.R.; Kusewitt, D.F.; Nayak, T.K.; Anderson, T.L.; de Jong, M.; Garmestani, K.; Brechbiel, M.W.; Kvols, L.K. 213Bi-[DOTA0, Tyr3]octreotide peptide receptor radionuclide therapy of pancreatic tumors in a preclinical animal model. *Clin. Cancer Res.* **2006**, *12*, 897–903. [CrossRef]

65. Kratochwil, C.; Giesel, F.L.; Bruchertseifer, F.; Mier, W.; Apostolidis, C.; Boll, R.; Murphy, K.; Haberkorn, U.; Morgenstern, A. (213)Bi-DOTATOC receptor-targeted alpha-radionuclide therapy induces remission in neuroendocrine tumours refractory to beta radiation: A first-in-human experience. *Eur. J. Nucl. Med. Mol. Imaging* **2014**, *41*, 2106–2119. [CrossRef]

66. Chan, H.S.; Konijnenberg, M.W.; de Blois, E.; Koelewijn, S.; Baum, R.P.; Morgenstern, A.; Bruchertseifer, F.; Breeman, W.A.; de Jong, M. Influence of tumour size on the efficacy of targeted alpha therapy with (213)Bi-[DOTA(0),Tyr(3)]-octreotate. *EJNMMI Res.* **2016**, *6*, 6. [CrossRef] [PubMed]

67. Tafreshi, N.K.; Tichacek, C.J.; Pandya, D.N.; Doligalski, M.L.; Budzevich, M.M.; Kil, H.; Bhatt, N.B.; Kock, N.D.; Messina, J.L.; Ruiz, E.E.; et al. Melanocortin 1 Receptor-Targeted alpha-Particle Therapy for Metastatic Uveal Melanoma. *J. Nucl. Med.* **2019**, *60*, 1124–1133. [CrossRef] [PubMed]

68. Miao, Y.; Figueroa, S.D.; Fisher, D.R.; Moore, H.A.; Testa, R.F.; Hoffman, T.J.; Quinn, T.P. 203Pb-labeled alpha-melanocyte-stimulating hormone peptide as an imaging probe for melanoma detection. *J. Nucl. Med.* **2008**, *49*, 823–829. [CrossRef] [PubMed]

69. Li, M.; Liu, D.; Lee, D.; Kapoor, S.; Gibson-Corley, K.N.; Quinn, T.P.; Sagastume, E.A.; Mott, S.L.; Walsh, S.A.; Acevedo, M.R.; et al. Enhancing the Efficacy of Melanocortin 1 Receptor-Targeted Radiotherapy by Pharmacologically Upregulating the Receptor in Metastatic Melanoma. *Mol. Pharm.* **2019**. [CrossRef]

70. Chang, M.-Y.; Seideman, J.; Sofou, S. Enhanced Loading Efficiency and Retention of 225Ac in Rigid Liposomes for Potential Targeted Therapy of Micrometastases. *Bioconjug. Chem.* **2008**, *19*, 1274–1282. [CrossRef]

71. Woodward, J.; Kennel, S.J.; Stuckey, A.; Osborne, D.; Wall, J.; Rondinone, A.J.; Standaert, R.F.; Mirzadeh, S. LaPO4 Nanoparticles Doped with Actinium-225 that Partially Sequester Daughter Radionuclides. *Bioconjug. Chem.* **2011**, *22*, 766–776. [CrossRef]

72. Zhu, C.; Bandekar, A.; Sempkowski, M.; Banerjee, S.R.; Pomper, M.G.; Bruchertseifer, F.; Morgenstern, A.; Sofou, S. Nanoconjugation of PSMA-Targeting Ligands Enhances Perinuclear Localization and Improves Efficacy of Delivered Alpha-Particle Emitters against Tumor Endothelial Analogues. *Mol. Cancer Ther.* **2016**, *15*, 106–113. [CrossRef]

73. Ballangrud, A.M.; Yang, W.H.; Palm, S.; Enmon, R.; Borchardt, P.E.; Pellegrini, V.A.; McDevitt, M.R.; Scheinberg, D.A.; Sgouros, G. Alpha-particle emitting atomic generator (Actinium-225)-labeled trastuzumab (herceptin) targeting of breast cancer spheroids: Efficacy versus HER2/neu expression. *Clin. Cancer Res.* **2004**, *10*, 4489–4497. [CrossRef]

74. Jaggi, J.S.; Seshan, S.V.; McDevitt, M.R.; LaPerle, K.; Sgouros, G.; Scheinberg, D.A. Renal Tubulointerstitial Changes after Internal Irradiation with α-Particle–Emitting Actinium Daughters. *J. Am. Soc. Nephrol.* **2005**, *16*, 2677–2689. [CrossRef]

75. Singh Jaggi, J.; Kappel, B.J.; McDevitt, M.R.; Sgouros, G.; Flombaum, C.D.; Cabassa, C.; Scheinberg, D.A. Efforts to Control the Errant Products of a Targeted In vivo Generator. *Cancer Res.* **2005**, *65*, 4888–4895. [CrossRef]

76. Orozco, J.J.; Bäck, T.; Kenoyer, A.; Balkin, E.R.; Hamlin, D.K.; Wilbur, D.S.; Fisher, D.R.; Frayo, S.L.; Hylarides, M.D.; Green, D.J.; et al. Anti-CD45 radioimmunotherapy using (211)At with bone marrow transplantation prolongs survival in a disseminated murine leukemia model. *Blood* **2013**, *121*, 3759–3767. [CrossRef]

77. Green, D.J.; Shadman, M.; Jones, J.C.; Frayo, S.L.; Kenoyer, A.L.; Hylarides, M.D.; Hamlin, D.K.; Wilbur, D.S.; Balkan, E.R.; Lin, Y.; et al. Astatine-211 conjugated to an anti-CD20 monoclonal antibody eradicates disseminated B-cell lymphoma in a mouse model. *Blood* **2015**, *125*, 2111–2119. [CrossRef]

78. Yokota, T.; Milenic, D.E.; Whitlow, M.; Schlom, J. Rapid Tumor Penetration of a Single-Chain Fv and Comparison with Other Immunoglobulin Forms. *Cancer Res.* **1992**, *52*, 3402–3408.

79. Hudson, P.J.; Souriau, C. Engineered antibodies. *Nat. Med.* **2003**, *9*, 129–134. [CrossRef]

80. Steffen, A.C.; Almqvist, Y.; Chyan, M.K.; Lundqvist, H.; Tolmachev, V.; Wilbur, D.S.; Carlsson, J. Biodistribution of 211At labeled HER-2 binding affibody molecules in mice. *Oncol. Rep.* **2007**, *17*, 1141–1147. [CrossRef]

81. D'Huyvetter, M.; Xavier, C.; Caveliers, V.; Lahoutte, T.; Muyldermans, S.; Devoogdt, N. Radiolabeled nanobodies as theranostic tools in targeted radionuclide therapy of cancer. *Expert. Opin. Drug Deliv.* **2014**, *11*, 1939–1954. [CrossRef]

82. Jadvar, H.; Challa, S.; Quinn, D.I.; Conti, P.S. One-Year Postapproval Clinical Experience with Radium-223 Dichloride in Patients with Metastatic Castrate-Resistant Prostate Cancer. *Cancer Biother. Radiopharm.* **2015**, *30*, 195–199. [CrossRef]

83. Takalkar, A.; Adams, S.; Subbiah, V. Radium-223 dichloride bone-targeted alpha particle therapy for hormone-refractory breast cancer metastatic to bone. *Exp. Hematol. Oncol.* **2014**, *3*, 1–7. [CrossRef]

84. Kozempel, J.; Vlk, M.; Málková, E.; Bajzíková, A.; Bárta, J.; Santos-Oliveira, R.; Malta Rossi, A. Prospective carriers of 223Ra for targeted alpha particle therapy. *J. Radioanal. Nucl. Chem.* **2014**, *304*, 443–447. [CrossRef]

85. Schwartz, J.; Jaggi, J.S.; O'Donoghue, J.A.; Ruan, S.; McDevitt, M.; Larson, S.M.; Scheinberg, D.A.; Humm, J.L. Renal uptake of bismuth-213 and its contribution to kidney radiation dose following administration of actinium-225-labeled antibody. *Phys. Med. Biol.* **2011**, *56*, 721–733. [CrossRef]

86. McLaughlin, M.F.; Woodward, J.; Boll, R.A.; Wall, J.S.; Rondinone, A.J.; Kennel, S.J.; Mirzadeh, S.; Robertson, J.D. Gold Coated Lanthanide Phosphate Nanoparticles for Targeted Alpha Generator Radiotherapy. *PLoS ONE* **2013**, *8*, e54531. [CrossRef]

87. Harrison, M.R.; Wong, T.Z.; Armstrong, A.J.; George, D.J. Radium-223 chloride: A potential new treatment for castration-resistant prostate cancer patients with metastatic bone disease. *Cancer Manag. Res.* **2013**, *5*, 1–14. [CrossRef]

88. Wilbur, D.S. Chemical and radiochemical considerations in radiolabeling with alpha-emitting radionuclides. *Curr. Radiopharm.* **2011**, *4*, 214–247. [CrossRef]

89. de Kruijff, R.M.; Wolterbeek, H.T.; Denkova, A.G. A Critical Review of Alpha Radionuclide Therapy-How to Deal with Recoiling Daughters? *Pharmaceuticals (Basel)* **2015**, *8*, 321–336. [CrossRef]

90. Zalutsky, M.R.; Reardon, D.A.; Pozzi, O.R.; Vaidyanathan, G.; Bigner, D.D. Targeted alpha-particle radiotherapy with 211At-labeled monoclonal antibodies. *Nucl. Med. Biol.* **2007**, *34*, 779–785. [CrossRef]

91. Hassfjell, S.; Brechbiel, M.W. The development of the alpha-particle emitting radionuclides 212Bi and 213Bi, and their decay chain related radionuclides, for therapeutic applications. *Chem. Rev.* **2001**, *101*, 2019–2036. [CrossRef]

92. Morgenstern, A.; Bruchertseifer, F.; Apostolidis, C. Targeted alpha therapy with 213Bi. *Curr. Radiopharm.* **2011**, *4*, 295–305. [CrossRef]

93. Raes, F. Description of the properties of unattached 218Po and 212Pb particles by means of the classical theory of cluster formation. *Health Phys.* **1985**, *49*, 1177–1187. [CrossRef]

94. Yong, K.; Brechbiel, M. Application of Pb for Targeted alpha-particle Therapy (TAT): Pre-clinical and Mechanistic Understanding through to Clinical Translation. *AIMS Med. Sci.* **2015**, *2*, 228–245. [CrossRef]

95. Gott, M.; Steinbach, J.; Mamat, C. The Radiochemical and Radiopharmaceutical Applications of Radium. *Open Chem.* **2016**, *14*, 118–129. [CrossRef]

96. Scheinberg, D.A.; McDevitt, M.R. Actinium-225 in targeted alpha-particle therapeutic applications. *Curr. Radiopharm.* **2011**, *4*, 306–320. [CrossRef]

97. Moss, L.; Edelstein, N.; Fuger, J. Actinium. In *The Chemistry of the Actinide and TRANSACTINIDE Elements*; Springer: Amsterdam, The Netherlands, 2006; pp. 18–51. [CrossRef]

98. Diamond, R.; Street Jr, K.; Seaborg, G. An ion-exchange study of possible hybridized 5f bonding in the actinides. *J. Am. Chem. Soc.* **1954**, *76*, 1461–1469. [CrossRef]

99. *Summary and Comparison of the Properties of the Actinide and Transactinide Elements*; Moss, L.; Edelstein, N.; Fuger, J. (Eds.) Springer: Amsterdam, The Netherlands, 2006; pp. 1753–1835.

100. Gorden, A.E.; DeVore, M.A., 2nd; Maynard, B.A. Coordination chemistry with f-element complexes for an improved understanding of factors that contribute to extraction selectivity. *Inorg. Chem.* **2013**, *52*, 3445–3458. [CrossRef]

101. Chappell, L.L.; Ma, D.; Milenic, D.E.; Garmestani, K.; Venditto, V.; Beitzel, M.P.; Brechbiel, M.W. Synthesis and evaluation of novel bifunctional chelating agents based on 1,4,7,10-tetraazacyclododecane-*N,N′,N″,N‴*-tetraacetic acid for radiolabeling proteins. *Nucl. Med. Biol.* **2003**, *30*, 581–595. [CrossRef]

102. Chappell, L.L.; Deal, K.A.; Dadachova, E.; Brechbiel, M.W. Synthesis, conjugation, and radiolabeling of a novel bifunctional chelating agent for (225)Ac radioimmunotherapy applications. *Bioconjug. Chem.* **2000**, *11*, 510–519. [CrossRef]

103. Davis, I.A.; Glowienka, K.A.; Boll, R.A.; Deal, K.A.; Brechbiel, M.W.; Stabin, M.; Bochsler, P.N.; Mirzadeh, S.; Kennel, S.J. Comparison of 225actinium chelates: Tissue distribution and radiotoxicity. *Nucl. Med. Biol.* **1999**, *26*, 581–589. [CrossRef]

104. McDevitt, M.R.; Ma, D.; Simon, J.; Frank, R.K.; Scheinberg, D.A. Design and synthesis of 225Ac radioimmunopharmaceuticals. *Appl. Radiat. Isot.* **2002**, *57*, 841–847. [CrossRef]

105. Gouin, S.G.; Gestin, J.F.; Monrandeau, L.; Segat-Dioury, F.; Meslin, J.C.; Deniaud, D. Synthesis and metal complexation properties of Ph-DTPA and Ph-TTHA: Novel radionuclide chelating agents for use in nuclear medicine. *Org. Biomol. Chem.* **2005**, *3*, 454–461. [CrossRef]

106. Thiele, N.A.; Brown, V.; Kelly, J.M.; Amor-Coarasa, A.; Jermilova, U.; MacMillan, S.N.; Nikolopoulou, A.; Ponnala, S.; Ramogida, C.F.; Robertson, A.K.H.; et al. An Eighteen-Membered Macrocyclic Ligand for Actinium-225 Targeted Alpha Therapy. *Angew. Chem. Int. Ed. Engl.* **2017**, *56*, 14712–14717. [CrossRef]

107. Escorcia, F.E.; Henke, E.; McDevitt, M.R.; Villa, C.H.; Smith-Jones, P.; Blasberg, R.G.; Benezra, R.; Scheinberg, D.A. Selective killing of tumor neovasculature paradoxically improves chemotherapy delivery to tumors. *Cancer Res.* **2010**, *70*, 9277–9286. [CrossRef]

108. Maguire, W.F.; McDevitt, M.R.; Smith-Jones, P.M.; Scheinberg, D.A. Efficient 1-step radiolabeling of monoclonal antibodies to high specific activity with 225Ac for alpha-particle radioimmunotherapy of cancer. *J. Nucl. Med.* **2014**, *55*, 1492–1498. [CrossRef]

109. Poty, S.; Membreno, R.; Glaser, J.M.; Ragupathi, A.; Scholz, W.W.; Zeglis, B.M.; Lewis, J.S. The inverse electron-demand Diels-Alder reaction as a new methodology for the synthesis of (225)Ac-labelled radioimmunoconjugates. *Chem. Commun. (Camb)* **2018**, *54*, 2599–2602. [CrossRef]

110. Sofou, S.; Kappel, B.J.; Jaggi, J.S.; McDevitt, M.R.; Scheinberg, D.A.; Sgouros, G. Enhanced retention of the alpha-particle-emitting daughters of Actinium-225 by liposome carriers. *Bioconjug. Chem.* **2007**, *18*, 2061–2067. [CrossRef]

111. Sofou, S.; Thomas, J.L.; Lin, H.Y.; McDevitt, M.R.; Scheinberg, D.A.; Sgouros, G. Engineered liposomes for potential alpha-particle therapy of metastatic cancer. *J. Nucl. Med.* **2004**, *45*, 253–260.

112. Matson, M.L.; Villa, C.H.; Ananta, J.S.; Law, J.J.; Scheinberg, D.A.; Wilson, L.J. Encapsulation of alpha-Particle-Emitting 225Ac3+ Ions Within Carbon Nanotubes. *J. Nucl. Med.* **2015**, *56*, 897–900. [CrossRef]

113. McDevitt, M.R.; Chattopadhyay, D.; Kappel, B.J.; Jaggi, J.S.; Schiffman, S.R.; Antczak, C.; Njardarson, J.T.; Brentjens, R.; Scheinberg, D.A. Tumor targeting with antibody-functionalized, radiolabeled carbon nanotubes. *J. Nucl. Med.* **2007**, *48*, 1180–1189. [CrossRef]

114. Mulvey, J.J.; Villa, C.H.; McDevitt, M.R.; Escorcia, F.E.; Casey, E.; Scheinberg, D.A. Self-assembly of carbon nanotubes and antibodies on tumours for targeted amplified delivery. *Nat. Nanotechnol.* **2013**, *8*, 763–771. [CrossRef]

115. Ruggiero, A.; Villa, C.H.; Holland, J.P.; Sprinkle, S.R.; May, C.; Lewis, J.S.; Scheinberg, D.A.; McDevitt, M.R. Imaging and treating tumor vasculature with targeted radiolabeled carbon nanotubes. *Int. J. Nanomed.* **2010**, *5*, 783–802. [CrossRef]

116. Gouard, S.; Pallardy, A.; Gaschet, J.; Faivre-Chauvet, A.; Bruchertseifer, F.; Morgenstern, A.; Maurel, C.; Matous, E.; Kraeber-Bodere, F.; Davodeau, F.; et al. Comparative analysis of multiple myeloma treatment by CD138 antigen targeting with bismuth-213 and Melphalan chemotherapy. *Nucl. Med. Biol.* **2014**, *41*, e30–e35. [CrossRef]

117. Hermanson, G.T. *Bioconjugate Techniques*, 3rd ed.; Hermanson, G.T., Ed.; Academic Press: Cambridge, MA, USA, 2013.

118. Tavaré, R.; Wu, W.H.; Zettlitz, K.A.; Salazar, F.B.; McCabe, K.E.; Marks, J.D.; Wu, A.M. Enhanced immunoPET of ALCAM-positive colorectal carcinoma using site-specific 64Cu-DOTA conjugation. *Protein Eng. Des. Sel.* **2014**, *27*, 317–324. [CrossRef]

119. Li, L.; Olafsen, T.; Anderson, A.-L.; Wu, A.; Raubitschek, A.A.; Shively, J.E. Reduction of Kidney Uptake in Radiometal Labeled Peptide Linkers Conjugated to Recombinant Antibody Fragments. Site-Specific Conjugation of DOTA-Peptides to a Cys-Diabody. *Bioconjug. Chem.* **2002**, *13*, 985–995. [CrossRef]

120. Akizawa, H.; Imajima, M.; Hanaoka, H.; Uehara, T.; Satake, S.; Arano, Y. Renal Brush Border Enzyme-Cleavable Linkages for Low Renal Radioactivity Levels of Radiolabeled Antibody Fragments. *Bioconjug. Chem.* **2013**, *24*, 291–299. [CrossRef]

121. Loevinger, R.; Budinger, T.F.; Watson, E.E. *MIRD Primer for Absorbed Dose Calculations, Revised Edition*; The Society of Nuclear Medicine, Inc: New York, NY, USA, 1991.

122. Kellerer, A.M.; Chmelevsky, D. Criteria for the applicability of LET. *Radiat. Res.* **1975**, *63*, 226–234. [CrossRef]

123. Fisher, K.J.; Jooss, K.; Alston, J.; Yang, Y.; Haecker, S.E.; High, K.; Pathak, R.; Raper, S.E.; Wilson, J.M. Recombinant adeno-associated virus for muscle directed gene therapy. *Nat. Med.* **1997**, *3*, 306–312. [CrossRef]

124. Zubal, I.G.; Harrell, C.R.; Smith, E.O.; Rattner, Z.; Gindi, G.; Hoffer, P.B. Computerized three-dimensional segmented human anatomy. *Med. Phys.* **1994**, *21*, 299–302. [CrossRef]

125. Bolch, W.E.; Bouchet, L.G.; Robertson, J.S.; Wessels, B.W.; Siegel, J.A.; Howell, R.W.; Erdi, A.K.; Aydogan, B.; Costes, S.; Watson, E.E.; et al. MIRD pamphlet No. 17: The dosimetry of nonuniform activity distributions–radionuclide S values at the voxel level. Medical Internal Radiation Dose Committee. *J. Nucl. Med.* **1999**, *40*, 11S–36S.

126. Stabin, M.G.; Sparks, R.B.; Crowe, E. OLINDA/EXM: The second-generation personal computer software for internal dose assessment in nuclear medicine. *J. Nucl. Med.* **2005**, *46*, 1023–1027.

127. Sgouros, G.; Frey, E.; Wahl, R.; He, B.; Prideaux, A.; Hobbs, R. Three-dimensional imaging-based radiobiological dosimetry. *Semin. Nucl. Med.* **2008**, *38*, 321–334. [CrossRef]

128. Gil, A.V.; Pérez, M.C.; Aroche, L.T.; Pacilio, M.; Botta, F.; Cremonesi, M. MCID: A personalized dosimetric tool associating voxel-based models with MCNP5. In Proceedings of the IAEA International Conference on Radiation Protection in Medicine, Setting the Scene for the Next Decade, Bonn, Germany, 3–7 December 2012.

129. Chiavassa, S.; Bardies, M.; Guiraud-Vitaux, F.; Bruel, D.; Jourdain, J.R.; Franck, D.; Aubineau-Laniece, I. OEDIPE: A personalized dosimetric tool associating voxel-based models with MCNPX. *Cancer Biother. Radiopharm.* **2005**, *20*, 325–332. [CrossRef]

130. Yoriyaz, H.; Stabin, M.G.; dos Santos, A. Monte Carlo MCNP-4B-based absorbed dose distribution estimates for patient-specific dosimetry. *J. Nucl. Med.* **2001**, *42*, 662–669.

131. Prideaux, A.R.; Song, H.; Hobbs, R.F.; He, B.; Frey, E.C.; Ladenson, P.W.; Wahl, R.L.; Sgouros, G. Three-dimensional radiobiologic dosimetry: Application of radiobiologic modeling to patient-specific 3-dimensional imaging-based internal dosimetry. *J. Nucl. Med.* **2007**, *48*, 1008–1016. [CrossRef]

132. Liu, X.; Ljungberg, M.; Strand, S.E. DOSIMG: A 3D voxel-based Monte Carlo program for absorbed dose calculations. *J. Nucl. Med.* **2001**, *42*, 243P.

133. Nelson, W.R.; Hirayama, H.; Rogers, D.W.O. *The EGS4 Code System*; National Technical Information Service, U.S. Department of Commerce: Springfield, VA, USA; Stanford University Linear Accelerator Center: Stanford, CA, USA, 1985.

134. Marcatili, S.; Pettinato, C.; Daniels, S.; Lewis, G.; Edwards, P.; Fanti, S.; Spezi, E. Development and validation of RAYDOSE: A Geant4-based application for molecular radiotherapy. *Phys. Med. Biol.* **2013**, *58*, 2491–2508. [CrossRef]

135. Besemer, A.E.; Yang, Y.M.; Grudzinski, J.J.; Hall, L.T.; Bednarz, B.P. Development and Validation of RAPID: A Patient-Specific Monte Carlo Three-Dimensional Internal Dosimetry Platform. *Cancer Biother. Radiopharm.* **2018**, *33*, 155–165. [CrossRef]

136. Agostinelli, S.; Allison, J.; Amako, K.; Apostolakis, J.; Araujo, H.; Arce, P.; Asai, M.; Axen, D.; Banerjee, S.; Barrand, G.; et al. GEANT4-a simulation toolkit. *Nucl. Instrum. Methods Phys. Res. Sect. A Accel. Spectrometers Detect. Assoc. Equip.* **2003**, *506*, 250–303. [CrossRef]

137. Sempau, J.; Wilderman, S.J.; Bielajew, A.F. DPM, a fast, accurate Monte Carlo code optimized for photon and electron radiotherapy treatment planning dose calculations. *Phys. Med. Biol.* **2000**, *45*, 2263–2291. [CrossRef]

138. Miller, B.W.; Gregory, S.J.; Fuller, E.S.; Barrett, H.H.; Barber, B.; Furenlid, L.R. The iQID camera: An ionizing-radiation quantum imaging detector. *Nucl. Instrum. Methods Phys. Res. Sect. A Accel. Spectrometers Detect. Assoc. Equip.* **2014**, *767*, 146–152. [CrossRef]

139. Back, T.; Jacobsson, L. The alpha-camera: A quantitative digital autoradiography technique using a charge-coupled device for ex vivo high-resolution bioimaging of alpha-particles. *J. Nucl. Med.* **2010**, *51*, 1616–1623. [CrossRef]

140. Demartis, S.; Tarli, L.; Borsi, L.; Zardi, L.; Neri, D. Selective targeting of tumour neovasculature by a radiohalogenated human antibody fragment specific for the ED-B domain of fibronectin. *Eur. J. Nucl. Med.* **2001**, *28*, 534–539. [CrossRef]

141. Park, S.I.; Shenoi, J.; Pagel, J.M.; Hamlin, D.K.; Wilbur, D.S.; Orgun, N.; Kenoyer, A.L.; Frayo, S.; Axtman, A.; Back, T.; et al. Conventional and pretargeted radioimmunotherapy using bismuth-213 to target and treat non-Hodgkin lymphomas expressing CD20: A preclinical model toward optimal consolidation therapy to eradicate minimal residual disease. *Blood* **2010**, *116*, 4231–4239. [CrossRef]

142. Robinson, M.K.; Shaller, C.; Garmestani, K.; Plascjak, P.S.; Hodge, K.M.; Yuan, Q.A.; Marks, J.D.; Waldmann, T.A.; Brechbiel, M.W.; Adams, G.P. Effective treatment of established human breast tumor xenografts in immunodeficient mice with a single dose of the alpha-emitting radioisotope astatine-211 conjugated to anti-HER2/neu diabodies. *Clin. Cancer Res.* **2008**, *14*, 875–882. [CrossRef] [PubMed]

143. Zhang, M.; Yao, Z.; Garmestani, K.; Axworthy, D.B.; Zhang, Z.; Mallett, R.W.; Theodore, L.J.; Goldman, C.K.; Brechbiel, M.W.; Carrasquillo, J.A.; et al. Pretargeting radioimmunotherapy of a murine model of adult T-cell leukemia with the alpha-emitting radionuclide, bismuth 213. *Blood* **2002**, *100*, 208–216. [CrossRef] [PubMed]

144. Poty, S.; Carter, L.M.; Mandleywala, K.; Membreno, R.; Abdel-Atti, D.; Ragupathi, A.; Scholz, W.W.; Zeglis, B.M.; Lewis, J.S. Leveraging Bioorthogonal Click Chemistry to Improve (225)Ac-Radioimmunotherapy of Pancreatic Ductal Adenocarcinoma. *Clin. Cancer Res.* **2019**, *25*, 868–880. [CrossRef]

145. Li, Y.; Song, E.; Abbas Rizvi, S.M.; Power, C.A.; Beretov, J.; Raja, C.; Cozzi, P.J.; Morgenstern, A.; Apostolidis, C.; Allen, B.J.; et al. Inhibition of micrometastatic prostate cancer cell spread in animal models by 213Bilabeled multiple targeted alpha radioimmunoconjugates. *Clin. Cancer Res.* **2009**, *15*, 865–875. [CrossRef]

146. Makvandi, M.; Lieberman, B.P.; LeGeyt, B.; Hou, C.; Mankoff, D.A.; Mach, R.H.; Pryma, D.A. The pre-clinical characterization of an alpha-emitting sigma-2 receptor targeted radiotherapeutic. *Nucl. Med. Biol.* **2016**, *43*, 35–41. [CrossRef]

147. Willhauck, M.J.; Samani, B.R.; Wolf, I.; Senekowitsch-Schmidtke, R.; Stark, H.J.; Meyer, G.J.; Knapp, W.H.; Goke, B.; Morris, J.C.; Spitzweg, C. The potential of 211Astatine for NIS-mediated radionuclide therapy in prostate cancer. *Eur. J. Nucl. Med. Mol. Imaging* **2008**, *35*, 1272–1281. [CrossRef]

148. Borchardt, P.E.; Yuan, R.R.; Miederer, M.; McDevitt, M.R.; Scheinberg, D.A. Targeted actinium-225 in vivo generators for therapy of ovarian cancer. *Cancer Res.* **2003**, *63*, 5084–5090.

149. Miederer, M.; McDevitt, M.R.; Sgouros, G.; Kramer, K.; Cheung, N.K.; Scheinberg, D.A. Pharmacokinetics, dosimetry, and toxicity of the targetable atomic generator, 225Ac-HuM195, in nonhuman primates. *J. Nucl. Med.* **2004**, *45*, 129–137.

150. Miederer, M.; McDevitt, M.R.; Borchardt, P.; Bergman, I.; Kramer, K.; Cheung, N.K.; Scheinberg, D.A. Treatment of neuroblastoma meningeal carcinomatosis with intrathecal application of alpha-emitting atomic nanogenerators targeting disialo-ganglioside GD2. *Clin. Cancer Res.* **2004**, *10*, 6985–6992. [CrossRef]

151. Miederer, M.; Henriksen, G.; Alke, A.; Mossbrugger, I.; Quintanilla-Martinez, L.; Senekowitsch-Schmidtke, R.; Essler, M. Preclinical evaluation of the alpha-particle generator nuclide 225Ac for somatostatin receptor radiotherapy of neuroendocrine tumors. *Clin. Cancer Res.* **2008**, *14*, 3555–3561. [CrossRef]

152. Song, H.; Hobbs, R.F.; Vajravelu, R.; Huso, D.L.; Esaias, C.; Apostolidis, C.; Morgenstern, A.; Sgouros, G. Radioimmunotherapy of breast cancer metastases with alpha-particle emitter 225Ac: Comparing efficacy with 213Bi and 90Y. *Cancer Res.* **2009**, *69*, 8941–8948. [CrossRef]

153. Essler, M.; Gartner, F.C.; Neff, F.; Blechert, B.; Senekowitsch-Schmidtke, R.; Bruchertseifer, F.; Morgenstern, A.; Seidl, C. Therapeutic efficacy and toxicity of 225Ac-labelled vs. 213Bi-labelled tumour-homing peptides in a preclinical mouse model of peritoneal carcinomatosis. *Eur. J. Nucl. Med. Mol. Imaging* **2012**, *39*, 602–612. [CrossRef]

154. Drecoll, E.; Gaertner, F.C.; Miederer, M.; Blechert, B.; Vallon, M.; Muller, J.M.; Alke, A.; Seidl, C.; Bruchertseifer, F.; Morgenstern, A.; et al. Treatment of peritoneal carcinomatosis by targeted delivery of the radio-labeled tumor homing peptide bi-DTPA-[F3]2 into the nucleus of tumor cells. *PLoS ONE* **2009**, *4*, e5715. [CrossRef]

155. Sattiraju, A.; Solingapuram Sai, K.K.; Xuan, A.; Pandya, D.N.; Almaguel, F.G.; Wadas, T.J.; Herpai, D.M.; Debinski, W.; Mintz, A. IL13RA2 targeted alpha particle therapy against glioblastomas. *Oncotarget* **2017**, *8*, 42997–43007. [CrossRef]

156. Sattiraju, A.; Xiong, X.; Pandya, D.N.; Wadas, T.J.; Xuan, A.; Sun, Y.; Jung, Y.; Sai, K.K.S.; Dorsey, J.F.; Li, K.C.; et al. Alpha Particle Enhanced Blood Brain/Tumor Barrier Permeabilization in Glioblastomas Using Integrin Alpha-v Beta-3-Targeted Liposomes. *Mol. Cancer* **2017**, *16*, 2191–2200. [CrossRef]

157. McLaughlin, M.F.; Robertson, D.; Pevsner, P.H.; Wall, J.S.; Mirzadeh, S.; Kennel, S.J. LnPO4 nanoparticles doped with Ac-225 and sequestered daughters for targeted alpha therapy. *Cancer Biother. Radiopharm.* **2014**, *29*, 34–41. [CrossRef]

158. Nedrow, J.R.; Josefsson, A.; Park, S.; Back, T.; Hobbs, R.F.; Brayton, C.; Bruchertseifer, F.; Morgenstern, A.; Sgouros, G. Pharmacokinetics, microscale distribution, and dosimetry of alpha-emitter-labeled anti-PD-L1 antibodies in an immune competent transgenic breast cancer model. *EJNMMI Res.* **2017**, *7*, 57. [CrossRef]

159. Pfannkuchen, N.; Bausbacher, N.; Pektor, S.; Miederer, M.; Rosch, F. In vivo Evaluation of [(225)Ac]Ac-DOTA(ZOL) for alpha-Therapy of Bone Metastases. *Curr. Radiopharm.* **2018**, *11*, 223–230. [CrossRef]

160. Kelly, J.M.; Amor-Coarasa, A.; Ponnala, S.; Nikolopoulou, A.; Williams, C., Jr.; Thiele, N.A.; Schlyer, D.; Wilson, J.J.; DiMagno, S.G.; Babich, J.W. A Single Dose of (225)Ac-RPS-074 Induces a Complete Tumor Response in a LNCaP Xenograft Model. *J. Nucl. Med.* **2018**. [CrossRef]

161. Zalutsky, M.R.; McLendon, R.E.; Garg, P.K.; Archer, G.E.; Schuster, J.M.; Bigner, D.D. Radioimmunotherapy of neoplastic meningitis in rats using an alpha-particle-emitting immunoconjugate. *Cancer Res.* **1994**, *54*, 4719–4725.

162. Zalutsky, M.R.; Stabin, M.G.; Larsen, R.H.; Bigner, D.D. Tissue distribution and radiation dosimetry of astatine-211-labeled chimeric 81C6, an alpha-particle-emitting immunoconjugate. *Nucl. Med. Biol.* **1997**, *24*, 255–261. [CrossRef]

163. Andersson, H.; Elgqvist, J.; Horvath, G.; Hultborn, R.; Jacobsson, L.; Jensen, H.; Karlsson, B.; Lindegren, S.; Palm, S. Astatine-211-labeled antibodies for treatment of disseminated ovarian cancer: An overview of results in an ovarian tumor model. *Clin. Cancer Res.* **2003**, *9*, 3914S–3921S. [PubMed]

164. Andersson, H.; Lindegren, S.; Back, T.; Jacobsson, L.; Leser, G.; Horvath, G. Radioimmunotherapy of nude mice with intraperitoneally growing ovarian cancer xenograft utilizing 211At-labelled monoclonal antibody MOv18. *Anticancer Res.* **2000**, *20*, 459–462. [PubMed]

165. Andersson, H.; Lindegren, S.; Back, T.; Jacobsson, L.; Leser, G.; Horvath, G. The curative and palliative potential of the monoclonal antibody MOv18 labelled with 211At in nude mice with intraperitoneally growing ovarian cancer xenografts–a long-term study. *Acta Oncol.* **2000**, *39*, 741–745. [CrossRef]

166. Andersson, H.; Palm, S.; Lindegren, S.; Back, T.; Jacobsson, L.; Leser, G.; Horvath, G. Comparison of the therapeutic efficacy of 211At- and 131I-labelled monoclonal antibody MOv18 in nude mice with intraperitoneal growth of human ovarian cancer. *Anticancer Res.* **2001**, *21*, 409–412.

167. Elgqvist, J.; Andersson, H.; Jensen, H.; Kahu, H.; Lindegren, S.; Warnhammar, E.; Hultborn, R. Repeated Intraperitoneal alpha-Radioimmunotherapy of Ovarian Cancer in Mice. *J. Oncol.* **2010**, *2010*, 394913. [CrossRef]

168. Elgqvist, J.; Bernhardt, P.; Hultborn, R.; Jensen, H.; Karlsson, B.; Lindegren, S.; Warnhammar, E.; Jacobsson, L. Myelotoxicity and RBE of 211At-conjugated monoclonal antibodies compared with 99mTc-conjugated monoclonal antibodies and 60Co irradiation in nude mice. *J. Nucl. Med.* **2005**, *46*, 464–471.

169. Zhang, M.; Yao, Z.; Patel, H.; Garmestani, K.; Zhang, Z.; Talanov, V.S.; Plascjak, P.S.; Goldman, C.K.; Janik, J.E.; Brechbiel, M.W.; et al. Effective therapy of murine models of human leukemia and lymphoma with radiolabeled anti-CD30 antibody, HeFi-1. *Proc. Natl. Acad. Sci. USA* **2007**, *104*, 8444–8448. [CrossRef]

170. Cheng, J.; Ekberg, T.; Engstrom, M.; Nestor, M.; Jensen, H.J.; Tolmachev, V.; Anniko, M. Radioimmunotherapy with astatine-211 using chimeric monoclonal antibody U36 in head and neck squamous cell carcinoma. *Laryngoscope* **2007**, *117*, 1013–1018. [CrossRef]

171. Nakamae, H.; Wilbur, D.S.; Hamlin, D.K.; Thakar, M.S.; Santos, E.B.; Fisher, D.R.; Kenoyer, A.L.; Pagel, J.M.; Press, O.W.; Storb, R.; et al. Biodistributions, myelosuppression, and toxicities in mice treated with an anti-CD45 antibody labeled with the alpha-emitting radionuclides bismuth-213 or astatine-211. *Cancer Res.* **2009**, *69*, 2408–2415. [CrossRef]

172. Palm, S.; Back, T.; Claesson, I.; Danielsson, A.; Elgqvist, J.; Frost, S.; Hultborn, R.; Jensen, H.; Lindegren, S.; Jacobsson, L. Therapeutic efficacy of astatine-211-labeled trastuzumab on radioresistant SKOV-3 tumors in nude mice. *Int. J. Radiat. Oncol. Biol. Phys.* **2007**, *69*, 572–579. [CrossRef] [PubMed]

173. Eriksson, S.E.; Back, T.; Elgstrom, E.; Jensen, H.; Nilsson, R.; Lindegren, S.; Tennvall, J. Successful radioimmunotherapy of established syngeneic rat colon carcinoma with 211At-mAb. *EJNMMI Res.* **2013**, *3*, 23. [CrossRef] [PubMed]

174. Ohshima, Y.; Sudo, H.; Watanabe, S.; Nagatsu, K.; Tsuji, A.B.; Sakashita, T.; Ito, Y.M.; Yoshinaga, K.; Higashi, T.; Ishioka, N.S. Antitumor effects of radionuclide treatment using alpha-emitting meta-(211)At-astato-benzylguanidine in a PC12 pheochromocytoma model. *Eur. J. Nucl. Med. Mol. Imaging* **2018**, *45*, 999–1010. [CrossRef] [PubMed]

175. Li, H.K.; Hasegawa, S.; Nakajima, N.I.; Morokoshi, Y.; Minegishi, K.; Nagatsu, K. Targeted cancer cell ablation in mice by an alpha-particle-emitting astatine-211-labeled antibody against major histocompatibility complex class I chain-related protein A and B. *Biochem. Biophys. Res. Commun.* **2018**, *506*, 1078–1084. [CrossRef] [PubMed]

176. Behr, T.M.; Behe, M.; Stabin, M.G.; Wehrmann, E.; Apostolidis, C.; Molinet, R.; Strutz, F.; Fayyazi, A.; Wieland, E.; Gratz, S.; et al. High-linear energy transfer (LET) alpha versus low-LET beta emitters in radioimmunotherapy of solid tumors: Therapeutic efficacy and dose-limiting toxicity of 213Bi- versus 90Y-labeled CO17-1A Fab' fragments in a human colonic cancer model. *Cancer Res.* **1999**, *59*, 2635–2643.

177. Huneke, R.B.; Pippin, C.G.; Squire, R.A.; Brechbiel, M.W.; Gansow, O.A.; Strand, M. Effective alpha-particle-mediated radioimmunotherapy of murine leukemia. *Cancer Res.* **1992**, *52*, 5818–5820. [PubMed]

178. Hartmann, F.; Horak, E.M.; Garmestani, K.; Wu, C.; Brechbiel, M.W.; Kozak, R.W.; Tso, J.; Kosteiny, S.A.; Gansow, O.A.; Nelson, D.L.; et al. Radioimmunotherapy of nude mice bearing a human interleukin 2 receptor alpha-expressing lymphoma utilizing the alpha-emitting radionuclide-conjugated monoclonal antibody 212Bi-anti-Tac. *Cancer Res.* **1994**, *54*, 4362–4370.

179. Nikula, T.K.; McDevitt, M.R.; Finn, R.D.; Wu, C.; Kozak, R.W.; Garmestani, K.; Brechbiel, M.W.; Curcio, M.J.; Pippin, C.G.; Tiffany-Jones, L.; et al. Alpha-emitting bismuth cyclohexylbenzyl DTPA constructs of recombinant humanized anti-CD33 antibodies: Pharmacokinetics, bioactivity, toxicity and chemistry. *J. Nucl. Med.* **1999**, *40*, 166–176.

180. Milenic, D.; Garmestani, K.; Dadachova, E.; Chappell, L.; Albert, P.; Hill, D.; Schlom, J.; Brechbiel, M. Radioimmunotherapy of human colon carcinoma xenografts using a 213Bi-labeled domain-deleted humanized monoclonal antibody. *Cancer Biother. Radiopharm.* **2004**, *19*, 135–147. [CrossRef]

181. Bloechl, S.; Beck, R.; Seidl, C.; Morgenstern, A.; Schwaiger, M.; Senekowitsch-Schmidtke, R. Fractionated locoregional low-dose radioimmunotherapy improves survival in a mouse model of diffuse-type gastric cancer using a 213Bi-conjugated monoclonal antibody. *Clin. Cancer Res.* **2005**, *11*, 7070s–7074s. [CrossRef]

182. Knor, S.; Sato, S.; Huber, T.; Morgenstern, A.; Bruchertseifer, F.; Schmitt, M.; Kessler, H.; Senekowitsch-Schmidtke, R.; Magdolen, V.; Seidl, C. Development and evaluation of peptidic ligands targeting tumour-associated urokinase plasminogen activator receptor (uPAR) for use in alpha-emitter therapy for disseminated ovarian cancer. *Eur. J. Nucl. Med. Mol. Imaging* **2008**, *35*, 53–64. [CrossRef] [PubMed]

183. Pfost, B.; Seidl, C.; Autenrieth, M.; Saur, D.; Bruchertseifer, F.; Morgenstern, A.; Schwaiger, M.; Senekowitsch-Schmidtke, R. Intravesical alpha-radioimmunotherapy with 213Bi-anti-EGFR-mAb defeats human bladder carcinoma in xenografted nude mice. *J. Nucl. Med.* **2009**, *50*, 1700–1708. [CrossRef] [PubMed]

184. Milenic, D.E.; Brady, E.D.; Garmestani, K.; Albert, P.S.; Abdulla, A.; Brechbiel, M.W. Improved efficacy of alpha-particle-targeted radiation therapy: Dual targeting of human epidermal growth factor receptor-2 and tumor-associated glycoprotein 72. *Cancer* **2010**, *116*, 1059–1066. [CrossRef] [PubMed]

185. Wild, D.; Frischknecht, M.; Zhang, H.; Morgenstern, A.; Bruchertseifer, F.; Boisclair, J.; Provencher-Bolliger, A.; Reubi, J.C.; Maecke, H.R. Alpha- versus beta-particle radiopeptide therapy in a human prostate cancer model (213Bi-DOTA-PESIN and 213Bi-AMBA versus 177Lu-DOTA-PESIN). *Cancer Res.* **2011**, *71*, 1009–1018. [CrossRef] [PubMed]

186. Fichou, N.; Gouard, S.; Maurel, C.; Barbet, J.; Ferrer, L.; Morgenstern, A.; Bruchertseifer, F.; Faivre-Chauvet, A.; Bigot-Corbel, E.; Davodeau, F.; et al. Single-Dose Anti-CD138 Radioimmunotherapy: Bismuth-213 is More Efficient than Lutetium-177 for Treatment of Multiple Myeloma in a Preclinical Model. *Front. Med. (Lausanne)* **2015**, *2*, 76. [CrossRef]

187. Seidl, C.; Zockler, C.; Beck, R.; Quintanilla-Martinez, L.; Bruchertseifer, F.; Senekowitsch-Schmidtke, R. 177Lu-immunotherapy of experimental peritoneal carcinomatosis shows comparable effectiveness to 213Bi-immunotherapy, but causes toxicity not observed with 213Bi. *Eur. J. Nucl. Med. Mol. Imaging* **2011**, *38*, 312–322. [CrossRef]

188. Cherel, M.; Gouard, S.; Gaschet, J.; Sai-Maurel, C.; Bruchertseifer, F.; Morgenstern, A.; Bourgeois, M.; Gestin, J.F.; Bodere, F.K.; Barbet, J.; et al. 213Bi radioimmunotherapy with an anti-mCD138 monoclonal antibody in a murine model of multiple myeloma. *J. Nucl. Med.* **2013**, *54*, 1597–1604. [CrossRef]

189. Fazel, J.; Rotzer, S.; Seidl, C.; Feuerecker, B.; Autenrieth, M.; Weirich, G.; Bruchertseifer, F.; Morgenstern, A.; Senekowitsch-Schmidtke, R. Fractionated intravesical radioimmunotherapy with (213)Bi-anti-EGFR-MAb is effective without toxic side-effects in a nude mouse model of advanced human bladder carcinoma. *Cancer Biol.* **2015**, *16*, 1526–1534. [CrossRef]

190. Milenic, D.E.; Baidoo, K.E.; Kim, Y.S.; Brechbiel, M.W. Evaluation of cetuximab as a candidate for targeted alpha-particle radiation therapy of HER1-positive disseminated intraperitoneal disease. *MAbs* **2015**, *7*, 255–264. [CrossRef] [PubMed]

191. Miao, Y.; Hylarides, M.; Fisher, D.R.; Shelton, T.; Moore, H.; Wester, D.W.; Fritzberg, A.R.; Winkelmann, C.T.; Hoffman, T.; Quinn, T.P. Melanoma therapy via peptide-targeted {alpha}-radiation. *Clin. Cancer Res.* **2005**, *11*, 5616–5621. [CrossRef]

192. Boudousq, V.; Bobyk, L.; Busson, M.; Garambois, V.; Jarlier, M.; Charalambatou, P.; Pelegrin, A.; Paillas, S.; Chouin, N.; Quenet, F.; et al. Comparison between internalizing anti-HER2 mAbs and non-internalizing anti-CEA mAbs in alpha-radioimmunotherapy of small volume peritoneal carcinomatosis using 212Pb. *PLoS ONE* **2013**, *8*, e69613. [CrossRef] [PubMed]

193. Milenic, D.E.; Garmestani, K.; Brady, E.D.; Albert, P.S.; Ma, D.; Abdulla, A.; Brechbiel, M.W. Alpha-particle radioimmunotherapy of disseminated peritoneal disease using a (212)Pb-labeled radioimmunoconjugate targeting HER2. *Cancer Biother. Radiopharm.* **2005**, *20*, 557–568. [CrossRef] [PubMed]

194. Milenic, D.E.; Garmestani, K.; Brady, E.D.; Albert, P.S.; Abdulla, A.; Flynn, J.; Brechbiel, M.W. Potentiation of high-LET radiation by gemcitabine: Targeting HER2 with trastuzumab to treat disseminated peritoneal disease. *Clin. Cancer Res.* **2007**, *13*, 1926–1935. [CrossRef] [PubMed]

195. Kasten, B.B.; Arend, R.C.; Katre, A.A.; Kim, H.; Fan, J.; Ferrone, S.; Zinn, K.R.; Buchsbaum, D.J. B7-H3-targeted (212)Pb radioimmunotherapy of ovarian cancer in preclinical models. *Nucl. Med. Biol.* **2017**, *47*, 23–30. [CrossRef] [PubMed]

196. Kasten, B.B.; Gangrade, A.; Kim, H.; Fan, J.; Ferrone, S.; Ferrone, C.R.; Zinn, K.R.; Buchsbaum, D.J. (212)Pb-labeled B7-H3-targeting antibody for pancreatic cancer therapy in mouse models. *Nucl. Med. Biol.* **2018**, *58*, 67–73. [CrossRef]

197. Kasten, B.B.; Oliver, P.G.; Kim, H.; Fan, J.; Ferrone, S.; Zinn, K.R.; Buchsbaum, D.J. (212)Pb-Labeled Antibody 225.28 Targeted to Chondroitin Sulfate Proteoglycan 4 for Triple-Negative Breast Cancer Therapy in Mouse Models. *Int. J. Mol. Sci.* **2018**, *19*, 925. [CrossRef]

198. Milenic, D.E.; Kim, Y.S.; Baidoo, K.E.; Wong, K.J.; Barkley, R.; Delgado, J.; Brechbiel, M.W. Exploration of a F(ab′)2 Fragment as the Targeting Agent of alpha-Radiation Therapy: A Comparison of the Therapeutic Benefit of Intraperitoneal and Intravenous Administered Radioimmunotherapy. *Cancer Biother. Radiopharm.* **2018**, *33*, 182–193. [CrossRef]

199. Dahle, J.; Jonasdottir, T.J.; Heyerdahl, H.; Nesland, J.M.; Borrebaek, J.; Hjelmerud, A.K.; Larsen, R.H. Assessment of long-term radiotoxicity after treatment with the low-dose-rate alpha-particle-emitting radioimmunoconjugate (227)Th-rituximab. *Eur. J. Nucl. Med. Mol. Imaging* **2010**, *37*, 93–102. [CrossRef]

200. Abbas, N.; Heyerdahl, H.; Bruland, O.S.; Borrebaek, J.; Nesland, J.; Dahle, J. Experimental alpha-particle radioimmunotherapy of breast cancer using 227Th-labeled p-benzyl-DOTA-trastuzumab. *EJNMMI Res.* **2011**, *1*, 18. [CrossRef]

201. Hagemann, U.B.; Mihaylova, D.; Uran, S.R.; Borrebaek, J.; Grant, D.; Bjerke, R.M.; Karlsson, J.; Cuthbertson, A.S. Targeted alpha therapy using a novel CD70 targeted thorium-227 conjugate in in vitro and in vivo models of renal cell carcinoma. *Oncotarget* **2017**, *8*, 56311–56326. [CrossRef]

202. Westrom, S.; Bonsdorff, T.B.; Bruland, O.S.; Larsen, R.H. Therapeutic Effect of alpha-Emitting (224)Ra-Labeled Calcium Carbonate Microparticles in Mice with Intraperitoneal Ovarian Cancer. *Transl. Oncol.* **2018**, *11*, 259–267. [CrossRef] [PubMed]

203. Briel, A. Innovative diagnostics enhances and advances the impact of in vivo small-animal imaging in drug discovery and pharmaceutical development. *Mod. Biopharm.* **2013**, 183–209. [CrossRef]

204. Chaudhury, S.; Thakur, B.; Chatterjee, S.; Ray, P. Molecular Imaging Aided Improvement in Drug Discovery and Development. *Curr. Biotechnol. (SharjahUnited Arab Emir.)* **2014**, *3*, 218–237. [CrossRef]

205. Medhi, B.; Misra, S.; Avti Pramod, K.; Kumar, P.; Kumar, H.; Singh, B. Role of neuroimaging in drug development. *Rev. Neurosci.* **2014**, *25*, 663–673. [CrossRef] [PubMed]

206. Poels, E.M.P.; Kegeles, L.S.; Kantrowitz, J.T.; Slifstein, M.; Javitt, D.C.; Lieberman, J.A.; Abi-Dargham, A.; Girgis, R.R. Imaging glutamate in schizophrenia: Review of findings and implications for drug discovery. *Mol. Psychiatry* **2014**, *19*, 20–29. [CrossRef]

207. Pecking, A.P.; Bellet, D.; Alberini, J.L. Immuno-SPET/CT and immuno-PET/CT: A step ahead to translational imaging. *Clin. Exp. Metastasis* **2012**, *29*, 847–852. [CrossRef]

208. Chappell, L.L.; Dadachova, E.; Milenic, D.E.; Garmestani, K.; Wu, C.; Brechbiel, M.W. Synthesis, characterization, and evaluation of a novel bifunctional chelating agent for the lead isotopes 203Pb and 212Pb. *Nucl. Med. Biol.* **2000**, *27*, 93–100. [CrossRef]

209. Sgouros, G.; Ballangrud, A.M.; Jurcic, J.G.; McDevitt, M.R.; Humm, J.L.; Erdi, Y.E.; Mehta, B.M.; Finn, R.D.; Larson, S.M.; Scheinberg, D.A. Pharmacokinetics and dosimetry of an alpha-particle emitter labeled antibody: 213Bi-HuM195 (anti-CD33) in patients with leukemia. *J. Nucl. Med.* **1999**, *40*, 1935–1946.

210. Lohrmann, C.; Zhang, H.; Thorek, D.L.; Desai, P.; Zanzonico, P.B.; O'Donoghue, J.; Irwin, C.P.; Reiner, T.; Grimm, J.; Weber, W.A. Cerenkov Luminescence Imaging for Radiation Dose Calculation of a 90Y-Labeled Gastrin-Releasing Peptide Receptor Antagonist. *J. Nucl. Med.* **2015**, *56*, 805–811. [CrossRef]

211. Ruggiero, A.; Holland, J.P.; Lewis, J.S.; Grimm, J. Cerenkov luminescence imaging of medical isotopes. *J. Nucl. Med.* **2010**, *51*, 1123–1130. [CrossRef]

212. Das, S.; Thorek, D.L.; Grimm, J. Cerenkov imaging. *Adv. Cancer Res.* **2014**, *124*, 213–234. [CrossRef] [PubMed]

213. Thorek, D.; Robertson, R.; Bacchus, W.A.; Hahn, J.; Rothberg, J.; Beattie, B.J.; Grimm, J. Cerenkov imaging—A new modality for molecular imaging. *Am. J. Nucl. Med. Mol. Imaging* **2012**, *2*, 163–173.

214. Beattie, B.J.; Thorek, D.L.; Schmidtlein, C.R.; Pentlow, K.S.; Humm, J.L.; Hielscher, A.H. Quantitative modeling of Cerenkov light production efficiency from medical radionuclides. *PLoS ONE* **2012**, *7*, e31402. [CrossRef] [PubMed]

215. Ackerman, N.L.; Graves, E.E. The potential for Cerenkov luminescence imaging of alpha-emitting radionuclides. *Phys. Med. Biol.* **2012**, *57*, 771–783. [CrossRef] [PubMed]

216. Sgouros, G. Long-lived alpha emitters in radioimmunotherapy: The mischievous progeny. *Cancer Biother. Radiopharm.* **2000**, *15*, 219–221. [CrossRef] [PubMed]

217. Pandya, D.N.; Hantgan, R.; Budzevich, M.M.; Kock, N.D.; Morse, D.L.; Batista, I.; Mintz, A.; Li, K.C.; Wadas, T.J. Preliminary Therapy Evaluation of ^{225}Ac-DOTA-c(RGDyK) Demonstrates that Cerenkov Radiation Derived from ^{225}Ac Daughter Decay Can be Detected by Optical Imaging for In vivo Tumor Visualization. *Theranostics* **2016**, *6*, 698–709. [CrossRef]

218. Chen, X.; Hou, Y.; Tohme, M.; Park, R.; Khankaldyyan, V.; Gonzales-Gomez, I.; Bading, J.R.; Laug, W.E.; Conti, P.S. Pegylated Arg-Gly-Asp peptide: 64Cu labeling and PET imaging of brain tumor alphavbeta3-integrin expression. *J. Nucl. Med.* **2004**, *45*, 1776–1783.

219. Chen, X.; Liu, S.; Hou, Y.; Tohme, M.; Park, R.; Bading, J.R.; Conti, P.S. MicroPET imaging of breast cancer alphav-integrin expression with 64Cu-labeled dimeric RGD peptides. *Mol. Imaging Biol.* **2004**, *6*, 350–359. [CrossRef]

220. Chen, X.; Park, R.; Tohme, M.; Shahinian, A.H.; Bading, J.R.; Conti, P.S. MicroPET and autoradiographic imaging of breast cancer alpha v-integrin expression using 18F- and 64Cu-labeled RGD peptide. *Bioconjug. Chem.* **2004**, *15*, 41–49. [CrossRef]

221. Chen, X. Integrin Targeted Imaging and Therapy. *Theranostics* **2011**, *2011*, 28–29. [CrossRef] [PubMed]

222. Li, X.; Patterson, J.T.; Sarkar, M.; Pedzisa, L.; Kodadek, T.; Roush, W.R.; Rader, C. Site-Specific Dual Antibody Conjugation via Engineered Cysteine and Selenocysteine Residues. *Bioconjug. Chem.* **2015**, *26*, 2243–2248. [CrossRef] [PubMed]

223. van Rij, C.M.; Frielink, C.; Goldenberg, D.M.; Sharkey, R.M.; Lütje, S.; McBride, W.J.; Oyen, W.J.G.; Boerman, O.C. Pretargeted Radioimmunotherapy of Prostate Cancer with an Anti-TROP-2×Anti-HSG Bispecific Antibody and a (177)Lu-Labeled Peptide. *Cancer Biother. Radiopharm.* **2014**, *29*, 323–329. [CrossRef]

224. Frampas, E.; Rousseau, C.; Bodet-Milin, C.; Barbet, J.; Chatal, J.-F.; Kraeber-Bodéré, F. Improvement of Radioimmunotherapy Using Pretargeting. *Front. Oncol.* **2013**, *3*, 159. [CrossRef] [PubMed]

225. Jourdan, M.; Ferlin, M.; Legouffe, E.; Horvathova, M.; Liautard, J.; Rossi, J.F.; Wijdenes, J.; Brochier, J.; Klein, B. The myeloma cell antigen syndecan-1 is lost by apoptotic myeloma cells. *Br. J. Haematol.* **1998**, *100*, 637–646. [CrossRef] [PubMed]

226. Adumeau, P.; Sharma, S.K.; Brent, C.; Zeglis, B.M. Site-Specifically Labeled Immunoconjugates for Molecular Imaging–Part 2: Peptide Tags and Unnatural Amino Acids. *Mol. Imaging Biol.* **2016**, *18*, 153–165. [CrossRef] [PubMed]

227. Adumeau, P.; Sharma, S.K.; Brent, C.; Zeglis, B.M. Site-Specifically Labeled Immunoconjugates for Molecular Imaging–Part 1: Cysteine Residues and Glycans. *Mol. Imaging Biol.* **2016**, *18*, 1–17. [CrossRef]

228. Schwarz, S.W.; Decristoforo, C.; Goodbody, A.E.; Singhal, N.; Saliba, S.; Ruddock, R.S.; Zukotynski, K.; Ross, A.A. Harmonization of U.S., European Union, and Canadian First-in-Human Regulatory Requirements for Radiopharmaceuticals: Is This Possible? *J. Nucl. Med.* **2019**, *60*, 158–166. [CrossRef]

229. Krolicki, L.; Bruchertseifer, F.; Kunikowska, J.; Koziara, H.; Krolicki, B.; Jakucinski, M.; Pawlak, D.; Apostolidis, C.; Mirzadeh, S.; Rola, R.; et al. Prolonged survival in secondary glioblastoma following local injection of targeted alpha therapy with (213)Bi-substance P analogue. *Eur. J. Nucl. Med. Mol. Imaging* **2018**, *45*, 1636–1644. [CrossRef]

230. Krolicki, L.; Bruchertseifer, F.; Kunikowska, J.; Koziara, H.; Krolicki, B.; Jakucinski, M.; Pawlak, D.; Apostolidis, C.; Mirzadeh, S.; Rola, R.; et al. Safety and efficacy of targeted alpha therapy with (213)Bi-DOTA-substance P in recurrent glioblastoma. *Eur. J. Nucl. Med. Mol. Imaging* **2018**. [CrossRef]

231. Autenrieth, M.E.; Seidl, C.; Bruchertseifer, F.; Horn, T.; Kurtz, F.; Feuerecker, B.; D'Alessandria, C.; Pfob, C.; Nekolla, S.; Apostolidis, C.; et al. Treatment of carcinoma in situ of the urinary bladder with an alpha-emitter immunoconjugate targeting the epidermal growth factor receptor: A pilot study. *Eur. J. Nucl. Med. Mol. Imaging* **2018**, *45*, 1364–1371. [CrossRef]

232. Autenrieth, M.E.; Horn, T.; Kurtz, F.; Nguyen, K.; Morgenstern, A.; Bruchertseifer, F.; Schwaiger, M.; Blechert, M.; Seidl, C.; Senekowitsch-Schmidtke, R.; et al. [Intravesical radioimmunotherapy of carcinoma in situ of the urinary bladder after BCG failure]. *Urol. A* **2017**, *56*, 40–43. [CrossRef] [PubMed]

233. Hadaschik, B. Re: 225Ac-PSMA-617 for PSMA-Targeting Alpha-radiation Therapy of Patients with Metastatic Castration-resistant Prostate Cancer. *Eur. Urol.* **2016**, *70*, 1080–1081. [CrossRef] [PubMed]

234. Kratochwil, C.; Bruchertseifer, F.; Giesel, F.; Apostolidis, C.; Haberkorn, U.; Morgenstern, A. Ac-225-DOTATOCan empiric dose finding for alpha particle emitter based radionuclide therapy of neuroendocrine tumors. *J. Nucl. Med.* **2015**, *56*, 1232.

235. Jurcic, J.G.; Levy, M.Y.; Park, J.H.; Ravandi, F.; Perl, A.E.; Pagel, M.J.; Smith, D.B.; Estey, E.H.; Kantarjian, H.; Cicic, D.; et al. Phase I Trial of Targeted Alpha-Particle Therapy with Actinium-225 (225Ac)-Lintuzumab and Low-Dose Cytarabine (LDAC) in Patients Age 60 or Older with Untreated Acute Myeloid Leukemia (AML). In Proceedings of the ASH Annual Meeting, Atlanta, GA, USA, 9–12 December 2017; p. 4050.

236. Rathke, H.; Kratochwil, C.; Hohenberger, R.; Giesel, F.L.; Bruchertseifer, F.; Flechsig, P.; Morgenstern, A.; Hein, M.; Plinkert, P.; Haberkorn, U.; et al. Initial clinical experience performing sialendoscopy for salivary gland protection in patients undergoing (225)Ac-PSMA-617 RLT. *Eur. J. Nucl. Med. Mol. Imaging* **2019**, *46*, 139–147. [CrossRef] [PubMed]

237. Sathekge, M.; Bruchertseifer, F.; Vorster, M.; Lawal, I.; Knoesen, O.; Mahapane, J.; Davis, C.; Reyneke, F.; Maes, A.; Kratochwil, C.; et al. PREDICTORS OF OVERALL AND DISEASE FREE SURVIVAL IN METASTATIC CASTRATION-RESISTANT PROSTATE CANCER PATIENTS RECEIVING (225)Ac-PSMA-617 RADIOLIGAND THERAPY. *J. Nucl. Med.* **2019**. [CrossRef]

238. Zalutsky, M.R.; Reardon, D.A.; Akabani, G.; Coleman, R.E.; Friedman, A.H.; Friedman, H.S.; McLendon, R.E.; Wong, T.Z.; Bigner, D.D. Clinical experience with alpha-particle emitting 211At: Treatment of recurrent brain tumor patients with 211At-labeled chimeric antitenascin monoclonal antibody 81C6. *J. Nucl. Med.* **2008**, *49*, 30–38. [CrossRef]

239. Andersson, H.; Cederkrantz, E.; Back, T.; Divgi, C.; Elgqvist, J.; Himmelman, J.; Horvath, G.; Jacobsson, L.; Jensen, H.; Lindegren, S.; et al. Intraperitoneal alpha-particle radioimmunotherapy of ovarian cancer patients: Pharmacokinetics and dosimetry of (211)At-MX35 F(ab')2—A phase I study. *J. Nucl. Med.* **2009**, *50*, 1153–1160. [CrossRef]

240. Jurcic, J.G.; Larson, S.M.; Sgouros, G.; McDevitt, M.R.; Finn, R.D.; Divgi, C.R.; Ballangrud, A.M.; Hamacher, K.A.; Ma, D.; Humm, J.L.; et al. Targeted alpha particle immunotherapy for myeloid leukemia. *Blood* **2002**, *100*, 1233–1239. [CrossRef]

241. Rosenblat, T.L.; McDevitt, M.R.; Mulford, D.A.; Pandit-Taskar, N.; Divgi, C.R.; Panageas, K.S.; Heaney, M.L.; Chanel, S.; Morgenstern, A.; Sgouros, G.; et al. Sequential cytarabine and alpha-particle immunotherapy with bismuth-213-lintuzumab (HuM195) for acute myeloid leukemia. *Clin. Cancer Res.* **2010**, *16*, 5303–5311. [CrossRef]

242. Heeger, S.; Moldenhauer, G.; Egerer, G.; Wesch, H.; Martin, S.; Nikula, T.K.; Apostolidis, C.; Brechbiel, M.; Ho, A.; Haas, R. Alpha radioimmunotherapy of B-lineage non-Hodgkin's lymphoma using 213Bi-labeled anti-CD19- and anti-CD20-CHX-A"-DTPA conjugates. *J. Clin. Oncol.* **2004**, *22* (Suppl. S14), 2625. [CrossRef]

243. Kneifel, S.; Cordier, D.; Good, S.; Ionescu, M.C.; Ghaffari, A.; Hofer, S.; Kretzschmar, M.; Tolnay, M.; Apostolidis, C.; Waser, B.; et al. Local targeting of malignant gliomas by the diffusible peptidic vector 1,4,7,10-tetraazacyclododecane-1-glutaric acid-4,7,10-triacetic acid-substance p. *Clin. Cancer Res.* **2006**, *12*, 3843–3850. [CrossRef] [PubMed]

244. Allen, B.J.; Singla, A.A.; Rizvi, S.M.; Graham, P.; Bruchertseifer, F.; Apostolidis, C.; Morgenstern, A. Analysis of patient survival in a Phase I trial of systemic targeted alpha-therapy for metastatic melanoma. *Immunotherapy* **2011**, *3*, 1041–1050. [CrossRef] [PubMed]

245. Raja, C.; Graham, P.; Abbas Rizvi, S.M.; Song, E.; Goldsmith, H.; Thompson, J.; Bosserhoff, A.; Morgenstern, A.; Apostolidis, C.; Kearsley, J.; et al. Interim analysis of toxicity and response in phase 1 trial of systemic targeted alpha therapy for metastatic melanoma. *Cancer Biol.* **2007**, *6*, 846–852. [CrossRef] [PubMed]

246. Meredith, R.; Torgue, J.; Shen, S.; Fisher, D.R.; Banaga, E.; Bunch, P.; Morgan, D.; Fan, J.; Straughn, J.M., Jr. Dose escalation and dosimetry of first-in-human alpha radioimmunotherapy with 212Pb-TCMC-trastuzumab. *J. Nucl. Med.* **2014**, *55*, 1636–1642. [CrossRef]

247. Meredith, R.F.; Torgue, J.; Azure, M.T.; Shen, S.; Saddekni, S.; Banaga, E.; Carlise, R.; Bunch, P.; Yoder, D.; Alvarez, R. Pharmacokinetics and imaging of 212Pb-TCMC-trastuzumab after intraperitoneal administration in ovarian cancer patients. *Cancer Biother. Radiopharm.* **2014**, *29*, 12–17. [CrossRef]

248. Castello, A.; Macapinlac, H.A.; Lopci, E.; Santos, E.B. Prostate-specific antigen flare induced by (223)RaCl2 in patients with metastatic castration-resistant prostate cancer. *Eur. J. Nucl. Med. Mol. Imaging* **2018**, *45*, 2256–2263. [CrossRef]

249. Dizdarevic, S.; Petersen, P.M.; Essler, M.; Versari, A.; Bourre, J.C.; la Fougere, C.; Valdagni, R.; Paganelli, G.; Ezziddin, S.; Kalinovsky, J.; et al. Interim analysis of the REASSURE (Radium-223 alpha Emitter Agent in non-intervention Safety Study in mCRPC popUlation for long-teRm Evaluation) study: Patient characteristics and safety according to prior use of chemotherapy in routine clinical practice. *Eur. J. Nucl. Med. Mol. Imaging* **2019**, *46*, 1102–1110. [CrossRef]

250. Hoskin, P.; Sartor, O.; O'Sullivan, J.M.; Johannessen, D.C.; Helle, S.I.; Logue, J.; Bottomley, D.; Nilsson, S.; Vogelzang, N.J.; Fang, F.; et al. Efficacy and safety of radium-223 dichloride in patients with castration-resistant prostate cancer and symptomatic bone metastases, with or without previous docetaxel use: A prespecified subgroup analysis from the randomised, double-blind, phase 3 ALSYMPCA trial. *Lancet Oncol.* **2014**, *15*, 1397–1406. [CrossRef]

251. Parker, C.; Finkelstein, S.E.; Michalski, J.M.; O'Sullivan, J.M.; Bruland, O.; Vogelzang, N.J.; Coleman, R.E.; Nilsson, S.; Sartor, O.; Li, R.; et al. Efficacy and Safety of Radium-223 Dichloride in Symptomatic Castration-resistant Prostate Cancer Patients With or Without Baseline Opioid Use From the Phase 3 ALSYMPCA Trial. *Eur. Urol.* **2016**, *70*, 875–883. [CrossRef]

252. Jo, K.I.; Kim, M.S.; Yeon, J.Y.; Kim, J.S.; Hong, S.C. Recurrent Bleeding in Hemorrhagic Moyamoya Disease: Prognostic Implications of the Perfusion Status. *J. Korean Neurosurg. Soc.* **2016**, *59*, 117–121. [CrossRef]

253. Falkmer, U.; Jarhult, J.; Wersall, P.; Cavallin-Stahl, E. A systematic overview of radiation therapy effects in skeletal metastases. *Acta Oncol* **2003**, *42*, 620–633. [CrossRef] [PubMed]

254. Silberstein, E.B. Dosage and response in radiopharmaceutical therapy of painful osseous metastases. *J. Nucl. Med.* **1996**, *37*, 249–252. [PubMed]

255. Pandit-Taskar, N.; Batraki, M.; Divgi, C.R. Radiopharmaceutical therapy for palliation of bone pain from osseous metastases. *J. Nucl. Med.* **2004**, *45*, 1358–1365. [PubMed]

256. Henriksen, G.; Fisher, D.R.; Roeske, J.C.; Bruland, O.S.; Larsen, R.H. Targeting of osseous sites with alpha-emitting 223Ra: Comparison with the beta-emitter 89Sr in mice. *J. Nucl. Med.* **2003**, *44*, 252–259. [PubMed]

257. Nilsson, S.; Larsen, R.H.; Fossa, S.D.; Balteskard, L.; Borch, K.W.; Westlin, J.E.; Salberg, G.; Bruland, O.S. First clinical experience with alpha-emitting radium-223 in the treatment of skeletal metastases. *Clin. Cancer Res.* **2005**, *11*, 4451–4459. [CrossRef] [PubMed]

258. Lewington, V.J. Bone-seeking radionuclides for therapy. *J. Nucl. Med.* **2005**, *46* (Suppl. 1), 38S–47S.

259. Dauer, L.T.; Williamson, M.J.; Humm, J.; O'Donoghue, J.; Ghani, R.; Awadallah, R.; Carrasquillo, J.; Pandit-Taskar, N.; Aksnes, A.K.; Biggin, C.; et al. Radiation safety considerations for the use of (2)(2)(3)RaCl(2) DE in men with castration-resistant prostate cancer. *Health Phys.* **2014**, *106*, 494–504. [CrossRef]

260. Nilsson, S.; Strang, P.; Aksnes, A.K.; Franzen, L.; Olivier, P.; Pecking, A.; Staffurth, J.; Vasanthan, S.; Andersson, C.; Bruland, O.S. A randomized, dose-response, multicenter phase II study of radium-223 chloride for the palliation of painful bone metastases in patients with castration-resistant prostate cancer. *Eur. J. Cancer* **2012**, *48*, 678–686. [CrossRef]

261. Sartor, O.; Coleman, R.; Nilsson, S.; Heinrich, D.; Helle, S.I.; O'Sullivan, J.M.; Fossa, S.D.; Chodacki, A.; Wiechno, P.; Logue, J.; et al. Effect of radium-223 dichloride on symptomatic skeletal events in patients with castration-resistant prostate cancer and bone metastases: Results from a phase 3, double-blind, randomised trial. *Lancet. Oncol.* **2014**, *15*, 738–746. [CrossRef]

262. Nilsson, S.; Cislo, P.; Sartor, O.; Vogelzang, N.J.; Coleman, R.E.; O'Sullivan, J.M.; Reuning-Scherer, J.; Shan, M.; Zhan, L.; Parker, C. Patient-reported quality of life analysis of radium-223 dichloride from the phase 3 ALSYMPCA study. *Ann. Oncol.* **2016**. [CrossRef]

263. Crawford, E.D.; Higano, C.S.; Shore, N.D.; Hussain, M.; Petrylak, D.P. Treating Patients with Metastatic Castration Resistant Prostate Cancer: A Comprehensive Review of Available Therapies. *J. Urol.* **2015**, *194*, 1537–1547. [CrossRef] [PubMed]

264. Morris, M.J.; Loriot, Y.; Sweeney, C.J.; Fizazi, K.; Ryan, C.J.; Shevrin, D.H.; Antonarakis, E.S.; Pandit-Taskar, N.; Deandreis, D.; Jacene, H.A.; et al. Radium-223 in combination with docetaxel in patients with castration-resistant prostate cancer and bone metastases: A phase 1 dose escalation/randomised phase 2a trial. *Eur. J. Cancer* **2019**, *114*, 107–116. [CrossRef] [PubMed]

265. Shore, N.D.; Tutrone, R.F.; Mariados, N.F.; Nordquist, L.T.; Mehlhaff, B.A.; Steere, K.J.; Harrelson, S.S. eRADicAte: A Prospective Evaluation Combining Radium-223 Dichloride and Abiraterone Acetate Plus Prednisone in Patients With Castration-Resistant Prostate Cancer. *Clin. Genitourin. Cancer* **2018**, *16*, 149–154. [CrossRef] [PubMed]

266. Smith, M.R.; Parker, C.C.; Saad, F.; Miller, K.; Tombal, B.; Ng, Q.S.; Bogemann, M.; Matveev, V.; Piulats, J.M.; Zucca, L.E.; et al. ERA 223: A phase 3 trial of radium-223 dichloride (Ra-223) in combination with abiraterone acetate (abiraterone) and prednisone in the treatment of asymptomatic or mildly symptomatic chemotherapy-naive patients (pts) with bone predominant metastatic castration-resistant prostate cancer (mCRPC). In Proceedings of the ESMO 2018 Congress, Munich, Germany, 19 October 2018.

267. van der Doelen, M.J.; Mehra, N.; Hermsen, R.; Janssen, M.J.R.; Gerritsen, W.R.; van Oort, I.M. Patient Selection for Radium-223 Therapy in Patients With Bone Metastatic Castration-Resistant Prostate Cancer: New Recommendations and Future Perspectives. *Clin. Genitourin. Cancer* **2019**, *17*, 79–87. [CrossRef]

268. Malamas, A.S.; Gameiro, S.R.; Knudson, K.M.; Hodge, J.W. Sublethal exposure to alpha radiation (223Ra dichloride) enhances various carcinomas' sensitivity to lysis by antigen-specific cytotoxic T lymphocytes through calreticulin-mediated immunogenic modulation. *Oncotarget* **2016**, *7*, 86937–86947. [CrossRef]

269. Nilsson, S.; Franzen, L.; Parker, C.; Tyrrell, C.; Blom, R.; Tennvall, J.; Lennernas, B.; Petersson, U.; Johannessen, D.C.; Sokal, M.; et al. Two-year survival follow-up of the randomized, double-blind, placebo-controlled phase II study of radium-223 chloride in patients with castration-resistant prostate cancer and bone metastases. *Clin. Genitourin. Cancer* **2013**, *11*, 20–26. [CrossRef] [PubMed]

270. Coleman, R.; Aksnes, A.K.; Naume, B.; Garcia, C.; Jerusalem, G.; Piccart, M.; Vobecky, N.; Thuresson, M.; Flamen, P. A phase IIa, nonrandomized study of radium-223 dichloride in advanced breast cancer patients with bone-dominant disease. *Breast Cancer Res. Treat.* **2014**, *145*, 411–418. [CrossRef]

271. Berenson, J.R.; Yellin, O.; Patel, R.; Duvivier, H.; Nassir, Y.; Mapes, R.; Abaya, C.D.; Swift, R.A. A phase I study of samarium lexidronam/bortezomib combination therapy for the treatment of relapsed or refractory multiple myeloma. *Clin. Cancer Res.* **2009**, *15*, 1069–1075. [CrossRef]

272. Anderson, P.M.; Subbiah, V.; Rohren, E. Bone-seeking radiopharmaceuticals as targeted agents of osteosarcoma: Samarium-153-EDTMP and radium-223. *Adv. Exp. Med. Biol.* **2014**, *804*, 291–304. [CrossRef]

A Monte Carlo Method for Determining the Response Relationship between Two Commonly Used Detectors to Indirectly Measure Alpha Particle Radiation Activity

Christopher J. Tichacek [1,2,3], **Mikalai M. Budzevich** [4]**, Thaddeus J. Wadas** [5] ,
David L. Morse [2,3,4,6,*] **and Eduardo G. Moros** [1,2,3,6,*]

1   Department of Radiation Oncology, H. Lee Moffitt Cancer Center & Research Institute, Tampa, FL 33612,
    USA; Christopher.Tichacek@moffitt.org
2   Department of Cancer Physiology, H. Lee Moffitt Cancer Center & Research Institute, Tampa, FL 33612, USA
3   Department of Physics, University of South Florida, Tampa, FL 33620, USA
4   Small Animal Imaging Laboratory, H. Lee Moffitt Cancer Center & Research Institute, Tampa, FL 33612,
    USA; Mikalai.Budzevich@moffitt.org
5   Department of Cancer Biology, Wake Forest University Health Sciences, Winston-Salem, NC 27157, USA;
    twadas@wakehealth.edu
6   Department of Oncologic Sciences, University of South Florida, Tampa, FL 33612, USA
*   Correspondence: David.Morse@moffitt.org (D.L.M.); Eduardo.Moros@moffitt.org (E.G.M.);
    Tel.: +1-813-745-8948 (D.L.M.); +1-813-745-4168 (E.G.M.)

Abstract: Using targeted ligands to deliver alpha-emitting radionuclides directly to tumor cells has become a promising therapeutic strategy. To calculate the radiation dose to patients, activities of parent and daughter radionuclides must be measured. Scintillation detectors can be used to quantify these activities; however, activities found in pre-clinical and clinical studies can exceed their optimal performance range. Therefore, a method of correcting scintillation detector measurements at higher activities was developed using Monte Carlo modeling. Because there are currently no National Institute of Standards and Technology traceable Actinium-225 (^{225}Ac) standards available, a well-type ionization chamber was used to measure 70.3 ± 7.0, 144.3 ± 14.4, 222.0 ± 22.2, 299.7 ± 30.0, 370.0 ± 37.0, and 447.7 ± 44.7 kBq samples of ^{225}Ac obtained from Oak Ridge National Lab. Samples were then placed in a well-type NaI(Tl) scintillation detector and spectra were obtained. Alpha particle activity for each species was calculated using gamma abundance per alpha decay. MCNP6 Monte Carlo software was used to simulate the 4π-geometry of the NaI(Tl) detector. Using the ionization chamber reading as activity input to the Monte Carlo model, spectra were obtained and compared to NaI(Tl) spectra. Successive simulations of different activities were run until a spectrum minimizing the mean percent difference between the two was identified. This was repeated for each sample activity. Ionization chamber calibration measurements showed increase in error from 3% to 10% as activities decreased, resulting from decreasing detection efficiency. Measurements of ^{225}Ac using both detector types agreed within 7% of Oak Ridge stated activities. Simulated Monte Carlo spectra of ^{225}Ac were successfully generated. Activities obtained from these spectra differed with ionization chamber readings up to 156% at 147.7 kBq. Simulated spectra were then adjusted to correct NaI(Tl) measurements to be within 1%. These were compared to ionization chamber readings and a response relationship was determined between the two instruments. Measurements of ^{225}Ac and daughter activity were conducted using a NaI(Tl) scintillation detector calibrated for energy and efficiency and an ionization chamber calibrated for efficiency using a surrogate calibration reference. Corrections provided by Monte Carlo modeling improve the accuracy of activity quantification for alpha-particle emitting radiopharmaceuticals in pre-clinical and clinical studies.

---

1. Introduction

The use of targeted ligands to deliver alpha particles directly to cancer cells has become a promising strategy to treat tumors [1–4]. This is because of their short path length of 40–80 μm and high linear energy transfer (LET~100 keV/μm) [5]. These two properties make alpha particles highly cytotoxic to targeted cells, with little damage to surrounding normal cells.

Owing to the large amount of energy deposited by alpha particles, it is important to quantify the radioactivity of the targeted radiopharmaceutical initially injected and its subsequent biodistribution, pharmacokinetics, and radiation dose deposited in various tissues. As a result of its short path length, the direct measurement of alpha particles' activity in tissues is not possible in most, if not all, preclinical scenarios. If a parent metastable radioisotope also emits gamma rays, indirect methods of detection such as gamma spectroscopy can be used to estimate activity using scintillation detectors and well-type ion chambers that are commonly available in research laboratories and nuclear medicine clinics.

Actinium-225 (^{225}Ac) was chosen as the radionuclide for alpha-particle therapy (TAT) targeted to the melanocortin 1 receptor for treatment of metastatic uveal melanoma [6], the prostate-specific membrane antigen (PSMA) for metastatic prostate cancer [1], and CD33 for acute myeloid leukemia [7]. Clinical studies have been carried out for the PSMA and CD33 TATs and others in pre-clinical development will soon go to clinical trials [6]

^{225}Ac has a 10-day half-life and decays via six daughter radionuclides resulting in a net of four alpha particles per Actinium disintegration (Figure 1.) [8,9]. ^{225}Ac and two of its daughters, ^{221}Fr and ^{213}Bi, also decay with accompanying isomeric gamma photons. Using gamma detection systems, such as ion chambers or scintillation detectors, it is possible to indirectly determine the alpha activity by gamma ray abundance per decay conversions.
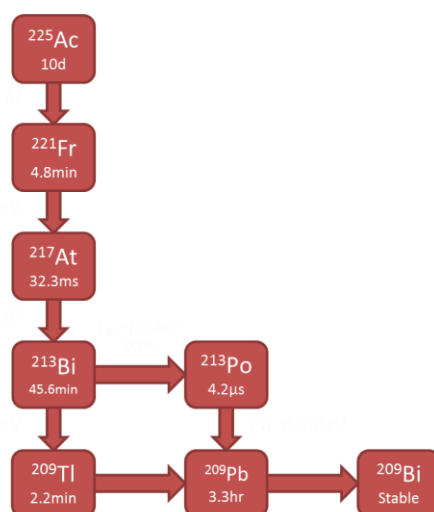

Figure 1. Decay chain of Actinium-225 (^{225}Ac).

In the clinic, ion chambers are readily available and their use is the standard of practice for checking activities for diagnostic and therapeutic agents. An ion chamber reading does not discriminate the collected charge between the parent and daughter radionuclides because it does not provide energy identification. In these situations, gamma spectroscopy using scintillation or semiconductor detectors, such as a sodium iodide doped with thallium scintillation detector [NaI(Tl)] or a high purity germanium (HPGe) detector, can be used. With this approach, it is possible to determine the activity of each gamma emitting daughter, which gives more information on how the decay species behave.

While HPGe seems to be the attractive option owing to its superior energy resolution, its performance suffers as a result of its low detection efficiency, cost, and requirement of sophisticated cooling systems. Despite the advantages of the NaI(Tl), dead time losses at higher activities and poor energy resolution may also provide incorrect activity measurements, leading to underestimation or overestimation of radiation dose [10].

In pre-clinical and clinical biodistribution studies, activity measurements of collected blood and tissues are used to calculate pharmacokinetics and radiation dosimetry. Therefore, accurate measurements for ^{225}Ac and daughters are needed. Hence, scintillation detector measurements are needed to generate these spectra. Alpha radiation dosimetry is performed using the methods recommended by the Committee on Medical Internal Radiation Dose [11]. It is essential that these measurements are accurate because the dosimetry estimates are then extrapolated to human estimations and, therefore, serve as the fundamental basis for all patient safety measures.

Scintillation detectors are calibrated by analyzing three aspects of the detector: energy, resolution, and efficiency [12]. Once the detector is fully calibrated, it can be used to perform gamma spectroscopic measurements in order to determine the activity of radioactive samples [13–18]. Ion chambers are calibrated by measuring a sample of the radiopharmaceutical in question with known activity, correcting for decay, and applying a calibration factor. The American National Standards Institute (ANSI) recommends that the applied calibration factor adjusts the measurement to within ±10% of the known activity [19]. Although reference standards have been developed for isotopes used in internal radiotherapy, for example, ^{177}Lu [20] ^{225}Ac standards are currently under development by NIST and are not yet available. For this study, ^{225}Ac provided by Oak Ridge National Lab was used as a cross-reference source.

While there are evident limitations in making clinical predictions when translating a radiopharmaceutical from mice to humans, it is important to minimize these limitations that are the result of instrumentation. Herein, a threshold is identified above which the scintillation detector cannot accurately measure the activities of ^{225}Ac and daughters. An activity response relationship between the ion chamber and scintillation detector measurements is reported and used in a method to improve activity determination above the threshold by correcting scintillation detector measurements via Monte Carlo simulations. These corrections improve the dosimetry of pre-clinical work and ultimately facilitate the translation of the new radiopharmaceutical to the human clinic.

2. Results

The system of ordinary differential equations describing the ^{225}Ac decay chain was solved to determine the daughters' activities as a function of time; these results are plotted in Figure 2 for ^{225}Ac, ^{221}Fr, and ^{213}Bi. For an initial activity of 3.7×10^4 kBq of ^{225}Ac, ^{221}Fr reaches secular equilibrium with ^{225}Ac in 55 minutes, while ^{213}Bi takes 380 minutes. Therefore, after 380 minutes (6.37 h), the parent and all daughter nuclides are in secular equilibrium.

To account for the statistical variance of physical spectra, a Gaussian energy broadening function was integrated with the ideal Monte Carlo simulation model. The parameters of this function were determined by nonlinear fitting of the measured FWHM versus energy. These parameters were determined to be a = 0.005616, b = 0.0521, and c = 2.027 with an R-squared value of 0.9984. This allowed the benchmark validation of the Monte Carlo model using the ^{137}Cs standard source (Figure 3). Simulating 155.4 kBq, the known source activity, showed a 1.02 mean percent difference at analogous bins between measured and simulated spectra.
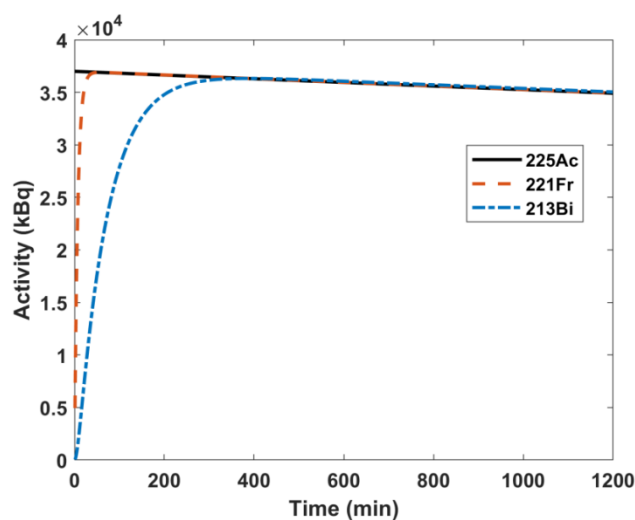
Figure 2. Solutions to system of decay ordinary differential equations of for an initial activity of 3.7×10^4 kBq of ^{225}Ac.
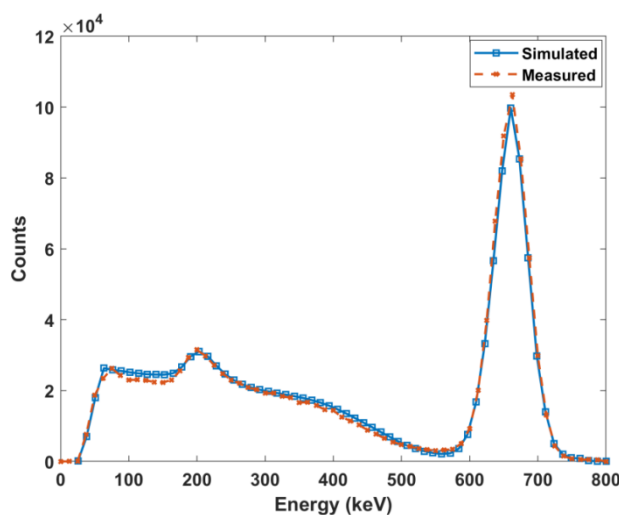

Figure 3. Comparison of measured and simulated spectra of ^{137}Cs.

The measured NaI(Tl) gamma spectrum and Gaussian peak fitting of ^{225}Ac and its daughters can be seen in Figure 4. The two source method was used to determine the dead time of the scintillation detector to characterize the saturation of the signal with increasing activity. The value was determined to be 4.6×10^{-5} s^{-1}. The dead time value was incorporated into the gamma spectrum fitting method that was used to determine the scintillation detector activities of ^{225}Ac, ^{221}Fr, and ^{213}Bi, and these values were compared to the ion chamber measurements (Table 1). All samples were in secular equilibrium during measurement, as shown in Figure 2. The ion chamber manufacturer error is reported as 3%. Measurements using NIST-traceable sources within the activity range of 5.705 to 39.257 MBq had 3% uncertainties. However, when measuring NIST-traceable sources at the lower activities of 158.73 and 391.09 kBq, the uncertainties were 9.7% and 9.6%, respectively.
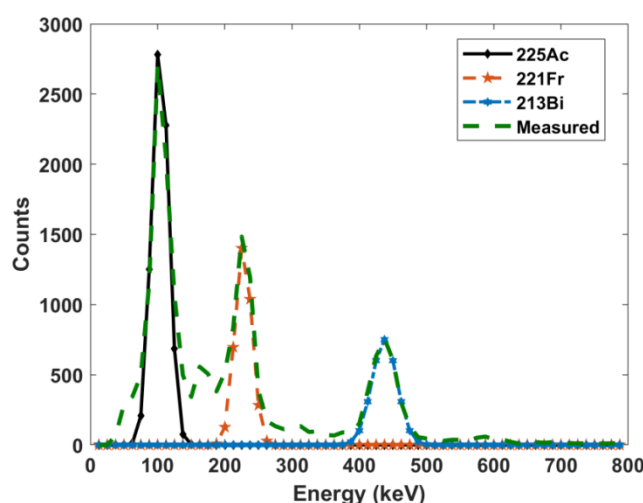
Figure 4. NaI(Tl) measured gamma spectrum with Gaussian fitting.

Table 1. Ion chamber and NaI(Tl) measured activities. Single measurements were taken in each detector. Notice that as the ion chamber readings increase, the discrepancies with the NaI(Tl) increase. All values in kBq. Note that the uncertainties in the ion chamber readings are expressed as 10% in accordance with the calibration measurements in the activity range (above). The NaI(Tl) uncertainties are expressed as the propagation of uncertainties in all steps of the calculation. The difference between the ion chamber readings and the NaI(Tl) determined activity for ^{225}Ac are indicated in the last column to the right.

Ion Chamber Reading	NaI(Tl) Determined Activities			
	^{225}Ac	^{221}Fr	^{213}Bi	^{225}Ac Percent Difference
70.3 ± 7.0	57.35 ± 7.57	66.97 ± 8.18	63.64 ± 7.98	20.23
144.3 ± 14.4	96.20 ± 9.81	115.07 ± 10.73	111.74 ± 10.57	40.00
222.0 ± 22.2	124.69 ± 11.17	152.81 ± 12.36	143.93 ± 12.00	56.14
299.7 ± 30.0	140.23 ± 11.84	177.97 ± 13.34	165.39 ± 12.86	72.50
370.0 ± 37.0	152.07 ± 12.33	198.32 ± 14.08	182.41 ± 13.51	83.49
447.7 ± 44.7	140.23 ± 11.84	211.64 ± 14.55	187.59 ± 13.70	104.59

The spectra acquired by the scintillation detector (Figure 4) have overlapping multiple peaks that are further masked by the poor resolution of the detector. Monte Carlo simulations with 1 keV resolution were run for the parent and gamma emitting daughter radioisotopes. As observed in Figure 5, ^{225}Ac, ^{221}Fr, and ^{213}Bi all exhibit many peaks in the 90 to 200 keV range. Monte Carlo simulations allowed for the accounting of contributions from each individual radioisotope to the overlapping gamma spectra.

Monte Carlo simulations were run using the bin width of the NaI(Tl) detector and ion chamber readings. The resulting spectra were compared to the corresponding scintillation detector spectra and it was observed that as the readings increased, the percent difference between the measured and simulated spectra increased. The percent differences ranged from 19% at 70.3 kBq up to 156% at 447.7 kBq. This is illustrated in Figure 6. The readings that minimized the mean percent differences were used as the equilibrium input activities in the Monte Carlo simulations. Figure 7 shows the matching of simulated spectra to measured spectra for all six of the samples of different quantities. This procedure was repeated for all ion chamber readings. Figure 8 shows the ion chamber reading and the simulated activity that matches to within 1% of the NaI(Tl) spectra for all of the samples. At low readings, the measured and simulated quantities agree reasonably well: 70.3 kBq measured in the ion chamber matched with 62.9 kBq equilibrium Monte Carlo activity and 144.3 kBq measured in the ion chamber matched with 107.3 kBq Monte Carlo activity. For larger ion chamber readings, the matched response began to plateau.
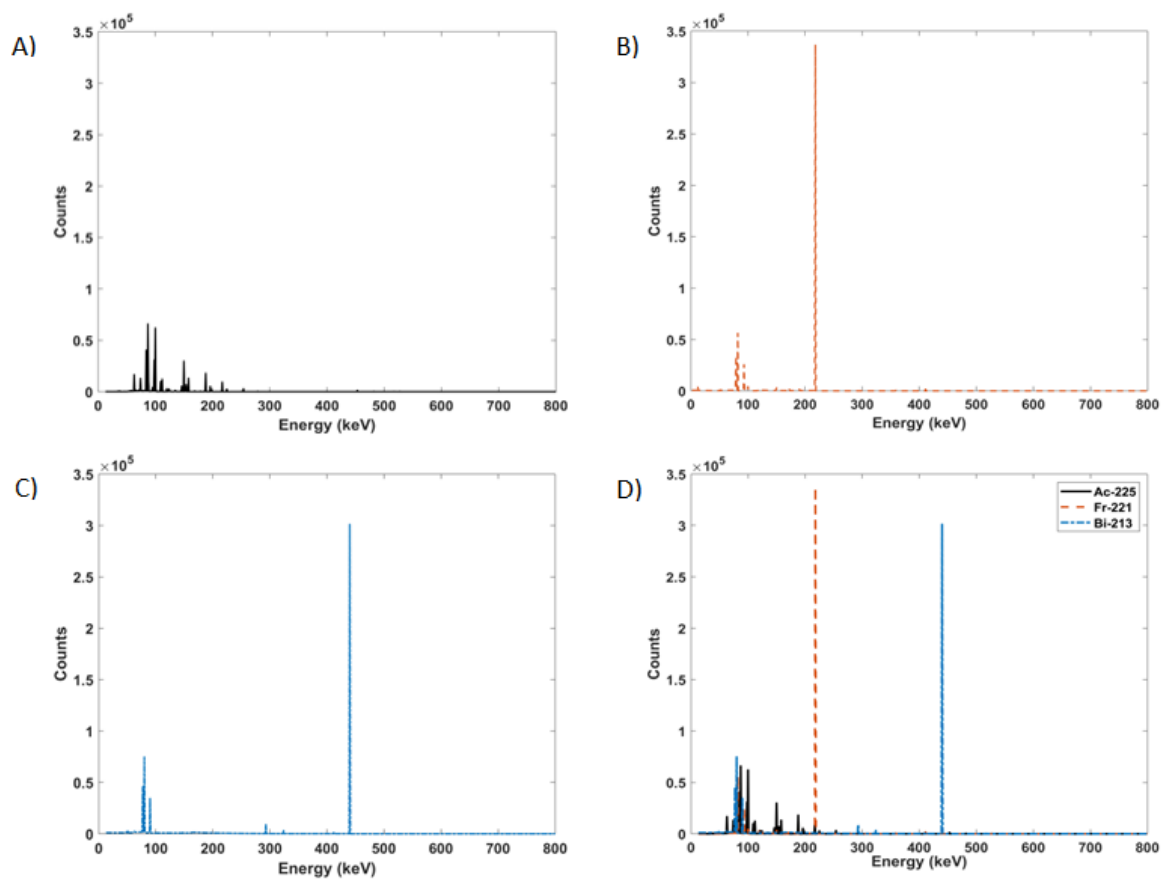
Figure 5. High definition Monte Carlo simulated gamma spectra of (**A**) ^{225}Ac, (**B**) ^{221}Fr, (**C**) ^{213}Bi, and (**D**) all three superimposed.
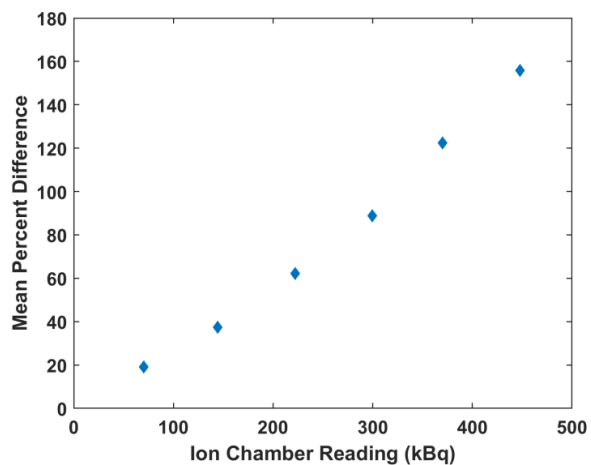

Figure 6. The mean percent difference between measured spectra and simulated spectra using the ion chamber reading measurement as input for the Monte Carlo model.
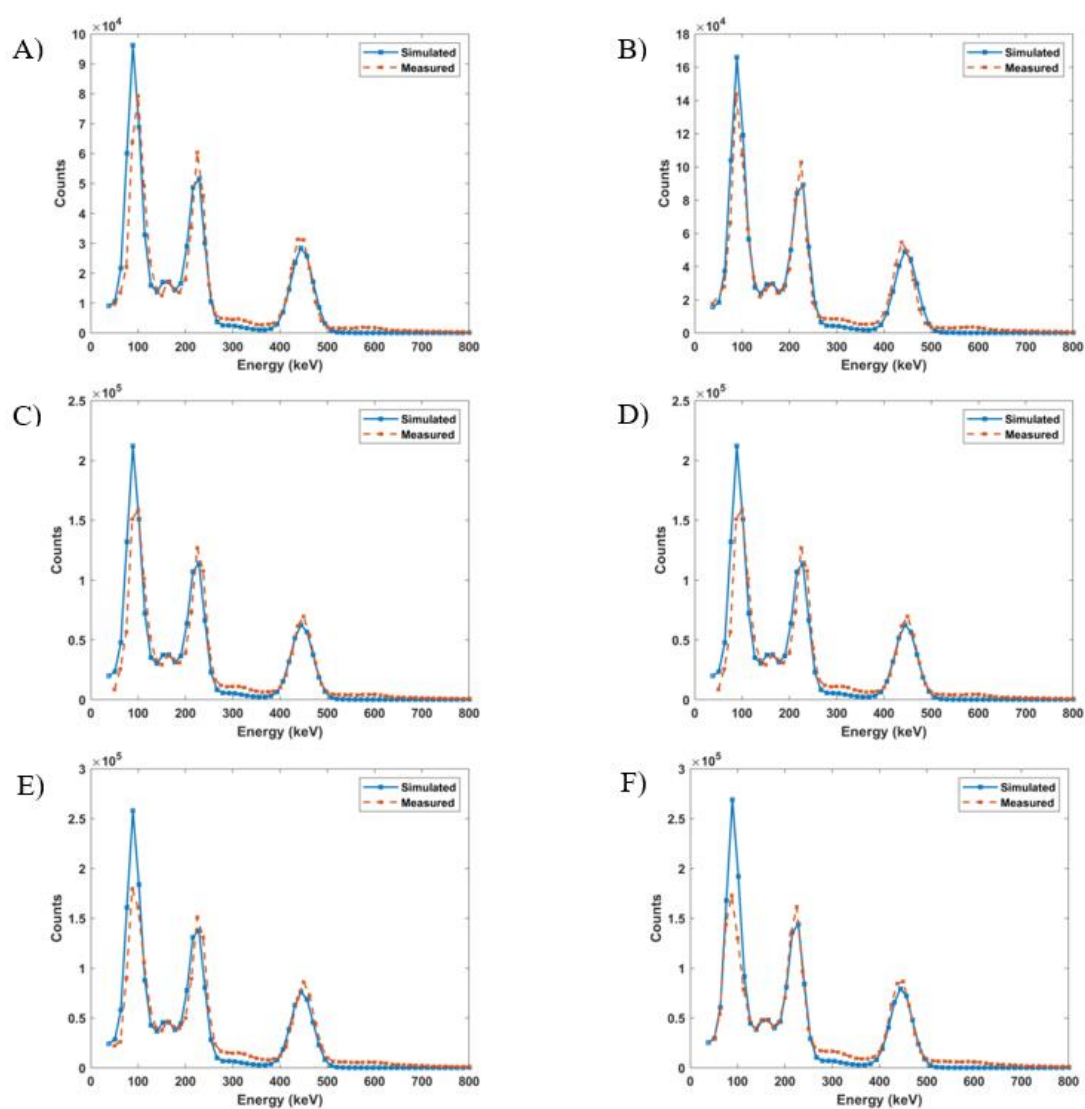
Figure 7. Measured vs. simulated ^{225}Ac spectra for (**A**) 70.3 kBq (0.17%), (**B**) 144.3 kBq (0.5%), (**C**) 222.0 kBq (0.19%), (**D**) 299.7 kBq (0.99%), (**E**) 370.0 kBq (0.11%), and (**F**) 447.7 kBq (0.02%). The values in parentheses are the mean percent differences between the two spectra.
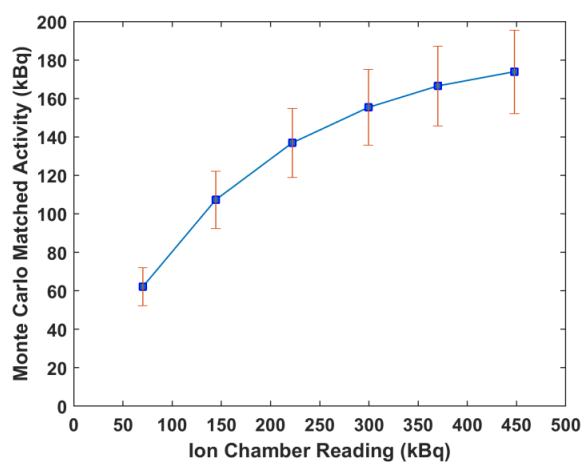

Figure 8. Activity response relationship between ion chamber reading and Monte Carlo-NaI(Tl) corrected spectra activity.

3. Discussion

The purpose of this work is to develop a method to determine the activities of ^{225}Ac and daughters in samples using standard clinical instruments. This is important for the determination of blood clearance pharmacokinetics and tissue biodistribution, both of which are used for radiation dosimetry calculations. In this work, an activity response relationship is determined between two radiation detectors commonly used for pre-clinical and clinical applications, a well-type NaI(Tl) scintillation detector and an ion chamber, respectively, where ^{225}Ac activities between the range of 70 to 450 kBq are not accurately measured by the scintillation detector. This relationship was used to inform Monte Carlo simulations that corrected scintillation detector measurements for accurate readings within this range. Although the error of the ion chamber measurements increased to ~10% within this activity range, compared with errors of 3% observed when measuring activities as low as 6 MBq, the error within this range for the scintillation detector as compared with the benchmarked Monte Carlo simulations ranged from 20% to 160% (Figure 6).

Several preclinical studies have reported using a NaI(Tl) gamma counter to measure ^{225}Ac injection and biodistribution activities [21–25]. Ion chambers are commonly used in nuclear medicine departments to prepare radiopharmaceuticals for patient injection. Measuring the activity of radioisotopes with complicated decay pathways, such as in the case of ^{225}Ac, the readings are not only the result of the parent's activity, but also from the contributions from the daughters' activities. From the solution of the system of decay equations, it was determined that ^{225}Ac and its daughters reached secular equilibrium in less than seven hours. While the daughters emit alpha particles and/or beta particles, the ranges of these particles are not penetrative enough to enter the ion chamber. Therefore, the ion chamber reading is a result of the gamma rays emitted from ^{225}Ac, ^{221}Fr, and ^{213}Bi. For example, a recent human ^{225}Ac therapy study reported injection activities for ^{225}Ac, but it was not clear if the reported values were from bulk measurements or if spectra were acquired and only ^{225}Ac emissions were considered [1].

Several groups have built Monte Carlo models of NaI(Tl) detectors to simulate response functions based on standard benchmark simulations and measurements of ^{137}Cs without description of further extensions of their models [26–31]. Herein, this procedure was extended to include the detector response for ^{225}Ac and its daughters. Implementation of the adjustment coefficients obtained by the nonlinear fitting into the Monte Carlo model adequately described the Gaussian spread of the detector pulses and was evident in benchmark testing. For all simulations, it was assumed that ^{225}Ac, ^{221}Fr, and ^{213}Bi were in secular equilibrium and thus had equal activities. The high-definition Monte Carlo simulations showed that both ^{221}Fr and ^{213}Bi exhibit peaks in the energy range of ^{225}Ac gamma pulse height distribution. Because of the 12.5 keV energy resolution of the NaI(Tl) detector, these peaks are summed to form a larger composite photopeak resulting in greater net counts, and thus over-calculated activities.

Gamma spectroscopic measurements were performed using the NaI(Tl) scintillation detector. All samples were measured after the calculated time to reach secular equilibrium, but the resulting activities were not equal. Further, the sum of activities for all three species greatly overestimated the ion chamber readings. Although the activities determined for the three isotopes should theoretically be identical, discrepancies are the result of the low energy bin resolution of the detector and the dead time count saturation. Using the measured ion chamber readings as input to the Monte Carlo simulations (Figure 6) largely overestimated the measured NaI(Tl) spectrum.

After minimizing the difference between each sample spectra and the Monte Carlo output, an activity response function relationship was determined for the two detectors (Figure 8). Both the Monte Carlo activity and the ion chamber reading represent the sum of the activities of ^{225}Ac, ^{221}Fr, and ^{213}Bi. The plot shows a curve with a decreasing positive slope as the ion chamber measurements increased beyond 148 kBq. This is a result of the NaI(Tl) dead time losses. As the activity of a sample increases, more pulses are lost, leading to errors in counting. The discrepancy between the low energy measured and simulated peaks in Figure 7 is also a result of dead time effects. The ratio of simulated

to measured peaks increases with increasing activity because the Monte Carlo model does not account for dead time. Further, the disagreement in the simulated and measured spectra in the low count region arises from the fact that the model represents an idealized detector and does not account for the metallic impurities of a real detector.

Standard NIST-traceable samples of ^{225}Ac are currently unavailable, so ^{225}Ac obtained from Oak Ridge was used as a surrogate calibration reference. These samples did not come with uncertainty estimations. As measurements using the recommended dial number agreed with the Oak Ridge surrogate reference samples to less than 10%, the readings of the ionization chamber were considered reliable for the study carried out in this work. The scintillation detector's measured energy resolution and detection efficiency over the energy range of ^{225}Ac gamma emissions (40-662 keV) agreed with other published studies and reports [28,32–34]. Consequently, this detector was also considered to be calibrated in efficiency and energy for ^{225}Ac analysis. The calibration sources used were all less than 185 kBq. When calibrating the ion chamber with sources with activity above 5.71 MBq, the error was less than 3%. When testing with sources in the lower activity range, error in the measurements increased to 10%, which is still within ANSI recommended tolerance. The measurement results showed that the responses from these two detectors do not correlate well in the activity range of 70 to 450 kBq, even though both detectors were calibrated for efficiency and energy resolution according to their respective recommended methods. The Monte Carlo model developed herein corrects NaI(Tl) measurements, allowing for a more accurate estimate of ^{225}Ac and daughter activities over a range of activities useful for both pre-clinical and clinical use.

4. Materials and Methods

4.1. Mathematical Model

The ^{225}Ac decay chain can be characterized by a system of ordinary differential equations that describe the activities and abundances of each species as a function of time (Figure 9) [35].

$$\frac{dN_{Ac^{225}}}{dt} = -\lambda_{Ac^{225}} \times N_{Ac^{225}}$$

$$\frac{dN_{Fr^{221}}}{dt} = -\lambda_{Fr^{221}} \times N_{Fr^{221}} + \lambda_{Ac^{225}} \times N_{Ac^{225}}$$

$$\frac{dN_{At^{217}}}{dt} = -\lambda_{At^{217}} \times N_{At^{217}} + \lambda_{Fr^{221}} \times N_{Fr^{221}}$$

$$\frac{dN_{Bi^{213}}}{dt} = -\lambda_{Bi^{213}} \times N_{Bi^{213}} + 0.9999 \times \lambda_{At^{217}} \times N_{At^{217}}$$

$$\frac{dN_{Rn^{217}}}{dt} = -\lambda_{Rn^{217}} \times N_{Rn^{217}} + 0.0001 \times \lambda_{At^{217}} \times N_{At^{217}}$$

$$\frac{dN_{Po^{213}}}{dt} = -\lambda_{Po^{213}} \times N_{Po^{213}} + 0.98 \times \lambda_{Bi^{213}} \times N_{Bi^{213}} + \lambda_{Rn^{217}} \times N_{Rn^{217}}$$

$$\frac{dN_{Tl^{209}}}{dt} = -\lambda_{Tl^{209}} \times N_{Tl^{209}} + 0.02 \times \lambda_{Bi^{213}} \times N_{Bi^{213}}$$

$$\frac{dN_{Pb^{209}}}{dt} = -\lambda_{Pb^{209}} \times N_{Pb^{209}} + \times \lambda_{Po^{213}} \times N_{Po^{213}} + \lambda_{Tl^{209}} \times N_{Tl^{209}}$$

$$\frac{dN_{Bi^{209}}}{dt} = \lambda_{Pb^{209}} \times N_{Pb^{209}}$$

Figure 9. System of equations describing the decay of ^{225}Ac to the very long-lived ^{209}Bi.

In Figure 9, N_x and λ_x denote the number of atoms of radionuclide and the decay constant of radionuclide X, respectively. These equations were simultaneously solved in Mathematica with the initial (time zero) ^{225}Ac activity set to 3.7×10^4 kBq and all daughters' activities set to 0 kBq to determine the times at which daughter products reach equilibrium with the parent.

4.2. Monte Carlo Model

The Monte Carlo N-Particle version 6.1 (MCNP6.1) package was used to simulate the pulse height gamma distribution from ^{225}Ac [36]. A computational model of the 2″ × 2″ NaI(Tl) 4π detector

was built using the material compositions and dimensions given in the manufacturer's manual, as illustrated in Figure 10 [32].
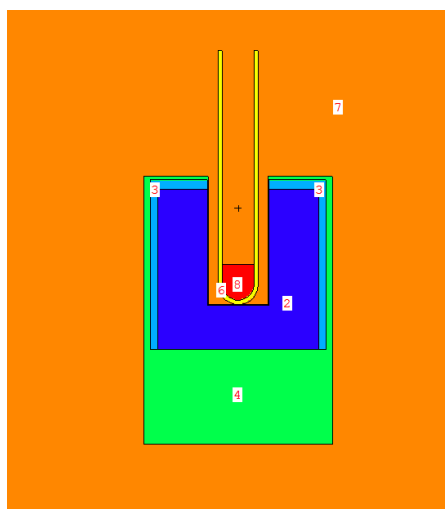

Figure 10. Geometry of the Monte Carlo model wipe test scintillator detector. Image generated using the Visual Editor software for MCNP. 2: NaI; 3: MgO; 4: Al; 6: polyethylene; 7: air; 8: H_2O with ^{225}Ac, ^{221}Fr, ^{213}Bi source distributions.

A standard 5 mL polyethylene test tube filled with 1 mL of water was placed in the well of the detector. The source was defined to be uniformly distributed in the 1 mL water volume. All 75 photon emissions from ^{225}Ac, ^{221}Fr, and ^{213}Bi were defined by energy and abundance [9]. The photomultiplier tube was modeled as a 30 mm diameter aluminum cylinder to account for backscatter [26].

Photon transport was conducted using the mcplib84 photoatomic data library and detailed photon physics interactions [37]. These include Thomson scattering, Compton scattering, and photoelectric absorption with the creation of fluorescence photons or Auger electrons. Full photon and electron simulations were performed and spectra were compared to those obtained from only photon transport. Photon and electron cell importances were set to 1 for all cells in the geometry. A mean percent difference of less than 1% between photon/electron transport and photon only transport was observed in benchmark generated spectra of ^{137}Cs. There were also less than 1% differences in the Compton edge and Compton regions. Therefore, the computationally expensive tracking of electrons was omitted in subsequent simulations and electron cell importances were set to 0. In this case, the electrons generated are assumed to deposit their energy locally. Any electron induced bremsstrahlung photons produced are accounted for in the thick-target bremsstrahlung model [38]. This model skips the electron tracking step and transports the generated photon in the direction of the parent electron.

The pulse height distribution tally (F8) was used to calculate the deposited energy in the NaI(Tl) crystal. This tally accumulates the kinetic energy lost by local photon-induced secondary electrons, per history, in a specified volume. The tally was divided into 64 bins, each with a 12.5 keV width to match the energy resolution of the detector. To relate the simulated response to activity, values for the number of gamma emissions per disintegration for each isotope, scaled by the activity, were placed on the source probability card in the source definition. The resulting tallies were then multiplied by the sum of these values, the live acquisition time, and an activity conversion factor containing photon abundance per decay. For each simulation, 2×10^8 histories were run to achieve less than 1% error under each photopeak.

MCNP6.1 models an ideal detector and thus does not take into account the Gaussian shape of experimental NaI(Tl) energy resolution resulting from intrinsic light collection inefficiency, statistical fluctuation in charge multiplication in the photomultiplier tube, and electronic noise [39]. To account for the statistical variance of physical spectra, a Gaussian energy broadening function (MCNP6.1

FT8 GEB) was applied to the simulated pulse height distribution. The GEB function was obtained experimentally from measurements of the detector's specific full width at half maximum (FWHM) from a set of isotopes of differing energies. Spectra from five isotopes were measured and the FWHM of each peak was calculated. The isotopes used and their physical characteristics are listed in Table 2.

Table 2. Physical characteristics of the radioactive sources used for NaI(Tl) detector energy response measurements [9].

Source	Half-Life	Energy (keV)
^{129}I	1.6^7 yr	39.5
^{241}Am	432.6 yr	59.5
^{57}Co	271.7 d	122.0
^{68}Ga	67.7 m	511.0
^{137}Cs	30.1 yr	661.6

A curve of FWHM as a function of energy was fit with the following nonlinear function shown in Equation (1) [36]:

$$FWHM = a + b\sqrt{E + cE^2}, \tag{1}$$

where E is the incident energy of the incident photon in keV; and a, b, and c are parameters that were determined by least squares fitting and input in the FT8 command.

4.3. Monte Carlo Simulations

There are no standard NIST-traceable calibration sources for ^{225}Ac to validate the detector model. Instead, the spectrum of a NIST-traceable 155.4 kBq ^{137}Cs (662 keV photopeak) source was measured in the NaI(Tl) detector and compared to a simulated spectrum of the same activity for validation.

After the model was validated, a high definition version of the F8 pulse height tally (1 keV bin width) was simulated with only ^{225}Ac defined as the source. This was followed by separate high definition simulations of ^{221}Fr and ^{213}Bi. These simulations were done to see what radiations contribute to each peak, which are masked by the poor energy resolution of the NaI(Tl) detector.

4.4. Experimental Measurements

The ^{225}Ac used in this work was obtained from Oak Ridge National Laboratory (ORNL). The Atomlab^{TM} Wipe Test Counter (Biodex Medical Systems, Inc., Shirley, New York, USA) was used to perform gamma spectroscopy measurements with ^{225}Ac. The wipe test counter is a 2″ × 2″ NaI(Tl) well-type scintillation detector with 1.2 cm of lead shielding. The multichannel analyzer associated with the wipe test NaI(Tl) detector has 64 12.5 keV channels ranging from 0 to 800 keV. Spectra obtained with the NaI(Tl) detector for 30 s acquisition time and full energy window to include gamma counts from ^{225}Ac, with composite peak at 99.8 keV, and from its two gamma-emitting daughters, ^{221}Fr ($T_{1/2}$ = 4.9 min) with a peak at 218.1 keV and ^{213}Bi ($T_{1/2}$ = 46 min) with a peak at 440.5 keV. Background spectrum measurements were performed and subtracted from all obtained ^{225}Ac spectra. The net background readings for the NaI(Tl) detector were in the range of 100 to 200 net counts per minute. The net counts for an ^{225}Ac sample of 45 kBq activity was 444,000 per minute.

Dead time measurements and calculations were performed according to the two-source method [10]. Two different sources of ^{22}Na with different activities were each measured individually and then in combination.

In-house software was developed using MATLAB to calculate the net number of gamma counts, N, by fitting each peak with a Gaussian fit and integrating. Alpha particle activity for each species was calculated using factors for gamma abundance (Y) per alpha decay: ^{225}Ac (1%), ^{221}Fr (11.4%), ^{213}Bi (25.9%) [9].

The detector efficiency, ε, and energy calibration for the NaI(Tl) detector were determined by performing measurements of NIST-traceable ^{137}Cs, [133]Ba, and [57]Co sources. These radionuclides have numerous photopeaks covering the gamma energy spectrum of [225]Ac. The activity is then given by the following Equation (2):

$$A = \frac{N}{t * \varepsilon * Y},$$ (2)

where t is live time. The activity of [225]Ac determined using this approach was compared to a decay corrected sample of known activity from ORNL. A factor of 0.082 was applied to Equation (2) to obtain [225]Ac activity values to within 5% of the ORNL specified [225]Ac activity. The uncertainty in the NaI(Tl)-determined activity was calculated by propagating individual uncertainties in the net number of counts and the efficiency measurements, as is typically done in nuclear counting measurements.

The Atomlab[TM] 500 Dose Calibrator is a well-type pressured ion chamber filled with argon gas that is commonly used in the clinic. This instrument was calibrated for energy and efficiency with the following NIST-traceable sources: [137]Cs (6.63 MBq), [57]Co (39.26 MBq), and [133]Ba (5.71 MBq) by the vendor. Lower activity NIST-traceable sources provided by Eckert & Ziegler were also used: [137]Cs with 158.73 kBq and [57]Co with 391.09 kBq activities. No significant variation in the calibration coefficient as a function of photon energy was observed. An ion chamber linearity test was performed with ^{18}F in the activity range of 1.2 GBq to 266.0 kBq and a variance of 1.4% was observed. The dial number was set at 38.2 for [225]Ac, as indicated by the vendor and confirmed by our comparison with two decay corrected samples of different activities obtained from Oak Ridge. Measurements of these samples in the ion chamber agreed with the Oak Ridge measurements to within 7%. In order to determine the relationship between this ion chamber and the NaI(Tl) detector, six different activities of [225]Ac samples were measured using the ion chamber: 70.3 ± 7.0, 144.3 ± 14.4, 222.0 ± 22.2, 299.7 ± 30.0, 370.0 ± 37.0, and 447.7 ± 44.7 kBq. Each sample was measured and placed in the NaI(Tl) detector, and a spectrum was obtained and compared. Using the activity reading from the ion chamber as the initial parent–daughter equilibrium activity input for the Monte Carlo model, simulated spectra were calculated and compared to the measured spectra from the NaI(Tl) detector. Mean absolute percent differences at analogous bins between the experimental and simulated spectra were calculated. Using the ion chamber measured activity as input to the Monte Carlo simulations underestimated the readings from the NaI(Tl), so several successive runs were completed using different activities as input in symmetrical range around the initial point in order to match the spectra. The percent differences were plotted against input activity and fitted with a linear model. The x-intercept was found in order to determine the minimum mean percent difference between the measured and simulated spectra. This process was repeated for each sample and an activity response function relationship was determined between the ion chamber and the NaI(Tl) detector. The uncertainty in the activity relationship determined using this methodology was analyzed by adding the uncertainties in the NaI(Tl) measurements, σ_{NaI}^2; the ion chamber measurements, σ_{IC}^2; and the Monte Carlo calculations, σ_{MC}^2, in quadrature (Equation (3)):

$$\sigma_A = \sqrt{\sigma_{NaI}^2 + \sigma_{IC}^2 + \sigma_{MC}^2}.$$ (3)

5. Conclusions

In this work, the [225]Ac activity response function between two commonly used instruments was investigated, a range of activities (70 to 450 kBq) was identified, and a method was developed using Monte Carlo simulations to correct scintillation detector measurements within this range. The scintillation detector was calibrated in energy and efficiency using NIST-traceable sources covering a broad energy range, while the ion chamber was calibrated in efficiency using a surrogate calibration reference. The error of ion chamber measurements increased with decreasing activity, but remained within the ANSI recommended value of 10%. The NaI(Tl) performed poorly from 70 to 450 kBq. Therefore, a Monte Carlo model was built to correct the NaI(Tl) measurements, thereby providing

improved accuracy. The corrections provided by the Monte Carlo model will provide a useful tool to make corrections to the activity values measured by the well-type NaI(Tl) detector. This allows for the better quantification of alpha-particle emitting radiopharmaceuticals and daughter byproducts in pre-clinical and clinical studies. In this case, use of scintillation gamma spectroscopy will be the preferred method.

References

1. Kratochwil, C.; Bruchertseifer, F.; Giesel, F.L.; Weis, M.; Verburg, F.A.; Mottaghy, F.; Kopka, K.; Apostolidis, C.; Haberkorn, U.; Morgenstern, A. 225Ac-PSMA-617 for PSMA-Targeted alpha-Radiation Therapy of Metastatic Castration-Resistant Prostate Cancer. *J. Nucl. Med.* **2016**, *57*, 1941–1944. [CrossRef] [PubMed]

2. Kratochwil, C.; Bruchertseifer, F.; Rathke, H.; Bronzel, M.; Apostolidis, C.; Weichert, W.; Haberkorn, U.; Giesel, F.L.; Morgenstern, A. Targeted alpha-Therapy of Metastatic Castration-Resistant Prostate Cancer with (225)Ac-PSMA-617: Dosimetry Estimate and Empiric Dose Finding. *J. Nucl. Med.* **2017**, *58*, 1624–1631. [CrossRef] [PubMed]

3. Parikh, S.; Murray, L.; Kenning, L.; Bottomley, D.; Din, O.; Dixit, S.; Ferguson, C.; Handforth, C.; Joseph, L.; Mokhtar, D.; et al. Real-world Outcomes and Factors Predicting Survival and Completion of Radium 223 in Metastatic Castrate-resistant Prostate Cancer. *Clin. Oncol.* **2018**, *30*, 548–555. [CrossRef] [PubMed]

4. Deshayes, E.; Roumiguie, M.; Thibault, C.; Beuzeboc, P.; Cachin, F.; Hennequin, C.; Huglo, D.; Rozet, F.; Kassab-Chahmi, D.; Rebillard, X.; et al. Radium 223 dichloride for prostate cancer treatment. *Drug Des. Dev. Ther.* **2017**, *11*, 2643–2651. [CrossRef] [PubMed]

5. Kozak, R.W.; Atcher, R.W.; Gansow, O.A.; Friedman, A.M.; Hines, J.J.; Waldman, T.A. Bismuth-212-Labeled Anti-Tac Monoclonal Antibody α-Particle-Emitting Radionuclides as Modalities for Radioimmunotherapy. *Proc. Natl. Acad. Sci. USA* **1986**, *86*, 474–478. [CrossRef] [PubMed]

6. Tafreshi, N.K.; Tichacek, C.J.; Pandya, D.N.; Doligalski, M.L.; Budzevich, M.M.; Kil, H.; Bhatt, N.B.; Kock, N.D.; Messina, J.L.; Ruiz, E.E.; et al. Melanocortin 1 Receptor Targeted Alpha-Particle Therapy for Metastatic Uveal Melanoma. *J. Nucl. Med.* **2019**, *60*, 1124–1133. [CrossRef]

7. Jurcic, J.G. Clinical Studies with Bismuth-213 and Actinium-225 for Hematologic Malignancies. *Curr. Radiopharm.* **2018**, *11*, 192–199. [CrossRef]

8. Miederer, M.; Scheinberg, D.A.; McDevitt, M.R. Realizing the potential of the Actinium-225 radionuclide generator in targeted alpha-particle therapy applications. *Adv. Drug Deliv. Rev.* **2008**, *60*, 1371–1382. [CrossRef]

9. Be, M.M.; Chisté, V.; Dulieu, C.; Mougeot, X.; Browne, E.; Chechev, V.; Kuzmenko, N.; Kondev, F.; Luca, A.; Galan, M.; et al. *Table of Radionuclides*; Laboratoire National Henri Becquerel: Gif-sur-Yvette Cedex, France, 2009; Volume 5, pp. 1–14.

10. Knoll, G.F. *Radiation Detection and Measurement*; Wiley: Hoboken, NJ, USA, 2010.

11. Bolch, W.E.; Eckerman, K.F.; Sgouros, G.; Thomas, S.R. MIRD pamphlet No. 21: A generalized schema for radiopharmaceutical dosimetry–standardization of nomenclature. *J. Nucl. Med.* **2009**, *50*, 477–484. [CrossRef]

12. Gilmore, G.; Hemingway, J.D. *Practical Gamma-Ray Spectrometry*; Wiley: Hoboken, NJ, USA, 1995.

13. Faanu, A.; Emi-Reynolds, G.; Darko, E.; Awudu, A.R.; Glover, E.; Adukpo, O.; Otoo, F.; Kpeglo, D.O.; Lawluvi, H. Calibration and performance testing of sodium iodide, NaI (Tl), detector at the food and environmental laboratory of the radiation protection institute of the Ghana atomic energy commission. *West Afr. J. Appl. Ecol.* **2012**, *19*, 39–52.

14. Lodge, M.A.; Holt, D.P.; Kinahan, P.E.; Wong, D.F.; Wahl, R.L. Performance assessment of a NaI(Tl) gamma counter for PET applications with methods for improved quantitative accuracy and greater standardization. *EJNMMI Phys.* **2015**, *2*, 11. [CrossRef]

15. Bergeson, S.D.; Ware, M.; Hawk, J. On the use of NaI scintillation for high stability nuclear decay rate measurements. *arXiv* **2017**, arXiv:170703392.

16. Vitorelli, J.; Silva, A.; Crispim, V.; Da Fonseca, E.; Pereira, W. Monte Carlo simulation of response function for a NaI(Tl) detector for gamma rays from 241Am/Be source. *Appl. Radiat. Isot.* **2005**, *62*, 619–622. [CrossRef] [PubMed]

17. Cengiz, A. An approximation for response function to γ-rays of NaI(Tl) detectors up to 1.5MeV. *Appl. Radiat. Isot.* **2008**, *66*, 1371–1376. [CrossRef]

18. Casanovas, R.; Morant, J.; Salvado, M. Energy and resolution calibration of NaI(Tl) and LaBr3(Ce) scintillators and validation of an EGS5 Monte Carlo user code for efficiency calculations. *Nucl. Instrum. Methods Phys. Res. Sect. A Accel. SpectrometersDetect. Assoc. Equip.* **2012**, *675*, 78–83. [CrossRef]

19. American National Standards Institute. *ANSI N42.13-2004 (Reaffirmation of ANSI N42.13-1986): American National Standard Calibration and Usage of "Dose Calibrator" Ionization Chambers for the Assay of Radionuclides*; IEEE: New York, NY, USA, 2004.

20. Capogni, M.; Cozzella, M.; De Felice, P.; Fazio, A. Comparison between two absolute methods used for 177Lu activity measurements and its standardization. *Appl. Radiat. Isot.* **2012**, *70*, 2075–2080. [CrossRef]

21. McDevitt, M.R.; Ma, D.; Lai, L.T.; Simon, J.; Borchardt, P.; Frank, R.K.; Wu, K.; Pellegrini, V.; Curcio, M.J.; Miederer, M.; et al. Tumor Therapy with Targeted Atomic Nanogenerators. *Science* **2001**, *294*, 1537–1540. [CrossRef] [PubMed]

22. Borchardt, P.E.; Yuan, R.R.; Miederer, M.; McDevitt, M.R.; Scheinberg, D.A. Targeted actinium-225 in vivo generators for therapy of ovarian cancer. *Cancer Res.* **2003**, *63*, 5084–5090.

23. Miederer, M.; McDevitt, M.R.; Sgouros, G.; Kramer, K.; Cheung, N.K.V.; Scheinberg, D.A. Pharmacokinetics, dosimetry, and toxicity of the targetable atomic generator, 225Ac-HuM195, in nonhuman primates. *J. Nucl. Med.* **2004**, *45*, 129–137. [PubMed]

24. Miederer, M.; McDevitt, M.R.; Borchardt, P.; Bergman, I.; Kramer, K.; Cheung, N.K.; Scheinberg, D.A. Treatment of neuroblastoma meningeal carcinomatosis with intrathecal application of alpha-emitting atomic nanogenerators targeting disialo-ganglioside GD2. *Clin. Cancer Res.* **2004**, *10*, 6985–6992. [CrossRef]

25. Miederer, M.; Henriksen, G.; Alke, A.; Mossbrugger, I.; Quintanilla-Martinez, L.; Senekowitsch-Schmidtke, R.; Essler, M. Preclinical evaluation of the alpha-particle generator nuclide 225Ac for somatostatin receptor radiotherapy of neuroendocrine tumors. *Clin. Cancer Res.* **2008**, *14*, 3555–3561. [CrossRef] [PubMed]

26. Shi, H.X.; Chen, B.X.; Li, T.Z.; Yun, D. Precise Monte Carlo simulation of gamma-ray response functions for an NaI(Tl) detector. *Appl. Radiat. Isot.* **2002**, *57*, 517–524. [CrossRef]

27. Tam, H.D.; Yen, N.T.H.; Tran, L.B.; Chuong, H.D.; Thanh, T.T. Optimization of the Monte Carlo simulation model of NaI(Tl) detector by Geant4 code. *Appl. Radiat. Isot.* **2017**, *130*, 75–79.

28. Salgado, C.; Brandão, L.; Schirru, R.; Pereira, C.; Conti, C. Validation of a NaI(Tl) detector's model developed with MCNP-X code. *Prog. Nucl. Energy* **2012**, *59*, 19–25. [CrossRef]

29. Amgarou, K.; Domingo, C.; Bouassoule, T.; Fernandez, F. Monte Carlo simulation of the NaI(Tl) detector response to measure gold activated foils. *Nucl. Instrum. Methods Phys. Res. Sect. B Beam Interact. Mater. At.* **2009**, *267*, 2944–2951. [CrossRef]

30. Wirawan, R.; Waris, A.; Djamal, M.; Handayani, G. Simulation of energy absorption spectrum in NaI crystal detector for multiple gamma energy using Monte Carlo method. *AIP Conf. Proc.* **2015**, *1656*, 060008.

31. Olaniyi, H.; Owojori, A.; Olise, F. Monte Carlo simulation of a NaI[Tl] detector's response function. *J. Instrum.* **2017**, *12*, 12015. [CrossRef]

32. Biodex Medical Systems Inc. *Atomlab^{T.M.} Wipe Test Counter: Operation and Service Manual*; Biodex Medical Systems Inc.: Shirley, NY, USA, 2017.

33. Demir, D.; Ün, A.; Şahin, Y. Efficiency Determination for NaI (Tl) Detectors in the 23 keV to 1333 keV Energy Range. *Instrum. Sci. Technol.* **2008**, *36*, 291–301. [CrossRef]

34. Mouhti, L.; Elanique, A.; Messous, M. Monte Carlo modelling of a NaI(Tl) scintillator detectors using MCNP simulation code. *J. Mater. Environ. Sci.* **2017**, *8*, 4560–4565. [CrossRef]

35. Bateman, H. Solution of a system of differential equations occurring in the theory of radioactive transformation. *Proc. Camb. Philos. Soc.* **1910**, *15*, 423–427.

36. Goorley, T.; James, M.; Booth, T.; Brown, F.; Bull, J.; Cox, L.J.; Durkee, J.; Elson, J.; Fensin, M.; Forster, R.A.; et al. Initial MCNP6 Release Overview. *Nucl. Technol.* **2012**, *180*, 298–315. [CrossRef]

37. White, M.C. *Photoatomic Data Library MCPLIB04: A New Photoatomic Library Based on Data from ENDF/B-VI Release 8*; Internal Memorandum X-5: MCW-02-111; Los Alamos National Laboratory: Los Alamos, NM, USA, 2002.

38. Team, X.M.C. *LA-UR-03-1987MCNP–Version 5: Overview and Theory*; Los Alamos National Laboratory: Los Alamos, NM, USA, 2003; Volume 1.

39. Moszyński, M.; Zalipska, J.; Balcerzyk, M.; Kapusta, M.; Mengesha, W.; Valentine, J.D. Intrinsic energy resolution of NaI(Tl)11Support for this work was provided by the Polish Committee for Scientific Research, Grant No 8 T10C 002 20. *Nucl. Instrum. Methods Phys. Res. Sect. A Accel. Spectrometers Detect. Assoc. Equip.* **2002**, *484*, 259–269. [CrossRef]

Genomic Mutation as a Potential Driver of the Development of Bone-Related Cancers

Sun H Park and Yusuke Shiozawa, Department of Cancer Biology and Comprehensive Cancer Center, Wake Forest University Health Sciences, Winston-Salem, NC, United States

Nomenclature

AID	Activation-induced cytidine deaminase
CML	Chronic myeloid leukemia
CSR	Class switch recombination
DSBs	Double strand breaks
Ig	Immunoglobulin
MAPK	Mitogen-activated protein kinase
mTOR	Mammalian target of rapamycin
NSG	The next-generation sequencing
Ph	Philadelphia chromosome mutation or Philadelphia translocation
PI3K	Phosphoinositide 3-kinases
PTHrP	Parathyroid hormone-related protein
RANKL	Receptor activator of nuclear factor κB ligand
RB1	Retinoblastoma 1
SOH	Somatic hypermutation
TGF-β	Transforming growth factor-beta

Introduction

"What causes cancer?" This is still an unanswered, and likely unanswerable (for now), question, despite recent advances in understanding the molecular and cellular basis of cancer development and progression. One might conclude that cancer is an aging-related disease. Seventy-eight percent of people in US who are diagnosed with cancer are older than 55 years (American Cancer Society, 2015). Indeed, the average ages when patients are diagnosed with breast, lung, and prostate cancer, are around 61, 70, and 66 years, respectively (Zullig et al., 2012). These epidemiological data clearly support the notion that aging impacts cancer development. However, this doesn't explain why cancer also often occurs in younger age groups, including pediatric populations. Moreover, a recent trend has shown that the incidence of cancer is rising among young adults (Sung et al., 2019). Mechanisms of carcinogenesis between young and old age patients may not be the same.

Although it is still controversial, the development of some of the pediatric cancers are thought to be associated with inherited gene mutations or alterations. In Alfred Knudson's observation of patients of retinoblastoma (Knudson, 1971), a pediatric cancer of retinal cells, he found that (1) there are inherited and non-inherited (sporadic) types of retinoblastoma; and (2) the inherited retinoblastoma occurs more often bilaterally at early age, whereas the sporadic retinoblastoma usually presents unilaterally at later age. Based on these findings, Knudson hypothesized that the inherited retinoblastoma already acquires one mutation or a "hit" (e.g. the tumor suppressor retinoblastoma 1 (RB1) gene mutation) on one allele of all genes and therefore another "hit" can happen easily and on the multiple genes. On the contrary, it is very difficult to develop the second "hit" on a single gene, when there is no inherited mutation. Thus, it usually takes a long period of time to develop the sporadic retinoblastoma and it happens unilaterally. This is now known as the two-hit theory. If this theory is plausible, the notion that the risk of developing cancer increases as we grow older certainly makes sense, since most genes do not show phenotypic changes unless two or multiple "hits" occur in the specific locations (Knudson, 1971). Although we all have some inherited gene mutations, the prevalence of cancer risk-associated inherited gene mutations is not very high. Therefore, it takes time to develop multiple mutations on one single gene. Moreover, genes are

more frequently mutated in older individuals. Older people have been exposed to more carcinogens, such as UV light, tobacco, and alcohol, than younger people. Carcinogens are known to cause mutations, such as in the TP53 gene, which is associated with P53 protein production (Ouhtit et al., 1998; Rivlin et al., 2011; Ronchetti et al., 2004). P53 serves as a tumor suppressor protein by inducing cell cycle arrest or cell death of fast dividing cells, which may eventually become cancerous. Because gene mutations or alterations can contribute to cancer at any age, the determination of oncologic gene signatures is a useful first step toward understanding cancer development and progression.

Cancer genomic research has been intensively conducted in the last 30–40 years (Stratton et al., 2009), in parallel with the improvement of high-throughput DNA sequencing technology. The recent development of the next-generation sequencing (NGS) technologies have allowed for the production of large volumes of sequencing data rapidly (4 h/run vs. 24 h/run with the first-generation sequencing technologies) and cost effectively (4 cents/kilobyte vs. 20 cents/kilobyte with the first-generation sequencing technologies) (Kchouk et al., 2017). Using NGS, thousands of innate and acquired mutations associated with cancer development (e.g. BRCA1 and BRCA2, known to be associated with development of breast and ovarian cancers Mersch et al., 2015) have been discovered (Kamps et al., 2017). Although these findings result in deeper understanding of cancer genomics, and improvement of diagnoses and treatments of cancer, we are still losing the battle against particularly "metastatic disease." Bone is one of the major metastatic sites (Coleman, 2001). When cancer patients with cancer develop bone metastases, their 5-year survival rate declines by more than 70% (Svensson et al., 2017) and the median survival time is approximately 2–3 years (Bienz and Saad, 2015). Although bisphosphonate and denosumab, a human monoclonal anti-receptor activator of nuclear factor κB ligand (RANKL) antibody, which both decrease bone resorption, are established treatments for bone metastases, they ultimately fail to improve overall survival (Stopeck et al., 2010; Fizazi et al., 2011). Radium-223, which forms complexes with hydroxyapatite in bone (Badrising et al., 2016; Vignani et al., 2016; Abou et al., 2016), can extend overall survival of prostate cancer patients with bone metastases (Parker et al., 2013), but only by a few months (average = 3 months). Since these treatments mainly target the bone microenvironment, targeting mechanisms other than the bone microenvironment are needed if eradicating bone metastasis is to be an achievable clinical goal.

Targeted therapies against BCR-ABL gene mutation with small molecular kinase inhibitors (e.g. imatinib) have successfully improved overall survival of patients with chronic myeloid leukemia (CML) (Iqbal and Iqbal, 2014; Massoud et al., 2017; Hochhaus et al., 2017). Since specific mutations associated with development and progression of cancers found in bone (or bone-related cancers), not only bone metastatic cancers, but also cancers with mesenchymal origin (e.g. osteosarcoma) and cancers with hematopoietic origin (e.g. multiple myeloma, leukemia) have recently been discovered, targeting the mutations can lead to new therapeutic approaches for these cancers. In this review, we will discuss (i) the recent discovery of gene mutations in bone-related cancers; (ii) progress and shortcomings of the mutation-targeted therapies for bone-related cancers; and (iii) future directions for genomic studies in bone-related cancers.

Gene Mutations in Bone Metastasis

Each cancer with metastatic ability has a particular preference for organs where it disseminates. For example, prostate cancer preferably metastasizes to bone, but rarely spreads to brain (Taddei et al., 2012; Sutton et al., 1996). Surprisingly, the anatomical location of cancers and blood flow patterns do not explain preference of metastatic sites of cancers. The metastatic process requires the interaction between cancer cells and the secondary sites, or metastatic microenvironment. Stephen Paget first hypothesized (Ribatti et al., 2006; Paget, 1989; Fidler and Poste, 2008), and recent evidence now strongly supports, that the metastatic microenvironment (soil) controls the metastatic fate of cancer cells (seed) (Liu et al., 2017). Moreover, it has been demonstrated that subpopulations of tumor cells can metastasize to certain organs (Langley and Fidler, 2007). This is believed to be due in part to heterogeneous nature of cancer. In fact, there is a distinct pattern between gene expression among cancer cells that possess different organ-tropisms (Chiang and Massague, 2008; Weigelt et al., 2003), suggesting that there could be gene expression patterns associated with bone metastatic potential.

Parathyroid hormone-related protein (PTHrP) is one of the well-studied molecules that are relevant for bone metastatic progression. PTHrP derived from bone metastatic cancer cells stimulates osteoblasts to release RANKL, which enhances osteoclastogenesis, resulting in osteolytic bone lesions (Soki et al., 2012). This bone resorption process enables bone matrix to release transforming growth factor- beta (TGF-ß) which further induces PTHrP release from bone metastatic cancer cells (Clines and Guise, 2005). Along with this notion, 90% of breast cancer tissues found in bone metastatic sites express high levels of PTHrP, whereas only 17% of those found in metastatic sites other than bone highly express PTHrP (Powell et al., 1991). Interestingly, the oncogenic KRAS gene mutation correlates with increased PTHrP levels in cancer (Kamai et al., 2001; Rudduck et al., 1993). The KRAS mutation is specifically associated with poor prognosis of lung adenocarcinoma patients with bone metastases, while KRAS mutation fails to affect prognosis of those patients with other metastases (Lohinai et al., 2017). Although further studies are clearly needed, these findings suggest that KRAS mutation plays a crucial role in metastatic progression in bone by increasing PTHrP levels in bone metastatic cancer. Furthermore, a recent NGS study identifying gene mutations associated with bone metastasis in 8 bone metastatic samples obtained from non-small cell lung cancer patients revealed that among 3620 mutated genes discovered, mutations of hepatocyte nuclear factor 1 alpha, adenomatous polyposis coli, and CD22 are found in all 8 samples and have higher consistent mutations (>50%) (75%, 62.5%, and 50%, respectively) (Zhang et al., 2016). These findings suggest that gene mutations also play a crucial role in the development of bone metastasis, and that targeting gene mutations can be a potential alternative therapeutic approach for bone metastasis.

Gene Mutations in Osteosarcoma

Osteosarcoma is one of the most common malignant cancers of mesenchymal origin. Osteosarcoma cells are potentially derived from cells along the differentiation spectrum from mesenchymal stem cells to mature osteoblasts (Le Nail et al., 2018; Marina et al., 2004). Osteoblast-lineage cells are naturally slow-growing. During growth spurts and puberty, these cells undergo rapid cell division, resulting in an increased error rate in DNA synthesis (Cotterill et al., 2004). The accumulation of DNA errors and/or genomic instability is thought to cause transformation of osteoblasts to osteosarcoma (Yang et al., 2017; Martin et al., 2012). Osteosarcoma therefore occurs more often in adolescence. Although fairly uncommon, osteosarcoma can also be found in older patients. Unlike other types of cancers, adult osteosarcoma is not considered a lifestyle-related cancer. Instead, adult osteosarcoma is believed to be associated with genetic disorders caused by both somatic and germline gene mutations, such as multiple exostoses syndrome and tuberous sclerosis (Bukara et al., 2018; Farid and Ngeow, 2016). Therefore, genomic mutation is a key driver of the development of osteosarcoma.

Osteosarcoma is often associated with complex karyotypes due to a high frequency of chromosomal translocations, amplifications, and deletions (Biegel et al., 1989). The deletion mutation of a tumor suppressor TP53 is a hallmark of osteosarcoma (Guo et al., 1996). It has been revealed that more than 50% of osteosarcoma tissue samples have allelic deletion on chromosome 17p13 (where the TP53 gene is located) (Guo et al., 1996). Additionally, about 25% of samples without 17p13 deletion showed rearrangements (addition of exon fragments) and point mutations (nonsense) in the TP53 gene, resulting in loss-of-function mutation (Toguchida et al., 1992). Consistently, a study using a whole genome sequencing analysis of 34 osteosarcoma tumor samples found that 80% of the tumors have mutations in both alleles of the TP53 gene and 90% have mutations in at least one allele (Chen et al., 2014). It has been suggested that loss of TP53 functions, such as cell cycle arrest, DNA repair, and apoptosis, are responsible for the development of many cancers including osteosarcoma (Rivlin et al., 2011). TP53 is also known to inhibit DNA damage (e.g. gene amplification and deletion) mediated by genotoxic treatments like radiation, further suggesting that loss of TP53 functions leads to genetic alterations in other oncogenes and tumor suppressor genes (Overholtzer et al., 2003). Consistently, studies have shown that treatments of PRIMA-1 [2,2-bis (hydroxymethyl)-3-quinuclidinone], which is a compound that can restore mutant TP53 activities by converting its protein conformation to a wild type TP53 (Rangel et al., 2019), inhibits proliferation of a mutant TP53-expressing human osteosarcoma cell line SaOS-2 by restoring a pro-apoptotic pathway induced by TP53 (Bykov et al., 2002; Bykov et al., 2005; Rokaeus et al., 2007; Lambert et al., 2009). In addition, the PRIMA-1 analog PRIMA-1MEt (APR-246) inhibited growth of a chemotherapeutic agent camptothecin-resistant osteosarcoma, lung cancer, prostate cancer, and ovarian cancer cells due to their TP53 mutation (Bykov et al., 2005). Although PRIMA-1 and APR-26 have not yet been tested in a clinical trial in osteosarcoma patients, the safety and clinical activity of APR-246 in combination with chemotherapies are currently tested in prostate cancer, ovarian cancer, and melanoma patients (Parrales and Iwakuma, 2015). An oncogenic E3 ubiquitin-protein ligase MDM2 promotes degradation of TP53 through indirect binding (Moll and Petrenko, 2003; Kussie et al., 1996; Haupt et al., 1997). A potent MDM2 antagonist RG7388 (Idasanutlin) has been entered phase III clinical trials in acute myeloid leukemia patents (Tisato et al., 2017). However, RG7388 failed to induce apoptosis in TP53 mutation-positive osteosarcoma cells, resulting in development of resistance to RG7388 (Skalniak et al., 2018). Although RG7388 might be a potential therapeutic option for osteosarcoma since it can inhibit degradation of TP53 protein, further investigations are warranted.

Besides TP53, the mutation of a tumor suppressor Rb1 gene, a key regulator of cell cycle, is also frequently found in osteosarcoma (39–64%) (Chen et al., 2014) and often presents as a null or dysfunctional mutation (Harbour and Dean, 2000; Scholz et al., 1992). Similar to TP53 loss, the loss of Rb1 increases genomic instability (van Harn et al., 2010). Interestingly, in 25–30% of hereditary retinoblastoma, which is caused by a germline Rb1 mutation, patients develop osteosarcoma (Hansen et al., 1985). Rb1 protein induces cell cycle progression by binding to the E2F transcription factor in G1 phase (Giacinti and Giordano, 2006). This binding can be disrupted when Rb1 is phosphorylated by CDK4 or CDK6 kinases, and consequently Rb1 becomes inactive (Knudsen and Wang, 1997). Therefore, activation of Rb1 function can be achieved by the inhibition of CDK4/6 kinases (Spring et al., 2016). Although not in osteosarcoma, preclinical studies in Rb1 mutation-positive breast and pancreas cancer cells have shown anti-tumor effect of CDK4/6 inhibitors in combination with other cytotoxic agents, such as chemotherapies, targeted signaling inhibitors, and endocrine therapies (Spring et al., 2016).

Amplifications and gain-of-function mutations in an oncogene phosphoinositide 3-kinases (PI3K) are also seen in osteosarcoma (Zhang et al., 2015). Indeed, missense mutations in the PIK3CA and PIK3R1 genes and deletion and/or nonsense mutations in the PIK3R5, PIK3R6, and PIK3C3 genes were observed in osteosarcoma patient samples (Perry et al., 2014; Chen et al., 2014). A PI3K inhibitor BKM120 (buparlisib) inhibited proliferation and induced apoptosis of osteosarcoma cells by disrupting Akt/mammalian target of rapamycin (mTOR) pathway, a major downstream targets of PI3K (Bavelloni et al., 2019). Phase II clinical trials of a potent mTOR inhibitor everolimus in advanced osteosarcoma patients with progressive disease after standard targeted therapies, including sorafenib, anthracycline and ifosfamide, revealed that 29%–45% of patients are progression free at 4–6 months (Grignani et al., 2015; Yoo et al., 2013; Mita et al., 2013; Chawla et al., 2012).

Gene Mutations in Hematopoietic Malignancies

Within the bone marrow, cells of hematopoietic origin can also be cancerous. These types of cancer are called "liquid cancers" or "blood cancers" and can be mainly classified as leukemias, lymphomas, and myeloma. When plasma cells, which produce antibodies, become mutated and grow in an uncontrolled manner in the marrow, they progress into multiple myeloma. Although the mechanisms responsible for the development of multiple myeloma remain yet unclear, studies have suggested that genetic alterations that occur during the differentiation and maturation process of plasma cells cause multiple myeloma (Boyle et al., 2014). During the antibody production process, immature B cells, which migrate from bone marrow to the germline center of lymph nodes, undergo affinity maturation that involves two processes; somatic hypermutation (SOH) and class switch recombination (CSR) (Gonzalez et al., 2007). SOH occurs in the variable antigen-binding coding sequence of immunoglobulin (Ig) genes that regulates specificity and binding affinity of antibodies (Klein et al., 1998; Neuberger and Milstein, 1995). CSR occurs in the constant region of the heavy chain producing genes to generate antibodies of different immunoglobulin isotypes, such as IgG, IgA, and IgM (Stavnezer, 1996; Honjo et al., 2002). Both SOH and CSR processes are regulated by activation-induced cytidine deaminase (AID, an enzyme that creates point mutations in DNA converting cytosine bases to thymidine bases) (Stavnezer et al., 2008; Chaudhuri and Alt, 2004). AID is also known to create DNA damage, such as double strand breaks (DSBs), in Ig loci during the affinity maturation process (Peled et al., 2008; Stavnezer, 2011). These DSBs are usually repaired within the region where Ig genes locate, but also results in the abnormal chromosomal translocations (~1000 cells per day) (Adams et al., 1982; Ramiro et al., 2004). Mutations in oncogenes or tumor suppressor genes can be induced by the accumulation of the abnormal chromosomal translocations overtime, and these mutations cause malfunction in matured plasma cells, eventually becoming myeloma (Bandelow et al., 2007). Additionally, although it is rare, AID can also induce DSBs in ATM genes, associated with the DNA repair system and responsible for activation of TP53-dependent apoptosis (Cheng and Chen, 2010). Indeed, 7181C/T mutation in the ATM gene is observed in a subpopulation of multiple myeloma patient tumor samples where ATM expression significantly decreases (Austen et al., 2008). This study also suggested that the loss of ATM function is one of the underlying mechanisms of myeloma development (Austen et al., 2008). Moreover, despite low frequency (4%), the association between ATM mutations and aggressiveness of multiple myeloma has recently been demonstrated. Whole-exome sequencing in 463 myeloma patient samples revealed that ATM mutations are associated with impaired progression-free survival (median, 15.4 vs. 26.6 months, $P = 0.05$) and 2-year overall survival (95% CI, 50% vs. 80%, $P = 0.01$) (Walker et al., 2015).

Whole genome sequencing studies have identified that recurrent mutations in NRAS, KRAS, and BRAF oncogenes are frequently detected in myeloma patient samples (Lionetti et al., 2015). NRAS, KRAS, and BRAF genes are associated with RAS protein kinases, which are the most common proto-oncogenes in cancers (Prior et al., 2012; Davies et al., 2002; Pratilas et al., 2012). These RAS protein kinases are downstream of mitogen-activated protein kinase (MAPK) pathway, known as a critical signal transduction pathway that regulates cell proliferation and survival (Burotto et al., 2014). Among them, BRAF mutation is the most common mutation (~90%) in melanoma and several BRAF inhibitors have been used as targeted therapies for melanoma patients (Cheng et al., 2018). Besides MAPK pathway associated genes, mutations in PI3K are also detected in a subpopulation of multiple myeloma. The phosphorylated form of Akt, a direct downstream target of PI3K (Franke et al., 1995), and the mutation of DEP domain-containing mTOR-interacting protein, a positive regulator of PI3K (Boyd et al., 2010), have been found in myeloma patient samples.

Leukemia is another type of blood cancer that is derived from white blood cells. Several gene mutations have also been identified in leukemia. Among them, Philadelphia chromosome mutation or Philadelphia translocation (Ph) is a well-known genomic alteration associated with acute and chronic leukemia (Kang et al., 2016). Ph was originally found in the patients with CML (Nowell, 1962). Ph is a resultant product of the chromosomal translocation between chromosome 22 which contains breakpoint cluster region (BCR) gene and chromosome 9 which contains proto-oncogene tyrosine protein kinase (ABL1) (Collins and Groudine, 1983). The BCR-ABL1 fusion protein is closely associated with development of CML; more than 95% CML patients are Ph positive (Faderl et al., 1999). ABL1 is a tyrosine kinase which is involved in cell differentiation and regulates normal cell cycle (Wang, 2014). The fusion of ABL1 with BCR results in abnormal cell proliferation by generating the constitutively active form of a tyrosine kinase (Pendergast et al., 1991). A kinase inhibitor against BCR-ABL1, imatinib mesylate, has been widely used and very successful for treatment of Ph positive CML (Shah et al., 2002). However, some patients develop resistance to imatinib. A study examining the mutations of CML cells obtained from 32 CML patients who develop resistance to imatinib revealed that 29 samples out of 32 imatinib-resistant CML cells possess BCR-ABL1-dependent mutations, which prevent the binding of imatinib to the kinase domain of BCR-ABL1 protein (Shah et al., 2002). Although several BCR-ABL1-independent resistant mechanisms have been identified, BCR-ABL1-dependent mutations are thought to be major drivers of resistance to imatinib (Gorre et al., 2001). Thereafter, the second- and third-generation of BCR-ABL1 inhibitors, such as dasatinib, nilotinib, bosutinib, and ponatinib, have been developed and clinically tested (Rossari et al., 2018). These inhibitors can target almost all resistance-related mutations, except for the T315I mutation (Rossari et al., 2018). To overcome T315I mutation-dependent BCR-ABL1 inhibitor resistance, newer generation BCR-ABL1 inhibitors (e.g. bafetinib, rebastinib, tozasertib, danusertib, HG-7-85-01, GNF-2, and 1,3,4-thiadiazole derivatives) are currently under preclinical evaluation (Rossari et al., 2018). Although the results seem to be promising, further validation studies are required prior to clinical use.

Future Direction and Conclusions

The recent advancement in DNA sequencing technologies has enabled us to discover many important oncogenes and tumor suppressor genes responsible for the development of cancer, including bone-related cancers. Based on these findings, small molecule inhibitors that can target specific mutations have been made clinically available (Fig. 1). Like other cytotoxic agents, such as chemotherapies and radiation, most of these mutation-targeted inhibitors initially show anti-tumor effects, but eventually cause treatment resistance. It could be due in part to the activation of compensatory pathways mediated by the blockade of mutation-specific downstream pathways. If this is the case, the mutations targeted with these inhibitors may not be the key drivers leading to cancer development. Therefore, further studies identifying the initial mutations, which regulate hundreds or thousands of the mutations in oncogenes and tumor suppressor genes, are necessary in order to develop more effective targeted therapies.

Although treatments targeting mutations in cancer cells sounds promising, bone-related cancers are still difficult to eradicate since their progression is also influenced by the bone marrow microenvironment, or the "niche" (Decker et al., 2016; Zhang et al., 2019; Ren et al., 2015; Shiozawa et al., 2011; Park et al., 2018). When the *dicer1* gene is deleted in osteoblastic hematopoietic stem cell niche, the abnormal osteoblastic niche induces bone marrow dysfunction with myelodysplasia (Raaijmakers et al., 2010), suggesting the involvement of bone marrow microenvironment in the oncogenesis of bone-related cancers. In this regard, attention needs to be paid not only to genomic mutations in bone-related cancers, but also to those in the bone marrow microenvironment.

Particularly in bone metastasis, current treatments often target the bone marrow microenvironment. Although these bone-targeted therapies can reduce the onset of skeletal-related events (e.g. bone pain, pathological fractures, spinal cord compression) (Tsuzuki et al., 2016), they are primarily palliative. Targeting only the bone marrow microenvironment may not be sufficient to eradicate bone metastatic disease. Since bone metastasis-specific gene mutations have been discovered (Lohinai et al., 2017; Zhang et al., 2016), bone-targeted therapies can be combined with small molecules which target these mutations, if available. Alternatively, these bone metastasis-specific gene mutations can be used to guide precision treatment decisions.

Although cancer genome research has made available novel gene-targeted treatment options for bone-related cancers, there is still a gap to be filled if we want to further lower mortality of these patients. Therefore, we must continue to promote scientific and technological progress in the both fields of the cancer genome and bone-related cancer. Further multidisciplinary and multi-institutional research efforts are clearly warranted.
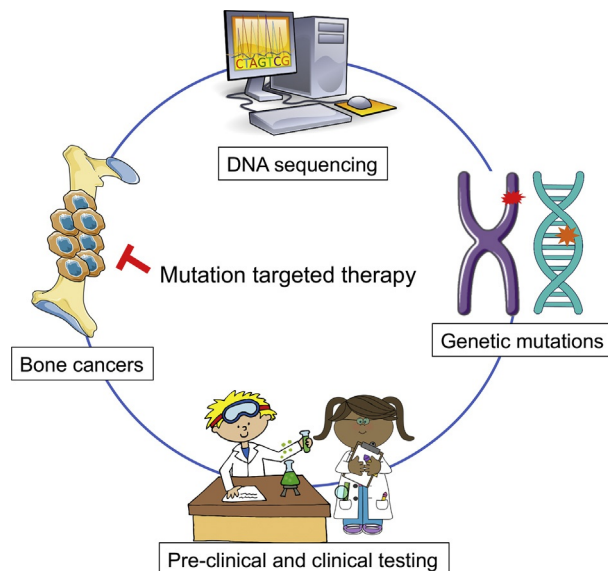
Acknowledgments

Fig. 1   Development of mutation-targeted therapies for bone-related cancers. Development of small molecule inhibitors specifically targeting gene mutations involves multiple steps. Once bone-related cancer is detected, a bone biopsy is performed to determine the precise diagnosis of cancer type. In some cases, biopsy samples are sent to the clinical laboratory to run DNA sequencing. The mutational status of oncogenes and tumor suppressor genes in these samples is analyzed, and the functions of these mutations and their therapeutic potential are assessed in preclinical settings. Successful preclinical studies eventually lead to the development of small molecule inhibitors. After preclinical validation, these potential inhibitors are moved into clinical trials and finally become available in the clinic when the results from the trials turn out to be positive. Graphics are adapted from Smart Servier Medical Art (https://smart.servier.com/) and Fly clipart (https://flyclipart.com/).

References

Abou DS, Ulmert D, Doucet M, Hobbs RF, Riddle RC, and Thorek DL (2016) Whole-body and microenvironmental localization of radium-223 in naive and mouse models of prostate Cancer metastasis. *Journal of the National Cancer Institute* 108.

Adams JM, Gerondakis S, Webb E, Mitchell J, Bernard O, and Cory S (1982) Transcriptionally active DNA region that rearranges frequently in murine lymphoid tumors. *Proceedings of the National Academy of Sciences of the United States of America* 79: 6966–6970.

American Cancer Society (2015) *Cancer Facrs & Figures 2015*. Atlanta: American Cancer Society.

Austen B, Barone G, Reiman A, Byrd PJ, Baker C, Starczynski J, Nobbs MC, Murphy RP, Enright H, Chaila E, Quinn J, Stankovic T, Pratt G, and Taylor AM (2008) Pathogenic ATM mutations occur rarely in a subset of multiple myeloma patients. *British Journal of Haematology* 142: 925–933.

Badrising SK, Van Der Noort V, Hamberg P, Coenen JL, Aarts MJ, Van Oort IM, Van Den Eertwegh AJ, Los M, Van Den Berg HP, Gelderblom H, Vrijaldenhoven S, Kerver ED, Van Voorthuizen T, De Jong IJ, Haanen JB, and Bergman AM (2016) Enzalutamide as a fourth- or fifth-line treatment option for metastatic castration-resistant prostate cancer. *Oncology* 91: 267–273.

Bandelow B, Seidler-Brandler U, Becker A, Wedekind D, and Ruther E (2007) Meta-analysis of randomized controlled comparisons of psychopharmacological and psychological treatments for anxiety disorders. *The World Journal of Biological Psychiatry* 8: 175–187.

Bavelloni A, Focaccia E, Piazzi M, Orsini A, Ramazzotti G, Cocco L, Blalock W, and Faenza I (2019) Therapeutic potential of nvp-bkm120 in human osteosarcomas cells. *Journal of Cellular Physiology* 234: 10907–10917.

Biegel JA, Womer RB, and Emanuel BS (1989) Complex karyotypes in a series of pediatric osteosarcomas. *Cancer Genetics and Cytogenetics* 38: 89–100.

Bienz M and Saad F (2015) Management of bone metastases in prostate cancer: A review. *Current Opinion in Supportive and Palliative Care* 9: 261–267.

Boyd KD, Walker BA, Wardell CP, Ross FM, Gregory WM, Davies FE, and Morgan GJ (2010) High expression levels of the mammalian target of rapamycin inhibitor DEPTOR are predictive of response to thalidomide in myeloma. *Leukemia & Lymphoma* 51: 2126–2129.

Boyle EM, Davies FE, Leleu X, and Morgan GJ (2014) Understanding the multiple biological aspects leading to myeloma. *Haematologica* 99: 605–612.

Bukara E, Buteera AM, Karakire R, Manirakiza F, Muhumuza S, Rudakemwa E, and Kyokunda L (2018) Osteoblastic osteosarcoma arising beneath an osteochondroma in an 11-year-old male with multiple hereditary exostoses. *Case Reports in Orthopedics* 2018: 8280415.

Burotto M, Chiou VL, Lee JM, and Kohn EC (2014) The MAPK pathway across different malignancies: A new perspective. *Cancer* 120: 3446–3456.

Bykov VJ, Issaeva N, Shilov A, Hultcrantz M, Pugacheva E, Chumakov P, Bergman J, Wiman KG, and Selivanova G (2002) Restoration of the tumor suppressor function to mutant p53 by a low-molecular-weight compound. *Nature Medicine* 8: 282–288.

Bykov VJ, Zache N, Stridh H, Westman J, Bergman J, Selivanova G, and Wiman KG (2005) PRIMA-1(MET) synergizes with cisplatin to induce tumor cell apoptosis. *Oncogene* 24: 3484–3491.

Chaudhuri J and Alt FW (2004) Class-switch recombination: Interplay of transcription, DNA deamination and DNA repair. *Nature Reviews. Immunology* 4: 541–552.

Chawla SP, Staddon AP, Baker LH, Schuetze SM, Tolcher AW, D'amato GZ, Blay JY, Mita MM, Sankhala KK, Berk L, Rivera VM, Clackson T, Loewy JW, Haluska FG, and Demetri GD (2012) Phase II study of the mammalian target of rapamycin inhibitor ridaforolimus in patients with advanced bone and soft tissue sarcomas. *Journal of Clinical Oncology* 30: 78–84.

Chen X, Bahrami A, Pappo A, Easton J, Dalton J, Hedlund E, Ellison D, Shurtleff S, Wu G, Wei L, Parker M, Rusch M, Nagahawatte P, Wu J, Mao S, Boggs K, Mulder H, Yergeau D, Lu C, Ding L, Edmonson M, Qu C, Wang J, Li Y, Navid F, Daw NC, Mardis ER, Wilson RK, Downing JR, Zhang J, Dyer MA, and St. Jude Children'S Research Hospital-Washington University Pediatric Cancer Genome, P (2014) Recurrent somatic structural variations contribute to tumorigenesis in pediatric osteosarcoma. *Cell Reports* 7: 104–112.

Cheng Q and Chen J (2010) Mechanism of p53 stabilization by ATM after DNA damage. *Cell Cycle* 9: 472–478.

Cheng L, Lopez-Beltran A, Massari F, MacLennan GT, and Montironi R (2018) Molecular testing for BRAF mutations to inform melanoma treatment decisions: A move toward precision medicine. *Modern Pathology* 31: 24–38.

Chiang AC and Massague J (2008) Molecular basis of metastasis. *The New England Journal of Medicine* 359: 2814–2823.

Clines GA and Guise TA (2005) Hypercalcaemia of malignancy and basic research on mechanisms responsible for osteolytic and osteoblastic metastasis to bone. *Endocrine-Related Cancer* 12: 549–583.

Coleman RE (2001) Metastatic bone disease: Clinical features, pathophysiology and treatment strategies. *Cancer Treatment Reviews* 27: 165–176.

Collins SJ and Groudine MT (1983) Rearrangement and amplification of c-abl sequences in the human chronic myelogenous leukemia cell line K-562. *Proceedings of the National Academy of Sciences of the United States of America* 80: 4813–4817.

Cotterill SJ, Wright CM, Pearce MS, Craft AW, and UKCCSG/MRC Bone Tumour Working Group (2004) Stature of young people with malignant bone tumors. *Pediatric Blood & Cancer* 42: 59–63.

Davies H, Bignell GR, Cox C, Stephens P, Edkins S, Clegg S, Teague J, Woffendin H, Garnett MJ, Bottomley W, Davis N, Dicks E, Ewing R, Floyd Y, Gray K, Hall S, Hawes R, Hughes J, Kosmidou V, Menzies A, Mould C, Parker A, Stevens C, Watt S, Hooper S, Wilson R, Jayatilake H, Gusterson BA, Cooper C, Shipley J, Hargrave D, Pritchard-Jones K, Maitland N, Chenevix-Trench G, Riggins GJ, Bigner DD, Palmieri G, Cossu A, Flanagan A, Nicholson A, Ho JW, Leung SY, Yuen ST, Weber BL, Seigler HF, Darrow TL, Paterson H, Marais R, Marshall CJ, Wooster R, Stratton MR, and Futreal PA (2002) Mutations of the BRAF gene in human cancer. *Nature* 417: 949–954.

Decker AM, Jung Y, Cackowski F, and Taichman RS (2016) The role of hematopoietic stem cell niche in prostate cancer bone metastasis. *Journal of Bone Oncology* 5: 117–120.

Faderl S, Talpaz M, Estrov Z, O'brien S, Kurzrock R, and Kantarjian HM (1999) The biology of chronic myeloid leukemia. *The New England Journal of Medicine* 341: 164–172.

Farid M and Ngeow J (2016) Sarcomas associated with genetic Cancer predisposition syndromes: A review. *The Oncologist* 21: 1002–1013.

Fidler IJ and Poste G (2008) The "seed and soil" hypothesis revisited. *The Lancet Oncology* 9: 808.

Fizazi K, Carducci M, Smith M, Damiao R, Brown J, Karsh L, Milecki P, Shore N, Rader M, Wang H, Jiang Q, Tadros S, Dansey R, and Goessl C (2011) Denosumab versus zoledronic acid for treatment of bone metastases in men with castration-resistant prostate cancer: A randomised, double-blind study. *Lancet* 377: 813–822.

Franke TF, Yang SI, Chan TO, Datta K, Kazlauskas A, Morrison DK, Kaplan DR, and Tsichlis PN (1995) The protein kinase encoded by the Akt proto-oncogene is a target of the PDGF-activated phosphatidylinositol 3-kinase. *Cell* 81: 727–736.

Giacinti C and Giordano A (2006) RB and cell cycle progression. *Oncogene* 25: 5220–5227.

Gonzalez D, Van Der Burg M, Garcia-Sanz R, Fenton JA, Langerak AW, Gonzalez M, Van Dongen JJ, San Miguel JF, and Morgan GJ (2007) Immunoglobulin gene rearrangements and the pathogenesis of multiple myeloma. *Blood* 110: 3112–3121.

Gorre ME, Mohammed M, Ellwood K, Hsu N, Paquette R, Rao PN, and Sawyers CL (2001) Clinical resistance to STI-571 cancer therapy caused by BCR-ABL gene mutation or amplification. *Science* 293: 876–880.

Grignani G, Palmerini E, Ferraresi V, D'ambrosio L, Bertulli R, Asaftei SD, Tamburini A, Pignochino Y, Sangiolo D, Marchesi E, Capozzi F, Biagini R, Gambarotti M, Fagioli F, Casali PG, Picci P, Ferrari S, Aglietta M, and Italian Sarcoma G (2015) Sorafenib and everolimus for patients with unresectable high-grade osteosarcoma progressing after standard treatment: A non-randomised phase 2 clinical trial. *Lancet Oncology* 16: 98–107.

Guo W, Wang X, and Feng C (1996) P53 gene abnormalities in osteosarcoma. *Chinese Medical Journal* 109: 752–755.

Hansen MF, Koufos A, Gallie BL, Phillips RA, Fodstad O, Brogger A, Gedde-Dahl T, and Cavenee WK (1985) Osteosarcoma and retinoblastoma: A shared chromosomal mechanism revealing recessive predisposition. *Proceedings of the National Academy of Sciences of the United States of America* 82: 6216–6220.

Harbour JW and Dean DC (2000) Rb function in cell-cycle regulation and apoptosis. *Nature Cell Biology* 2: E65–E67.

Haupt Y, Maya R, Kazaz A, and Oren M (1997) Mdm2 promotes the rapid degradation of p53. *Nature* 387: 296–299.

Hochhaus A, Larson RA, Guilhot F, Radich JP, Branford S, Hughes TP, Baccarani M, Deininger MW, Cervantes F, Fujihara S, Ortmann CE, Menssen HD, Kantarjian H, O'brien SG, Druker BJ, and Investigators I (2017) Long-term outcomes of Imatinib treatment for chronic myeloid leukemia. *The New England Journal of Medicine* 376: 917–927.

Honjo T, Kinoshita K, and Muramatsu M (2002) Molecular mechanism of class switch recombination: Linkage with somatic hypermutation. *Annual Review of Immunology* 20: 165–196.

Iqbal N and Iqbal N (2014) Imatinib: A breakthrough of targeted therapy in cancer. *Chemotherapy Research and Practice* 2014: 357027.

Kamai T, Arai K, Koga F, Abe H, Nakanishi K, Kambara T, Furuya N, Tsujii T, and Yoshida KI (2001) Higher expression of K-ras is associated with parathyroid hormone-related protein-induced hypercalcaemia in renal cell carcinoma. *BJU International* 88: 960–966.

Kamps R, Brandao RD, Bosch BJ, Paulussen AD, Xanthoulea S, Blok MJ, and Romano A (2017) Next-generation sequencing in oncology: Genetic diagnosis, Risk Prediction and Cancer Classification. *International Journal of Molecular Sciences* 18.

Kang ZJ, Liu YF, Xu LZ, Long ZJ, Huang D, Yang Y, Liu B, Feng JX, Pan YJ, Yan JS, and Liu Q (2016) The Philadelphia chromosome in leukemogenesis. *Chinese Journal of Cancer* 35: 48.

Kchouk M, Gibrat J-F, and Elloumi M (2017) Generations of sequencing technologies: From first to next generation. *Biologie et Médecine* 9.

Klein U, Goossens T, Fischer M, Kanzler H, Braeuninger A, Rajewsky K, and Kuppers R (1998) Somatic hypermutation in normal and transformed human B cells. *Immunological Reviews* 162: 261–280.

Knudsen ES and Wang JY (1997) Dual mechanisms for the inhibition of E2F binding to RB by cyclin-dependent kinase-mediated RB phosphorylation. *Molecular and Cellular Biology* 17: 5771–5783.

Knudson AG Jr. (1971) Mutation and cancer: Statistical study of retinoblastoma. *Proceedings of the National Academy of Sciences of the United States of America* 68: 820–823.

Kussie PH, Gorina S, Marechal V, Elenbaas B, Moreau J, Levine AJ, and Pavletich NP (1996) Structure of the MDM2 oncoprotein bound to the p53 tumor suppressor transactivation domain. *Science* 274: 948–953.

Lambert JM, Gorzov P, Veprintsev DB, Soderqvist M, Segerback D, Bergman J, Fersht AR, Hainaut P, Wiman KG, and Bykov VJ (2009) PRIMA-1 reactivates mutant p53 by covalent binding to the core domain. *Cancer Cell* 15: 376–388.

Langley RR and Fidler IJ (2007) Tumor cell-organ microenvironment interactions in the pathogenesis of Cancer metastasis. *Endocrine Reviews* 28: 297–321.

Le Nail LR, Brennan M, Rosset P, Deschaseaux F, Piloquet P, Pichon O, Le Caignec C, Crenn V, Layrolle P, Herault O, De Pinieux G, and Trichet V (2018) Comparison of tumor- and bone marrow-derived mesenchymal stromal/stem cells from patients with high-grade osteosarcoma. *International Journal of Molecular Sciences* 19.

Lionetti M, Barbieri M, Todoerti K, Agnelli L, Marzorati S, Fabris S, Ciceri G, Galletti S, Milesi G, Manzoni M, Mazzoni M, Greco A, Tonon G, Musto P, Baldini L, and Neri A (2015) Molecular spectrum of BRAF, NRAS and KRAS gene mutations in plasma cell dyscrasias: Implication for MEK-ERK pathway activation. *Oncotarget* 6: 24205–24217.

Liu Q, Zhang H, Jiang X, Qian C, Liu Z, and Luo D (2017) Factors involved in cancer metastasis: A better understanding to "seed and soil" hypothesis. *Molecular Cancer* 16: 176.

Lohinai Z, Klikovits T, Moldvay J, Ostoros G, Raso E, Timar J, Fabian K, Kovalszky I, Kenessey I, Aigner C, Renyi-Vamos F, Klepetko W, Dome B, and Hegedus B (2017) KRAS-mutation incidence and prognostic value are metastatic site-specific in lung adenocarcinoma: Poor prognosis in patients with KRAS mutation and bone metastasis. *Scientific Reports* 7: 39721.

Marina N, Gebhardt M, Teot L, and Gorlick R (2004) Biology and therapeutic advances for pediatric osteosarcoma. *The Oncologist* 9: 422–441.

Martin JW, Squire JA, and Zielenska M (2012) The genetics of osteosarcoma. *Sarcoma* 2012: 627254.

Massoud M, Sakr R, Kerbage F, Makdissi J, Hawi J, Rached L, Nasr F, and Chahine G (2017) Analysis of survival of patients with chronic myeloid leukemia treated with Imatinib in the last 15 years in Lebanon. *Clinical Lymphoma, Myeloma & Leukemia* 17S: S111–S115.

Mersch J, Jackson MA, Park M, Nebgen D, Peterson SK, Singletary C, Arun BK, and Litton JK (2015) Cancers associated with BRCA1 and BRCA2 mutations other than breast and ovarian. *Cancer* 121: 269–275.

Mita MM, Poplin E, Britten CD, Tap WD, Rubin EH, Scott BB, Berk L, Rivera VM, Loewy JW, Dodion P, Haluska F, Sarantopoulos J, Mita A, and Tolcher A (2013) Phase I/IIa trial of the mammalian target of rapamycin inhibitor ridaforolimus (AP23573; MK-8669) administered orally in patients with refractory or advanced malignancies and sarcoma. *Annals of Oncology* 24: 1104–1111.

Moll UM and Petrenko O (2003) The MDM2-p53 interaction. *Molecular Cancer Research* 1: 1001–1008.

Neuberger MS and Milstein C (1995) Somatic hypermutation. *Current Opinion in Immunology* 7: 248–254.

Nowell PC (1962) The minute chromosome (Phl) in chronic granulocytic leukemia. *Blut* 8: 65–66.

Ouhtit A, Nakazawa H, Armstrong BK, Kricker A, Tan E, Yamasaki H, and English DR (1998) UV-radiation-specific p53 mutation frequency in normal skin as a predictor of risk of basal cell carcinoma. *Journal of the National Cancer Institute* 90: 523–531.

Overholtzer M, Rao PH, Favis R, Lu XY, Elowitz MB, Barany F, Ladanyi M, Gorlick R, and Levine AJ (2003) The presence of p53 mutations in human osteosarcomas correlates with high levels of genomic instability. *Proceedings of the National Academy of Sciences of the United States of America* 100: 11547–11552.

Paget S (1989) The distribution of secondary growths in cancer of the breast. *Cancer Metastasis Reviews* 8: 98–101.

Park SH, Keller ET, and Shiozawa Y (2018) Bone marrow microenvironment as a regulator and therapeutic target for prostate Cancer bone metastasis. *Calcified Tissue International* 102: 152–162.

Parker C, Nilsson S, Heinrich D, Helle SI, O'sullivan JM, Fossa SD, Chodacki A, Wiechno P, Logue J, Seke M, Widmark A, Johannessen DC, Hoskin P, Bottomley D, James ND, Solberg A, Syndikus I, Kliment J, Wedel S, Boehmer S, Dall'oglio M, Franzen L, Coleman R, Vogelzang NJ, O'bryan-Tear CG, Staudacher K, Garcia-Vargas J, Shan M, Bruland OS, Sartor O, and Investigators A (2013) Alpha emitter radium-223 and survival in metastatic prostate cancer. *The New England Journal of Medicine* 369: 213–223.

Parrales A and Iwakuma T (2015) Targeting oncogenic mutant p53 for cancer therapy. *Frontiers in Oncology* 5: 288.

Peled JU, Kuang FL, Iglesias-Ussel MD, Roa S, Kalis SL, Goodman MF, and Scharff MD (2008) The biochemistry of somatic hypermutation. *Annual Review of Immunology* 26: 481–511.

Pendergast AM, Muller AJ, Havlik MH, Maru Y, and Witte ON (1991) BCR sequences essential for transformation by the BCR-ABL oncogene bind to the ABL SH2 regulatory domain in a non-phosphotyrosine-dependent manner. *Cell* 66: 161–171.

Perry JA, Kiezun A, Tonzi P, Van Allen EM, Carter SL, Baca SC, Cowley GS, Bhatt AS, Rheinbay E, Pedamallu CS, Helman E, Taylor-Weiner A, McKenna A, Deluca DS, Lawrence MS, Ambrogio L, Sougnez C, Sivachenko A, Walensky LD, Wagle N, Mora J, De Torres C, Lavarino C, Dos Santos Aguiar S, Yunes JA, Brandalise SR, Mercado-Celis GE, Melendez-Zajgla J, Cardenas-Cardos R, Velasco-Hidalgo L, Roberts CW, Garraway LA, Rodriguez-Galindo C, Gabriel SB, Lander ES, Golub TR, Orkin SH, Getz G, and Janeway KA (2014) Complementary genomic approaches highlight the PI3K/mTOR pathway as a common vulnerability in osteosarcoma. *Proceedings of the National Academy of Sciences of the United States of America* 111: E5564–E5573.

Powell GJ, Southby J, Danks JA, Stillwell RG, Hayman JA, Henderson MA, Bennett RC, and Martin TJ (1991) Localization of parathyroid hormone-related protein in breast cancer metastases: Increased incidence in bone compared with other sites. *Cancer Research* 51: 3059–3061.

Pratilas CA, Xing F, and Solit DB (2012) Targeting oncogenic BRAF in human cancer. *Current Topics in Microbiology and Immunology* 355: 83–98.

Prior IA, Lewis PD, and Mattos C (2012) A comprehensive survey of Ras mutations in cancer. *Cancer Research* 72: 2457–2467.

Raaijmakers MH, Mukherjee S, Guo S, Zhang S, Kobayashi T, Schoonmaker JA, Ebert BL, Al-Shahrour F, Hasserjian RP, Scadden EO, Aung Z, Matza M, Merkenschlager M, Lin C, Rommens JM, and Scadden DT (2010) Bone progenitor dysfunction induces myelodysplasia and secondary leukaemia. *Nature* 464: 852–857.

Ramiro AR, Jankovic M, Eisenreich T, Difilippantonio S, Chen-Kiang S, Muramatsu M, Honjo T, Nussenzweig A, and Nussenzweig MC (2004) AID is required for c-myc/IgH chromosome translocations in vivo. *Cell* 118: 431–438.

Rangel LP, Ferretti GDS, Costa CL, Andrade S, Carvalho RS, Costa DCF, and Silva JL (2019) p53 reactivation with induction of massive apoptosis-1 (PRIMA-1) inhibits amyloid aggregation of mutant p53 in cancer cells. *The Journal of Biological Chemistry* 294: 3670–3682.

Ren G, Esposito M, and Kang Y (2015) Bone metastasis and the metastatic niche. *Journal of Molecular Medicine (Berlin, Germany)* 93: 1203–1212.

Ribatti D, Mangialardi G, and Vacca A (2006) Stephen Paget and the 'seed and soil' theory of metastatic dissemination. *Clinical and Experimental Medicine* 6: 145–149.

Rivlin N, Brosh R, Oren M, and Rotter V (2011) Mutations in the p53 tumor suppressor gene: Important milestones at the various steps of tumorigenesis. *Genes & Cancer* 2: 466–474.

Rokaeus N, Klein G, Wiman KG, Szekely L, and Mattsson K (2007) PRIMA-1(MET) induces nucleolar accumulation of mutant p53 and PML nuclear body-associated proteins. *Oncogene* 26: 982–992.

Ronchetti D, Neglia CB, Cesana BM, Carboni N, Neri A, Pruneri G, and Pignataro L (2004) Association between p53 gene mutations and tobacco and alcohol exposure in laryngeal squamous cell carcinoma. *Archives of Otolaryngology – Head & Neck Surgery* 130: 303–306.

Rossari F, Minutolo F, and Orciuolo E (2018) Past, present, and future of Bcr-Abl inhibitors: From chemical development to clinical efficacy. *Journal of Hematology & Oncology* 11: 84.

Rudduck C, Duncan L, Center R, and Garson OM (1993) Co-amplification of the gene for parathyroid hormone-related protein (PTHRP) and KRAS2 in a human lung cancer cell line. *Genes, Chromosomes & Cancer* 7: 213–218.

Scholz RB, Kabisch H, Weber B, Roser K, Delling G, and Winkler K (1992) Studies of the RB1 gene and the p53 gene in human osteosarcomas. *Pediatric Hematology and Oncology* 9: 125–137.

Shah NP, Nicoll JM, Nagar B, Gorre ME, Paquette RL, Kuriyan J, and Sawyers CL (2002) Multiple BCR-ABL kinase domain mutations confer polyclonal resistance to the tyrosine kinase inhibitor imatinib (STI571) in chronic phase and blast crisis chronic myeloid leukemia. *Cancer Cell* 2: 117–125.

Shiozawa Y, Pedersen EA, Havens AM, Jung Y, Mishra A, Joseph J, Kim JK, Patel LR, Ying C, Ziegler AM, Pienta MJ, Song J, Wang J, Loberg RD, Krebsbach PH, Pienta KJ, and Taichman RS (2011) Human prostate cancer metastases target the hematopoietic stem cell niche to establish footholds in mouse bone marrow. *The Journal of Clinical Investigation* 121: 1298–1312.

Skalniak L, Kocik J, Polak J, Skalniak A, Rak M, Wolnicka-Glubisz A, and Holak TA (2018) Prolonged Idasanutlin (RG7388) treatment leads to the generation of p53-mutated cells. *Cancers (Basel)* 10.

Soki FN, Park SI, and McCauley LK (2012) The multifaceted actions of PTHrP in skeletal metastasis. *Future Oncology* 8: 803–817.

Spring L, Bardia A, and Modi S (2016) Targeting the cyclin D-cyclin-dependent kinase (CDK) 4/6-retinoblastoma pathway with selective CDK 4/6 inhibitors in hormone receptor-positive breast cancer: Rationale, current status, and future directions. *Discovery Medicine* 21: 65–74.

Stavnezer J (1996) Antibody class switching. *Advances in Immunology* 61: 79–146.

Stavnezer J (2011) Complex regulation and function of activation-induced cytidine deaminase. *Trends in Immunology* 32: 194–201.

Stavnezer J, Guikema JE, and Schrader CE (2008) Mechanism and regulation of class switch recombination. *Annual Review of Immunology* 26: 261–292.

Stopeck AT, Lipton A, Body JJ, Steger GG, Tonkin K, De Boer RH, Lichinitser M, Fujiwara Y, Yardley DA, Viniegra M, Fan M, Jiang Q, Dansey R, Jun S, and Braun A (2010) Denosumab compared with zoledronic acid for the treatment of bone metastases in patients with advanced breast cancer: A randomized, double-blind study. *Journal of Clinical Oncology* 28: 5132–5139.

Stratton MR, Campbell PJ, and Futreal PA (2009) The cancer genome. *Nature* 458: 719–724.

Sung H, Siegel RL, Rosenberg PS, and Jemal A (2019) Emerging cancer trends among young adults in the USA: Analysis of a population-based cancer registry. *The Lancet Public Health* 4: e137–e147.

Sutton MA, Watkins HL, Green LK, and Kadmon D (1996) Intracranial metastases as the first manifestation of prostate cancer. *Urology* 48: 789–793.

Svensson E, Christiansen CF, Ulrichsen SP, Rorth MR, and Sorensen HT (2017) Survival after bone metastasis by primary cancer type: A Danish population-based cohort study. *BMJ Open* 7: e016022.

Taddei G, Marzi S, Coletti G, De Paulis D, Ricci A, and Galzio RJ (2012) Brain metastasis from prostate adenocarcinoma: Case report and review of literature. *World Journal of Clinical Oncology* 3: 83–86.

Tisato V, Voltan R, Gonelli A, Secchiero P, and Zauli G (2017) MDM2/X inhibitors under clinical evaluation: Perspectives for the management of hematological malignances and pediatric cancer. *Journal of Hematology & Oncology* 10: 133.

Toguchida J, Yamaguchi T, Ritchie B, Beauchamp RL, Dayton SH, Herrera GE, Yamamuro T, Kotoura Y, Sasaki MS, Little JB, et al. (1992) Mutation spectrum of the p53 gene in bone and soft tissue sarcomas. *Cancer Research* 52: 6194–6199.

Tsuzuki S, Park SH, Eber MR, Peters CM, and Shiozawa Y (2016) Skeletal complications in cancer patients with bone metastases. *International Journal of Urology* 23: 825–832.

van Harn T, Foijer F, Van Vugt M, Banerjee R, Yang F, Oostra A, Joenje H, and Te Riele H (2010) Loss of Rb proteins causes genomic instability in the absence of mitogenic signaling. *Genes & Development* 24: 1377–1388.

Vignani F, Bertaglia V, Buttigliero C, Tucci M, Scagliotti GV, and Di Maio M (2016) Skeletal metastases and impact of anticancer and bone-targeted agents in patients with castration-resistant prostate cancer. *Cancer Treatment Reviews* 44: 61–73.

Walker BA, Boyle EM, Wardell CP, Murison A, Begum DB, Dahir NM, Proszek PZ, Johnson DC, Kaiser MF, Melchor L, Aronson LI, Scales M, Pawlyn C, Mirabella F, Jones JR, Brioli A, Mikulasova A, Cairns DA, Gregory WM, Quartilho A, Drayson MT, Russell N, Cook G, Jackson GH, Leleu X, Davies FE, and Morgan GJ (2015) Mutational spectrum, copy number changes, and outcome: Results of a sequencing study of patients with newly diagnosed myeloma. *Journal of Clinical Oncology* 33: 3911–3920.

Wang JY (2014) The capable ABL: What is its biological function? *Molecular and Cellular Biology* 34: 1188–1197.

Weigelt B, Glas AM, Wessels LF, Witteveen AT, Peterse JL, and Van'T Veer LJ (2003) Gene expression profiles of primary breast tumors maintained in distant metastases. *Proceedings of the National Academy of Sciences of the United States of America* 100: 15901–15905.

Yang Y, Yang R, Roth M, Piperdi S, Zhang W, Dorfman H, Rao P, Park A, Tripathi S, Freeman C, Zhang Y, Sowers R, Rosenblum J, Geller D, Hoang B, Gill J, and Gorlick R (2017) Genetically transforming human osteoblasts to sarcoma: Development of an osteosarcoma model. *Genes & Cancer* 8: 484–494.

Yoo C, Lee J, Rha SY, Park KH, Kim TM, Kim YJ, Lee HJ, Lee KH, and Ahn JH (2013) Multicenter phase II study of everolimus in patients with metastatic or recurrent bone and soft-tissue sarcomas after failure of anthracycline and ifosfamide. *Investigational New Drugs* 31: 1602–1608.

Zhang J, Yu XH, Yan YG, Wang C, and Wang WJ (2015) PI3K/Akt signaling in osteosarcoma. *Clinica Chimica Acta* 444: 182–192.

Zhang K, Zhang M, ZHU J, and Hong W (2016) Screening of gene mutations associated with bone metastasis in nonsmall cell lung cancer. *Journal of Cancer Research and Therapeutics* 12: C186–C190.

Zhang W, Bado I, Wang H, Lo HC, and Zhang XH (2019) Bone metastasis: Find your niche and fit in. *Trends Cancer* 5: 95–110.

Zullig LL, Jackson GL, Dorn RA, Provenzale DT, McNeil R, Thomas CM, and Kelley MJ (2012) Cancer incidence among patients of the U.S. veterans affairs health care system. *Military Medicine* 177: 693–701.

The Roles of Bone Marrow-Resident Cells as a Microenvironment for Bone Metastasis

5

Yusuke Shiozawa

Abstract

It has been appreciated that the cross talk between bone metastatic cancer cells and bone marrow microenvironment influence one another to worsen bone metastatic disease progression. Bone marrow contains various cell types, including (1) cells of mesenchymal origin (e.g., osteoblasts, osteocytes, and adipocytes), (2) cells of hematopoietic origin (e.g., osteoclast and immune cells), and (3) others (e.g., endothelial cells and nerves). The recent studies have enabled us to discover many important cancer-derived factors responsible for the development of bone metastasis. However, many critical questions regarding the roles of bone microenvironment in bone metastatic progression remain elusive. To answer these questions, a deeper understanding of the cross talk between bone metastatic cancer and bone marrow microenvironment is clearly warranted.

Y. Shiozawa (✉)
Department of Cancer Biology and Comprehensive Cancer Center, Wake Forest University Health Sciences, Winston-Salem, NC, USA
e-mail: yshiozaw@wakehealth.edu

5.1 Introduction

Bone metastasis is one of the major causes of cancer death. Full understanding of the underlying mechanisms of bone metastasis, however, remains unrevealed. The presence of micrometastatic cells in the marrow at early stage of cancer has been associated with a poor prognosis [1] since micrometastatic cells can result in full-blown bone metastases at later stage [2] and metastatic progression of these cells may be environmentally directed by influences from the bone marrow-resident cells (Fig. 5.1). Indeed, it has been suggested that the cross talk between bone metastatic cancer cells and bone marrow microenvironment plays a crucial role in regulating the dissemination cascade of cancer cells to the bone and the progression of micrometastatic cells within the bone [3–5].

Bone marrow contains many cell types, including cells of hematopoietic and mesenchymal origin. Interactions among these cells are crucial for regulating blood and bone formation. Osteoblasts [6–8], adipocytes [9, 10], endothelial cells [11, 12], and nerves [13, 14] are known to serve as a specific microenvironment for hematopoietic stem cells. Osteoblasts, osteoclasts, osteocytes, and endothelial cells collectively
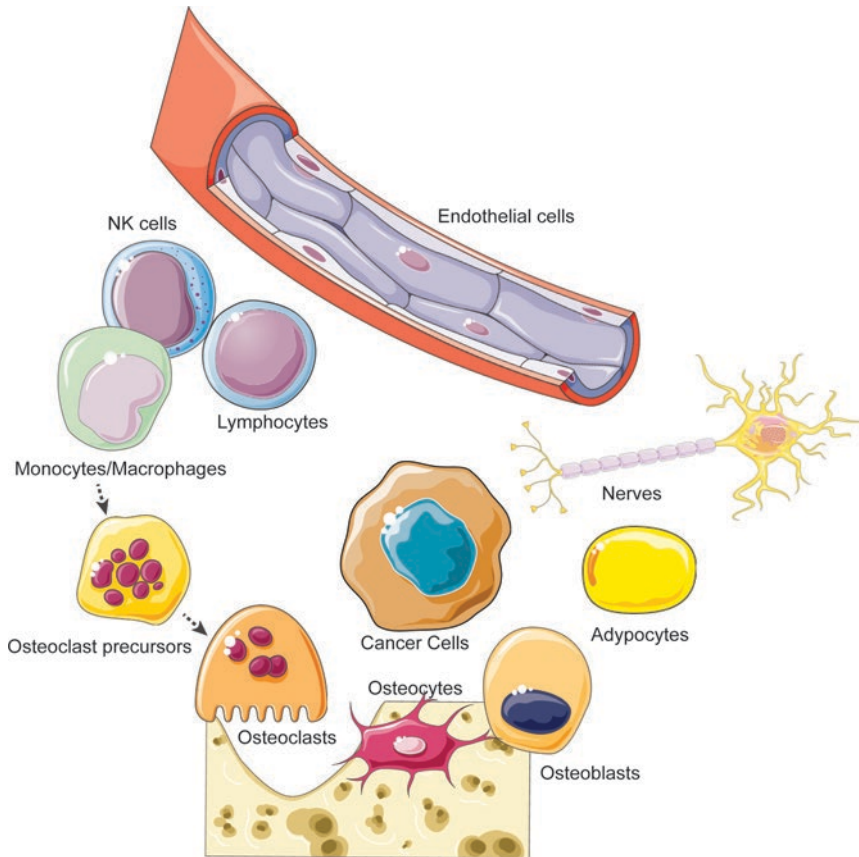
Fig. 5.1 The model of the bone marrow tumor microenvironment Bone marrow contains many cell types that directly influence blood formation (e.g., osteoblasts, adipocytes, endothelial cells, nerves) and bone formation (e.g., osteoblasts, osteocytes, osteoclasts, endothelial cells). Recent studies have revealed that bone metastatic cancer cells adopt mechanisms whereby these bone-resident cells maintain hematopoiesis and bone remodeling in order to gain access to and grow within the bone. Bone marrow-resident immune cells are also involved in the process of bone metastasis in both a direct and an indirect manner. By interacting one another, all these cells play crucial roles in controlling bone metastatic progression as a bone marrow tumor microenvironment. Graphics adapted from Smart Servier Medical Art (https://smart.servier.com/)

organize bone remodeling [15]. We have demonstrated that bone metastatic cancer cells target and commandeer the microenvironment for hematopoietic stem cells, using similar mechanisms whereby hematopoietic stem cells home to the marrow to gain access to the bone [16]. Furthermore, bone metastatic cancer cells cause "vicious cycle" of bone metastasis by disrupting the balance between normal osteoclastogenesis and osteoclastogenesis [17, 18]. These evidences suggest that a microenvironment in the marrow also conversely affects the development and progression of bone metastasis.

Stephen Paget famously hypothesized in his "seed and soil" theory that metastatic cancer cells (seed) seek a specific metastatic site (soil) in order to survive outside of the primary tumor site [19]. Although the molecular mechanisms whereby bone metastatic cancer cells (seed) disseminate to bone have been extensively studied, tumor-supportive roles of bone marrow microenvironment (soil) are still largely unknown. In this review, we will explore what is currently known about bone marrow microenvironment-mediated bone metastatic progression and also suggest future directions for the microenvironment-targeted therapies for bone metastatic disease.

5.2   Bone Marrow Tumor Microenvironment

5.2.1   Cells of Mesenchymal Origin

5.2.1.1   Osteoblasts

Osteoblasts are the cells of mesenchymal origin, responsible for new bone formation, and known to be involved in regulating the homing and maintenance of hematopoietic stem cells [20]. Several lines of evidence suggest that osteoblasts also play significant roles in the development of bone metastasis. When human prostate cancer cell line PC-3 cells (intracardiac injection) and hematopoietic stem cells (intravenous injection) were simultaneously injected into irradiated severe combined immunodeficient (SCID) mice, both PC-3 cells and hematopoietic stem cells homed to osteoblasts and localized very closely each other [16]. Moreover, PC-3 cells and human prostate cancer cell line C4-2B cells prevented the binding of hematopoietic stem cells to murine primary calvarial osteoblasts [16]. Likewise, more numbers of intracardially inoculated human prostate cancer cell line PC-3NW1 cells homed to lateral endocortical surfaces of tibia of athymic nude mice where more osteoblasts reside compared to medial endocortical surfaces [21]. However, there were no differences in between the minimum distance from disseminated PC-3NW1 cells to lateral endocortical surfaces and medial endocortical surfaces [21]. When animals were treated with a C-X-C motif chemokine receptor 4 (CXCR4) antagonist AMD3100, differential dissemination patterns of PC-3NW1 cells to lateral and medial endocortical surfaces were no longer detected, and the minimum distance from disseminated PC-3NW1 cells to both endocortical surfaces was extended [21]. When human breast cancer cell line MCF-7 cells were inoculated into athymic nude mice by an intra-iliac artery injection, they initially colonized to alkaline phosphatase (ALP)-positive/collagen I-positive osteoblasts through E-cadherin (MCF-7 cells) and N-cadherin (osteoblasts) interaction [22]. This cancer-to-osteoblast interaction activated mammalian target of rapamycin (mTOR) pathway, and mTOR inhibitors torin 1 and rapamycin delayed the early colonization of MCF-7 cells to osteoblasts [22]. Similarly, human prostate cancer cell line C4-2B4 cells [23] and human breast cancer cell line MDA-MB-231 cells [24] bound to murine pre-osteoblast cell line MC3T3-E1 cells through homophilic cadherin-11–cadherin-11 interaction.

The interaction between bone metastatic cancer cells and osteoblasts might be involved in the bone metastatic progression within the marrow. More PC-3 cells bound to murine primary calvarial osteoblasts obtained from Annexin II (Anxa2) wild-type mice than those from Anxa2 knockout mice, and PC-3 cells grew greater on Anxa2 wild-type osteoblasts [25]. When PC-3 cells were implanted into athymic nude mice with vertebral bodies obtained from either Anxa2 wild-type or Anxa2 knockout mice, more growth of PC-3 within Anxa2 wild-type vertebral bodies was observed compared to that within Anxa2 knockout vertebral bodies [25]. When receptor for Anxa2 were downregulated in PC-3 cells, metastatic burdens within athymic nude mice were inhibited [25]. Anxa2 treatments induced AXL expression, a receptor for growth arrest-specific 6 (GAS6), in PC-3 cells [26]. Similarly, when PC-3 cells were cocultured with MC3T3-E1 cells, PC-3 cells become dormant by upregulating AXL expression [27]. Additionally, when primary human osteoblasts were cocultured with PC-3 cells, the secretion of GAS6 from osteoblasts was increased [26]. The GAS6 (osteoblasts)/AXL (PC-3 cells) interaction induced the expression of transforming growth factor (TGF)-β1, TGF-β2, TGF-β receptor 2 (TGFBR2), and TGFBR3 in PC-3 cells [27]. TGF-β2 was responsible for osteoblast-mediated PC-3 dormancy [27]. Moreover, PC-3 cells became stemlike phenotype (CD133 positive/CD44 positive) on wild-type murine primary calvarial osteoblasts, while the conversion of PC-3 cells to stemlike phenotype was prevented when they were cocultured with osteoblasts obtained from GAS6 knockout mice [28]. The GAS6 derived from osteoblasts induced the conversion of PC-3 cells into stemlike phenotype by activating mTOR pathway through another GAS6 receptor, Mer [28]. When PC-3 cells were

implanted into SCID mice with vertebral bodies obtained from either GAS6 wild-type or GAS6 knockout mice, more stemlike PC-3 cells were observed near osteoblasts within GAS6 wild-type vertebral bodies [28]. When PC-3 cells pretreated with rapamycin were intracardially inoculated into SCID mice, the stemlike conversion of PC-3 cells within the bone marrow were diminished [28].

When Jagged1-overexpressing bone-tropic MDA-MB-231 subline SCP28 cells were cocultured with MC3T3-E1 cells, SCP28-derived Jagged1 induced interleukin 6 (IL-6) secretion from MC3T3-E1 by upregulating Hey1 (a downstream of notch pathway), resulting in the increased proliferation of SCP28 cells on MC3T3-E1 cells [29]. The γ-secretase inhibitor MRK-003, which abolishes notch activity [29], and human monoclonal anti-Jagged1 antibody 15D11 [30] attenuated (1) the increased proliferation of Jagged1-overexpressing SCP28 cells mediated by MC3T3-E1 cells and (2) bone metastatic burden of intracardially inoculated Jagged1-overexpressing SCP28 cells in athymic nude mice. Moreover, the combination of 15D11 and paclitaxel synergistically prevented bone metastatic progression of Jagged1-overexpressing SCP28 cells compared to 15D11 or paclitaxel alone [30]. Interestingly, 15D11 and paclitaxel combination also inhibited bone metastatic progression of low Jagged1-expressing parental SCP28 cells since paclitaxel induced Jagged1 expression in osteoblasts, leading to chemoresistance [30]. When osteoblasts were induced into senescence using a conditional transgenic mouse model [fibroblasts accelerate stromal-supported tumorigenesis (FASST) mouse: Col-Cre-ER^{T2} mouse x ROSAlox-stop-lox-p27^{Kip1} mouse], greater numbers of intracardially injected murine breast cancer cell line NT2.5 cells disseminated to bone [31]. In FASST mice, senescent osteoblasts indirectly enhanced the growth of disseminated NT2.5 cells by stimulating osteoclastogenesis via IL-6 production [31]. In addition, bone disseminated murine multiple myeloma cell line 5TGM1 cells (intravenous injection into C57BL/KaLwRijHsd mice) became dormant and consequently resistant to melphalan when they localized near osteoblasts [32]. However, when animals were treated with receptor activator of nuclear factor κ-B ligand (RANKL) to stimulate osteoclast activities, the dormancy of 5TGM1 cells was reversed [32]. These data suggest that osteoblasts are important for the early dissemination and colonization of bone metastatic cancer cells as well as the regulation of dormancy, stem cell-like conversion, and later disease outgrowth of bone metastatic cancer cells.

5.2.1.2 Osteocytes

Bone is a dynamic organ continuously remodeled throughout life. Bone remodeling is controlled by proper balance between osteoblastogenesis and osteoclastogenesis [15]. Osteocytes are also known to be involved in regulating bone remodeling. Osteocytes negatively regulate osteoblastic activities by releasing dickkopf-1 (DKK1) and sclerostin (inhibitors of Wnt pathway which are important for osteoblastic differentiation) and enhance osteoclastic resorption by releasing RANKL when they undergo programmed cell death [15, 33–35]. Osteocytes are the terminally differentiated cells of osteoblastic lineage and reside within the bone matrix [33–35]. Approximately 90–95% of adult skeletal tissues consist of osteocytes [33–35]. However, it has been only recently appreciated the roles of osteocytes as a tumor microenvironment. Osteocyte death and enhanced osteoclast activity were observed in osteolytic bone lesions of multiple myeloma patients [36]. Higher levels of pro-osteoclastogenesis cytokine IL-11 were found in bones of multiple myeloma patients with osteolytic lesions than those without osteolytic lesions [36]. Conditioned medium (CM) obtained from the coculture between human multiple myeloma cell line JJN3 cells and human pre-osteocyte cell line HOB-01 cells stimulated osteoclastic formation of human primary peripheral blood mononuclear cells by enhancing the secretion of IL-11 and C-C motif chemokine ligand 3 (CCL3) [36]. These data suggest that osteocytes create favorable environment for bone metastatic cancer cells by promoting osteolytic bone damage.

Osteocytes not only provide the environment for cancer but also directly influence cancer progression. CM obtained from murine osteocyte cell line MLO-Y4 cells stimulated in vitro cell proliferation of human prostate cancer cell lines (PC-3 and DU145) and human breast cancer cell lines (MDA-MB-231 and MCF-7) [37]. CM obtained from murine osteocyte cell line MLO-A5 cells also enhanced the proliferation of murine breast cancer cell line 4 T1.2 cells [38, 39]. However, when 4T1.2 cells were three-dimensional (3D) cocultured with MLO-A5 cells, the size of MLO-A5/4T1.2 spheroid was shrank [38, 39]. Additionally, in vitro 3D coculture system between human osteocytes and prostate cancer organoids revealed that prostate cancer organoids significantly impair bone structure through the induction of osteocyte apoptosis while promoting bone mineralization [40]. In this model, prostate cancer organoids significantly enhanced the protein expression of fibroblast growth factor 23 (FGF23) and DKK1 in osteocytes but reduced sclerostin [40]. However, these changes failed to be observed in 2D coculture conditions [40], suggesting that the 3D culture system provides a unique opportunity to study the interaction between osteocytes and cancer cells.

MLO-Y4 CM also enhanced the anchorage-independent growth, migration, and invasion of MDA-MB-231 cells and murine breast cancer cell line Py8119 cells [41]. These phenomenon were inhibited with bisphosphonate [alendronate and zoledronic acid (ZOL)] treatments and fluid flow-induced shear stress by opening connexin 43 hemichannels in osteocytes [41]. The growth of Py8119 cells in the bone mediated by intratibial injections was enhanced when cells were injected into osteocyte-specific connexin 43 knockout mice or mice with osteocyte-specific connexin 43 junction impairment [41]. Alendronate upregulated ATP release from MLO-Y4 cells, and this ATP inhibited the MLO-Y4 CM-mediated anchorage-independent growth, migration, and invasion and in vivo primary tumor growth of MDA-MB-231 cells and Py8119 cells through P2X7 receptors [42]. In addition, these were reversed by adenosine treat-ment [42]. ATP treatments prevented the growth of intratibially injected Py8119 cells [42]. Likewise, CM from MLO-Y4 cells primed with CM of human prostate cancer cell lines (PC-3 and C4-2B) induced the growth, migration, and invasion of PC-3 and C4-2B cells by upregulating growth-derived factor 15 (GDF15) in MLO-Y4 cells and enhancing early growth response 1 (EGR1) expression in prostate cancer cells [43]. When C4-2B cells were co-inoculated with murine primary osteocytes into the flank of mice, these osteocyte/C4-2B mixtures grow greater than C4-2B cells alone, due in part to the upregulation of EGR1 in C4-2B cells [43]. The growth of osteocyte/C4-2B mixture was diminished when GDF15 was downregulated in osteocytes [43]. When PC-3 or C4-2B cells were injected into the tibia of mice in which GDF15 expression in tibia was downregulated using siRNA, prostate cancer cell growth in bones and EGR1 expression in prostate cancer cells were decreased compared to those in bones infected with control siRNA [43]. However, MLO-A5-CM conversely reduced the migratory ability of 4T1.2 cells through type I collagen by downregulating SNAIL [an epithelial to mesenchymal transition (EMT) inducer] and upregulating phosphorylation of Akt [38, 39]. Further study is warranted to conclude the effects of osteocytes on migratory ability of bone metastatic cancer cells.

Osteocytes are mechanosensitive cells [33–35], and the impact of mechanical stress on tumor microenvironmental abilities of osteocytes has been elucidated. Fluid flow-induced shear stress stimulated the differentiation of MLO-Y4 cells regardless of the existence of CM derived from MDA-MB-231 in the culture [44]. Fluid flow-induced shear stress on the 3D coculture between MLO-Y4 cells and human umbilical vein endothelial cells (HUVECs) inhibited the extravasation of MDA-MB-231 cells [45–47]. This was in part due to the reduction of IL-6 in MLO-Y4 cells (chemoattractant for cancer cells; inhibition of osteoclast apoptosis), the reduction of intercellular adhesion molecule 1 (ICAM-1) in HUVECs (cancer cell adhesion to endothelial cells; inhibition of osteoclast apoptosis), and the reduction of matrix metallopeptidase 9 (MMP9) in

MDA-MB-231 cells (cancer cell migration; reduction of endothelial junctional integrity) [45–47]. When hydrostatic pressure was applied to MLO-Y4 cells, MLO-Y4-CM promoted the growth, migration, and invasion of human prostate cancer cell lines (PC-3, DU145, and LNCaP) in part due to the upregulation of CCL5 and MMP2 and MMP9 [48].

When human multiple myeloma cell line RPMI 8226 cells were cocultured with HOB-01 cells or MLO-Y4 cells, RPMI 8226 cells induced death of HOB-01 and MLO-Y4 cells by activating autophagy [49]. This multiple myeloma-induced osteocyte death and autophagy were inhibited by proteasome inhibitors, bortezomib, and MG 262 [49]. Consistently, multiple myeloma patients treated with regimens including bortezomib showed significantly higher osteocyte viability in the bone lesions compared to those treated with regimens without bortezomib ($p = 0.017$) [49]. Moreover, a combination agent of nanoparticle loaded with a natural compound, plumbagin and ZOL (PUCZP), prevented the MLO-Y4-mediated osteoclastogenesis of murine bone marrow monocytes mediated by downregulating of RANKL and sclerostin expression in MLO-Y4 cells [50]. PUCZP also attenuated bone metastatic progression and cancer-induced bone resorption in athymic nude mice intracardially inoculated with MDA-MB-231 cells by downregulating of RANKL and sclerostin expression in osteocytes, reducing osteoclastogenesis, and inducing apoptosis of tumor cells [50]. These findings suggest that targeting osteocytes is a potential new therapeutic strategy for bone metastatic disease.

5.2.1.3 Bone Marrow Adipocytes

Bone marrow is known to contain significant numbers of adipocytes. Bone marrow adipocytes take up about 70% of marrow space in adults [51] and serve as one of the major components of the bone marrow microenvironment for hematopoietic stem cells [9, 10]. However, the effects of bone marrow adipocyte on bone metastatic progression have been only recently uncovered [52–59]. Direct contact between human primary bone marrow mesenchymal stem cell (MSC)-derived adipocytes (BMMAs) and promyelocytic leukemia protein-retinoic acid receptor α (PML-RARα)-expressing human acute promyelocytic leukemia cell line U937/PR9 cells protected U937/PR9 cells from apoptosis through the leptin (adipocytes)/leptin receptor (leukemia) axis [60]. Additionally, BMMAs activated the phosphorylation of signal transducer and activator of transcription 3 (STAT3) and ERK mitogen-activated protein kinase (MAPK) in U937/PR9 cells [60]. Likewise, coculture with human primary BMMAs protected human acute monocytic leukemia cell line U937 cells from spontaneous apoptosis by increasing leukemia cells' free fatty acid intake and consequent fatty acid β-oxidation [61]. This is in part due to the upregulation of peroxisome proliferator-activated receptor γ (PPARγ), fatty acid binding protein 4 (FABP4), CD36, and B-cell lymphoma 2 (BCl2) genes; the phosphorylation of AMP-activated protein kinase (AMPK) and p38 MAPK; and the upregulation of antiapoptotic chaperone 70-kDa heat-shock protein (HSP70) [61]. Human primary BMMAs also supported the proliferation of human primary acute myeloid leukemia (AML) blasts by upregulating FABP4 in adipocytes and enhancing lipids intake and fatty acid β-oxidation in AML cells [62]. When connective tissue growth factor (CTGF) was downregulated in human bone marrow MSCs, these MSCs differentiated into adipocyte lineage [63]. When CTGF-downregulated MSCs were implanted with endothelial cells into the flank of nonobese diabetic/severe combined immunodeficiency (NOD/SCID) IL-2rγ^{null} (NSG) mice, they contained more adipocytes than the implants of CTGF-normal MSCs with endothelial cells [63]. Intravenously inoculated human AML cell line Molm13 cells and acute lymphoblastic leukemia cell line Nalm6 cells homed better to CTGF-downregulated MSC implants compared to those with CTGF-normal MSCs since adipocytic CTGF-downregulated MSC implants expressed higher levels of C-X-C motif chemokine ligand 12 (CXCL12) and leptin [63]. Moreover, bone marrow of multiple myeloma patients contained more adipocytes than that of healthy counterparts [64]. The 5TGM1 cells migrated toward CM

from murine pre-adipocyte cell line 3T3-L1 cells through CCL2 and CXCL12 [64]. When 5TGM1 cells were cocultured with 3T3-L1 cells, 3T3-L1 cells enhances the viability of 5TGM1 cells by activating β-catenin and inhibiting caspase3 in 5TGM1 cells [64]. When 5TGM1 cells primed with 3T3-L1 cells were intravenously injected into C57BL/KaLwRij mice, these 3T3-L1-primed 5TGM1 cells grew greater in the bone than those without 3T3-L1 priming [64]. These findings suggest that bone marrow adipocytes are also crucial components of microenvironment for hematopoietic malignancies, similar to their roles for hematopoietic stem cell [9, 10].

Recent studies have also revealed the impact of bone marrow adipocytes on bone metastatic progression on solid tumors. When MDA-MB-231 cells were cocultured with bone fragments obtained from patients who undergo hip replacement, MDA-MB-231 cells migrated toward bone fragments and extensively colonized within the bone marrow adipose tissue compartment [65]. When human bone marrow stromal cells were transformed into adipocytic lineage with omega-6 polyunsaturated fatty acid (PUFA) treatments, more PC-3 cells migrated toward these omega-6 PUFA-treated human bone marrow stromal cells [66, 67]. Additionally, more lipid intake of PC-3 cells from bone marrow stromal cells was observed [66, 67]. Murine primary BMMAs also induced glycolytic shift in human prostate cancer cell lines PC-3 and ARCaP(M) cells by upregulating glycolytic markers [enolase 2 (ENO2), lactate dehydrogenase (LDHa), hexokinase 2 (HK2), pyruvate dehydrogenase kinase 1 (PDK1), and phosphorylated pyruvate dehydrogenase (p-PDH)], increasing lactate release, reducing oxygen consumption rate, and decreasing ATP levels [68]. This was due to the upregulation of HIF-1α target genes [carbonic anhydrase 9 (CA9), vascular endothelial growth factor (VEGF), and glucose transporter 1 (GULT1)] [68]. Conversely, CM from PC-3 and ARCaP(M) cells promoted lipolysis in murine primary BMMAs by increasing free glycerol release, which was uptaken by prostate cancer cells [68]. Bone metastatic samples obtained from prostate cancer patients with bone metastases showed

higher levels of heme oxygenase 1 (HO-1; a protector from oxidative cell damage) compared to primary prostate tumors or samples from other metastatic sites [69]. When PC-3 and ARCaP(M) cells were cocultured with murine primary BMMAs, the expression of HO-1 and endoplasmic reticulum (ER) stress chaperone glucose-regulated protein 78 (GRP78; another protector from oxidative cell damage) was enhanced [69]. Adipocyte-induced oxidative stress and overexpression of HO-1 in PC-3 and ARCaP(M) cells promoted the invasion of these cells [69]. Similarly, CM of murine primary BMMAs induced the invasion of PC-3 cells by upregulating HO-1, IL-1β, and FABP4 but downregulating PPARγ in PC-3 cells [70]. Overexpression of HO-1 in PC-3 and ARCaP(M) cells also induced the enhanced levels of GRP78 and pro-survival factors Bcl-xl and survivin in prostate cancer cells. HO-1 overexpression significantly increased growth in the bone of intratibially injected PC-3 and ARCaP(M) cells compared to those with control vector infection [69].

Intratibial injections of PC-3 and ARCaP(M) cells into mice with high-fat diet (60 kcal% fat) showed the enhanced numbers of bone marrow adipocytes osteolytic lesions [71]. CM from PC-3 and ARCaP(M) cells stimulated the secretion of CXCL1 and CXCL2 from murine primary BMMAs, and BMMA-derived CXCL1 and CXCL2 induced osteoclastogenesis of murine bone marrow macrophages [71]. Along with this notion, when murine melanoma cell line B16-F10 cells were directly injected into the tibia of high-fat diet-fed C57BL/6 N mice, more growth of B16-F10 cells in the bone was observed along with the increased numbers of bone marrow adipocytes and osteoclasts, and enhanced osteolytic lesions, compared to those in the bone of C57BL/6 N mice with normal diet (10 kcal% fat) [72]. Additionally, serums of tumor-bearing mice with high-fat diet, and macrophages and osteoclasts found in their bone expressed higher levels of osteopontin than those from animals with normal diet [72]. Murine primary BMMAs induced IL-6 mRNA expression in B16-F10 cells, and higher serum IL-6 concentration was observed in of tumor-bearing mice with high-fat diet [72].

Neutralizing anti-osteopontin antibody and neutralizing anti-IL-6 antibody or Janus kinase 2 (JAK2; a downstream of IL-6) inhibitor AG490 reduced the enhanced B16-F10 growth in the bone of tumor-bearing mice with high-fat diet [72]. When B16-F10 cells were injected into C57BL/6 mice by intracardiac injection, the numbers of bone marrow adipocytes and the serum levels of leptin increased at day 7 of injection, and these increased adipocytes and leptin levels decreased by day 10 [73]. Similar trend was observed in osteoclast activities [73]. Interestingly, B16-F10 cells localized around bone marrow adipocytes [73]. Consistent with the observations in in vivo, CM from B16-F10 cells induced differentiation of murine primary BMMAs while mature BMMAs were dedifferentiated into immature BMMAs when they were cocultured with B16-F10 cells [73]. On the other hands, CM from murine primary BMMAs induced proliferation and accelerated cell cycle of B16-F10 cells [73]. Similarly, CM from murine primary BMMAs enhanced DNA synthesis of murine multiple myeloma cell line 5T33MM cells, stimulated their migration toward adipocyte CM, and protected from apoptosis [74]. These data suggest that bone marrow adipocytes also play an important role in the regulation of bone metastatic progression of solid tumors.

5.2.2 Cells of Hematopoietic Origin

5.2.2.1 Osteoclasts

Osteoclasts are the multinucleated cells derived from a monocyte/macrophage lineage and are associated with the development of osteolytic bone metastatic lesions. Osteoclasts are known to indirectly serve as a bone marrow tumor microenvironment. Osteoclasts create a sufficient space for bone metastatic cancer cells to grow by resorbing bone matrix [75]. Indeed, osteolytic bone metastatic lesions in athymic nude mice inoculated with SCP28 cells (intracardiac injection) were prevented by treatment of microRNA (miR)-141 and miR-219 which downregulated in activated osteoclasts, while miR-141 and miR-219 did not directly affect SCP28 cells prolifera-

tion [76]. Osteoclasts promote extracellular calcium release and create extracellular acidic environments during bone resorption. Higher levels of calcium-sensing receptor were observed in bone metastatic tumor samples of prostate cancer [77] and renal cell carcinoma patients [78] compared to primary tumor samples. Extracellular calcium stimulated the proliferation of human breast cancer cell lines BT474 and MDA-MB-231-1833 cells [79] and PC-3 cells [80] through calcium-sensing receptor. Extracellular pH promoted the spheroid and colony formation of PC-3 cells [81]. Although there is no direct evidence yet, these findings suggest that osteoclasts may also play a crucial role as a bone marrow tumor microenvironment in an indirect manner by developing extracellular high-calcium and extracellular acidic environments.

5.2.2.2 Immune Cells

It has been extensively studied antitumor or protumor effects of immune system at primary tumor site. Although bone marrow contains various immune cells, the cross talk between bone metastatic cancer cells and bone marrow immune cells remains largely unexplored. Higher numbers of CD4-positive/Foxp3-positive regulatory T (Treg) cells were found in the bone marrow of prostate cancer patients with bone metastases than that of patients without bone metastases [82]. Treg cells obtained from bone metastatic prostate cancer patients had greater migratory and proliferative capacities and were responsible for the inhibition of osteoclasts, resulting in osteoblastic bone lesions [82]. Contrary, RANKL levels in CD3-positive T cells within the marrow of BALB/c mice in which 4 T1 cells were inoculated into mammary fat pad were enhanced compared to those of mice inoculated with nonmetastatic 4T1subline, 67NR cells [83]. However, there were no changes in the numbers of CD3-, CD4-, and CD8-positive T cells between 4T1- and 67NR-bearing mice [83]. Consequently, the enhancement of RANKL in T cells increased osteoclastic activities in the marrow, leading to bone metastatic colonization of 4 T1 cells [83]. Intracardiac injection of 4 T1 cells into BALB/c mice increased the numbers of B220-positive/

CD11c-positive plasmacytoid dendritic cells (pDCs) and the increased CD4-positive T cells in their marrow [84]. pDCs and CD4-positive T cells produced osteolytic bone lesions and subsequently increased tumor burden and bone damage [84]. Depletion of pDCs with PDCA-1 antibody led to decreased tumor burden and bone damage by reducing the numbers of CD4-positive T cells and CD11b/Gr-1 double-positive myeloid-derived suppressor cells (MDSCs) and activating cytotoxic CD8-positive T cells in the marrow [84].

More number of CD11b/Gr-1 double-positive MDSCs were observed in the marrow of C57BL6/KaLwRij mice intravenously injected with 5TGM1 cells compared to non-tumor-bearing mice [85]. The MDSCs from 5TGM1-bearing mice showed greater potential to differentiate into mature and functional osteoclasts than those from control mice [85]. When 5TGM1-bearing MDSCs were delivered to 5TGM1-bearing mice, osteolytic bone lesions were further enhanced compared to 5TGM1-bearing mice without MDSC treatments [85]. Additionally, the enhancement of osteoclastic activities mediated by 5TGM1-bearing MDSCs both in vitro and in vivo were inhibited by ZOL treatments [85]. Likewise, CD11b/Gr-1 double-positive MDSCs obtained from bone marrow cells of BALB/c mice which were intracardially inoculated with 4T1 cells and developed bone metastases differentiated into osteoclasts by increasing NO levels, but not MDSC from lung of 4T1-bearing mice with bone metastases or from bone marrow of 4 T1-bearing mice without bone metastases [86].

In bone samples obtained from prostate cancer patients with bone metastases, more CD68-positive macrophages were observed near tumor mass and pathological woven bone [87]. When F4/80-positive macrophages were depleted in the macrophage Fas-induced apoptosis (MAFIA) mice with AP20187 treatments, the growth of murine prostate cancer cell line RM-1 cells (intratibial inoculation) in their bone and resultant osteolytic lesions were significantly reduced [88]. Similarly, F4/80-positive macrophage depletion by clodronate liposome treatments resulted in the reduction of the growth of intrati-bially injected RM-1 cells (into C57BL6 mice) and PC-3 cells (into athymic nude mice) [88]. However, contrarily to MAFIA mice, depletion of macrophages by clodronate liposome treatments increased bone volume [88] but reduced pathological woven bone development [87]. When CD169-positive macrophages were depleted in the CD169-diphtheria toxin receptor (DTR) mice with DT treatments, the woven bone development in RM-1-bearing bone (intratibial injection) were attenuated, while CD169 macrophage depletion did not affect the tumor growth in the bone [87]. The treatments of anti-mouse CD115 monoclonal antibody which only target murine myeloid cells also inhibited osteolytic bone metastatic progression in athymic nude mice intracardially inoculated with MDA-MB-231 cells [89]. The beneficial effects of anti-mouse CD115 monoclonal antibody were comparable to ZOL [89]. When marrow-resident F4/80-positive/CD206-positive pro-tumorigenic M2-like macrophages, which enhance prostate cancer proliferation by efferocytosis, were reduced by trabectedin treatments, the growth of PC-3 cells (intratibial or intracardiac injection) in the bone of athymic nude mice was attenuated [90]. However, trabectedin treatments failed to change osteoclastic activities in the tumor-bearing bones [90]. These findings suggest that bone marrow immune cells also support bone metastatic progression as a bone marrow tumor microenvironment directly in an immunosuppressive manner and indirectly by influencing bone remodeling.

5.2.3 Other Components of Bone Marrow Microenvironment

5.2.3.1 Endothelial Cells

Bone is a highly vascularized organ and subsequently supplies hematopoietic cells and cytokines produced in the marrow. Although the vasculature is known to be crucial for tumor growth and metastasis, little is known as to the roles of bone marrow endothelial cells as a tumor microenvironment. Human breast cancer cell lines MDA-MB-231 cells (orthotopic inocula-

tion) and HMT-3522-T4-2 cells (intracardiac inoculation) disseminated into the bones of NOD/SCID mice, and those disseminated tumor cells became dormant when they localized microvascular endothelium [3]. Consistently, HMT-3522-T4-2 cells stayed dormant on the organotypic bone microvascular mimic (the mixture of HUVECs and murine primary bone marrow stromal cells) [3]. More dormant HMT-3522-T4-2 cells were observed when they reside on the thrombospondin 1 (TSP-1)-expressing mature endothelium, while TGF-β1 and periostin-expressing immature neovascular tips accelerated the growth of HMT-3522-T4-2 cells [3]. Murine breast cancer cell line 4T07 cells (orthotopic inoculation) disseminated closer to vasculature compared to megakaryocytes or osteoblasts, within the marrow of BALB/c mice, and vasculature-resident 4T07 cells had more resistance to chemotherapy (Adriamycin plus cyclophosphamide, AC) [91]. Coculture between the organotypic bone microvascular mimic and HMT-3522-T4-2 cells treated with doxorubicin revealed that the induction of chemoresistance mediated by vasculature was not due to the cell cycle arrest but the binding with vasculature through the integrinβ1/von Willebrand factor axis and the integrinαvβ3/vascular cell adhesion molecule (VCAM)-1 axis [91]. Indeed, the resistance of 4T07 cells to AC regimen in the marrow of BALB/c mice were reversed by (1) the downregulation of integrinβ1 and integrinαv in 4T07 cells using shRNA and (2) the treatments of the integrinβ1 inhibitory antibody AIIB2 and integrinαvβ3 inhibitory antibody LM609 [91]. More branching and sprouting of bone marrow vessels along with tumor burden and osteolytic bone lesions were observed by volumetric computed tomography (VCT) in the femur of nude rat injected with MDA-MB-231 cells through femoral artery [92]. When MDA-MB-231-bearing rat were treated with anti-VEGF antibody bevacizumab, branching and sprouting of bone marrow vessels as well as tumor burden and osteolytic bone lesions were inhibited [92]. These findings suggest that bone marrow endothelial cells are involved in the regulation of dormancy, chemoresistance, and outgrowth of bone metastatic cancer cells.

5.2.3.2 Nerves

The importance of nerves for cancer progression has been appreciated [93]. The sympathetic nervous system regulates the metastatic process of prostate cancer to bone [94], and denervation can suppress tumorigenesis and metastasis [94–97]. Moreover, the roles of sympathetic nervous system in bone metastatic progression have recently begun to be revealed. Chronic immobilization stress and a nonselective β1/β2 adrenergic receptor agonist isoproterenol treatments enhanced the colonization of intracardially injected MDA-MB-231 cells to the bone of athymic nude mice through the RANK (cancer)/RANKL (bone) axis by inducing the RANKL expression in bones [98] However, chronic immobilization stress and isoproterenol treatments did not affect the growth of MDA-MB-231 cells in the bone [98]. The enhancement of tumor colonization mediated by isoproterenol treatments was also thought to be due to the increased neovascularization of tumor-bearing bones [99]. Consistently, isoproterenol stimulated the VEGF secretion of MC3T3-E1 cells and murine primary bone marrow stromal cells [99]. The tube formation of HUVECs was increased when they were treated with CM from isoproterenol-treated murine primary bone marrow stromal cells [99]. The tube formation was prevented when cultures were treated with an antibody targeting VEGF-A:VEGF receptor 2 signaling mcr84 [99]. Isoproterenol-induced increased neovascularization and enhanced tumor colonization of MDA-MB-231 cells were reversed in (i) osteoblastic-specific β2 adrenergic receptor knockout mice (Rag2 background) and (ii) Rag2 mice treated with mcr84 [99]. Isoproterenol-treated promoted the adhesion between murine primary bone marrow endothelial cells or murine endothelial cell line C166 cells and MDA-MB-231 cells in vitro [100]. The expression levels of adhesion molecules E-selectin and P-selectin in murine primary bone marrow endothelial cells and C166 cells were increased via β2 adrenergic receptor when they were treated with CM from isoproterenol-treated murine primary bone marrow stromal cells [100]. High levels of IL-1β were observed in the CM of isoproterenol-treated

murine primary bone marrow stromal cells, and IL-1β treatments enhanced E-selectin and P-selectin expression in C166 cells and promoted the adhesion between C166 cells and MDA-MB-231 cells [100]. Additionally, when PC-3 cells were cocultured with murine primary calvarial osteoblasts, their proliferation was slowed and most of them were in the G1 cell cycle phase [101]. Norepinephrine induced the proliferation and G2-M cell cycle of PC-3 cells cocultured with murine primary wild-type calvarial osteoblasts, while norepinephrine did not affect the proliferation and cell cycle of PC-3 cells cocultured with murine primary GAS6 knockout calvarial osteoblasts [101]. Since bone is a richly innervated organ, further investigations on the impact of nerves on bone metastatic progression are clearly warranted.

5.3   Conclusions and Future Directions

When cancer patients develop bone metastases, their prognosis is very poor. Current treatments for bone metastases mainly target bone remodeling. Denosumab (a human monoclonal antibody against RANKL) and bisphosphonates (which suppress osteoclast activity) are established treatments for bone metastases and are thought to work by decreasing bone resorption. However, they ultimately fail to improve overall survival [102, 103]. Only a new α-emitting radiopharmaceutical radium-223, which binds to hydroxyapatite in the marrow, can extend overall survival and then only by three months [104]. Thus, approaches that target factors other than bone remodeling are needed to lower mortality of cancer patients with bone metastases. In recent years, the supportive roles of immune cells, adipocytes, and nerves as a tumor microenvironment have been appreciated, and in the bone marrow, as described above, the interactions between these cells and bone metastatic cancer cells also seem to influence disease processes. Although further studies are clearly warranted, treatments targeting these bone marrow-resident cells, or in combination with bone-targeted therapies, may be new thera-peutic strategies for bone metastatic disease. A better understanding of how bone metastatic cancer and bone marrow microenvironment influence one another to worsen bone metastatic disease progression will aid in discovering new therapeutic targets for bone metastatic cancer—area in which current therapies are wanting—to decrease suffering and improve the survival of cancer patients with bone metastases.

References

1. Aguirre-Ghiso JA (2007) Models, mechanisms and clinical evidence for cancer dormancy. Nat Rev Cancer 7:834–846
2. Jemal A, Siegel R, Ward E, Hao Y, Xu J, Murray T, Thun MJ (2008) Cancer statistics, 2008. CA Cancer J Clin 58:71–96
3. Ghajar CM, Peinado H, Mori H, Matei IR, Evason KJ, Brazier H, Almeida D, Koller A, Hajjar KA, Stainier DY, Chen EI, Lyden D, Bissell MJ (2013) The perivascular niche regulates breast tumour dormancy. Nat Cell Biol 15:807–817
4. Sleeman JP (2012) The metastatic niche and stromal progression. Cancer Metastasis Rev 31:429–440
5. Sosa MS, Bragado P, Aguirre-Ghiso JA (2014) Mechanisms of disseminated cancer cell dormancy: an awakening field. Nat Rev Cancer 14:611–622
6. Arai F, Hirao A, Ohmura M, Sato H, Matsuoka S, Takubo K, Ito K, Koh GY, Suda T (2004) Tie2/angiopoietin-1 signaling regulates hematopoietic stem cell quiescence in the bone marrow niche. Cell 118:149–161
7. Calvi LM, Adams GB, Weibrecht KW, Weber JM, Olson DP, Knight MC, Martin RP, Schipani E, Divieti P, Bringhurst FR, Milner LA, Kronenberg HM, Scadden DT (2003) Osteoblastic cells regulate the haematopoietic stem cell niche. Nature 425:841–846
8. Zhang J, Niu C, Ye L, Huang H, He X, Tong WG, Ross J, Haug J, Johnson T, Feng JQ, Harris S, Wiedemann

LM, Mishina Y, Li L (2003) Identification of the haematopoietic stem cell niche and control of the niche size. Nature 425:836–841

9. Naveiras O, Nardi V, Wenzel PL, Hauschka PV, Fahey F, Daley GQ (2009) Bone-marrow adipocytes as negative regulators of the haematopoietic microenvironment. Nature 460:259–263

10. Zhou BO, Yu H, Yue R, Zhao Z, Rios JJ, Naveiras O, Morrison SJ (2017) Bone marrow adipocytes promote the regeneration of stem cells and haematopoiesis by secreting SCF. Nat Cell Biol 19:891–903

11. Kiel MJ, Yilmaz OH, Iwashita T, Yilmaz OH, Terhorst C, Morrison SJ (2005) SLAM family receptors distinguish hematopoietic stem and progenitor cells and reveal endothelial niches for stem cells. Cell 121:1109–1121

12. Nombela-Arrieta C, Pivarnik G, Winkel B, Canty KJ, Harley B, Mahoney JE, Park SY, Lu J, Protopopov A, Silberstein LE (2013) Quantitative imaging of haematopoietic stem and progenitor cell localization and hypoxic status in the bone marrow microenvironment. Nat Cell Biol 15:533–543

13. Katayama Y, Battista M, Kao WM, Hidalgo A, Peired AJ, Thomas SA, Frenette PS (2006) Signals from the sympathetic nervous system regulate hematopoietic stem cell egress from bone marrow. Cell 124:407–421

14. Mendez-Ferrer S, Lucas D, Battista M, Frenette PS (2008) Haematopoietic stem cell release is regulated by circadian oscillations. Nature 452:442–447

15. Sims NA, Walsh NC (2012) Intercellular cross-talk among bone cells: new factors and pathways. Curr Osteoporos Rep 10:109–117

16. Shiozawa Y, Pedersen EA, Havens AM, Jung Y, Mishra A, Joseph J, Kim JK, Patel LR, Ying C, Ziegler AM, Pienta MJ, Song J, Wang J, Loberg RD, Krebsbach PH, Pienta KJ, Taichman RS (2011) Human prostate cancer metastases target the hematopoietic stem cell niche to establish footholds in mouse bone marrow. J Clin Invest 121:1298–1312

17. Cook LM, Shay G, Araujo A, Lynch CC (2014) Integrating new discoveries into the "vicious cycle" paradigm of prostate to bone metastases. Cancer Metastasis Rev 33:511–525

18. Guise TA (2002) The vicious cycle of bone metastases. J Musculoskelet Neuronal Interact 2:570–572

19. Paget S (1889) The distribution of secondary growth in cancer of the breast. Lancet 1:571–573

20. Shiozawa Y, Taichman RS (2012) Getting blood from bone: an emerging understanding of the role that osteoblasts play in regulating hematopoietic stem cells within their niche. Exp Hematol 40:685–694

21. Wang N, Docherty FE, Brown HK, Reeves KJ, Fowles AC, Ottewell PD, Dear TN, Holen I, Croucher PI, Eaton CL (2014) Prostate cancer cells preferentially home to osteoblast-rich areas in the early stages of bone metastasis: evidence from in vivo models. J Bone Miner Res 29:2688–2696

22. Wang H, Yu C, Gao X, Welte T, Muscarella AM, Tian L, Zhao H, Zhao Z, Du S, Tao J, Lee B, Westbrook TF, Wong ST, Jin X, Rosen JM, Osborne CK, Zhang XH (2015) The osteogenic niche promotes early-stage bone colonization of disseminated breast cancer cells. Cancer Cell 27:193–210

23. Huang CF, Lira C, Chu K, Bilen MA, Lee YC, Ye X, Kim SM, Ortiz A, Wu FL, Logothetis CJ, Yu-Lee LY, Lin SH (2010) Cadherin-11 increases migration and invasion of prostate cancer cells and enhances their interaction with osteoblasts. Cancer Res 70:4580–4589

24. Tamura D, Hiraga T, Myoui A, Yoshikawa H, Yoneda T (2008) Cadherin-11-mediated interactions with bone marrow stromal/osteoblastic cells support selective colonization of breast cancer cells in bone. Int J Oncol 33:17–24

25. Shiozawa Y, Havens AM, Jung Y, Ziegler AM, Pedersen EA, Wang J, Wang J, Lu G, Roodman GD, Loberg RD, Pienta KJ, Taichman RS (2008) Annexin II/annexin II receptor axis regulates adhesion, migration, homing, and growth of prostate cancer. J Cell Biochem 105:370–380

26. Shiozawa Y, Pedersen EA, Patel LR, Ziegler AM, Havens AM, Jung Y, Wang J, Zalucha S, Loberg RD, Pienta KJ, Taichman RS (2010) GAS6/AXL axis regulates prostate cancer invasion, proliferation, and survival in the bone marrow niche. Neoplasia 12:116–127

27. Yumoto K, Eber MR, Wang J, Cackowski FC, Decker AM, Lee E, Nobre AR, Aguirre-Ghiso JA, Jung Y, Taichman RS (2016) Axl is required for TGF-beta2-induced dormancy of prostate cancer cells in the bone marrow. Sci Rep 6:36520

28. Shiozawa Y, Berry JE, Eber MR, Jung Y, Yumoto K, Cackowski FC, Yoon HJ, Parsana P, Mehra R, Wang J, Mcgee S, Lee E, Nagrath S, Pienta KJ, Taichman RS (2016) The marrow niche controls the cancer stem cell phenotype of disseminated prostate cancer. Oncotarget 7:41217–41232

29. Sethi N, Dai X, Winter CG, Kang Y (2011) Tumor-derived JAGGED1 promotes osteolytic bone metastasis of breast cancer by engaging notch signaling in bone cells. Cancer Cell 19:192–205

30. Zheng H, Bae Y, Kasimir-Bauer S, Tang R, Chen J, Ren G, Yuan M, Esposito M, Li W, Wei Y, Shen M, Zhang L, Tupitsyn N, Pantel K, King C, Sun J, Moriguchi J, Jun HT, Coxon A, Lee B, Kang Y (2017) Therapeutic antibody targeting tumor- and osteoblastic niche-derived Jagged1 sensitizes bone metastasis to chemotherapy. Cancer Cell 32:731–747. e6

31. Luo X, Fu Y, Loza AJ, Murali B, Leahy KM, Ruhland MK, Gang M, Su X, Zamani A, Shi Y, Lavine KJ, Ornitz DM, Weilbaecher KN, Long F, Novack DV, Faccio R, Longmore GD, Stewart SA (2016) Stromal-initiated changes in the bone promote metastatic Niche development. Cell Rep 14:82–92

32. Lawson MA, Mcdonald MM, Kovacic N, Hua Khoo W, Terry RL, Down J, Kaplan W, Paton-Hough J, Fellows C, Pettitt JA, Neil Dear T, Van Valckenborgh E, Baldock PA, Rogers MJ, Eaton CL, Vanderkerken

K, Pettit AR, Quinn JM, Zannettino AC, Phan TG, Croucher PI (2015) Osteoclasts control reactivation of dormant myeloma cells by remodelling the endosteal niche. Nat Commun 6:8983

33. Bonewald LF (2007) Osteocytes as dynamic multifunctional cells. Ann N Y Acad Sci 1116:281–290

34. Bonewald LF (2011) The amazing osteocyte. J Bone Miner Res 26:229–238

35. Chen X, Wang L, Zhao K, Wang H (2018b) Osteocytogenesis: roles of physicochemical factors, collagen cleavage, and exogenous molecules. Tissue Eng Part B Rev 24:215–225

36. Giuliani N, Ferretti M, Bolzoni M, Storti P, Lazzaretti M, Dalla Palma B, Bonomini S, Martella E, Agnelli L, Neri A, Ceccarelli F, Palumbo C (2012) Increased osteocyte death in multiple myeloma patients: role in myeloma-induced osteoclast formation. Leukemia 26:1391–1401

37. Cui YX, Evans BA, Jiang WG (2016) New roles of osteocytes in proliferation, migration and invasion of breast and prostate cancer cells. Anticancer Res 36:1193–1201

38. Chen A, Wang L, Liu S, Wang Y, Liu Y, Wang M, Nakshatri H, Li BY, Yokota H (2018a) Attraction and compaction of migratory breast cancer cells by bone matrix proteins through tumor-osteocyte interactions. Sci Rep 8:5420

39. Liu S, Fan Y, Chen A, Jalali A, Minami K, Ogawa K, Nakshatri H, Li BY, Yokota H (2018) Osteocyte-driven downregulation of snail restrains effects of Drd2 inhibitors on mammary tumor cells. Cancer Res 78:3865–3876

40. Choudhary S, Ramasundaram P, Dziopa E, Mannion C, Kissin Y, Tricoli L, Albanese C, Lee W, Zilberberg J (2018) Human ex vivo 3D bone model recapitulates osteocyte response to metastatic prostate cancer. Sci Rep 8:17975

41. Zhou JZ, Riquelme MA, Gu S, Kar R, Gao X, Sun L, Jiang JX (2016) Osteocytic connexin hemichannels suppress breast cancer growth and bone metastasis. Oncogene 35:5597–5607

42. Zhou JZ, Riquelme MA, Gao X, Ellies LG, Sun LZ, Jiang JX (2015) Differential impact of adenosine nucleotides released by osteocytes on breast cancer growth and bone metastasis. Oncogene 34:1831–1842

43. Wang W, Yang X, Dai J, Lu Y, Zhang J, Keller ET (2019) Prostate cancer promotes a vicious cycle of bone metastasis progression through inducing osteocytes to secrete GDF15 that stimulates prostate cancer growth and invasion. Oncogene 38:4540–4559

44. Wang W, Sarazin BA, Kornilowicz G, Lynch ME (2018) Mechanically-loaded breast cancer cells modify osteocyte mechanosensitivity by secreting factors that increase osteocyte dendrite formation and downstream resorption. Front Endocrinol (Lausanne) 9:352

45. Ma YV, Lam C, Dalmia S, Gao P, Young J, Middleton K, Liu C, Xu H, You L (2018a) Mechanical regulation of breast cancer migration and apoptosis

via direct and indirect osteocyte signaling. J Cell Biochem 119:5665–5675

46. Ma YV, Xu L, Mei X, Middleton K, You L (2018b) Mechanically stimulated osteocytes reduce the bone-metastatic potential of breast cancer cells in vitro by signaling through endothelial cells. J Cell Biochem. https://doi.org/10.1002/jcb.28034

47. Mei X, Middleton K, Shim D, Wan Q, Xu L, Ma YV, Devadas D, Walji N, Wang L, Young EWK, You L (2019) Microfluidic platform for studying osteocyte mechanoregulation of breast cancer bone metastasis. Integr Biol (Camb) 11(4):119–129

48. Sottnik JL, Dai J, Zhang H, Campbell B, Keller ET (2015) Tumor-induced pressure in the bone microenvironment causes osteocytes to promote the growth of prostate cancer bone metastases. Cancer Res 75:2151–2158

49. Toscani D, Palumbo C, Dalla Palma B, Ferretti M, Bolzoni M, Marchica V, Sena P, Martella E, Mancini C, Ferri V, Costa F, Accardi F, Craviotto L, Aversa F, Giuliani N (2016) The proteasome inhibitor bortezomib maintains osteocyte viability in multiple myeloma patients by reducing both apoptosis and autophagy: a new function for proteasome inhibitors. J Bone Miner Res 31:815–827

50. Qiao H, Cui Z, Yang S, Ji D, Wang Y, Yang Y, Han X, Fan Q, Qin A, Wang T, He XP, Bu W, Tang T (2017) Targeting osteocytes to attenuate early breast cancer bone metastasis by theranostic upconversion nanoparticles with responsive Plumbagin release. ACS Nano 11:7259–7273

51. Fazeli PK, Horowitz MC, Macdougald OA, Scheller EL, Rodeheffer MS, Rosen CJ, Klibanski A (2013) Marrow fat and bone--new perspectives. J Clin Endocrinol Metab 98:935–945

52. Falank C, Fairfield H, Reagan MR (2016) Signaling interplay between bone marrow adipose tissue and multiple myeloma cells. Front Endocrinol (Lausanne) 7:67

53. Falank C, Fairfield H, Reagan MR (2017) Reflections on cancer in the bone marrow: adverse roles of adipocytes. Curr Mol Biol Rep 3:254–262

54. Hardaway AL, Herroon MK, Rajagurubandara E, Podgorski I (2014) Bone marrow fat: linking adipocyte-induced inflammation with skeletal metastases. Cancer Metastasis Rev 33:527–543

55. Luo G, He Y, Yu X (2018) Bone marrow adipocyte: an intimate partner with tumor cells in bone metastasis. Front Endocrinol (Lausanne) 9:339

56. Masarwi M, Deschiffart A, Ham J, Reagan MR (2019) Multiple myeloma and fatty acid metabolism. JBMR Plus 3:e10173

57. McDonald MM, Fairfield H, Falank C, Reagan MR (2017) Adipose, bone, and myeloma: contributions from the microenvironment. Calcif Tissue Int 100:433–448

58. Morris EV, Edwards CM (2016) The role of bone marrow adipocytes in bone metastasis. J Bone Oncol 5:121–123

59. Soley L, Falank C, Reagan MR (2017) MicroRNA transfer between bone marrow adipose and multiple myeloma cells. Curr Osteoporos Rep 15:162–170

60. Tabe Y, Konopleva M, Munsell MF, Marini FC, Zompetta C, McQueen T, Tsao T, Zhao S, Pierce S, Igari J, Estey EH, Andreeff M (2004) PML-RARalpha is associated with leptin-receptor induction: the role of mesenchymal stem cell-derived adipocytes in APL cell survival. Blood 103:1815–1822

61. Tabe Y, Yamamoto S, Saitoh K, Sekihara K, Monma N, Ikeo K, Mogushi K, Shikami M, Ruvolo V, Ishizawa J, Hail N Jr, Kazuno S, Igarashi M, Matsushita H, Yamanaka Y, Arai H, Nagaoka I, Miida T, Hayashizaki Y, Konopleva M, Andreeff M (2017) Bone marrow adipocytes facilitate fatty acid oxidation activating AMPK and a transcriptional network supporting survival of acute monocytic leukemia cells. Cancer Res 77:1453–1464

62. Shafat MS, Oellerich T, Mohr S, Robinson SD, Edwards DR, Marlein CR, Piddock RE, Fenech M, Zaitseva L, Abdul-Aziz A, Turner J, Watkins JA, Lawes M, Bowles KM, Rushworth SA (2017) Leukemic blasts program bone marrow adipocytes to generate a protumoral microenvironment. Blood 129:1320–1332

63. Battula VL, Chen Y, Cabreira MDAG, Ruvolo V, Wang Z, Ma W, Konoplev S, Shpall E, Lyons K, Strunk D, Bueso-Ramos C, Davis RE, Konopleva M, Andreeff M (2013) Connective tissue growth factor regulates adipocyte differentiation of mesenchymal stromal cells and facilitates leukemia bone marrow engraftment. Blood 122:357–366

64. Trotter TN, Gibson JT, Sherpa TL, Gowda PS, Peker D, Yang Y (2016) Adipocyte-lineage cells support growth and dissemination of multiple myeloma in bone. Am J Pathol 186:3054–3063

65. Templeton ZS, Lie WR, Wang W, Rosenberg-Hasson Y, Alluri RV, Tamaresis JS, Bachmann MH, Lee K, Maloney WJ, Contag CH, King BL (2015) Breast cancer cell colonization of the human bone marrow adipose tissue Niche. Neoplasia 17:849–861

66. Brown MD, Hart C, Gazi E, Gardner P, Lockyer N, Clarke N (2010) Influence of omega-6 PUFA arachidonic acid and bone marrow adipocytes on metastatic spread from prostate cancer. Br J Cancer 102:403–413

67. Brown MD, Hart CA, Gazi E, Bagley S, Clarke NW (2006) Promotion of prostatic metastatic migration towards human bone marrow stroma by Omega 6 and its inhibition by Omega 3 PUFAs. Br J Cancer 94:842–853

68. Diedrich JD, Rajagurubandara E, Herroon MK, Mahapatra G, Huttemann M, Podgorski I (2016) Bone marrow adipocytes promote the Warburg phenotype in metastatic prostate tumors via HIF-1alpha activation. Oncotarget 7:64854–64877

69. Herroon MK, Rajagurubandara E, Diedrich JD, Heath EI, Podgorski I (2018) Adipocyte-activated oxidative and ER stress pathways promote tumor survival in bone via upregulation of Heme Oxygenase 1 and Survivin. Sci Rep 8:40

70. Herroon MK, Rajagurubandara E, Hardaway AL, Powell K, Turchick A, Feldmann D, Podgorski I (2013) Bone marrow adipocytes promote tumor growth in bone via FABP4-dependent mechanisms. Oncotarget 4:2108–2123

71. Hardaway AL, Herroon MK, Rajagurubandara E, Podgorski I (2015) Marrow adipocyte-derived CXCL1 and CXCL2 contribute to osteolysis in metastatic prostate cancer. Clin Exp Metastasis 32:353–368

72. Chen GL, Luo Y, Eriksson D, Meng X, Qian C, Bauerle T, Chen XX, Schett G, Bozec A (2016) High fat diet increases melanoma cell growth in the bone marrow by inducing osteopontin and interleukin 6. Oncotarget 7:26653–26669

73. Wang J, Chen GL, Cao S, Zhao MC, Liu YQ, Chen XX, Qian C (2017) Adipogenic niches for melanoma cell colonization and growth in bone marrow. Lab Investig 97:737–745

74. Caers J, Deleu S, Belaid Z, De Raeve H, Van Valckenborgh E, De Bruyne E, Defresne MP, Van Riet I, Van Camp B, Vanderkerken K (2007) Neighboring adipocytes participate in the bone marrow microenvironment of multiple myeloma cells. Leukemia 21:1580–1584

75. Maurizi A, Rucci N (2018) The osteoclast in bone metastasis: player and target. Cancers (Basel) 10

76. Ell B, Mercatali L, Ibrahim T, Campbell N, Schwarzenbach H, Pantel K, Amadori D, Kang Y (2013) Tumor-induced osteoclast miRNA changes as regulators and biomarkers of osteolytic bone metastasis. Cancer Cell 24:542–556

77. Feng J, XU X, Li B, Brown E, Farris AB, Sun SY, Yang JJ (2014) Prostate cancer metastatic to bone has higher expression of the calcium-sensing receptor (CaSR) than primary prostate cancer. Receptors Clin Investig 1

78. Joeckel E, Haber T, Prawitt D, Junker K, Hampel C, Thuroff JW, Roos FC, Brenner W (2014) High calcium concentration in bones promotes bone metastasis in renal cell carcinomas expressing calcium-sensing receptor. Mol Cancer 13:42

79. Kim W, Takyar FM, Swan K, Jeong J, Vanhouten J, Sullivan C, Dann P, Yu H, Fiaschi-Taesch N, Chang W, Wysolmerski J (2016) Calcium-sensing receptor promotes breast cancer by stimulating intracrine actions of parathyroid hormone-related protein. Cancer Res 76:5348–5360

80. Liao J, Schneider A, Datta NS, McCauley LK (2006) Extracellular calcium as a candidate mediator of prostate cancer skeletal metastasis. Cancer Res 66:9065–9073

81. Huang S, Tang Y, Peng X, Cai X, Wa Q, Ren D, Li Q, Luo J, Li L, Zou X, Huang S (2016) Acidic extracellular pH promotes prostate cancer bone metastasis by enhancing PC-3 stem cell characteristics, cell invasiveness and VEGF-induced vasculogenesis of BM-EPCs. Oncol Rep 36:2025–2032

82. Zhao E, Wang L, Dai J, Kryczek I, Wei S, Vatan L, Altuwaijri S, Sparwasser T, Wang G, Keller ET, Zou W (2012) Regulatory T cells in the bone marrow microenvironment in patients with prostate cancer. Oncoimmunology 1:152–161

83. Monteiro AC, Leal AC, Goncalves-Silva T, Mercadante AC, Kestelman F, Chaves SB, Azevedo RB, Monteiro JP, Bonomo A (2013) T cells induce pre-metastatic osteolytic disease and help bone metastases establishment in a mouse model of metastatic breast cancer. PLoS One 8:e68171

84. Sawant A, Hensel JA, Chanda D, Harris BA, Siegal GP, Maheshwari A, Ponnazhagan S (2012) Depletion of plasmacytoid dendritic cells inhibits tumor growth and prevents bone metastasis of breast cancer cells. J Immunol 189:4258–4265

85. Zhuang J, Zhang J, Lwin ST, Edwards JR, Edwards CM, Mundy GR, Yang X (2012) Osteoclasts in multiple myeloma are derived from Gr-1+CD11b+myeloid-derived suppressor cells. PLoS One 7:e48871

86. Sawant A, Deshane J, Jules J, Lee CM, Harris BA, Feng X, Ponnazhagan S (2013) Myeloid-derived suppressor cells function as novel osteoclast progenitors enhancing bone loss in breast cancer. Cancer Res 73:672–682

87. Wu AC, He Y, Broomfield A, Paatan NJ, Harrington BS, Tseng HW, Beaven EA, Kiernan DM, Swindle P, Clubb AB, Levesque JP, Winkler IG, Ling MT, Srinivasan B, Hooper JD, Pettit AR (2016) CD169(+) macrophages mediate pathological formation of woven bone in skeletal lesions of prostate cancer. J Pathol 239:218–230

88. Soki FN, Cho SW, Kim YW, Jones JD, Park SI, Koh AJ, Entezami P, Daignault-Newton S, Pienta KJ, Roca H, McCauley LK (2015) Bone marrow macrophages support prostate cancer growth in bone. Oncotarget 6:35782–35796

89. Fend, L., Accart, N., Kintz, J., Cochin, S., Reymann, C., Le Pogam, F., Marchand, J. B., Menguy, T., Slos, P., Rooke, R., Fournel, S., Bonnefoy, J. Y., Preville, X. & Haegel, H. 2013. Therapeutic effects of anti-CD115 monoclonal antibody in mouse cancer models through dual inhibition of tumor-associated macrophages and osteoclasts. PLoS One, 8, e73310

90. Jones JD, Sinder BP, Paige D, Soki FN, Koh AJ, Thiele S, Shiozawa Y, Hofbauer LC, Daignault S, Roca H, McCauley LK (2019) Trabectedin reduces skeletal prostate cancer tumor size in association with effects on M2 macrophages and efferocytosis. Neoplasia 21:172–184

91. Carlson P, Dasgupta A, Grzelak CA, Kim J, Barrett A, Coleman IM, Shor RE, Goddard ET, Dai J, Schweitzer EM, Lim AR, Crist SB, Cheresh DA, Nelson PS, Hansen KC, Ghajar CM (2019) Targeting the perivascular niche sensitizes disseminated tumour cells to chemotherapy. Nat Cell Biol 21:238–250

92. Bauerle T, Hilbig H, Bartling S, Kiessling F, Kersten A, Schmitt-Graff A, Kauczor HU, Delorme S, Berger MR (2008) Bevacizumab inhibits breast cancer-induced osteolysis, surrounding soft tissue metastasis, and angiogenesis in rats as visualized by VCT and MRI. Neoplasia 10:511–520

93. Boilly B, Faulkner S, Jobling P, Hondermarck H (2017) Nerve dependence: from regeneration to cancer. Cancer Cell 31:342–354

94. Magnon C, Hall SJ, Lin J, Xue X, Gerber L, Freedland SJ, Frenette PS (2013) Autonomic nerve development contributes to prostate cancer progression. Science 341:1236361

95. Hayakawa Y, Sakitani K, Konishi M, Asfaha S, Niikura R, Tomita H, Renz BW, Tailor Y, Macchini M, Middelhoff M, Jiang Z, Tanaka T, Dubeykovskaya ZA, Kim W, Chen X, Urbanska AM, Nagar K, Westphalen CB, Quante M, Lin CS, Gershon MD, Hara A, Zhao CM, Chen D, Worthley DL, Koike K, Wang TC (2017) Nerve growth factor promotes gastric tumorigenesis through aberrant cholinergic signaling. Cancer Cell 31:21–34

96. Saloman JL, Albers KM, Li D, Hartman DJ, Crawford HC, Muha EA, Rhim AD, Davis BM (2016) Ablation of sensory neurons in a genetic model of pancreatic ductal adenocarcinoma slows initiation and progression of cancer. Proc Natl Acad Sci U S A 113:3078–3083

97. Zhao CM, Hayakawa Y, Kodama Y, Muthupalani S, Westphalen CB, Andersen GT, Flatberg A, Johannessen H, Friedman RA, Renz BW, Sandvik AK, Beisvag V, Tomita H, Hara A, Quante M, Li Z, Gershon MD, Kaneko K, Fox JG, Wang TC, Chen D (2014) Denervation suppresses gastric tumorigenesis. Sci Transl Med 6:250ra115

98. Campbell JP, Karolak MR, Ma Y, Perrien DS, Masood-Campbell SK, Penner NL, Munoz SA, Zijlstra A, Yang X, Sterling JA, Elefteriou F (2012) Stimulation of host bone marrow stromal cells by sympathetic nerves promotes breast cancer bone metastasis in mice. PLoS Biol 10:e1001363

99. Mulcrone PL, Campbell JP, Clement-Demange L, Anbinder AL, Merkel AR, Brekken RA, Sterling JA, Elefteriou F (2017) Skeletal colonization by breast cancer cells is stimulated by an osteoblast and beta2AR-dependent neo-angiogenic switch. J Bone Miner Res 32:1442–1454

100. Clement-Demange L, Mulcrone PL, Tabarestani TQ, Sterling JA, Elefteriou F (2018) beta2ARs stimulation in osteoblasts promotes breast cancer cell adhesion to bone marrow endothelial cells in an IL-1beta and selectin-dependent manner. J Bone Oncol 13:1–10

101. Decker AM, Jung Y, Cackowski FC, Yumoto K, Wang J, Taichman RS (2017) Sympathetic signaling reactivates quiescent disseminated prostate cancer cells in the bone marrow. Mol Cancer Res 15:1644–1655

102. Fizazi K, Carducci M, Smith M, Damiao R, Brown J, Karsh L, Milecki P, Shore N, Rader M, Wang H, Jiang Q, Tadros S, Dansey R, Goessl C (2011) Denosumab versus zoledronic acid for treatment

of bone metastases in men with castration-resistant prostate cancer: a randomised, double-blind study. Lancet 377:813–822

103. Stopeck AT, Lipton A, Body JJ, Steger GG, Tonkin K, De Boer RH, Lichinitser M, Fujiwara Y, Yardley DA, Viniegra M, Fan M, Jiang Q, Dansey R, Jun S, Braun A (2010) Denosumab compared with zoledronic acid for the treatment of bone metastases in patients with advanced breast cancer: a randomized, double-blind study. J Clin Oncol 28:5132–5139

104. Parker C, Nilsson S, Heinrich D, Helle SI, O'sullivan JM, Fossa SD, Chodacki A, Wiechno P, Logue J, Seke M, Widmark A, Johannessen DC, Hoskin P, Bottomley D, James ND, Solberg A, Syndikus I, Kliment J, Wedel S, Boehmer S, Dall'oglio M, Franzen L, Coleman R, Vogelzang NJ, O'bryan-Tear CG, Staudacher K, Garcia-Vargas J, Shan M, Bruland OS, Sartor O, Investigators A (2013) Alpha emitter radium-223 and survival in metastatic prostate cancer. N Engl J Med 369:213–223